CLINICAL NEURAL SCAFFOLD ENGINEERING FOR OLFACTORY ENSHEATHING CELLS

by

JACQUELINE LI-LING KUEH

B.Sc. in Biomedical Sciences 2003
Western Michigan University, USA

SUBMITTED FOR A DEGREE

IN

DOCTOR OF PHILOSOPHY IN

NEUROLOGY and BIOENGINEERING

AT

UNIVERSITY COLLEGE LONDON, UK

FEBRUARY 2012

I confirm that the work presented in this thesis is my own. Where information has been derived from other sources, I confirm that this has been indicated in the thesis.

_____

JACQUELINE KUEH

Foreword

Transplantation of olfactory ensheathing cells is currently a promising approach to repair injury in spinal cord. In translating the potential of olfactory ensheathing cells, the twin necessities of (a) obtaining sufficient cells for transplantation and (b) the problem of bridging the large gaps present in spinal cord injuries has become the focus of my PhD project. In addressing these twin necessities, my project has had to bridge disciplinary fields which traditionally afford few instances of interaction which I could use as a template. In carrying out the work of this thesis I have had the privilege of acting as a bridge between my inspirational collaborators/mentors from the bioengineering field and those from the neurobiological field. For these necessities the two central sections of this thesis deal with (a) the questions of cell source and proliferation, and (b) designing and fabricating nanofibre scaffolds for the olfactory ensheathing cells.

Following the writing-up of this thesis, the part of the content of this thesis has been submitted for

a) two publications in the following journals:

- **Kueh JL**, Raisman G, Li Y, Stevens R and Li D. (2011) Comparison of bulbar and mucosal olfactory ensheathing cells using FACS and simultaneous antigenic bivariate cell cycle analysis. Glia. 59(11), 1658-1671.

- **Kueh JL**, Raisman G, Li D, Li Y, Stevens R. (2011) Directionality and bipolarity of olfactory ensheathing cells on electrospun nanofibres. Nanomedicine. Nanomedicine. Accepted on 25 November.

b) an intellectual property application with Science & Technology Facilities Council Innovation Office, UK:

- **Kueh JL**, Jenkins DW, McKean R, Loader I, Greenall JS, Stevens RS. (2009) *Bespoke Tissue scaffold for clinical grade spinal repair therapies.* UK. Intellectual Property Filing.

Abstract

Transplantation of olfactory ensheathing cells (OEC) is one of the most promising current approaches to repair spinal cord injury. The encouraging results from transplantation of OECs in animal models have led to several clinical applications of these cells in spinal cord injury. The first controlled clinical trial was carried out by Mackay-Sim, Féron and colleagues (Mackay-Sim *et al.*, 2008). A number of neurosurgical teams have also implanted foetal OECs (Huang *et al.*, 2003) or minced whole mucosal tissue (Lima *et al.*, 2006) into spinal injuries. So far the reported functional benefits are only moderate. The Mackay-Sim team reported no improvements while others reported minor improvements (including an ongoing trial by Pawel Tabakow's team in Poland; personal communication). The basic conclusion is that OEC transplantation is feasible and safe. However, in the studies where suspensions of OECs were used there were not enough cells to fill the lesion, and no materials were used to bridge the gaps. In order to progress to more effective transplants the two areas addressed in this thesis will be important – what is the best source of adequate numbers of cells, and what biomaterials can be used to bridge the gaps.

In addressing the twin necessities of (a) identifying the tissue source needed to provide sufficient cells for transplantation and (b) the problem of bridging the large gaps present in spinal cord injuries, the results of this study were directed towards two issues.

(a) The questions of cell source and proliferation were addressed by establishing the quantitative baseline for the yield of primary cultures from the olfactory bulb, and the whole and split olfactory mucosa and characterising the heterogeneity of these cultures in search for any difference between bulbar and mucosal OECs. The study of flow cytometric simultaneous antigenic bivariate cell cycle of purified OECs and ONFs from these four sources revealed the evolution of population heterogeneity and its strikingly differences between these four sources of primary tissue with additional populations that were not previously described. An unexpected highly proliferative p75+ population in the stripped mucosal epithelium was also characterised. Correlation study of the cell proliferation and population evolution revealed cell autonomous among the difference sources.

(b) The feasibility of a synthesis biomaterial for the deployment of OECs and olfactory nerve fibroblasts (ONFs) as a transplant was addressed by designing and developing an electrospun PLGA nanocomposite nanofibre construct with a myriad of microfabrication techniques, focusing on how OECs and ONFs can be deployed during tissue culture and transplantation. The techniques included nanocomposite electrospinning, replica moulding from photolithographed silicon mould, design of tissue-culture membrane insert, and laser ablation. The biocompatibility study showed that when grown on a fibre mesh structured at the nano-scale, OECs responded by adopting the elongated form comparable to that which occurs when the convey regenerating fibres cross small lesions in *in vivo* transplants.

Preliminary functional studies of using the nanocomposite nanofibers as a neural scaffold in the organotypic entorhino-hippocampus slice co-culture data provide an

indication that the nanofibres are compatible with tissue and allow migration of astrocytes and growth of nerve fibres.

These observations will be important in future attempts to derive larger cell populations for transplantation. The anticipated use of the OEC nanofibre prosthesis would be in the application of autologous human OECs for bridging the gap in spinal cord lesions.

Acknowledgements

First and foremost I would like to thank my parents for their love and support in understanding my desire to pursue my post-baccalaureate studies, no matter how different a world is from theirs. Not forgetting my siblings in Kuching, my London and Singapore friends, they have been my key source of emotional support, personal motivation and encouragement which I could only give my utmost and sincere gratitude to. Without Vivien, Lisa, Chun Kiat, How Hua, Sie Liang Lau, Eu-Gene Toh, Mr. Tsuyoshi and Mrs. Hisako Shinokubo, Tien-Ju Lin, Mehri Daryouzeh, Berlinda Gooi, Frank Schuurmans and Peter Ericson, it could not have been such a smooth and rewarding PhD journey.

I would like to extend my deepest gratitude to Prof Bob Stevens for giving me this career-changing opportunity to lead this multidisciplinary spinal cord injury (SCI) repair project with Prof Geoffrey Raisman. Through his instrumental role as a co-supervisor, his confident support and down-to-earth mentorship have nurtured me into an independent technologist. More importantly, I am sincerely grateful for the opportunity to be supervised under Prof Geoffrey Raisman. He, together with Dr Daqing Li, has bestowed upon me new set of academic spectacles to appreciate the complexity of neuroanatomy and challenge me to explore OEC from the bioengineering perspective in the context of SCI. The impact of Geoff's meticulous guidance and inspirational mentorship is evident in my eventual career path as a scientist in academic instead of the technology entrepreneurship, my first intended goal as a 1st-year PhD student. Toward the end of my PhD training, the everyday interaction with Geoff is a treasure of precious intellectual and life experiences for a budding researcher, like me. However time-consuming and troublesome it would have been for him, Daqing's unwavering mentorship brought upon a subtle renaissance within me. It was only through their kind support and valuable advice without which I would have never grasp the essence of scientific research and art of theory conceptualization. The period in Raisman's lab has not only developed me as a scientist, but also a mindful human being with a sensible purpose. I am deeply appreciative for Geoff, Bob and Daqing's dedication in shaping me.

I would also like to thank all the members of Science & Technology Facilities Council, Technology, Micro & Nanotechnology Centre, with extended gratitude to Derek Jenkins and Dr Rob McKean. They could not have offered me more than valuable insight on the microfabrication, technical wisdom on electrospinning and a warm friendship. Besides, I am also grateful to all the great and wonderful members of Spinal Repair Unit in UCL Institute of Neurology for all their technical help and scientific banters, with special thanks to Dr Ying Li, Dr Mie Yamamoto and Stuart Law. They made my IoN experience enriching one. I would also like to thank Dr Ayad Eddoudi from the FACS facility at UCL Institute of Child Health for his in-depth technical knowledge and guidance in flow cytometry and cell cycle analysis, Dr. Kevin O'Byrne at King's College for all the generous rounds of EtO sterilization, and last but not least, both Dr. Peter Munro at UCL Institute of Opathmology and Prof. Andy Forge at UCL Ear Institute for their technical wisdom and compassionated help in specimen preparation and scanning electron microscopy.

This journey won't have started with the *vis a tergo* from my research technician days with Prof Ariff Bongso and Dr Lawrence Stanton prior to my PhD. Prof Bongso's achievement as a pioneer scientist in human embryonic stem cells and Singapore's first high-technology entrepreneur has inspired me to pursue on the possibility of being a scientist and an entrepreneur. Larry's belief in my technical skills and potential as a researcher has propelled me so much closer to that possibility, as that invisible force is still evident till now. Both mentors were the catalytic reason I decided to pursue my PhD in translational research.

I would like to also express my sincere thanks to UCL Enterprise Society for adding an alternative dimension to my science – high-tech entrepreneurship. During my student presidency and student advisory from 2007-2011, I expand my network of academic to different "walks" of commercialization and made long-lasting friends that have worked on start-up ideas together. They are Dr Ali Azarbagendan, Dr Sara Ho, Jolenta Cheung, Dr Tina Qianwen Liu, Dr Ragni Ghosh and Barbara Ngouyombo. With this group of strong and remarkable individuals, it is the opportunity to lead them that I came to understand the necessity but also the wondrous in failures and the art of harnessing support from peers toward a common goal.

This PhD work and thesis was made possible from significant amount of funding from various agencies including STFC Technology Partnership Program and British Neurology Research Trust for my project funding and my stipend; and UCL Overseas Research Awards for my research graduate scholarship.

To Charles, Deshon and Sander,

may Knowledge be the beacon of your life.

Table of Contents

List of Figures

List of Tables

Chapter 1 Rationale for Repair of CNS injuries by Transplantation of Olfactory Ensheathing Cells.

The central nervous system nervous (CNS) system presents a unique tissue arrangement in which the cell bodies of the neurons give rise to long nerve fibres (axons). Injuries severing nerve fibres in the adult brain and spinal cord result in permanent functional deficits (Gale *et al.*, 1985; Anderson, 2004). To a large extent, the cell bodies survive injury to the nerve fibres and the cut proximal ends of the axons sprout. Such observations are evident in both acute and chronic spinal cord injury. At least some functional improvements occur in all acute and chronic patients (Lamothe et al. 2011; Marino et al. 1999; Pouw et al. 2011). These could be due to resumption of function in surviving pathways, or formation of new, abnormal connections (plasticity) (Cajal, 1911; Raisman, 1969; Ivanco & Greenough, 2000; Bareyre *et al.*, 2004). Given the long term nature of human spinal cord injuries, there are no animal models which reflect the clinical observations of muscle atrophy and deterioration of joints.

So far there is little evidence of regeneration of the originally cut fibres to their former destinations (Raineteau & Schwab, 2001; Hagg & Oudega, 2006; Raisman & Li, 2007). To the extent that the injury entirely destroys a pathway carrying unique information (e.g. such as an optic tract) then sprouting cannot restore function (Seiler *et al.*, 2010). Furthermore, the damages and disruptions lead to death of oligodendrocytes (demyelination), change the anatomical arrangement of astrocytes (to form glial scar) and also lead to production of matrix of damage-induced

molecules (inhibitory environment cue) (Raisman, 2001). The glial scar has the beneficial effect of closing off the CNS injury, restoring the blood brain barrier, preventing ingress of inflammatory cells, and maintaining the CNS ionic environment which is necessary for nervous impulse transmission. The ultimate goal of repairing CNS injuries is to establish channels through the glial scar so that nerve fibres can cross the lesion site.

The question of why cut axons do not regenerate to their original destinations is not fully agreed. Attempts to produce regeneration by adding growth factors or interventions such as cAMP to the nerve cells (e.g. (Lu *et al.*, 2004, 2005; Pearse *et al.*, 2004; Thuret *et al.*, 2006) have been extensively tried, but have not so far resulted in effective clinical protocols. For the work of this thesis I have followed up the idea that repair of CNS injuries could be achieved using transplantation of olfactory ensheathing cells (OECs) to restore glial pathways along which axons could regenerate.

1.1 Pathway Hypothesis

Raisman has proposed the 'pathway hypothesis,' which places the cause of the failure not on the ability of the nerve fibres to grow, but on the inability of the glial cells to provide a pathway which the cut fibres need to regenerate (Raisman & Li, 2007). This is based on the following logic:

1. When axons are cut, the denervated postsynaptic sites are reinnervated by sprouting of adjacent intact synaptic terminals (Raisman, 1969). This demonstrated that adult axons are capable of responding by generating new synapses.

2. Embryonic neural transplants are capable of forming correct patterns of connections in the adult hippocampus (Li *et al.*, 1994, 1995, 1996). This demonstrated that the adult CNS is capable of receiving correct patterns of connections.

3. Following Cajal's suggestion (Cajal, 1911), Aguayo and colleagues demonstrated that cut central axons in the visual system and the spinal cord would regenerate for long distances along transplants of peripheral nerve graft (David & Aguayo, 1981; Richardson *et al.*, 1984; Benfey *et al.*, 1985; Vidal-Sanz *et al.*, 1987; Aguayo *et al.*, 1991). These transplants contained Schwann cells which could therefore provide a pathway for CNS axons. This was later repeated by the Bunges groups (Levi *et al.*, 1994; Xu *et al.*, 1995; Chen *et al.*, 1996; Guest *et al.*, 1997), and also using transplants of cultured Schwann cells deployed on collagen biomatrices (Paino & Bunge, 1991).

4. The work with peripheral nerve grafts and Schwann cells revealed a further block to regeneration: the regenerating fibres were unable to leave the grafts, failing to form meaningful connections (Houle & Johnson, 1989; Xu *et al.*, 1997; Fortun *et al.*, 2009). This has been variously ascribed to (a) that the graft environment is more conducive to axon growth, so that the fibres do not leave it, and/or (b) there is a block to exit provided by the glial scar, or by other CNS molecules, such as myelin.

5. Inhibitory proteins to both myelin (Schwab, 2010) and astrocytic chondroitin sulphate proteoglycan (Crespo *et al.*, 2007) have been used in attempts to induce

regeneration of cut CNS axons. The most recent findings suggest that their beneficial effects are due to increased sprouting rather than true regeneration across the lesion site (Ghosh *et al.*, 2010).

1.2 Olfactory Ensheathing Cells

My own interest has been in olfactory ensheathing cells (OECs). These cells have been studied in detailed on their development ability to open glial scars and allow regeneration of cut central axons.

1.2.1 Anatomical Description of OEC

Olfactory neurons have a limited life span of around 1 month in rats and mice (Graziadei & Monti-Graziadei, 1978). When they die, new neurons originating from neuroepithelial precursors located in the olfactory epithelium successfully reinnervate the olfactory bulb and form functional synapses (Graziadei & Monti-Graziadei, 1978; Kosaka *et al.*, 1998). Fascicles of olfactory axons are being ensheathed throughout the PNS (Doucette, 1991) and into the CNS (Raisman, 1985) by a glial cell, later termed olfactory ensheathing cells (OECs) (Ramón-Cueto & Valverde, 1995).

Anatomically, OECs are found in two interconnected but distinct environments: olfactory bulb in CNS and olfactory mucosa in PNS. In animals and in human, OECs reside in the olfactory nerve layer and glomeruli of the olfactory bulb, and in the olfactory mucosal tissue, lining the nasal septum, closest to the cribriform plate (Figure. 1). Compared with rodents and canines, the OECs tend to be more scattered and less discrete in the human nasal lining (Figure. 1C,E vs. D; pink).

Figure 1: Comparison of the location of the olfactory mucosa and olfactory bulb in human and rat.
Photographs of (A) the lateral wall of a dissected cadaveric human nose, and (B) similar view of rat nose, dissected as in Section 2.1 of Material and Methods Chapter. Outlines (C, D, E) of the above photographs. C, through turbinates and D, through septum of the human nose. OM, olfactory mucosa (pink), OB, olfactory bulb (orange). CH, cerebral hemisphere; RM, respiratory mucosa. A, reproduced from Fig 7.24 in Gosling et al. 1985 with permission (see letter from publisher in Appendix).

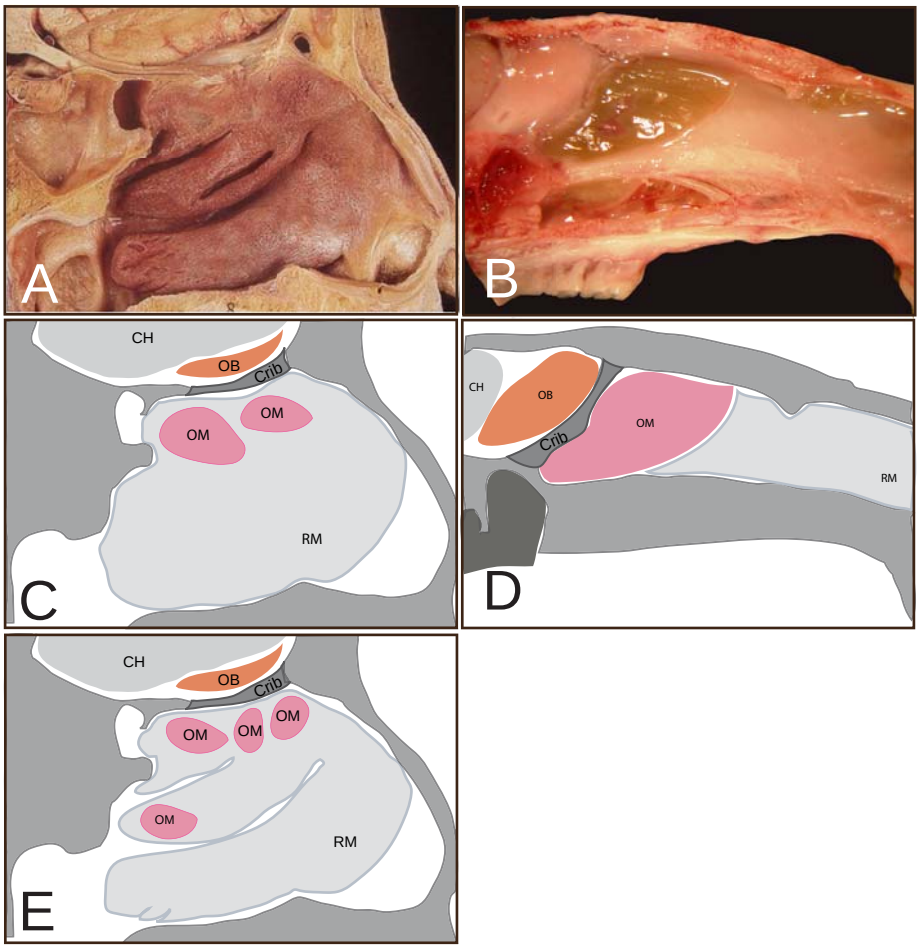
A
B
CH
OB
Crib
OM
OM
RM
C
CH
OB
Crib
OM
RM
D
CH
OB
Crib
OM
OM
OM
OM
RM
E

The histological finding of olfactory mucosa showed that whole mucosa (WM) *in situ* consists of two layers: a superficial layer olfactory epithelium (EPI) and a deeper layer, lamina propria (LP) (Choi *et al.*, 2008). Anatomically, the LP layer lies closer to the cribriform plate and the olfactory nerve layer at the bulb, when compared with the EPI layer. A biopsy-culture correlation study by Féron and colleagues revealed the mapping of the mucosal location with the highest percentage of OECs after screening from 23 healthy patients. Olfactory mucosal clusters are shown to be scattered around the ciliated respiratory mucosa on the turbinate bones (Féron *et al.*, 1998).

At the nano-scale level, OECs have a unique arrangement in which they give rise to very fine cytoplasmic processes that enclose huge numbers of unmyelinated olfactory axons (Raisman, 1985), as much as 1,000 axons per OEC. The special relationship with the olfactory nerve axons extends along from the peripheral, passing through the pores of the cribriform plate into CNS and as far as guiding those axons to their synaptic terminal in the glomeruli of the olfactory bulb (Raisman, 1985). At the synaptic terminals, the role of OEC is the intimate interaction with astrocytes, where processes from both cells interact and form a continuous channel for axons (Figure. 2)

The fasciculation of astrocytes on OEC-ensheathed axons is an attractive phenomenon for repairing spinal cord because of the potential for acting on the astrocytes of the ‘closed’ glial scar/gliosis. Astrocytic processes close over the injury by a glial-pia membrane. OECs have been shown to ‘open’ the glia scar,

Figure 2: Interaction of OECs and astrocytes
Schematic representation of the neuronal and glial relationships illustrating how the OECs (green) which convey the accessory olfactory axons (light grey) open the astrocytic 'door' (red) into a glomerulus of the olfactory bulb where they make synaptic contact with the mitral cell dendrites (dark grey). Adapted from Fig. 27 in Raisman 1985.

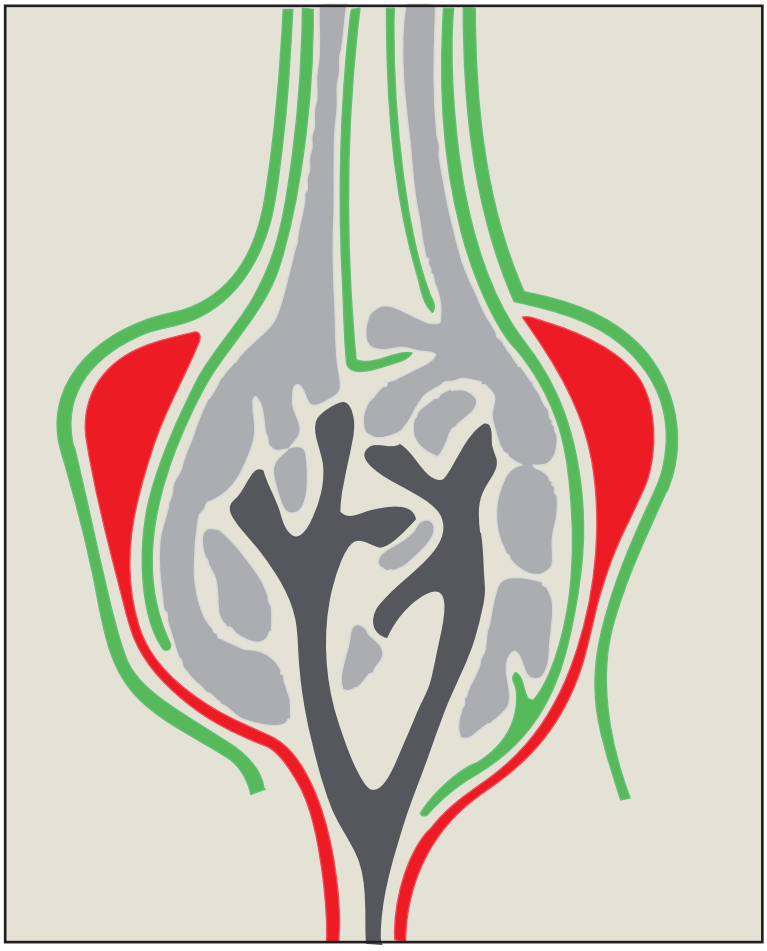

through their ability to form the same intimate interaction with astrocytes. Li et al 2005 demonstrated that interaction using severed dorsal roots, where numerous outgrowths of thick processes interweave intimately with the OEC processes, forming a ladder-like series of 'bridges'. These bridges serve as a conduit for the regenerating axons to enter from Schwann cell territory in PNS to the astrocytic environment in CNS (Li *et al.*, 2005*b*).

1.2.2 OEC as "Door Openers" of the Glial Scar

The extraordinary regenerative capacities of the adult olfactory system were demonstrated in the elegant studies of Graziadei (Graziadei & Monti Graziadei, 1980). It is known that the adult olfactory system is capable of replacing lost neurosensory cells and their axons can regenerate into the olfactory bulb and restore connections and functions (Doucette *et al.*, 1983). In fact not only after injury but also continuously throughout adult life olfactory neurosensory cells die and are replaced by newly formed cells whose axons grow along the olfactory ensheathing cells into the olfactory bulbs.

The pathway cells used by the olfactory axons are called OECs. They were first cultured by Doucette (Doucette & Devon, 1994). Subsequently cultures containing OECs and the accompanying olfactory nerve fibroblasts (ONFs; (Li *et al.*, 2005*a*)) have been transplanted into experimental CNS lesions. A number of groups have had success at re-establishing connections and restoring functions both in spinal cord and spinal roots (Ramón-Cueto *et al.*, 2000; Smith *et al.*, 2002; Lakatos *et al.*, 2003; Keyvan-Fouladi *et al.*, 2003; Radtke *et al.*, 2004; Boyd *et al.*, 2004; Richter *et al.*,

2005; Ibrahim *et al.*, 2009; Mackay-Sim & St John, 2011). Others have not achieved these positive results (Riddell *et al.*, 2004; Lu *et al.*, 2006).

The histological analysis of their transplants in the Li and Raisman series of papers shows that the OECs and ONFs cooperate to form a pathway which resembles peripheral nerve (Li *et al.*, 1998, 2003*b*), and, in the case of the corticospinal tract (but not the optic nerve) myelinates the CNS axons with peripheral type (P0 positive) myelin (Li *et al.*, 1998). In the successful rat studies the transplants formed a continuous bridge across the lesion site (Ramón-Cueto *et al.*, 1998; Plant *et al.*, 2003; Li *et al.*, 2003*a*).

If the OEC transplants are delayed until after the scar has formed the fibres still regenerate (Keyvan-Fouladi *et al.*, 2003). This indicates that the transplanted cells are able to 'open' the glial scar.

The possible variations of OECs along the olfactory pathway are not fully understood (Windus *et al.*, 2010). The original positive results were with OECs from the olfactory bulb. This involved access to an intracranial site, which would be less desirable for human application. However, OECs derived from the olfactory mucosa (which can be accessed through the nostrils; (Féron *et al.*, 2005) were less convincing, from the histological evidence (Yamamoto *et al.*, 2009). Whether mucosal OECs can be made effective at repair, or whether bulbar cells will be required for clinical application is currently a matter of discussion and investigation (Ramón-Cueto, 2011).

OECs are one of the most promising candidates for progression to clinical application. Following a clinical trial by Mackay-Sim et al (Mackay-Sim *et al.*, 2008), a number of neurosurgeons have used these cells in spinal cord injuries (Huang *et al.*, 2006*a*; Lima *et al.*, 2006) and a further clinical trial is underway in Poland (Pawel Tabakow, personal communication). In general the functional results of these trials are either no improvement or minor sensory improvement (3 dermatomes).

The limiting factor in these trials is that there are insufficient cells to fill the large gaps between the spinal cord stumps (Lima *et al.*, 2006). The purpose of my study is to try to identify the progenitor of adult OECs and to explore the use of electrospun nanocomposite (quantum dot) nanofibres as a biomaterial on which the cultured OECs could be deployed as a 'prosthesis' that simulates its development niche. This would enable the small number of cells available to be spread and cover the largest possible distance, preferably aligned in the axis needed for the regenerating fibres, and placed accurately and retained efficiently when transplanted.

Chapter 2 Experimental Methods

2.1 Primary olfactory cell preparation and cell culture

All animal procedures were performed in accordance with the UK Home Office regulations and guidelines. Female adult Albino Swiss rats (200-250g) were terminally anesthetized by intraperitoneal injection of 2-2.5ml of 2% Avertin (tribromoethanol) and the heads removed from the body for tissue collection under semi-sterile conditions in a fume hood.

The cranial structure was then stripped free from the skin, muscle and connective tissue using a pattern scissors and bone trimmer, exposing the upper part of cranium without the mandible. At the long axis the cranium was splitted into the half vertically between the incisors. The zygomatic bone, the premaxilla, maxillary and molars were first trimmed off to allow for the removal of the frontal bone and respiratory turbinates, revealing the respiratory and the olfactory mucosa on the septum.

2.1.1 Adult olfactory mucosa

The whole olfactory mucosal tissue sample was collected from the upper posterior surface of the nasal septum (Figure. 1D). The area with yellow colouration closest to the cribriform plate was separated from anteriorly placed translucent respiratory epithelium using a scalpel blade and collected into the complete culture medium made up of 10% foetal bovine serum (FBS) in DMEM/F12 supplemented with 1%

insulin-transferrin-selenium and 1% penicillin-streptomycin (all from Invitrogen, UK). The mucosal tissue was then washed twice in ice-cold Hank's balanced salt solution ([-] $CaCl_2$, [-] $MgCl_2$) supplemented with 1% penicillin-streptomycin (HBSS; Invitrogen) to remove excessive mucus. The separation of the mucosal tissue is illustrated in Figure. 3A.

2.1.1.1 Whole mucosa (WM):

The washed WM tissue was spread on a sterilized PVC cutting table disk and chopped at the thickness of 0.1mm using a McIlwain tissue chopper. The WM fragments were collected into a solution of 0.05% collagenase (Type I, 2.5g/ml; Sigma-Aldrich UK) in the complete medium and after incubating at 37°C for 5min, triturated consecutively 10-15 times using a 1000µl pipette and 5-8 times a 200µl pipette into cell suspension.

2.1.1.2 Lamina propria (LP) and epithelium (EPI):

Based on (Féron *et al.*, 1999) and (Li *et al.*, 2008), WM was incubated in dispase II solution (2.4 unit/ml; Roche UK) for 45min at 37°C and the superficial EPI layer and the underlying LP layer were gently separated using a microspatula under a Zeiss stereo microscope. LP tissue was transferred into HBSS to rinse off the remaining dispase, spread out on the cutting disk and chopped at the thickness of 0.1mm. The chopped LP fragments were further digested with collagenase and triturated into a cell suspension as with WM culture. The remaining EPI tissue was triturated into cell suspension in the dispase solution before they were transferred and washed in the whole medium.

Figure 3: Schematic illustrations of the derivation of the four tissue sources for the primary cultures.
A, septal olfactory mucosa cultured whole or separated into epithelium (EPI) and lamina propria (LP). B, separation of glomerular layer from the olfactory bulb. Grey arrows, dissection steps, black arrows, cells dissociation steps.

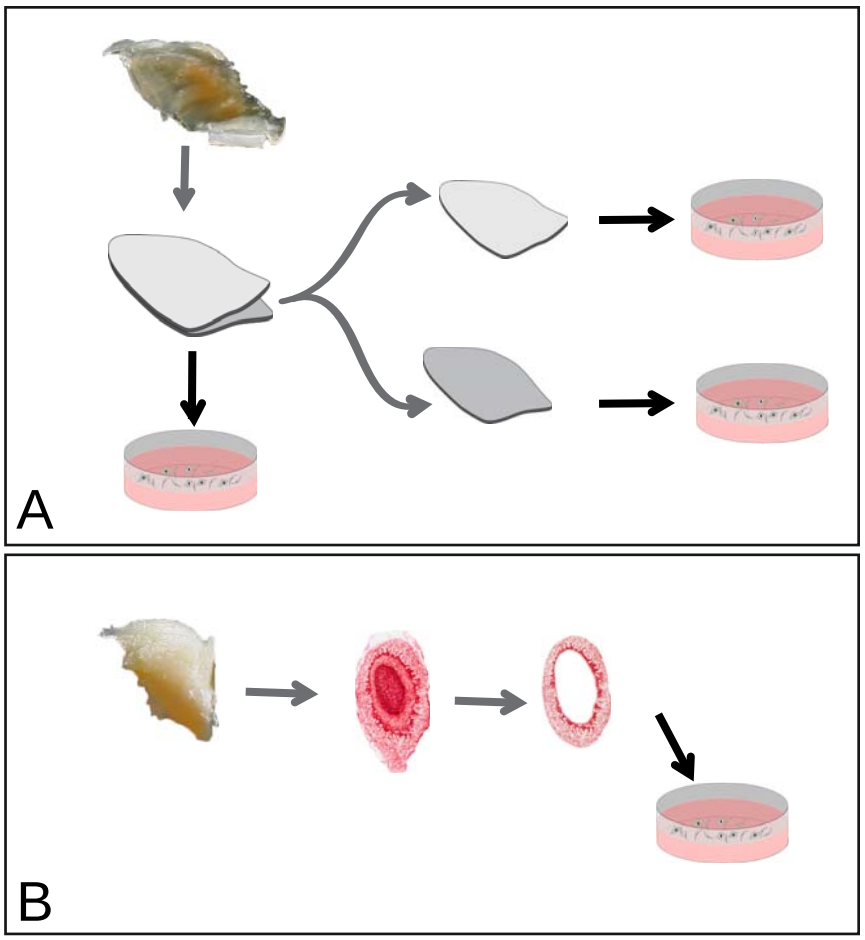
A
B

WM and LP cells were seeded at the density of 27,000 cells per cm^2 in 60mm poly-L-lysine (pLL) coated dishes and EPI cells at a much higher cell density of 270,000 cells per cm^2, as lower cell density for EPI culture has been shown to cause senescence (Rubio *et al.*, 2008).

2.1.2 Adult olfactory bulb

Culture was established as described in (Li *et al.*, 2003*a*). Through a dorsal craniotomy, the olfactory bulbs were severed from the brain and lifted off from the cribriform plate into ice cold Hank's Balanced Salt Solution (HBSS). In a sterile environment on a cold plate, the meninges around the bulb were carefully peeled off, the olfactory nerve fibre and glomerular layers were dissected out (Figure. 3B) and cut into $2mm^2$ fragments which were then incubated in 0.25% trypsin/EDTA solution (TE; Invitrogen) and DNase I (Sigma) at 37°C for 10min with intermittent trituration to facilitate the enzymatic activity. After triturating the tissue by passing them 5-8 times through a series of fire-polished Pasteur pipette tips, stopping trypsinization by adding the whole medium, spinning down and discarding the supernatant the precipitated cell pellet was re-suspended in the whole medium. The cells from 2 bulbs were seeded on to a 60mm poly-D-lysine (pDL) coated dish (Figure. 2B).

All cultures were maintained in the whole culture medium in a humidified incubator enriched with 5% CO_2 at 37°C and the culture medium was replaced every 3d. At the first two medium changes the cell containing supernatant was spun down, and the cells resuspended in fresh medium and replated.

2.2 Immunocytochemistry

For immunocytochemistry cells were fixed with 4% paraformaldehyde for 20min, washed three times in phosphate-buffered saline (PBS; TAAB, UK), permeabilized and blocked with 2% skim milk in PBS containing 0.1% Triton X-100 (TAAB). Primary antibodies were applied for 2h at room temperature (RT) or overnight at 4°C. Cells were washed three times and incubated with appropriate species fluorescent secondary antibodies for 1h at RT in the dark. After washing twice, cells were counter-stained and mounted using ProLong® Gold Antifade with DAPI (Invitrogen).

Primary antibodies were 1:250 mouse anti low affinity nerve growth factor receptor (anti-p75; clone 192-IgG Chemicon, Millipore, UK), 1:200 mouse anti-Thy1 (IgG clone MRC OX-7; AbCam, UK), 1:500 rabbit anti-S100β Ig (Dako, UK), 1:1000 rabbit anti-fibronectin Ig (FN; Dako), and 1:200 mouse anti-nestin (clone rat-401; Chemicon, Millipore). Secondary antibodies were Alexa Fluor 488 and Alex Fluor 546 chicken anti-mouse IgG, Alexa Fluor 546 goat anti-rabbit IgG, and Alexa Fluor 488 donkey anti-goat IgG (all 1:400; Molecular Probes, Invitrogen).

2.3 Antigenic fluorescent activated cell analysis

Fluorescent activated cell analysis and cell sorting was based on two surface markers, p75 and Thy1(Nash *et al.*, 2001; Au & Roskams, 2003; Ramer *et al.*, 2004; Rege & Hagood, 2006; Soleimani *et al.*, 2008). Cultures were washed three times with PBS and incubated in TE for 5min to lift the cells from culture dishes. TE activity was inactivated by adding the complete culture medium. Cell clusters were

triturated to obtain single-cell suspension and washed with ice-cold sterile PBS. A small aliquot of cells was counted using Trypan Blue and the concentration adjusted to 10^6 viable cells per ml for flow cytometric analysis.

Cells were fixed with freshly prepared cold 2% paraformaldehyde and washed in PBS prior to blocking with fresh cold 5% bovine serum albumin (BSA) and 2% FCS in PBS. The cultures were incubated with mouse anti-p75 (1:150, Chemicon, UK) diluted in 3% BSA and 2% FBS in PBS for 45min in the dark on ice, washed and incubated with Alexa Fluor 488 goat anti-mouse IgG (1:200, Molecular Probes, Invitrogen, UK) in the dark on ice 30min. The cells were washed twice to remove excessive antibody. Single labelled cells were used to calibrate the gating.

For dual labelling cells singly labelled for p75 as above were further blocked using mouse serum overnight at 4°C followed by mouse anti-Thy1 IgG, clone MRC OX-7, conjugated with phycoerythrin (Thy1-PE, 1: 150; AbCam, UK) for 45min on ice in the dark. (Thy1-PE was selected instead of its unconjugated clone (AbCam ab225) to avoid primary antibody host (Ms) cross reactivity with Ms anti p75-365 in dual immunolabelling steps.) After a quick wash with ice-cold PBS, the cells were re-suspended in cold 3% BSA, 2% FCS, and then filtered using 40μm cell strainers (BD Biosciences, UK), ready for analysis.

Fluorescent activated cell analysis of the fixed labelled cells was performed on a BD LSR II Flow Cytometer with FACSDiva software. Flow rate were kept on 250-400 events per second. A total of 30,000 events were acquired for each sample. Gating

was calibrated based on control (Figure. 4A and B; see Section 3.2.5 for detailed experimental analysis for selected antibodies).

2.4 Flow cytometric bivariate simultaneous antigenic and cell cycle assay

Click-IT^{TM} EdU flow cytometry assay (Pacific blue kit, Invitrogen, UK) was used for simultaneous identification of cell cycle markers in antigenically labelled OECs and ONFs after 7, 10 and 14d in the primary cultures (approx 10^6 cells). The mechanism of assay is 1) discriminate DNA content into cell cycle phases (G1/0, S and G2/M) using propidium iodide (PI-AF633), 2) detects the uptake Pacific-blue-tagged EdU into DNA of proliferating cells by replacing thymidine with EdU, and then 3) recognize the p75 and Thy1 surface marker of these PI and EdU-tagged cells.

1. The cultures were incubated for one hour with 5-ethynyl-2′-deoxyuridine (EdU) at a final concentration of 10μM, harvested with 0.25% TE, and then inactivated with the complete culture media.
2. p75 antigenic surface marker labelling of OECs was performed as described above.
3. The cultures were fixed with Click-IT fixative and permeabilized using Click-IT saponin based permeabilization solution. EdU was labelled with Pacific Blue azide. After incubating with RNAse A, total DNA was detected by staining with CellCycle 633-red.
4. Thy1-PE antigenic surface marker labelling of ONFs was performed as described above.

Figure 4: Flow cytometric bivariate simultaneous antigenic and cell proliferation assay

A-D shows an example of the sequence of FACS analysis of one sample for p75+ cells. **A**, Cellular aggregates-debris discrimination based on the forward (x-axis) and side (y-axis) scatter signals from each particle that is present. The gating discriminates live cells from debris and dead cells. This gated population is then used for cytometric analysis. **B**, Cytometric analysis of OECs (abscissa) and ONFs (ordinate) based on p75 and Thy1 fluorescence, delineated with gatings. Negative control is cells stained with only fluorophore conjugated antibody. Positive control for anti-p75 is Schwann cell line RT4-D6P2T, stained for only anti-p75 and anti-IgG AF488 (Hai et al., 2002). For anti-Thy1.1, the positive control is LP cells cultured for DIV17, stained for only anti-Thy1.1-PE. Each of the sub-populations is subsequently used for singleton-doubleton discrimination. **C**, DNA measurement and singletons-doubletons discrimination. The gating selects for only singletons, excluding doubletons or aneuploid cells. The singleton population is then used for cell cycle kinetic analysis. **D**, Cell cycle kinetic analysis, based on EdU Pacific Blue fluorescence intensity (y-axis) and total DNA content CellCycle 633-red intensity (x-axis), illustrating a typical horseshoe distribution. For the negative control cells from the same batch were stained as above without incubation with EdU. The left lower gated aggregate represents quiescent cells in the non-dividing G1/G0-phase, which do not incorporate EdU. The upper gated population represents the S-phase cells which incorporated EdU during their DNA multiplication. The right lower population represents EdU-negative cells which had reached their G2/M-phase of doubled DNA content prior to the administration of EdU.

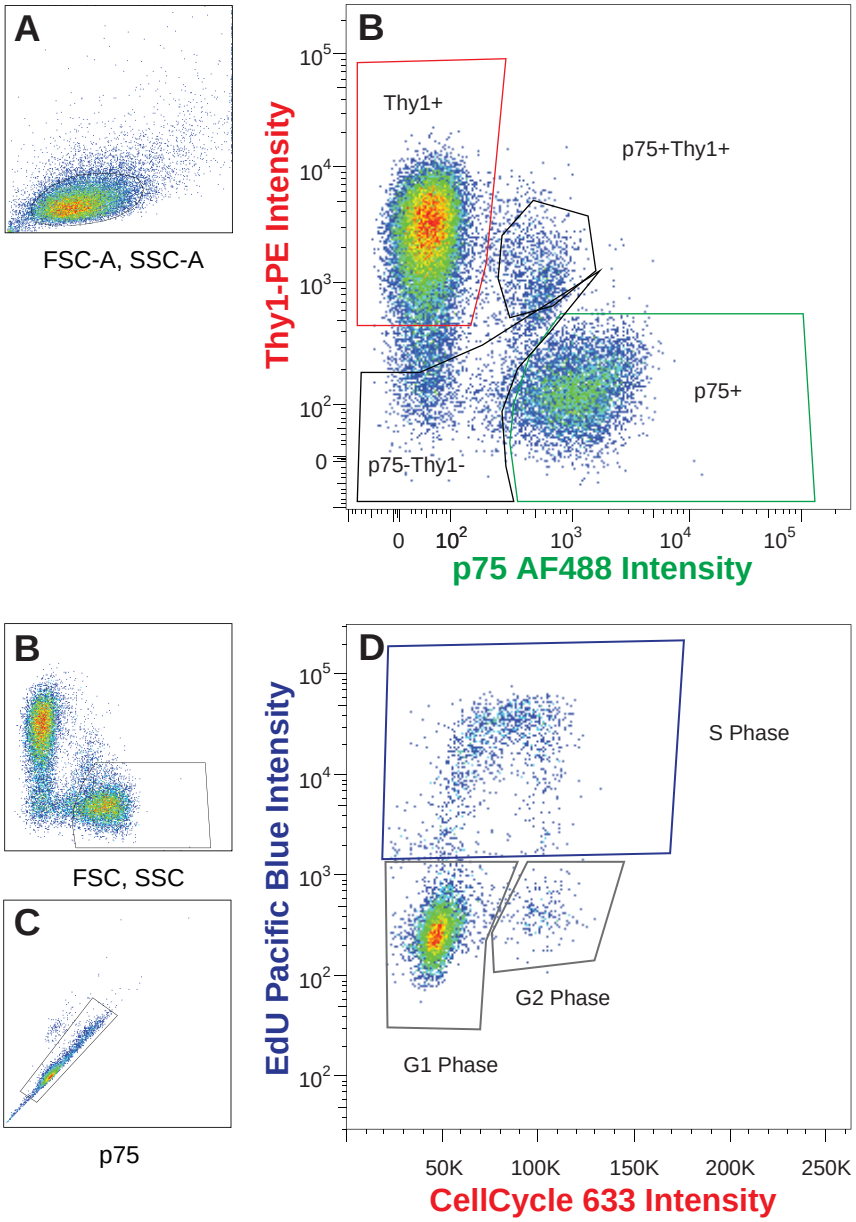
A
FSC-A, SSC-A
B
Thy1+
p75+Thy1+
p75+
p75-Thy1-
Thy1-PE Intensity
p75 AF488 Intensity
B
FSC, SSC
C
p75
D
S Phase
G2 Phase
G1 Phase
EdU Pacific Blue Intensity
CellCycle 633 Intensity

The cultures with these four simultaneous fluorescent labels were analyzed on a BD LSRII cytometer with parameters as above. The bivariate cell cycle profiles of the $p75^{+}Thy^{-}$ (OECs) and p75-Thy1+ (ONFs) populations were visualized based on the Pacific Blue-tagged EdU signals and the CellCycle 633 red-tagged DNA signals. After gating (Figure. 4A-E), G0/1-phase, S-phase and G2/M-phase were plotted to determine the cell cycle kinetics of each specific subpopulation of cells.

2.5 Histology

Under deep terminal anaesthesia tissues were fixed by transcardial perfusion with 4% paraformaldehyde in 0.1M phosphate buffer. 10μm cryostat cross sections were taken through the superficial layers of the olfactory bulb and the olfactory mucosa and immunostained with S100β and p75 as above.

2.6 Preparation of poly(lactic-co-glycolic acid) PLGA solution for protease degradation

For the proteolytic degradation, a total of four PLGA materials with different lactide:glycolide ratio, molecular weight (MW) and inherent viscosity (η) from various supplies were tested to select for the best suitable PLGA for replica mould and electrospinning. Among them are PLGA of lactide:glycolide ratio of 75:25, 50:50 and 30:70 (all from Sigma Aldrich, UK) which have low MW (from 40,000 – 75,000g/mol) and low η (0.55-0.75dL/g). In search of a polymer with high molecular entanglement ((Shenoy *et al.*, 2005); a prerequisite property needed to form continuous submicron-scale fibre for electrospinning), an additional PLGA of

lactide:glycolide ratio of 50:50 (PURAC, Netherlands) with MW of 153,000g/mol and η of 0.8-1.2 dL/g was also tested. In a chemically resistant vials (VWR, UK), all PLGA solutions were prepared by weighing out the appropriate amount of PLGA pellets and then together with hexafluoroisopropanol (HFIP; Merck, UK), based on the desired concentration percentage PLGA to HFIP (wt/wt). The mixtures of PLGA pellets and HFIP solvent were then completely dissolved with the aid of magnetic stirring rod. Procedures were carried out in a constant circulation fume hood for 30min.

2.7 Electrospinning

The electrospinning protocol was previously described (Ramakrishna *et al.*, 2005; Bhardwaj & Kundu, 2011). Briefly, the dissolved PLGA solution at the given concentration (see Section 2.6 above) was fed at a constant controlled feed rate through a stainless steel needle. The polymer solution was electrospun in an electrically charged environment at a fixed voltage. The tip-to-collector format was orientated in the vertical direction at a constant distance of 30cm. Voltage was evaluated within the range of 8kV to 25kV at feed rates from 100µl/h to 600µl/h. Each electrospinning process was completed in 2h.

2.7.1 Static vs. Rotating

The static and rotating electrospinning process was used to produce both random and aligned PLGA nanocomposite fibrous scaffold mesh using in-house fabricated rotating drums (static, Figure. 5A; rotating, Figure. 5B and C). For the random mesh rotating electrospinning process, the rotation was at 200rpm, while the rotating electrospinning process ran at 1200rpm for the aligned fibre mesh.

Figure 5: Machinery set up for flat static and rotating format electrospinning.
Photographs of, A, flat format static electrospinner; B, high speed rotating electrospinner for producing aligned fibres; C, low speed rotating electrospinner for random fibre orientation. Green arrow heads, collector; red arrow heads, microfabricated metallic needles in the various positions according to the machinery set up; hood, nanoparticles fume hood; pump, the flow syringe pump; pw, high voltage power source.


A
hood
pump
pw
B
C

2.7.2 Aligned fibres using dual-layer assembly

For the fabrication of the aligned fibre mesh, dual-layer assembly was used as the technique to increase the tensile and thickness of the fibre mesh for the use of cell culture. The layers included two types of electrospun nanofibre meshes: random and aligned, where the dual layers were fabricated with aligned fibres as the top layer and random fibres as the bottom layer, with the help of *membrane insert* (see section 2.11-2.13).

For the first layer of the dual-layer, the nanofibres were deposited on a flat, static, aluminium foil-wrapped counter electrode by electrospinning, described above. Thereafter, the fibre meshes were cast on to the relevant *membrane insert*. To complete the dual layer assembly, the fibre mesh-membrane cast was subsequently mounted onto the mould in the rotating drum for second layer aligned fibre collection. The tip-to-collector format was orientated in the horizontal direction, instead of vertical, as showed in Figure. 5C. A stable Taylor cone was formed at 12.5kV and the distance of the tip to the electrode collector was set at 33cm. The electrospinning process was completed after 15min. Upon removal of the *membrane insert* from the rotating drum, both layers were fastened to the *membrane insert MI-A* with the *Loop-ring* of *MI-A.* Excess fibre mesh was excised from the *insert*.

2.8 Proteolytic degradation of electrospun PLGA fibre meshes

The concentration used that produced electrospun fibres of submicron diameters in PLGA 75:25, 50:50 and 30:70 was 20%, while in PLGA 50:50 PURAC was 10%. The initial weight of respective electrospun PLGA fibre meshes was recorded. They

were then incubated in 10U/ml of protease XIV (Sigma), reconstituted in PBS, pH7.2 (Grubb, 1988). The buffered enzymatic solutions were changed every 4d and the dry mass loss measurements were made at specified time points. Samples were washed with sterile distilled water (ddH_2O), rinsed briefly with 70% ethanol for 10min and washed again with ddH_2O for 2h, and finally air-dried for at least 4h before each weighing session. The proteolytic degradation experiments were conducted over 5 weeks in 3 replicates.

The mass loss (M_L) was determined by the following formula, where M_0 is the initial mass and M_t is the mass after drying at the specified time.

$$M_L(\%) = \frac{M_0 - M_t}{M_0} \times 100$$

2.9 Nanocomposite electrospinning

The strategy employed for nanocomposite electrospinning process is similar to that implemented in CdTe-PVA electrospun nanofibres with minor modifications (Liu *et al.*, 2006; Li *et al.*, 2007). Briefly, CdSe/ZnS (5.2nm in diameter and 610nm (i.e. red in colour) quantum dots (core-shell type, Sigma-Aldrich UK)) were added into 6% PLGA/HFIP. The nanocomposite solution was then stirred vigorously with a stirrer bar magnet overnight to ensure an even dispersion of the quantum dots in the solution. Concentrations of 1% and 2% CdSe/ZnS were tested. To prevent aggregation within the viscous PLGA/HFIP solution, the solution was used immediately for electrospinning. The nanofibres were deposited using the same

format as described above. A stable Taylor cone was formed at 11.2kV with feed rate of 400µl/h. The distance of the tip to the electrode collector was set at 30cm. Each electrospinning process was completed in 2h, and the mesh was placed on a membrane insert which was then placed in a plastic culture dish.

2.10 Replica mould design and fabrication

The photomask layouts were designed based on the length and the width (10µm x 2µm) of a typical olfactory ensheathing cell with three widths grooves for the (2µm and 5 µm). The widths of the ridges were kept constant at 10µm. This design was done using AutoCAD 2000. Standard photolithographic and plasma etching techniques were utilized to produce "negative mould" silicon masters for the use in replica moulds (Figure. 6). Briefly, using the specially designed masked, a hydrofluoric acid dip cleaned 100mm diameter silicon wafer were coated with IX575WP photoresist (JSR, Japan) at 1.2µm thick, exposed using mask alignment, and postbaked. The wafer was patterned using one photolithography cycle. Features were etched using a multiplex etcher (STS, UK) using etch–passivation cycles. The remaining photoresist were stripped off in a series of methanol, isopropanol and acetone washes. These micromachined silicon masters were plasma cleaned (System 90, Oxford Instruments, UK) at 260mTorr and 250W for 150sec.

A spin coating solution of 10wt% PLGA (PURAC, Netherlands) was dissolved in hexa-fluoro-isopropanol (Merck, UK). This was then dispensed onto the mould and then spin-coated at 1800rpm for 1min to obtain the PLGA replica moulds, ones with microtopographic features and others with in the form of smooth sheets. The

Figure 6: Photolithography process for producing a negative replica mould

A hydrofluoric acid dip cleaned 100mm diameter silicon wafer were coated with IX575WP photoresist (JSR, Japan) at 1.2um thick, exposed using mask alignment, and postbaked. The wafer was patterned using one photolithography cycle. Features were etched using a multiplex etcher (STS, UK) using etch–passivation cycles. The remaining photoresist were stripped off in a series of methanol, isopropanol and acetone washes. These micromachined silicon masters were plasma cleaned (System 90, Oxford Instruments, UK) at 260mTorr and 250W for 150sec.

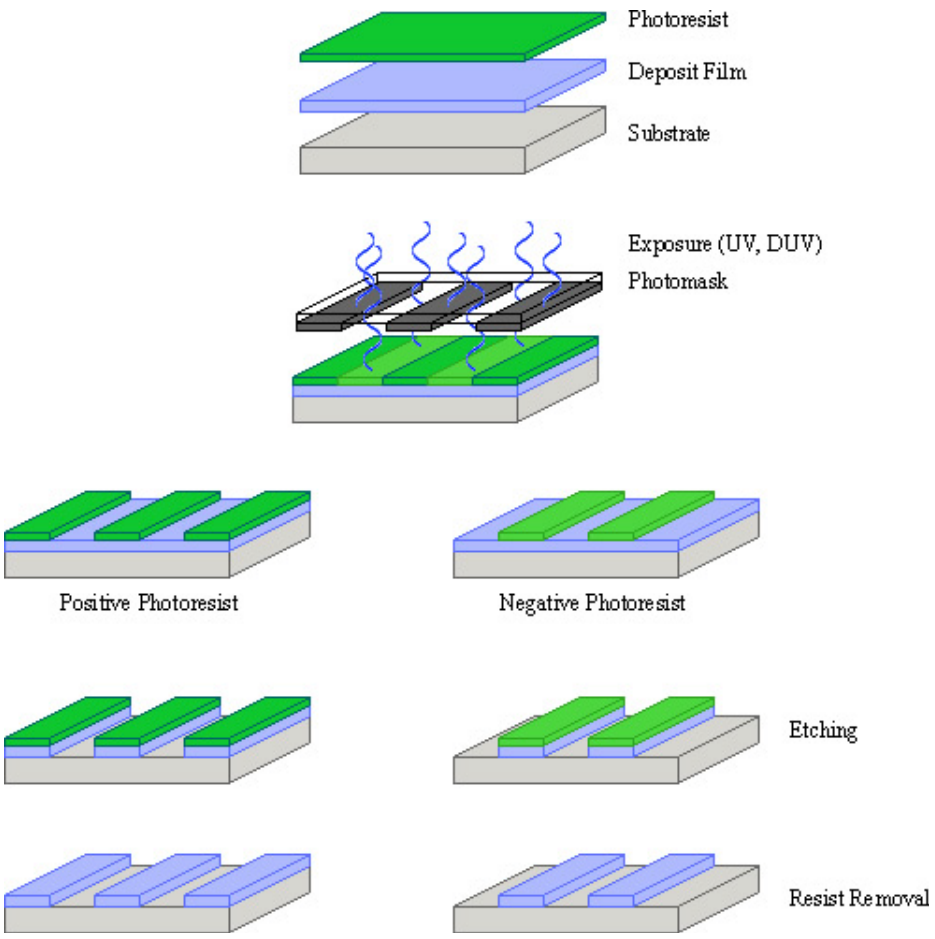
Photoresist
Deposit Film
Substrate
Exposure (UV, DUV)
Photomask
Positive Photoresist
Negative Photoresist
Etching
Resist Removal

thickness of the PLGA replica was adjusted by controlling the dispensed volume of material on to the moulds. The polymer was then cured at room temperature for 24h. The PLGA sheets were delaminated by manually detaching the polymer from the silicon master. Samples were then examined using scanning electron microscopy to evaluate the polymer.

2.11 Design of membrane insert

Based on the outline requirements for topographical cell culture, microporous interface tissue culture and bulk material manipulation, the *membrane insert* design was formulated and drafted using AutoCAD LT® 2000 (Autodesk, UK). After much consideration on the biocompatibility, ethylene oxide sterilization process, poly (methyl methacrylate) (PMMA, also known as acrylic) was selected as *insert* material. The designed membrane *insert* (*Base-ring* and *Loop-ring*) were then custom fabricated by Carville Ltd. in Surrey, UK.

2.12 Laser patterning of contact brass mask

Based on the cell culture, clinical requirement and the tensile nature of the electrospun fibre meshes, several designs for the contact mask were illustrated using AutoCAD LT® 2000. Brass plates were then cut using a trepanned 780nm femtosecond beam of the Exitech MicroAblater M2000 laser micromachining tool. The resulting stencil masks had a 1:1 scale ratio to the desire nanofibre scaffold.

2.13 Development of pattern design on nanofibres mesh

The dual layer of aligned fibres above the random fibres was used to test the two pattern design of the contact brass mask. Two orientation of brass stencil alignment with PLGA fibre mesh membrane insert were tested. Developing the patterned scaffold was done with the collaboration with Neil Sykes of Micronanics Ltd at Cardiff University. Using a standard mask projection machining approach, the fashioned millimetre scale structures were generated by first projected from the fabricated brass mask with a 0.1 mm × 4 mm aperture to shape and produce the laser beam of 193nm wavelength (Exitech PS2000) in conjunction with customized in-house optical projection system. The optical projection was scaled at 1:1 ratio, reflected using a dielectric coated mirror. All equipment was provided by Micronanics at Cardiff University, UK. A pulse repetition frequency of 1-3 Hz at the laser beam energy of 129–249 mJ/cm^2 was used to give the optimal compromise of process speed and feature accuracy. Optical demagnification of 1:1 projection format was tested for two different contact brass mask position.

2.14 Construction of fibre mesh-membrane insert

Two formats of electrospun nanofibre scaffold were fabricated. They were 1) single-layer random nanofibre mesh with the *membrane insert type R (MI-R)* and 2) dual-layer aligned nanofibre mesh with the *membrane insert type A (MI-A)*, where the dual layers were fabricated with aligned fibres as the top layer and random fibres as the bottom layer. The static and rotating electrospinning processes, as described in Section 2.7.1 abovewas used to produce both random and aligned PLGA nanocomposite fibrous scaffold mesh. The complementary groove-ridge fit

membrane insert system was used to fasten the nanocomposite fibre scaffold meshes to their respective *membrane inserts*, as described in Section 2.11 above. Briefly, the PLGA nanofibres were produced by electrospinning PLGA solution from a tip source, in vertical orientation to the collector. A stable Taylor cone were formed at 10.5kV and the distance of the tip to the electrode collector was set at 30cm. The process lasted for 2h approximately. Fibres were deposited on a flat, static, aluminium foil-wrapped counter electrode. Thereafter, depending on alignment requirements, the fibre mesh were casted on to the *MI-R* (random; single-layer) and/or *MI-A* (aligned; dual-layer).

In single-layer fibre mesh, the *Loop-ring* of *MI-R* was fastened on the base-ring. Excess fibres were excised from the *insert* and the scaffold-*membrane insert* was ready to be used.

For the dual-layer fibre scaffold, the random fibre mesh was taped temporarily on to *base-ring* of *MI-A* using masking tape and then subsequently mounted on the membrane insert frame in the rotating drum. This was for second layer aligned fibre collection to complete the layer by layer assembly. In this latter collection, the tip to collector format was orientated in the horizontal direction, instead of vertical. A stable Taylor cone was formed at 12.5kV and the distance of the tip to the electrode collector was set at 33cm. The electrospinning process was completed after 15mins. Upon removal of the membrane insert, *Loop-ring* of *MI-A* was used to fasten both layers on to the *base-ring* of *MI-A*. Excess fibres were excised from the *insert*.

2.15 Sterilization of fibre mesh-membrane insert

Three sterilization processes were tested: ultraviolet (UV) radiation, ethanol and ethylene oxide (EtO). For UV sterilization, the PLGA fibre mesh was treated with ultraviolet ray type B, using a UV oven (Luzchem, UK) for 15min to 1h. For ethanol sterilization, the PLGA fibre mesh was soaked in a series of incremental percentages of ethanol: 30%, 50%, and 70% for 15min respectively. For EtO sterilization, the PLGA fibre mesh was contained in Seal and Peel® packaging (Andersen Products, UK) and sealed with an impulse heat sealer. The sealed membrane inserts were then packed in designated liner bag together with a 5ml EtO ampoule (Andersen Products, UK). In an allocated fume hood, the ampoule was broken, and the package was placed in tight-lid container for overnight gas diffusion sterilization. Samples remained in the fume hood for another 24h to allow any EtO residues to be removed completely.

2.16 Functionalization of fibre meshes-membrane insert

Final concentration of 5μg/cm^2 of rat tail collagen Type I (Gibco, Invitrogen, UK), 20μg/cm^2 natural mouse laminin (Invitrogen, UK), 10μg/cm^2 poly-L-lysine (pLL) and 10μg/cm^2 poly-D-lysine (pDL) (both from Sigma) were used to coat the electrospun fibres mesh respectively. Collagen and laminin were reconstituted as manufacturer instruction, while pLL and pDL were reconstituted in sterile TC-grade water. To ensure uniform coating, the sterilized scaffold were soaked in PBS overnight and then transferred to the respective coating material for an hour respectively. After an hour of coating, the scaffolds were returned to PBS to remove excess biomolecules, prior to cell seeding.

2.17 Subcultivation of purified cells

The cell purification method are by flow cytometry on a MoFlo XDP (Beckman Coulter) operated on Summit software. 70μm nozzle were used at sheath pressure of 30psi and flow rate of 250-400 events per second were used as conditions optimized for neuronal cell analysis and sorting. Sort precision mode set for purity was the conditions for sorting.

Cells was sorted on the basis of p75 or Thy1, as labelling protocol described in section 2.3, except without paraformaldehyde fixation steps. Cells were collected within defined gates based on appropriate positive and negative controls (Figure. 4A and B) in the complete culture medium. A small aliquot was put through verification sorting, confirming 95-98% purity. Cells meeting this criterion were centrifuged, re-suspended in medium and plated on to chamber slides (NUNC Labtek II-CC^2) coated with pLL (for mucosal cells) or pDL (for bulbar cells). After a further culture for 4d the sorted cells were fixed and labelled using antibodies for p75 and FN.

For the nanotopography studies, purified OECs meeting 95-98% purity were centrifuged, re-suspended in medium and plated onto either the flat surface of the chamber slides (NUNC Labtek II-CC^2) or the surface of the PLGA electrospun Nano-700 and Nano-250 (see definitions in Section 4.2.4) fibres coated with poly-lysine, and cultured for a further found, after which the OEC bearing meshes were detached from the membrane insert and divided into two portions: one for scanning electron microscopy (SEM) and the other for immunofluorochemistry (IFC).

2.18 Confocal microscopy

Confocal images of fluorescent labelled cells were captured using LSM 510 Meta, a dual scanner and two-photon microscopy (Zeiss, Jena, Germany) at 200x magnification. Laser power and wavelength intensity settings were kept consistent across all the randomized micrographs taken in each session. Each fluorochrome dye within the same field was scanned separately by using a quasi-simultaneous mode, eliminating the possibility of signal "bleeding," which could generate false-positive results. For co-localisation images, a threshold of 0.8µm on the z-stack of optical sections were analysed to ensure the presence of both fluorochrome signals within that threshold. The emission signals of Alexa-488, Alexa-568, PI, Alexa 633 and DAPI were assigned to the green, red, red, yellow and blue channels respectively. Images were exported using LSM Image Browser software.

2.19 Scanning electron microscopy

2.19.1 Fibre characterization

The electrospun fibre meshes were carefully mounted on the scanning electron microscopy (SEM) stubs and sputter coated with platinum (Emitech K650TB, UK) prior to scanning microscopy imaging. SEM images were obtained using electron beam metrology and scanning electron microscopy system (Leica EBL40, Cambridge).

2.19.2 Characterisation of OEC fibre meshes

For SEM, OEC bearing meshes were fixed overnight in 3% glutaraldehyde, 1% paraformaldehyde in 0.08M sodium cacodylate buffer at pH 7.4. After 3x 10min

rinses of 0.1M sodium cacodylate buffer, followed by secondary fixation in 1% aqueous osmium tetroxide for 45min the samples again received three 10min rinses of 0.1M sodium cacodylate buffer followed by dehydration through a series of ascending alcohols for 10min each: 50%, 70%, 90% and three times at 100% . This step was followed by chemical drying with hexamethyldisilazane (HMDS – Merck, VWR, UK; which gave superior preservation to critical point freezing). After about 30min the fibre mesh turned opaque, indicating the completion of air drying, the samples were mounted on the Agar stub to be sputter coated with platinum using Emitech platinum sputter-coater. Scanning electron micrographs were taken using a Jeol JSM-6700F scanning electron microscope (UCL Ear Institute, UK).

2.20 Digital image and statistical analysis

2.20.1 Fibre characterisation

Digital image analyses were performed using ImageJ (NIH) processing software. SEM micrographs were calibrated to a standardized size of 1280 x 1040 pixels. Briefly, fibre diameter and length were measured at 35 different points along a randomly drawn straight line across the image.

The method adopted to characterize the fibre diameter is length weighted average fibre diameter, where the mean is based on a lognormal frequency distribution previously described (Dosunmu et al. 2006; Varabhas et al. 2008). Briefly, taking into account the different lengths which exist among the fibres, each fibre diameter (d_i) was weighted to its length (L_i). The frequency distribution of the length weighted fibre diameters is

$$\ln f_i = \frac{1}{\mathrm{d}} \frac{1}{\ln \sigma_g \sqrt{2\pi}} e^{\left(\frac{-(\ln d_i - \ln \bar{d}_g)^2}{2 \ln \sigma_g^2}\right)}$$

for a log mean diameter, $\ln(\bar{\mathrm{d}}_{\mathrm{g}})$ and the log standard deviation ($\ln \sigma_g$), expressed as

$$\ln(\bar{\mathrm{d}}_{\mathrm{g}}) = \frac{1}{\mathrm{L}_{\mathrm{total}}} \sum \mathrm{L}_{\mathrm{i}} \ln(\mathrm{d}_{\mathrm{i}})$$

and

$$\ln \sigma_g = \sqrt{\frac{\sum L_i (\ln d_i - \ln \bar{d}_g)^2}{L_{total}}}$$

was used to compare the fibre diameters in various experimental conditions in electrospinning parameters. Graphs were plotted based on the log-normal probability density, using the mathematic software, Wolfram Mathematica (UK). For concentration, voltage and flow rate of the electrospun fibre mesh experiments, data on each distribution were collected from a total of 3 SEM pictures in 3 experimental replicates. n=315. For nanocomposite electrospinning comparison, data on each distribution were collected from a total of 5 SEM pictures in 3 experimental replicate. n=525.

2.20.2 Cell counting

Methods for digital image analysis using NIH ImageJ were described in (Pool *et al.*, 2008) with slight modification. Briefly, all images were pre-processed based on the following sequential steps: colour-channels splitting, thresholding, watershedding and de-speckling. For nuclei counting (DAPI stack), "analyze particles" plugin was used to count the total number of cells in that image. In the p75 stack, OEC numbers were estimated using "ITCN" plugin (developed by Centre for Bio-image Informatics, UC Santa Barbara, USA). Fibronectin (in the FN stack) was estimated from measuring the total surface area, multiplied by the intensity (obtained from "plot contour" plugin).

Statistical analyses of data were performed with SPSS Statistic 17.0 (SPSS Inc., IBM, UK). Standard deviation (SD) is the square root of the variance (the variance being the average of the square differences from the mean.) The SD is included not as a test of the significance of differences, but simply to give the reader a indication of the dispersion of the variables. For correlation analysis, Pearson correlation coefficient was used for $n>30$, Spearman rho coefficient for $n<30$, significance by two-tailed Student t-test. The application of student t-test allows the comparison of two mean values where one values represents a nominal variable (e.g percentages of OEC) and other a measurement variable (e.g proportions of OEC in S-phase).

2.20.3 Cytomorphometric analysis

Cytomorphometric analyses of the purified OEC from the confocal images were performed in two steps: morphological identification of single cells in each image,

followed by cytomorphometric analysis of the identified cells. The image processing software used was Fiji (http://fiji.sc/wiki/index.php/Fiji), developed from NIH ImageJ and each image was magnified at an additional digital zoom of 9.6 times (3 clicks at 3.2x magnification each click). Morphological identification of bipolar and stellar OECs was performed using the "simple neurite tracer" plugin. The cell tracings were aided by the co-localisation of DAPI positive nuclei with the p75+ cell body and cytoplasmic branches. For images with more flattened cells, tracing using freehand selection with the aid of "ROI manager" was used in conjunction with "simple neurite tracer" plugin. For each surface (3 types), data were collected from a total of 4 confocal images in 3 experimental replicates. On average, 15 cells were traced in each image (n=315).

Once identified, all singly traced cells were measured for various morphological parameters using the "Measure" plugin to obtain perimeter (P), surface area (A), minimum Feret diameter, and the major axis (r_1). Major axis is obtained from the best fitted ellipse (determined by the shape descriptors, one of default function within "Measure" plugin) of the cell body. These measurements were used to calculate the circularity (C) and roundness (R) of each cell using the following formula:

i. circularity,

$$C = \frac{4\pi A}{P^2}$$

ii. roundness ,

$$R = \frac{4\mathrm{A}}{\pi {r_1}^2}$$

As the value of circularity and roundness approach 0.0, the morphology of the cells would be increasingly elongated. For elongated cells, at a given surface area, a stellar cell (i.e. a cell with more than two elongated processes) would have a shorter major axis, but a longer perimeter when compared to a spindle-like, bipolar cell.

Based on the equations above, a stellar cell has a higher roundness index but a lower circularity index than a bipolar cell.

2.20.4 Directionality of purified OECs

For the directionality, the "Directionality" plugin, based on the Fast Fourier Transform algorithm, was used to determine the pixel directionality of all traced cells in each image (Delgado-Rivera *et al.*, 2011). The computation of the algorithm was set on 180 bins, producing a directionality histogram of 180°. Each image was described by the dispersion index (i.e. standard deviation of the Gaussian distribution) and the goodness of the Gaussian fit to the histogram (1 good, 0 bad with multiple peaks). For each surfaces, data on each distribution were collected from a total of 4 confocal images in 3 experimental replicates (n=12). There is total 3 types of nanofibres, seeded with 2 types of OEC sources.

2.21 Brain tissue dissection

Tissue slices were prepared as reported previously (Li *et al.*, 1994; Stoppini *et al.*, 1991; Law *et al.*, 2010). All animals were maintained and used in accordance with UK Home Office regulations and guidelines for the care and use of laboratory animals. Briefly, in a laminar flow free area, under terminal anaesthesia of 2.5ml of 2% Avertin (tribromoethanol) per 100g body weight, Sprague Dawley rats at 7 to 8d postnatal (P7/P8) were decapitated using large scissors (Fine Science Tools (FST), UK) at the level of the foramen magnum. The skin was then slit using small dissecting scissors (FST) along the midline of the cranium from the posterior foramen magnum to the nares along the rostrocaudal axis. The cranium was exposed by pinching the skin rostrally, near the sinus area. Along the similar axis, a cut was made along the midline of the cranium from the posterior foramen magnum to the caudal side of the visible olfactory bulb structure. Subsequently, two bilateral cuts were made, caudally to the olfactory bulbs. The meninges were detached from the cranium using fire-polished fine spatula. Both detached pieces of cranium were then folded back to allow access to the complete brain. Using the same spatula to slide clear of any fibrous attachment, the brain was then lifted and placed into a dry 100mm sterile plastic Petri dish (Becton Dickson (BD)).

Brain slices were prepared using a fragmented piece of sterilized and acetone-free razor blade, fastened in a surgical blade holder (FST). The cerebellum was removed with a coronal cut at the caudal edge of the cerebral cortex. A similar cut was performed on the frontal 3-4mm of the forebrain. Subsequently, the excised brain section was positioned on its rostral cut surface, exposing the caudal cut surface.

Two cuts were made, each 0.5mm from the longitudinal fissure, removing the medial brain structure such as septal nuclei, thalamus and the ventricle. This removal reduced the total surface area in contact with the cutting blade, which facilitated smoother slicing of the brain; and minimized collapsing of neocortex that often result in damage on the entorhinal cortex. The dissected medial region of the brain was then removed to reconstitute the two hemispheres into one unit. These units were transferred for slicing. The time taken from brain extraction to hemispheres assembly was approximately 3-5min.

2.22 Entorhino-hippocampal formation slice preparation

Slice culture preparation techniques applied were reported previously (Stoppini *et al.*, 1991; Li *et al.*, 1996; Law *et al.*, 2010). Briefly, following the preparation of the dissected brain units, the rostral cut surface of the units was then placed gently onto the McIlwain cutting disk (Harvard Apparatus, UK). The brain units were arranged next to each other in dorsoventral orientation. Prior to affix to the chopper, the slicing razor blade was washed with acetone and then 70% ethanol, followed by brief flaming. Both the blade and the caudal surface of brain units were then moistened with ice-cold Gey's balanced salt solution (Gibco, Invitrogen, UK), enriched with 32.5mg/ml D-glucose (Gey's 5X). 350µm thick horizontal slices were cut on McIlwain tissue chopper (Harvard Apparatus, UK). Gently with the aid of the same ice-cold Gey's 5X, the brain slices were transferred to a 60-ml Petri dish containing 15ml ice cold Gey's 5X. The time taken from slicing to the immersion of tissue slice was approximately 5min.

Individual slices consisting of the hippocampal formation and entorhinal cortex in continuity with the perirhinal and neocortex were gently separated and trimmed in the ice-cold Gey's 5X. This was done using two clean, fine dissection spatula (FST) to separate and razor blade to trim, under a stereomicroscope with oblique base (Carl Zeiss, UK). Slices were collected without discriminating from the septotemporal location, and then assessed for any visible damage or broken parts, occurred during slicing. Predominantly the infrapyramidal region of the dentate gyrus and the outer layer (consisted of layer I and II) of the entorhinal cortex were confirmed to be in good shape to be selected for the experiments. Selected slices were then transferred to ice-cold Gey's balanced salt solution (Gibco, Invitrogen, UK), enriched with 6.5mg/ml D-glucose (Gey's 1X). The perirhinal area was then trimmed off at the rhinal fissure, radially through the entorhinal-perirhinal border to the deep white matter using razor blade. Slices with overall good intact structures were selected for control (SC-0), with all the hippocampal formation and entorhinal cortex intact as continuous slices. The remaining slices population was then used for sub-slice dissection.

2.23 Individual sub-slice dissection and co-culture control preparation

Sub-slice culture preparation techniques were as reported previously (Li et al. 1996). The remaining selected continuous slices are dissected further to the two sub-slices: hippocampus (HP) and entorhinal cortex (EC). Using a fresh sterilized fragmented razor blade, fastened in a surgical blade holder (FST), a cut was made radially at the entorhinal-parasubicular border and without lifting blade from the deep end of white

matter, then another radial cut across the presubiculum to the edge of the hippocampal fissure. These cuts excluded the intervening pre- and para-subiculum from the HP and EC. EC was subsequently detached from the hippocampal formation by gently opening the lateral ventricle to cut along the remaining angular bundle. Two types of slices, EC and HP (in continuity with the subiculum), were transferred respectively into two fresh ice-cold Gey's 1X prior for co-culture positioning.

Two different series, in term of EC position and orientation to HP, of co-culture control were prepared, and each series were used in quantitative study.

Type p: EC-HP, caudal position (e.g. SC-1*p*). EC slices were co-cultured with target HP slices placed in the normal orientation, caudal with the angular bundle and subiculum, apposed to the deep white matter of EC slice. This confrontation has the effect of retaining the normal perforated path and alvear path trajectories within the entorhino-dentate gyrus system.

Type q: EC-HP, ventral position (e.g. SC-1*q*). EC slices were co-cultured with HP slices placed ventrally, with the infrapyramidal blade of the dentate gyrus apposed to the deep white matter of the EC slices. This confrontation indeed has the effect of eliminating the need for the fibres to negotiate the perforant and alvear path trajectories.

2.24 Co-culture preparation: gap and scaffold introduction

For lesion simulation, gaps were subsequently introduced to the two different orientational series, as mentioned prior. Three different series, in term of gap distance between EC and HP, of co-culture were prepared, and each series were used in quantitative study.

Series A: Cut, no gap with either caudal (*p*) or ventral position (*q*) (SC-1*p* or SC-1*q*).

Series B: 0.5 and 1.0mm gap with either caudal (*p*) or ventral position (*q*) (i.e. SC-2*p* or SC-2*q* for 0.5mm and SC-3*p* or SC-3*q* for 1.0mm). Approximate 0.5mm and 1.0mm was introduced between the EC and HP in the previous mentioned two EC-HP orientations.

Series C: 2.0mm gap with either caudal (*p*) or ventral position (*q*) (SC-4*p* or SC-4*q*). Approximate 2.0mm was introduced between the EC and HP in the previous mentioned two EC-HP orientations.

To introduce the scaffold randomly orientated nanofibre meshes were placed in the gap introduced in Series C. The fabrication of the electrospun PLGA nanofibre scaffold (randomly orientated) was described previously in Section 2.7 above. The nanofibre meshes were subsequently casted on membrane insert and laser-patterned, as described in Section 2.11 above − 2.14 above, to obtain the 2.0mm (4mm in width) strip of scaffold meshes. Subsequently scaffold-casted membrane insert were sterilized and surface functionalized, as described in Section 2.15 above − 2.16 above. These 2.0mm scaffolds were then cut from the membrane and placed in

between the co-cultured EC and HP in series C. A total of three repeats were done for this series.

2.25 Organotypic culture

The organotypic culture methods were reported previously (Stoppini *et al.*, 1991; Li *et al.*, 1996), applied with slight modification. Briefly, based on the Stoppini static culture method, new PTFE hydrophilic membrane inserts (Millicell Cell Culture Insert, Millipore, UK) were pre-incubated with organotypic growth media (OGM) in 6-well tissue culture plate format (BD), one hour prior to co-culture plating. OGM was made up of 50% minimum essential media (MEM; Gibco, UK), 25% Earle's balanced salt solution (EBSS; Gibco, UK), and 25% horse serum (Gibco, UK), supplemented with 6.5mg/ml glucose. 1.0ml OGM was placed below the membrane and 0.5ml on the membrane.

The tissue slices were gently transferred to the Millicell membrane insert, using a fire-polished shortened Pasteur pipette, with a larger opening. This would minimize the stress incurred during nervous tissue transfer. In each Millipore membrane insert, four to five sets of co-cultured slices were oriented according to their series and organized around the peripheral of the inserts. Excess media (Gey's 1X) was then aspirated. Organotypic cultures were maintained at a constant temperature of 37°C in a 5% CO2 humidified incubator for tend. OGM was replaced thrice weekly.

2.26 Thionin staining

The collective tissue slices cultured on membrane insert were first rinsed twice with tissue-culture grade PBS from the complete culture media and then fixed with

primary fixation: 5% glacial acetic acid in 95% ethanol for 30min, followed by another rinse (twice) with normal grade PBS for 10min each. The rinsed tissue slices on the membrane insert were excised to individual pairs (EC and HP) to manageable size for handling, prior to 0.05% thionin staining for 5mins. Thionin (Sigma, UK) were reconstituted with distilled water. The individual pairs were then rinsed twice with distilled water and followed by, dehydrated through an ascending ethanol gradient: 50% for 5min once, 70% for 5min once, 90% for 5min once, 96% for 5min once and 100% for 5min twice. Any excess stain was removed by placing the slide into 96% ethanol containing Cajuput oil (Sigma, UK). The tissue slices were then placed twice in the clearing agent, Histoclear (National Diagnostics Ltd, Hessle, UK) for 5min. Then these slices on the membrane were mounted using viscous DPX mounting medium (Fisher Scientific, UK) on the 60°C slice rank to evenly spread the medium throughout the larger membrane. Any bubbles were gently pushed to the edge of the medium and cover slips were mounted on the warm medium with gentle pressure to flatten the slice.

2.27 Biocytin (orthograde) labeling and immunocytochemistry

At the penultimate termination day, small crystals of biocytin (Sigma, UK) were placed gently on the outer edge (layer II and III) entorhinal (origin) tissues, using a moistened tip of a fine tungsten needle (Micro-Tools set, Hampton Research, UK) as the transfer tool.

After washing with PBS, organotypic cultures were fixed with 4% paraformaldehyde (TAAB, UK) for 2h under gentle shaking. After fixing, each set of EC and HP was separated by cutting the membrane around the co-culture. Three 30min washes with

0.1M phosphate-buffered saline at pH7.4 (PBS) were applied with gentle shaking followed by permeabilising and blocking with 2% skim milk (Merck KGaA, Germany) in 0.1M phosphate-buffered saline (PBS) containing 0.1% Triton X-100 (TAAB, UK). Then primary antibodies were applied overnight at 4°C. Cells were washed three times for 30min and incubated with appropriate fluorescent secondary antibody for 2h at room temperature in the dark with gentle shaking. Subsequently, slices were counterstained with DAPI (Sigma, UK). After two 30min washing, the cells were counter-stained and mounted using ProLong® Gold Antifade (Invitrogen). The primary antibodies used were mouse anti Glial Fibrillary Acidic Protein-Cy3, clone G-A-5-IgG1 (GFAP-Cy3, 1:500; Sigma, UK), mouse NeuN, Alexa Fluor 488 conjugated, clone A60 (1:250, Chemicon, Millipore, UK), and mouse anti Calbindin-D-28K, clone CB-955 (Calb, 1:1000; Sigma, UK). Secondary antibodies used were Alexa Fluor 488 conjugate Streptavidin, Alexa Fluor 546 conjugate Streptavidin, Alexa Fluor 488 rabbit anti-mouse IgG and Alexa Fluor 546 rabbit anti-mouse IgG (all 1:400; Molecular Probes, Invitrogen, UK).

Chapter 3 Olfactory Ensheathing Cells *in vitro*

3.1 Introduction

3.1.1 Overview of transplantation of OEC in experimental lesion models

Transplantation of olfactory ensheathing cells (OECs) has been identified as a promising approach for anatomical and functional repair of injuries to nerve fibre tracts in the spinal cord, spinal roots, and potentially other CNS sites (Franklin & Barnett, 2000; Boyd *et al.*, 2003; Santos-Benito & Ramón-Cueto, 2003; Raisman & Li, 2007; Radtke *et al.*, 2008; Richter & Roskams, 2008; Lindsay *et al.*, 2010; Mackay-Sim & St John, 2011). There have, however, been major differences in reported outcomes, ranging from functional repair by regeneration of severed axons to functional amelioration by enhancement of surviving tissue (plasticity, sprouting etc), as well as reports of failure to achieve benefit (Ramón-Cueto *et al.*, 1998, 2000; Lu *et al.*, 2001; Smith *et al.*, 2002; Takami *et al.*, 2002; Nash *et al.*, 2002; Chuah *et al.*, 2004, 2004; Raisman & Li, 2007; Guest *et al.*, 2008; Bretzner *et al.*, 2008; Yamamoto *et al.*, 2009; Radtke *et al.*, 2010).

Apart from differences in lesion site and size, techniques of transplantation, and methods of functional assessment, there have been considerable differences in cell preparation (Chuah *et al.*, 2011). Examples include: (**a**) the source of the tissue: olfactory bulb, (Gudiño-Cabrera & Nieto-Sampedro, 1996; Franceschini & Barnett, 1996; Li *et al.*, 1997; Ramón-Cueto *et al.*, 1998), olfactory mucosa or lamina propria; (Lu et al., 2001; Au and Roskams, 2002; Steward et al., 2006; Richter et al.,

2005), (**b**) the age of the donor (adult, neonatal, or foetal; (Imaizumi *et al.*, 1998; Barnett & Roskams, 2008; Huang *et al.*, 2008), (**c**) the time in tissue culture (Ito *et al.*, 2006; Radtke *et al.*, 2010; García-Escudero *et al.*, 2010; Novikova *et al.*, 2011*b*), (**d**) whether the OECs are purified (in most studies, e.g. (Chuah & Au, 1993; Barnett & Chang, 2004)), or used as mixed primary cultures (Deumens *et al.*, 2006; Raisman & Li, 2007; Iwatsuki *et al.*, 2008), or cell lines (Franklin *et al.*, 1996; Audisio *et al.*, 2009; García-Escudero *et al.*, 2011), (**e**) the use of growth factors (Pollock *et al.*, 1999; Bianco *et al.*, 2004; Radtke *et al.*, 2004); (**f**) the species: apart from the rat, other OECs (Lindsay *et al.*, 2010; Wewetzer *et al.*, 2011) have been prepared from mouse (Richter *et al.*, 2008), pig (Radtke *et al.*, 2004), dog (Ito *et al.*, 2006; Krudewig *et al.*, 2006), monkey (Guest *et al.*, 2008) and human (Féron *et al.*, 1998; Barnett *et al.*, 2000; Lim *et al.*, 2010; Gorrie *et al.*, 2010).

OECs were first described in the olfactory nerve fibre layer of the olfactory bulb (Doucette, 1984; Raisman, 1985; Ramón-Cueto & Valverde, 1995) and the first transplant experiments were with cultures of bulbar OECs (Franklin et al. 1996; Imaizumi et al. 1998; Li et al. 1998; Ramón-Cueto and Nieto-Sampedro 1994). However, since OECs ensheathe olfactory nerve fibres throughout their course from the olfactory epithelium through the lamina propria and the nerve bundles crossing the cribriform plate of the ethmoid bone, the possibility of using these peripherally located OECs provided an attractive solution to avoid the need for intracranial surgery, and there has been considerable clinical use of mucosal OECs to date (Huang *et al.*, 2006*a*; Lima *et al.*, 2006; Mackay-Sim *et al.*, 2008; Mackay-Sim & St John, 2011). However, in experimental studies transplants of mucosal OECs have been less effective in inducing regeneration (Lu *et al.*, 2006; Yamamoto *et al.*, 2009).

Collectively, recent *in vivo* studies using both bulbar and mucosal OECs have now showed variability in degrees of regenerative capability, some with neurotrophic intervention. (OB: (Imaizumi *et al.*, 2000; Smith *et al.*, 2002; Takami *et al.*, 2002; Nash *et al.*, 2002; Keyvan-Fouladi *et al.*, 2003; Chuah *et al.*, 2004; Radtke *et al.*, 2004, 2010; Boyd *et al.*, 2004; Pearse *et al.*, 2007; Deng *et al.*, 2008; Guest *et al.*, 2008; Bretzner *et al.*, 2008; Aoki *et al.*, 2010); OM: (Lu *et al.*, 2001; Steward *et al.*, 2006; Iwatsuki *et al.*, 2008; Aoki *et al.*, 2010). Microarray studies have shown differences in the gene expression patterns of bulbar and mucosal OECs (Franssen *et al.*, 2008; Guérout *et al.*, 2010). To what extent this reflects an intrinsic difference between bulbar and mucosal OECs, or some other factor such as the lower proportion of p75 positive cells or the presence of different accompanying cell types is not clear.

The protocols for primary cultures bulbar and mucosal OECs differ. Both cultures are heterogeneous, with overlapping cells and wide regional variations. Accurate estimation of the proportions of OECs and olfactory nerve fibroblasts (ONFs) and their evolution with time in culture is essential to provide a baseline for establishing the reparative properties of transplants.

3.1.2 Heterogeneity of OEC populations

Phenotypically the bulb cultures revealed three types of cells (fusiform, macrophage-like and multipolar). Franceschini and Barnett named the fusiform cells S (Schwann-like) cells, later known as OEC and the multipolar cells originally designated A (for astrocyte-like) cells, later probably corresponding to the olfactory nerve fibroblasts (ONFs) (Franceschini & Barnett, 1996; Li *et al.*, 1998).

Immunocytochemistry showed the p75 reactivity for the S-cells and fibronectin for the A cells. Various protocols were then developed to obtain purified bulbar OEC by using combination of oligodendrocytes marker 4 (O4) and galactocerebroside C (GalC) as surface marker antigen in fluorescent activated cell sorting or Thy1.1 immunoabsorption or p75-NTR (low affinity NGFR) immunopanning or simply without purification (in sequential annotation: (Chuah & Au, 1993; Barnett *et al.*, 1993; Ramón-Cueto *et al.*, 1998).

With the increasing interest in the use of the more accessible peripheral (mucosal) source of OECs for transplantation, Féron and colleagues derived a protocol to establish OEC culture from the subepithelial layer of olfactory mucosa: lamina propria (LP) in 1999 (Féron *et al.*, 1999). It was observed that three main cell populations exist: OEC, fibroblasts and endothelium cells, with a small percentage of bipolar neurons that disappeared over time. Subsequent purification protocol was also developed to eliminate fibroblasts using cytotoxic lysis with anti-Thy1.1 hybridoma supernatant (Au & Roskams, 2002). Subsequent *in vivo* studies, using cells cultured from different mucosal tissue and its derivatives, with and without purification protocol have reported different results in axon regeneration. It remained unclear to what degree olfactory mucosa heterogeneity has an effect on the *in vivo* studies (Table 1).

Most experimental and clinical studies have obtained mucosal OECs from the LP after removing the epithelium. An exception is Lima group where dissociated tissue samples of entire uncultured autologous olfactory mucosa were used as autografts in patients (Lima *et al.*, 2006). Histologically the use of the separated LP was logical,

Table 1: Tissue sources and culture preparations of primary rat OECs.

Table summarized the variety of tissue sources (and their nomenclature used) and the culture preparation adopted to prepare the dissociated cells for cell cultures. Note, the purpose of this table is to show the variation in culture conditions used in different studies. To obtain a standard with which to derive a logical procedure, I have carried out a analysis of cell proportions and evolution of the cell types in culture. In view of the variation of techniques and interpretations a review of these publications does not allow a convincing evaluation of the different culture methods in terms of histological or functional outcome.

List of Culture Conditions for Olfactory Ensheathing Cells

Age	Described Anatomy	Tissue Source	DIV	Purification Steps	*In vitro* Expansion Protocol	OEC Percentage (p75 expression)	*in vivo* Transplantation
Olfactory Bulb							
Adult	OB	Olfactory nerve layer and glomeruli in Bulb	8	p75 Affinity Purification	Ramon-Cueto 1992	Not indicated	Ramon-Cueto 1994, Li 1997
Fetal	OB	Olfactory nerve layer at Primodium	0	No	Devon Doucette 1992, 1995	Not indicated	Boyd 2004
Neonatal	OB	Corpus Callosum, Cerebellum Hippocampus	7-10 d	FACS with O4 and GalC at day 0	Barnett SC 1993, Franceschini 1996	95%	Franklin 1996, Lakatos 2003, Riddell 2004; Toft2007, Richter 2008
Neonatal	OB	Olfactory nerve layer and glomeruli in Bulb	7-11.5 d	Gauze + Ara-C + Thy1 Immunoabsorption	Chuah 1993	>97%	Imaizumi 1998, Imaizumi 2000, Radtke 2004, Chuah 2004
Adult	OB	Olfactory nerve layer and glomeruli in Bulb	15 d	p75 Immunopanning	Ramon-Cueto 1998	98%	Pearse 2006, Takami 2002, Pearse 2004, Ruitenberg 2005, Guest 2008
Adult	OB	Olfactory nerve layer and glomeruli in Bulb	14-17 d	No	Li 1998, Li 2003	50%	Li 1998, Li 2003, Keyvan-Fouladi 2003, Andrews 2004, Andrews 2007
Adult	OB	Olfactory nerve layer and glomeruli in Bulb	10d	Chamber slides (18h+36h+48h), without p75 Immunopanning	Ramon-Cueto 1992, Nash 2001	≈93%	Nash 2002, Johannson 2005, Andrews 2007, Deng 2008
Adult	OB	Olfactory nerve layer in Bulb	0	No	Sasaki 2004	-	Sasaki 2005, Markais 2009
A & N	OB	Immortalized OEC Cell Line	∞	No	Chuah 1993, Moreno-Flores MT 2003	90%	Moreno-Flores MT 2006
Olfactory Mucosa							
Embryonic	Mucosa	Olfactory Septum - EPI	??	Remove LP	Chuah 1991	Not indicated	Polentes 2005
Adult	Mucosa	Olfactory Septum - LP	7-8	No (350,000 cells/cm2)	Feron 1999; Bianco 2004	70% (Bianco)	Lu 2001, Lu 2002, Feron 2005, Bretzner 2008
Neonatal	OM	Olfactory Septum and Turbinates - WM	11-16	Thy1.1 mediated complement lysis	Au & Roskams 2002	97%	Ramer 2004; Steward 2006; Lu 2006

* Used the in vitro protocol but for a different source of OEC from the protocol.

because histological evidence showed OECs are found in the LP. However, the stem cells for the olfactory neurons and glia are present in the epithelium (Murrell *et al.*, 2005; Murdoch & Roskams, 2008). As the subsequent results will show, paradoxically, the LP dividing population generate low p75+ cells.

Rationale of my studies: Cell counting based on immunolabelling is laborious and inevitably has a subjective element. To obtain more objective estimates I therefore carried out flow cytometric analysis of the evolution of the relative populations of OECs and ONFs cultured from tissue samples taken from the adult rat olfactory bulb (OB), the whole olfactory mucosa (WM), the mucosal lamina propria (LP) and a hitherto unexplored source of OECs, the olfactory mucosal epithelium (EPI). A novel four colour simultaneous antigenic bivariate cell cycle assay was used to determine the cell cycle kinetic distribution of the antigenically identified cells in the primary cultures and to explore the relationship of proliferation to the evolution of the population changes in the cultures. The further behaviour of the sorted cells was examined in post-purification culture.

3.2 Results

3.2.1 Histology

OECs accompany the olfactory nerve axons during their entire course from the olfactory mucosa to the OBs (Doucette, 1984; Raisman, 1985; Choi *et al.*, 2008). In the olfactory mucosa, OECs are located at the points where the olfactory axons penetrate the basal lamina interface between the olfactory EPI and the LP, where they ensheathe the massed bundles of olfactory nerve fibres. They are asymmetrical

cells that on one surface, face the olfactory nerve fibres, and on the other, face encircling fibroblastic processes from which they are separated by a basal lamina. OECs express the common glial antigen S100β (Figure. 7A, C and E) throughout the entire cell including the fine processes that are interposed among the olfactory nerve fibres (Turner & Perez-Polo, 1992). In contrast, the p75 antigen is expressed only on the circumferential OEC outer membranes facing the encircling fibroblast-apposed basal lamina, but is virtually absent from the inner OEC membranes interposed among the nerve fibres (Figure. 7D and F). In the OB, the OECs in the olfactory nerve layer express S100β but with this antibody they are indistinguishable from the S100β+ astrocytes of the glomerular and deeper layers (Figure. 7A). p75 is hardly detectable in any of these layers of the intact OB (Figure. 7B).

3.2.2 Culture

In this thesis I report studies of OECs and ONFs in cultures of tissue samples from the outer nerve fibre and glomerular layers of the OB, and from the olfactory mucosa taken either as a whole thickness sample (WM), or separated into its component LP and EPI. The characteristics of the cell populations cultured from these four sources will be described in terms of: (i) morphology, (ii) immunocytology, (iii) quantification by flow cytometry, (iv) analysis of cell proliferation, and (v) further culture of FACS purified cells.

A note on terminology: In cultures from the olfactory system, the histological entities represented by OECs and ONFs are generally identified as p75+, S100β+, nestin+, Thy1-, FN- and p75-, S100β-, nestin-, Thy1+, FN+, respectively. For convenience in reading, in this account, I use the terms OECs and ONFs simply to

Figure 7: Histological characterization of OECs.
In the EPI and LP layers of the OM (A,B) and the glomerular (GL) and nerve fibre layers (N) of the OB (C,D), OECs are identified using S100 (red) and p75 (green). Note the lower expression of p75 in olfactory epithelium relative to those in lamina propria. GL, bulbar glomerulus, N, nerve fibre layers, LP, lamina propria, EPI, epithelium. Scale bar, 100μm.

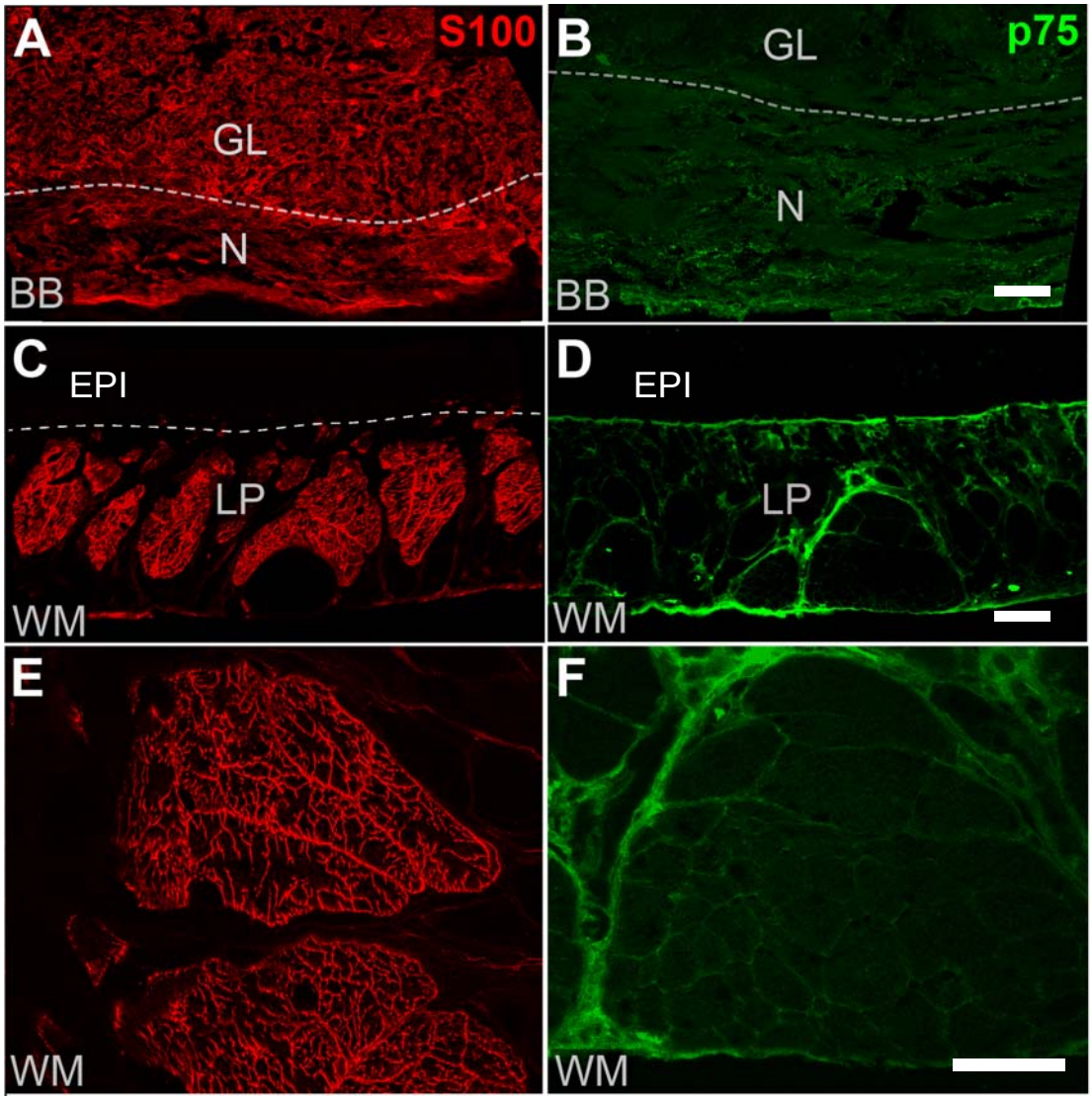
A
S100
GL
N
BB
B
GL
p75
N
BB
C
EPI
LP
WM
D
EPI
LP
WM
E
WM
F
WM

indicate these phenotypes, but with the provisos that the expression of p75 is regulated, and not all p75+ cells are necessarily OECs. Some cells are positive for both markers and, as will be seen below, and cells purified on the basis of p75+ can give rise to Thy1+ cells on subsequent culture. I have chosen the term ONF's, rather than simply ''fibroblasts'' in order to distinguish them from fibroblasts in other areas. It must also be borne in mind that the ONFs associated with the nerve bundles in the LP may differ from those associated with the nerve fibre layer in the OB.

3.2.3 Morphology

At initial plating the cultures consisted of free floating rounded cells with no processes. From 3DIV in the WM and LP cultures cells became adherent. In the case of OB and EPI cultures, significant amounts of cellular material and debris were lost at each media change and the cells only became adherent at around 5DIV. From 8DIV the morphology of the cells in all four cultures varied depending on the initial plating density. Plating density was taken as optimal when the cells separated into two distinct populations of spindle shaped cells and flattened multipolar cells, which corresponded antigenically to cells with OEC and ONF markers, respectively (see below) but with no signs of senescence. Trial of different plating densities (see Materials and Methods) showed that this result was achieved for the OB tissues by plating the samples from two OBs on a 60 cm^2 plate, or for WM and LP by plating at an initial density of 27,000 cells/cm^2, but EPI tissues required a 10-fold increase in plating density to 270,000 cells/cm^2. For tissues from all four sources plated at lower densities the cultures failed to become confluent, and there was a change in cell morphology. At around 8DIV, there was a spectrum of OEC shapes ranging from spindle-shaped cells with expanded ends to flattened multipolar cells. By 14DIV, the

majority of cells had become multipolar. Conversely, in WM and LP cultures plated at higher density (81,000 cells/cm^2) the majority of the cells, including ONFs, adopted spindle shaped morphology (Figure. 8).

3.2.4 Immunocytology

In culture, the OEC phenotype was identified as positive for p75, S100β, and nestin and negative for Thy1 and FN. ONFs are positive for Thy1 and FN, and negative for p75, S100β, and nestin. With the current matching of primary and secondary antibodies, cultures can be double immunostained either using p75 together with FN, or S100β together with Thy1. In cultures from all four sources at their respective optimal densities, immunocytochemistry showed (a) cells which were positive for the OEC markers p75 (Figure. 9 A1–4) and S100β (Figure. 9C-D), (b) cells positive for the ONF markers FN (Figure. 9 B1-4; Figure. 10 B1,3, D1,3) and Thy1 (Figure. 10 A2,3, B2,3, C2,3, D2,3) and (c) a small population of p75+FN+ cells in the WM cultures appearing from 7d in culture (Figure. 11 B). Figure. 10 B1–3, D1–3 shows the comparison between FN staining, which is initially associated with the ONF cell bodies and later becomes increasingly deposited in the extracellular matrix, and immunostaining of Thy1 (also known as CD90), which is a membrane associated glycoprotein (punctuate at high power) anchored to the cell surface of the ONFs. With increasing time in culture, the numbers of OECs fall dramatically (Figure. 10 E1,3, F1,3) and the FN staining, initially around cell bodies becomes widely spread over the matrix (Figure. 10 E2,3, F2,3). By 4 weeks, especially in the cultures started at lower densities, a number of the p75 and Thy1 cells are senescent, with greatly enlarged, flattened shapes with abnormal cytoplasmic granular and vacuolar inclusions, and long thin filamentous processes (Figure. 10 G,H).

Figure 8: Phase contrast stereo micrographs of OECs and ONFs in culture.
After 10DIV, culture of OB (A), OM (B), EPI (C) and LP (D) showed morphological evidence of spindle-shaped OECs and the multipolar-shaped ONFs at magnification from a 10X eyepiece and 10X objective lens.

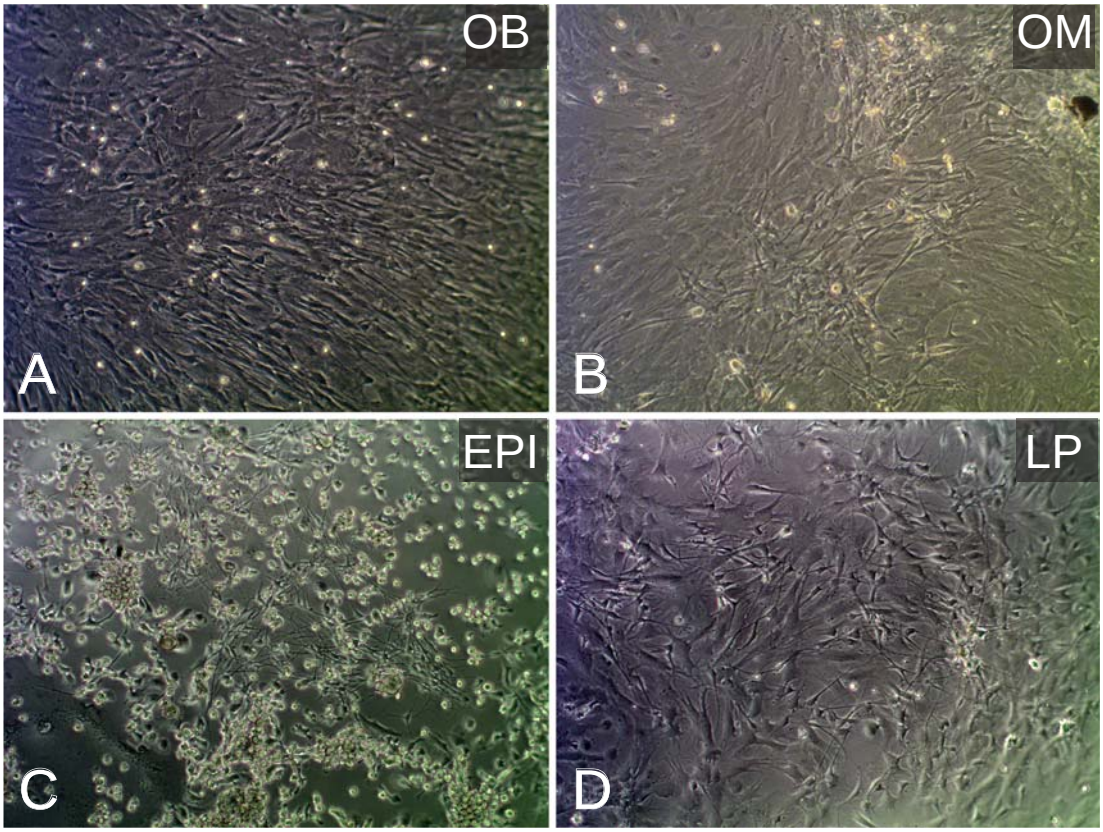
OB
A
OM
B
EPI
C
LP
D

Figure 9: Confocal images of OECs and ONFs in culture at DIV10 for all the olfactory derivatives.
Immunocytochemistry of cultures all 4 sources: OB (A1, B1, C and E), WM (A2, B2, D and F), EPI (A3, B3) and LP (A4, B4). p75 (green), FN (red), and overlay; overlay of p75 (green), S100 (red) and DAPI (blue); overlay of Nestin (green) and S100β (red). OB, olfactory bulb; OM, olfactory mucosa; LP, lamina propria; EPI, olfactory epithelium. Scale bars, 200μm.

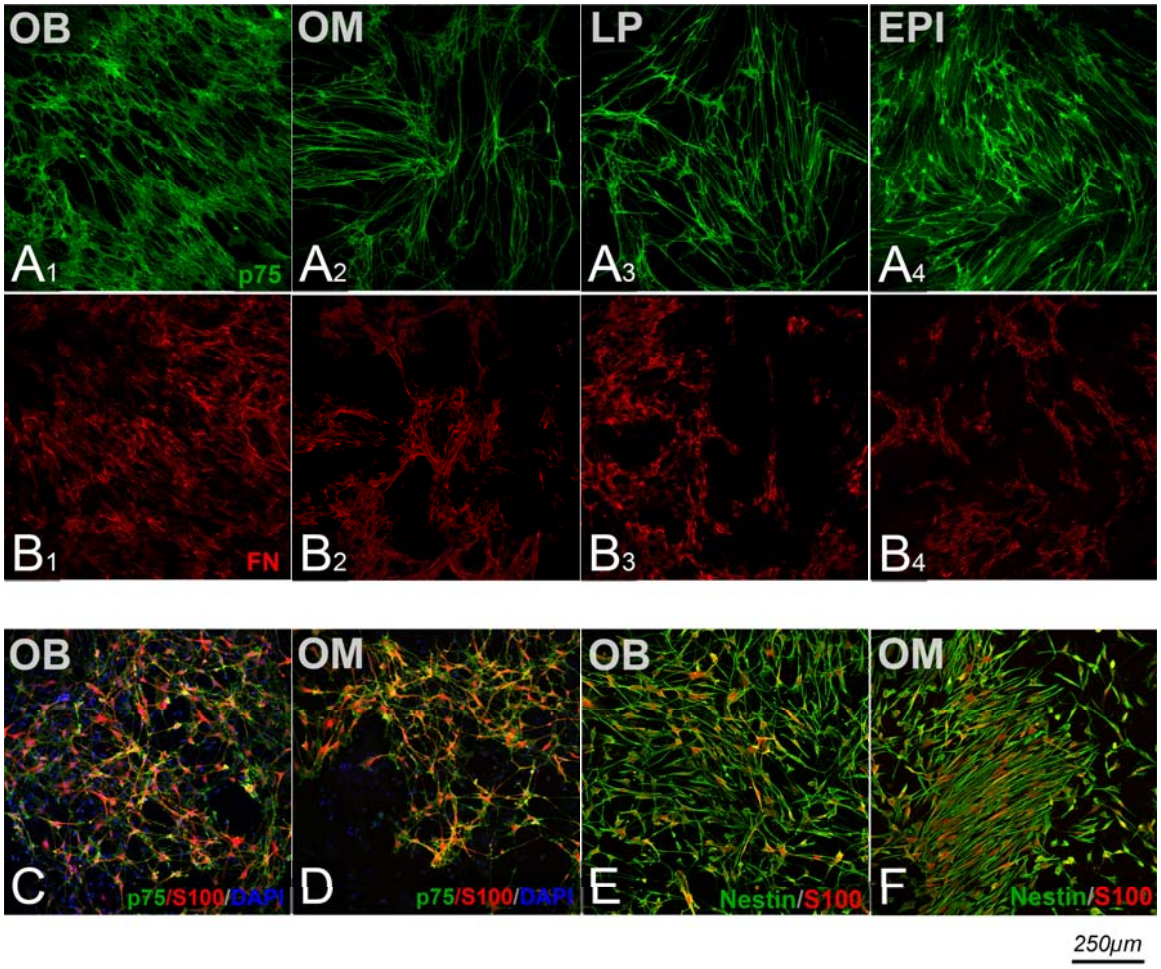
OB
OM
LP
EPI
A1
p75
A2
A3
A4
B1
FN
B2
B3
B4
OB
OM
OB
OM
C
p75/S100/DAPI
D
p75/S100/DAPI
E
Nestin/S100
F
Nestin/S100
250μm

Figure 10: Characterisation of OECs and ONFs in culture at DIV 10 and beyond.
Immunocytochemistry of OEC and ONF in cultures of OB (A, B) and WM (C, D) using S100 (red) and Thy1 (green) at DIV10. Comparison of the two ONF markers (FN, red and Thy1, green) in cultures of samples from OB (B 1-3) and WM (D 1-3) at DIV10. A1 and C1, Thy1 (green), A2 and C2, S100 (red),), and A3 and C3 overlay; B1 and D1, Thy1 (green), B2 and D2, FN (red), and B3 and D3 overlay. Evolution of changes in culture (OB) from 14DIV (E 1-3) to 28DIV (F 1-3). p75 (green); FN (red), and overlay. Abnormal, large cells in long term cultures (G, p75, green and H, Thy1, red). Scale bars, (A-F) 200 μm, (G-H) 100μm.

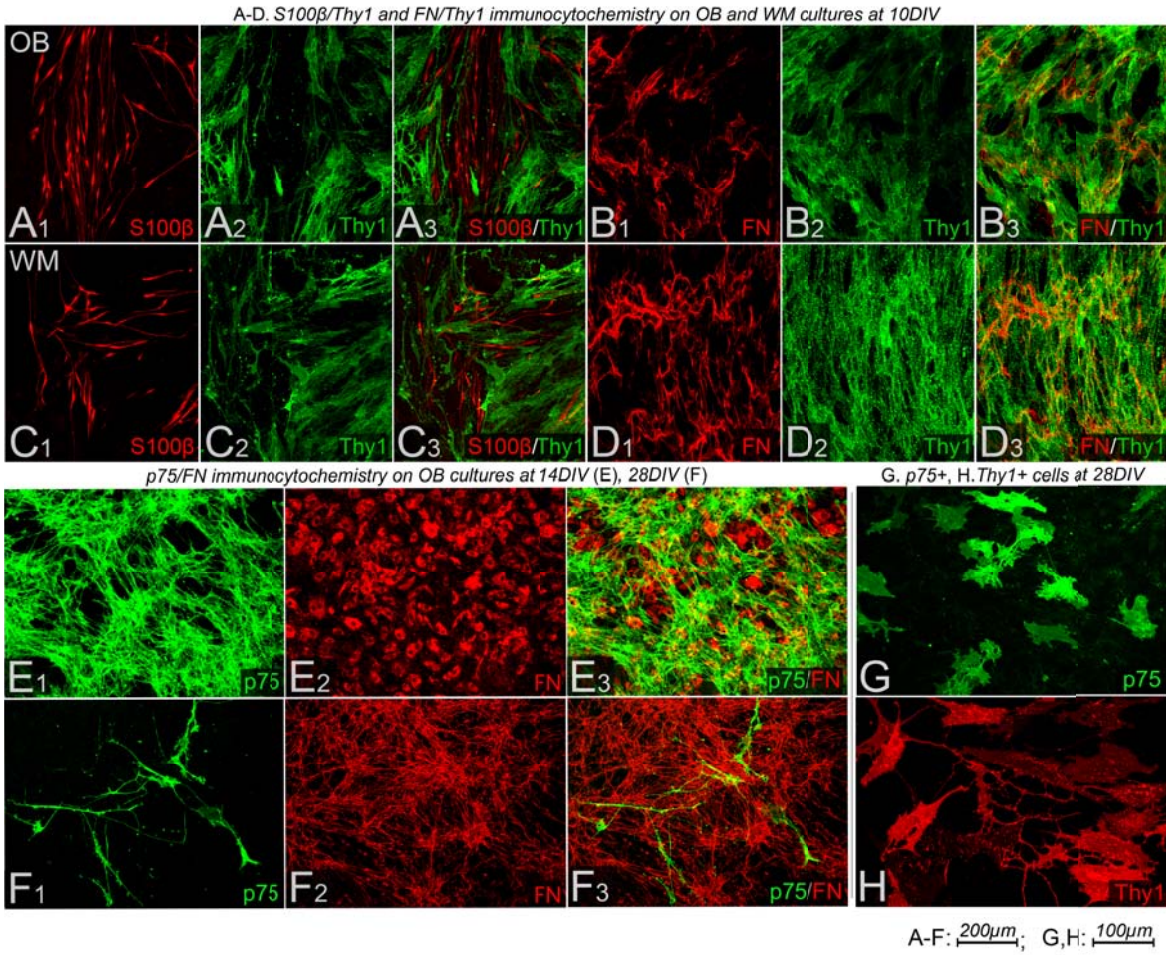
A-D. S100β/Thy1 and FN/Thy1 immunocytochemistry on OB and WM cultures at 10DIV
OB
A1 S100β
A2 Thy1
A3 S100β/Thy1
B1 FN
B2 Thy1
B3 FN/Thy1
WM
C1 S100β
C2 Thy1
C3 S100β/Thy1
D1 FN
D2 Thy1
D3 FN/Thy1
p75/FN immunocytochemistry on OB cultures at 14DIV (E), 28DIV (F)
G. p75+, H.Thy1+ cells at 28DIV
E1 p75
E2 FN
E3 p75/FN
G p75
F1 p75
F2 FN
F3 p75/FN
H Thy1
A-F: 200μm; G,H: 100μm

Figure 11: Characterisation of purified OECs and ONFs from OB and OM.

Confocal images of purified OECs (A,B), ONFs (C,D) and p75-Thy1- (E,F) population from OB (A,C E) and OM (B,D, F) after 4 day in culture. The p75 purified cells from the WM sourced cultures (B), but not the OB cultures (A), have generated a further small population of doubly labeled cells (B2, white arrowheads), identified by the deposition of FN (red) which overlaps with the p75+ cells (green). Neither OB nor WM sourced cells purified on the basis of Thy1 (C, D) generate a p75+ population. The p75-Thy1- population is predominantly FN positive with only a small proposition of in OM is also p75 positive (F). p75, green; FN, red; DAPI, blue. Scale bars, 200 μm.

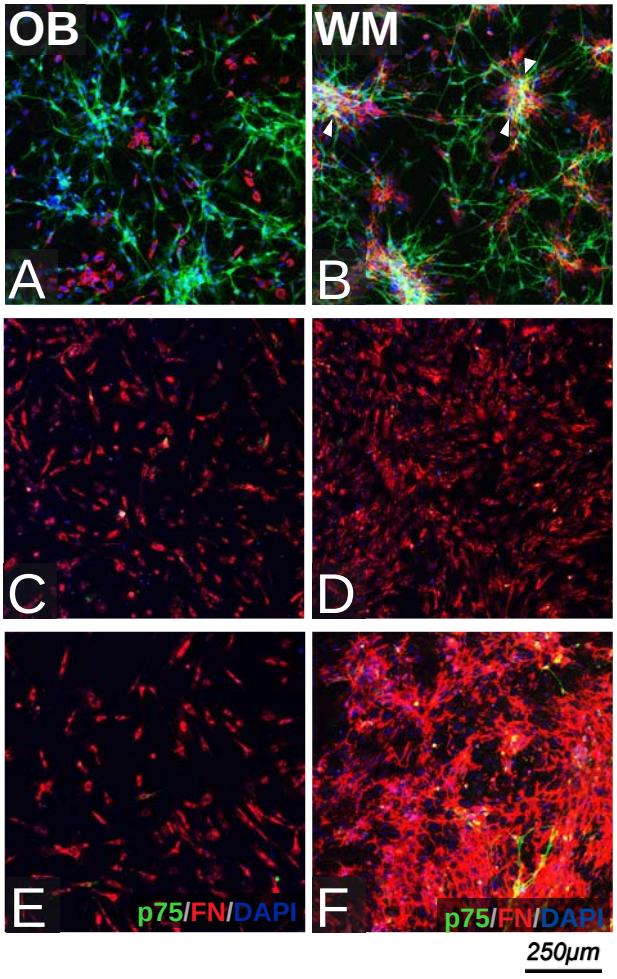
OB
WM
A
B
C
D
E
F
p75/FN/DAPI
p75/FN/DAPI
250µm

3.2.5 Antibody optimization for FACS

The characterization of the two cell populations: OECs and ONFs using FACS, involved 3 steps. First step was antibody selection. p75 from Chemicon (MAB365) and Abcam (ab8877 and ab8874), while Thy-1 from Abcam (ab8872 and ab33694) were shortlisted for this application based on supplier data sheets. Preliminary FACS analyses of selected p75 and Thy1.1 antibodies showed differential expression profiles respectively (data not shown). For p75, such variability occurred due to the polymorphism of genes encoding heavy chain variable regions that often exist on the antigen binding in different p75 antibodies available. This is evident in their DNA sequence used to develop the antibodies clones (available from manufacturer data sheet). To determine the right antibody, the percentage of p75+ region in histogram was compared with the p75+ approximation obtained from the immunostaining images. The closest correlation of the p75+ percentage is the acquisition obtained using p75-365 from Chemicon. For Thy1.1 antibody, only Thy1 ab33694 showed positive expression in the preliminary FACS analysis.

In the second step in characterisation, isotype, negative, positive and specificity control were used to proximate the relative fluorescent expression of the selected antibodies. For the isotype control: FACS analysis using mouse IgG isotype control showed a similar expression pattern to that of the negative control, with no non-specific IgG binding on the primary cells (Figure. 12 A and B, black line).

For the negative control, immunolabelling cells with only the corresponding fluorophore-bound secondary antibody only (i.e. anti-Ms Alexa Fluor 488 or anti-Ms

Figure 12: Analysis of flow cytometric histograms for p75 and Thy1.1 negative controls.
3D histograms of the p75 AF488 (A) and Thy1-PE (B)fluorescent signals from cells staining with only anti-mouse (Ms) phycoerythrin (PE) antibody (dark red), no antibody (green and blue), anti-mouse Alex Fluor 488 (AF488) antibody (yellow) and anti-mouse IgG immunoglobulin (black). Cells used for PE is OM after DIV10.

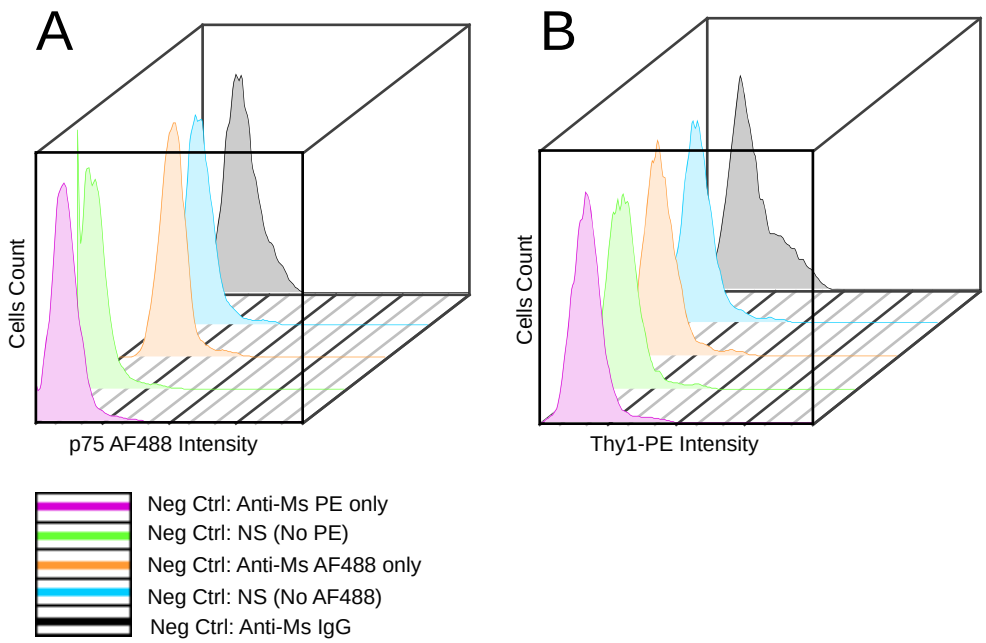
A
B
Cells Count
Cells Count
p75 AF488 Intensity
Thy1-PE Intensity
Neg Ctrl: Anti-Ms PE only
Neg Ctrl: NS (No PE)
Neg Ctrl: Anti-Ms AF488 only
Neg Ctrl: NS (No AF488)
Neg Ctrl: Anti-Ms IgG

PE) or no immunostaining (NS) were performed on the same primary cultured cells. Figure. 12 showed the expression profiles of these negative controls for both p75 (Figure. 12A) and Thy1 (Figure. 12B) antibody. These controls were also routinely used to prime and proximate the cytometer parameters such as 1) forward and side scatter signals and 2) the argon laser threshold for the FITC and PE spectral channel. For both WM and BB, negative control results consistently showed a noticeable level of autofluorescence between the FITC and PE channels, depicting by the diagonal signal in the dual-parameter FACS cytograms (Figure. 4 & 15). The autofluorescence signals were gated out based on control, excluding any false positive for p75 or Thy1 in any subsequent analyses.

The positive control used for p75-NTR antibody was Schwann cell line SC16, immunolabelled with both primary (anti-p75-NTR) and secondary antibody (FITC conjugated IgG), while for Thy1 was LP 17DIV primary cultured cells, immunolabelled with phycoerythrin conjugated primary antibody (PE conjugated anti-Thy1) (Figure. 13).

For selection of Thy1 antibody, as there was no antibody that was used routinely to identify the morphology ONF at the immunocytochemistry aspect, it was not possible to confirm the FACS analysis of the expression of chosen Thy1.1 antibodies used in my trials. Hence a specificity control test was performed to establish its specificity to the fibroblasts in olfactory cultures.

Thy-1 specificity control was performed by incubating Thy1-PE with the unconjugated Thy-25 in the same sample to reveal the competitiveness of the

Figure 13: Analysis of flow cytometric histograms for p75 and Thy1.1 positive controls.
3D histograms of the p75 AF488 fluorescent signals from Schwanns cells (A) and Thy1-PE fluorescent signals (B) from lamina propria (LP) cultured for 17 days, using a combinatorial of relevant antibodies: Schwann cell line RT4-D6P2T (known to be p75-positive) and LP DIV17 (Thy1-positive).

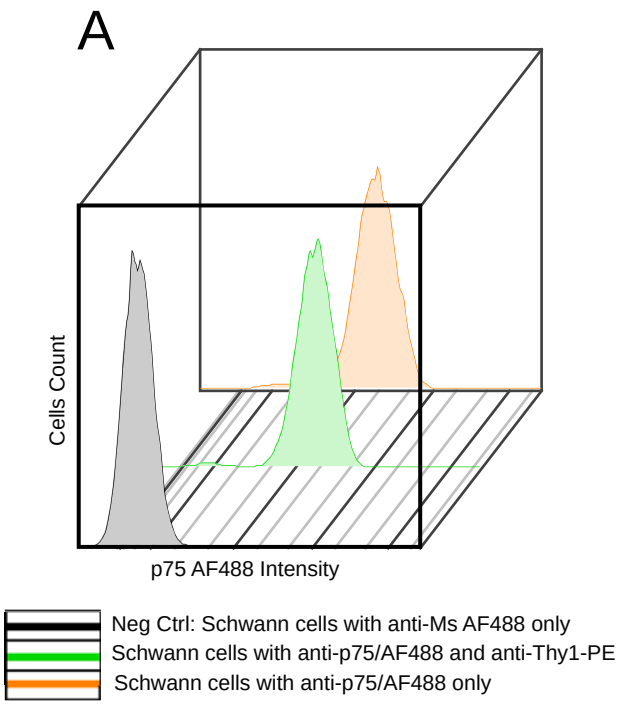
A
Cells Count
p75 AF488 Intensity
Neg Ctrl: Schwann cells with anti-Ms AF488 only
Schwann cells with anti-p75/AF488 and anti-Thy1-PE
Schwann cells with anti-p75/AF488 only

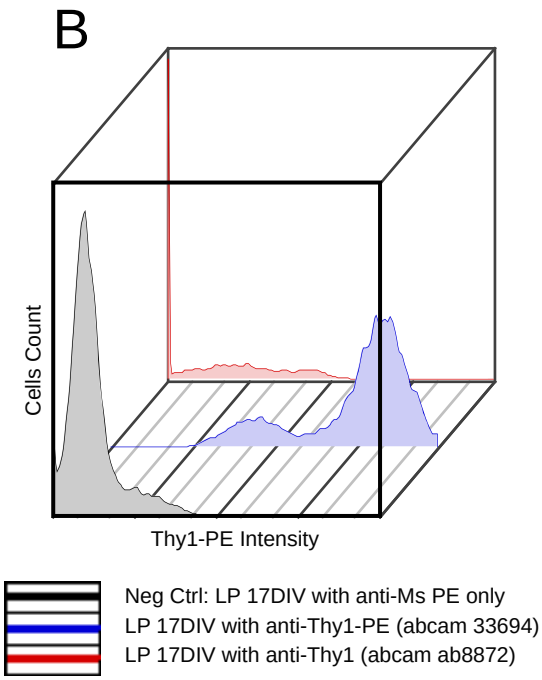
B
Cells Count
Thy1-PE Intensity
Neg Ctrl: LP 17DIV with anti-Ms PE only
LP 17DIV with anti-Thy1-PE (abcam 33694)
LP 17DIV with anti-Thy1 (abcam ab8872)

antibody to Thy-1 receptor on fibroblasts in olfactory culture. Both Thy1-PE and Thy1-25 were the antibodies produced from the same clone: clone MRC OX 7, with only Thy1-PE conjugated with fluorophore PE. Figure. 14 showed the Thy-1 specificity control experiment using lamina propria cell culture, cultured for 17d to obtain overgrowth fibroblasts (LP 17DIV). When incubated with its unconjugated corresponding antibody: Thy1-25, the expression of Thy1-PE decreased significantly in both WM and OB culture, seen in the reduced expression profile (Figure 14, A, green; B, purple). This showed the competitive characteristic of both antibodies to bind to the same receptor, Thy1, a clear indicator of Thy1 presence in fibroblasts.

The last step is mutual exclusivity of the p75+ only and Thy-1+ only population to discern OECs from ONFs and *vice versa*. Dual parameter FACS cytograms were used with p75+ fluorescent intensity on x-axis and Thy-1+ fluorescent intensity on y-axis. After appropriate spectrum compensation to reduce the cross spectral signal from the FITC and PE, the FACS cytograms (Figure. 4B) confirmed the presence of two distinct, non-overlapping populations at 10DIV: p75+Thy1- (putative OECs) and p75-Thy1+ (putative fibroblasts (ONFs)) cells, as well as an uncharacterized double negative (p75-Thy1-) population. In addition, only the WM cultures contained a small population of double positive (p75+Thy1+) cells.

3.2.6 Evolution of the subpopulations over time

Figure. 9 illustrates the practical difficulty in counting cell subpopulations in mixed cultures from the confocal micrographs. To provide a more reliable assessment of cell numbers, the cell surface markers p75 and Thy1 were used for the two-parameter FACS analysis. Before culture (0DIV), the freshly dissociated cells

Figure 14: Analysis of dual parametric cytograms for Thy1.1 specificity controls.
Thy1-PE specificity to olfactory fibroblast was verified using antigenic competitive analysis. Thy1-25, a non-phycoerythrin conjugated Thy1.1 antibody, derived from the same MRC OX-7clone, was used to compete with its conjugated counter-antibody, Thy1-PE to determine for antibody specificity for ONF in OM DIV10 (A) and OB DIV10 (B).

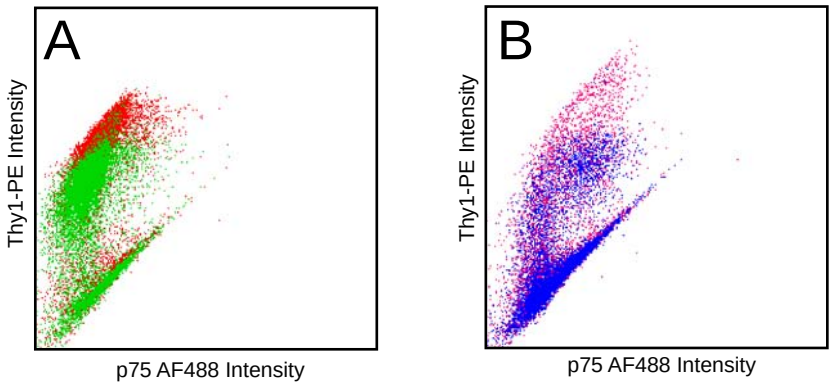

OM 10DIV with anti-Thy1-PE and Thy1-25 (both clone MRC OX-7),

OM 10DIV with anti-Thy1-PE (clone MRC OX-7),

OB 10DIV with anti-Thy1-PE and Thy1-25 (both clone MRC OX-7),

OB 10DIV with anti-Thy1-PE (clone MRC OX-7),

showed a clear antigenic difference between the predominantly p75-Thy1+ cells from the OB and the double negative cells from the OM (Figure. 15 top row).

When cultured, however, these seemingly homogeneous populations give rise to a variety of phenotypes comparable to those seen in immunocytochemistry. Cytograms (lower panels of Figure. 15) for the OB, WM and the split EPI and LP populations over 7, 10, and 14d in culture confirm the development of distinct, non-overlapping populations of p75+Thy1- (OECs) and p75-Thy1+ (ONFs), as well as an uncharacterized double negative (p75-Thy1-) population.

In OB, the entire cellular population subsequently shifted downwards p75− Thy1− by 7DIV, with a small minority considered to be p75+ Thy1− and p75− Thy1+, based on positive control (Figure. 16). By 10DIV, the cellular composition was made up of two evolving non-overlapping subpopulations: p75+ Thy1− and p75− Thy1+. At 14DIV both populations ceased to evolve further, with majority of the cells reside on the p75-positive only or the Thy1+ only quadrant (Figure 15).

Meanwhile, as early as 7DIV, WM culture was already composed of two non-overlapping populations. Subsequently from 10DIV onwards, WM cultures also developed a small population of double positive (p75+Thy1+) cells, which were not seen in the cytograms of cultures of the bulbar tissue or the separated mucosal EPI and LP samples (see Figure. 15). The salient features arising from this quantitative analysis are that in the OB cultures OECs predominate over ONFs, and the reverse in the WM cultures. However, cells in the split mucosal cultures behave quite differently.

Figure 15: Dual parametric cytograms for Antigenic Subpopulations in samples of four olfactory derivatives over time.

Cytograms showing evolution of the 4 antigenic subpopulations (p75+Thy1, p75-Thy1+, p75-Thy1- and p75+Thy1+) in samples of OB and WM at 0, 7, 10 and 14 DIV and EPI and LP at 7,10 and 14 DIV. X-axis, intensity of AF488 labelling for p75; y-axis, the intensity of PE labeling for Thy1. Cell density from blue (low) to red (high). The cytograms confirm the immunocytochemistry observation of the development of distinct, non-overlapping populations of p75+Thy1- (OECs) and p75-Thy1+ (ONFs), as well as a double negative (p75-Thy1-) population and, in the WM cultures, a population of double positive (p75+Thy1+) cells.

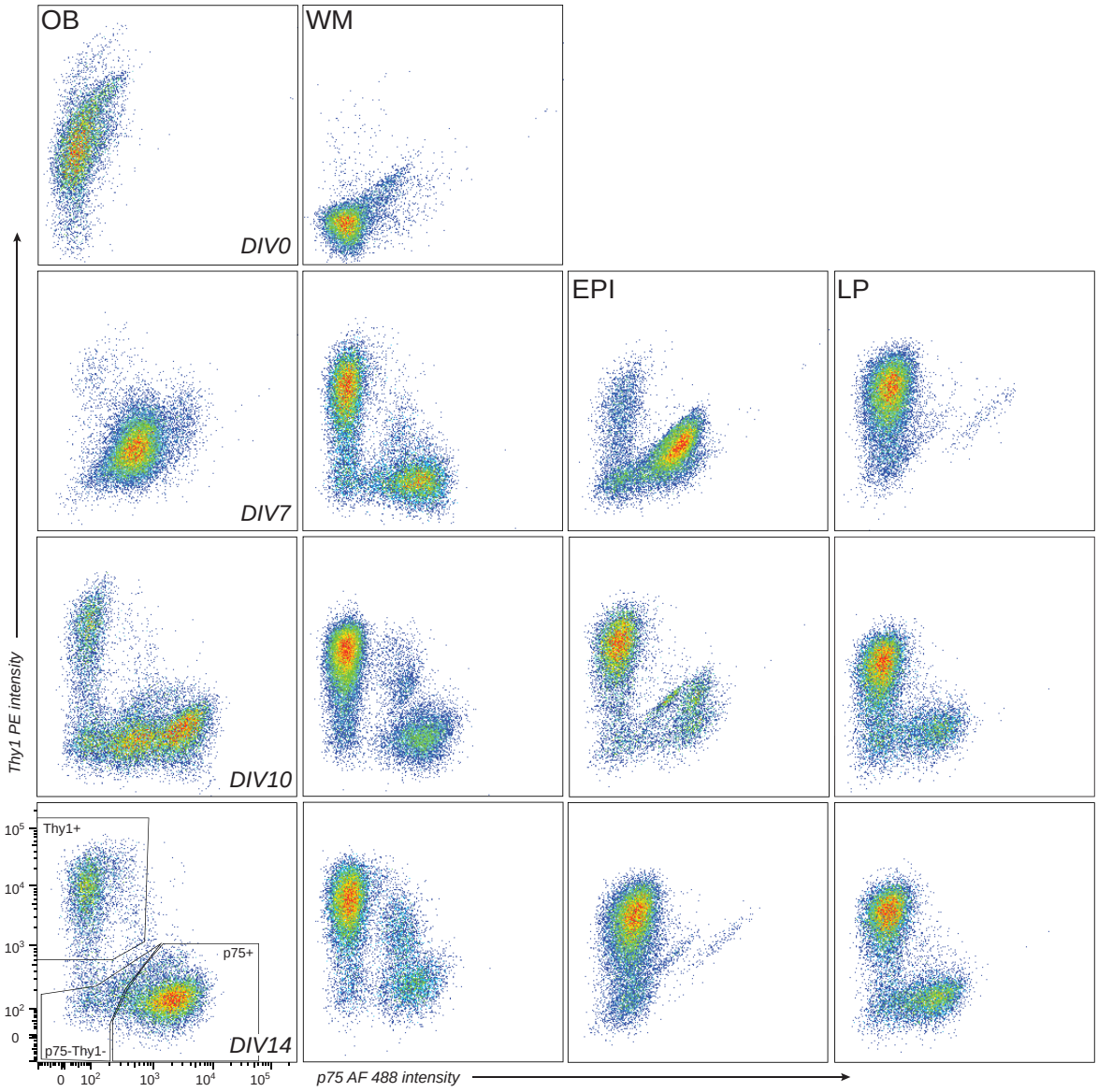
OB
WM
EPI
LP
DIV0
DIV7
DIV10
DIV14
Thy1 PE intensity
p75 AF 488 intensity
Thy1+
p75+
p75-Thy1-
0
10²
10³
10⁴
10⁵

Figure 16: Bar charts of percentage of OECs and ONFs population from four olfactory derivatives over time

Changes in the cell populations at 7, 10 and 14 days in culture shown by flow cytometry. Data points show the mean ± SD of 5 repeats for each of the four tissue sources (OB, WM, EPI and LP). Total number of samples = 60, error bar, 1 SD.

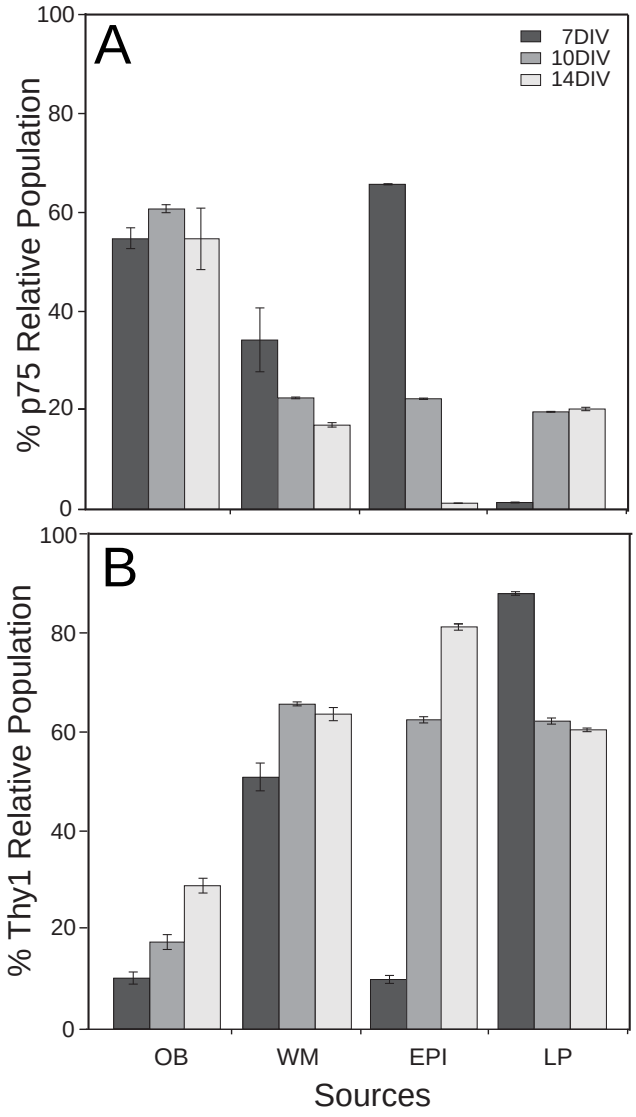
A
7DIV
10DIV
14DIV
% p75 Relative Population
100
80
60
40
20
0
B
% Thy1 Relative Population
100
80
60
40
20
0
OB
WM
EPI
LP
Sources

Unexpectedly, in view of the high proportion of OECs in *in situ* histology (Figure. 7C-F), LP samples generated the lowest proportion of OECs (less than 20%) of any sample. In striking contrast, EPI samples (with no detectable OECs histologically; Figure. 7C and D) generated the highest proportion of OECs (over 60%) of any tissue sample at 7DIV, falling rapidly at 10–14DIV.

This detailed dual parametric cytofluoroanalysis of WM and OB from 0d to 14d revealed the populations shift within the subpopulations.

3.2.7 Quantification by fluorescent activated cell sorting analysis

Using the FACS analysis as a cell quantifying tool, I investigated the proportion changes for two dominant populations: p75+Thy1- (representing OEC) and p75-Thy1+ (representing ONFs) over time (Table 2, Figure. 16). The quantified subpopulation (p75+Thy1- and p75- Thy1+), expressed as percentage of the whole population based on the gating showed in Figure. 4B, were then compared among the 4 adult olfactory derivatives over these three time points.

As shown in Figure. 16, proportion changes observed over time for both p75+Thy1- and p75- Thy1+ populations in all 4 cell sources are significantly different (0.000 <**P<0.054). The $p75^{+}Thy1^{-}$ subpopulation from OB peaked at 59.78% in number at 10DIV, while its ONF population, p75- Thy1+ steadily increased from 10.23% to 30.44% by DIV14. Conversely, the WM p75+Thy1- exhibited a different population growth pattern where the relative percentage of the population decreased from 33.58% to 16.99 % over the same period of time, while WM p75- Thy1+ peaked at 68.95% on 10DIV.

Table 2: The relative percentage proportions of OECs, ONFs, and double negative and double positive cells in the 4 cultures over time.

Five replications for all phenotypes from all sources at 7-14 DIV, except 3 for WM p75+Thy1+, and 2 OB and WM at DIV0.

	p75+Thy1-				*p75-Thy1+*				*p75-Thy1-*				*p75+Thy1+*			
	OB	**WM**	**EPI**	**LP**	**OB**	**WM**	**EPI**	**LP**	**OB**	**WM**	**EPI**	**LP**	**OB**	**WM**	**EPI**	**LP**
0DIV	0.10±0.09	2.84±0.13			88.29±2.18	1.65±0.13			10.89±1.07	94.88±0.84						
7DIV	53.60±2.66	33.58±6.83	64.89±0.11	1.14±0.05	10.23±0.89	50.45±2.63	10.03±0.16	87.11±0.46	32.99±2.25	11.39±4.93	17.34±0.11	6.92±0.10		0.81±0.44		
10DIV	59.78±1.08	21.14±6.58	21.79±0.27	15.30±0.14	17.43±1.67	68.95±7.39	61.88±0.69	68.83±13.93	17.99±0.65	5.00±0.23	10.59±0.34	12.28±0.26		3.37±1.22		
14DIV	45.86±6.44	16.88±0.53	1.03±0.06	15.51±8.63	30.44±3.60	66.42±6.76	80.79±0.10	63.34±6.58	13.68±4.44	7.10±2.86	10.97±0.14	10.78±0.21		4.32±3.38		

Five replications for all phenotypes from all sources at 7-14 DIV, except 3 for WM p75+Thy1+, and 2 OB and WM at DIV0.

As one of the derivatives from the whole mucosa, EPI culture surprisingly had the largest percentage of p75+Thy1- population (68%) among four sources at all time points. The population then displayed a sharp decrease, where the percentage fell from 64.89% to 1.03% at rate of 35 fold. Meanwhile, EPI p75-Thy1+ has a population increase 5.2 fold in a short 3 d period, from10.03% at 7DIV to 61.88% at 10DIV, and a subsequent 0.3 fold increase to 80.79% by 14DIV. In contrast, for LP, a commonly used peripheral OEC source, p75+Thy1- only account for 1.14% of total cell populations at 7DIV, but then showed a 15.9 fold increase at 10DIV to plateau by 14DIV at 19.82%. Although the p75-Thy1+ population showed a large proportion of population (87.11%) at 7DIV, this population decreased 0.29 fold and too reached a plateau by 14DIV at 60%.

These results provide evidence of a time-linked differential pattern in subpopulation proportion for both peripheral and central OEC and ONFs.

3.2.8 Cell cycle kinetics of olfactory derivatives

To investigate the extent to which proliferation contributes to the observed population changes, I developed a novel four colour simultaneous antigenic bivariate cell cycle assay with EdU as the S-phase marker to characterize the dynamics of cell proliferation separately within the individual OEC and ONF subpopulations of the OB, WM, LP, and EPI cultures at the different times in culture.

Figure. 4E showed cell cycle kinetic analysis of typical example for a single population of OECs, based on EdU Pacific Blue fluorescence intensity (y-axis) and total DNA content CellCycle 633-red intensity (x-axis). For the negative control

cells from the same batch without incubation with EdU, the dot plot showed that the presence of two cell aggregates, joined by a small row of cell aggregate at the lower quadrant. The low quadrant represents cells without EdU. The concentration of all the cells at the lower quadrant in the negative control also determined that there was no false positive signal of EdU from the population of cells itself. For the experimental samples, the dot plot of a horseshoe distribution is a typical illustration of a cell population that is cycling in cell cycle. The left lower gated aggregate represents quiescent cells in the non-dividing G1/G0-phase, which do not incorporate EdU. This population of cells has half of the total DNA content, based on the intensity of CellCycle 633-red signal. The upper gated population represents the S-phase cells which incorporated EdU during their DNA multiplication. The right lower population represents EdU-negative cells which had reached their G2/M-phase of doubled DNA content prior to the administration of EdU.

Table 3, summarized in Figure. 17, shows that the majority of cells in all four types of cultures were quiescent (G0/1-phase of the cell cycle) over the 7–14DIV period. The G2/M-phase (the mitogenic state) consistently had the lowest percentage. For the S-phase, the most striking features were in the EPI cultures (reflected to a lower extent in the WM cultures), which exhibited a high percentage of OECs in S-phase (DNA multiplication) at 7 and 10DIV, falling sharply by 14DIV, and a high percentage of ONFs in S-phase at 7DIV. In the WM cultures, there was a high proportion of the doubly labelled (p75+FN+) cells in S-phase at 10DIV, rising further at 14DIV. Apart from these, the remaining OB, WM, and EPI cultures showed low proliferative activity (S-phase percentage).

Table 3: The relative percentage proportions of OECs, ONFs, and double negative and double positive cells in S-, G0/1- and G2/M-phases over DIV10.

The proportions of cells in S-, G0/1- and G2/M-phases in 36 OB, WM, EPI and LP samples at 7, 10 and 14DIV (3 replications of each sample at each time point).

p75+Thy1-

	OB			*WM*			*EPI*			*LP*		
	7DIV	**10DIV**	**14DIV**	**7DIV**	**10DIV**	**14DIV**	**7DIV**	**10DIV**	**14DIV**	**7DIV**	**10DIV**	**14DIV**
G0/1	85.76±0.61	91.63±0.89	95.41±0.90	76.57±1.90	92.68±0.38	91.99±4.19	34.28±0.88	46.50±2.78	77.74±2.83	62.34±3.72	85.60±0.80	74.51±0.65
S	9.33±0.28	3.05±0.10	1.43±0.56	21.05±2.52	4.11±0.06	6.23±4.07	56.30±0.78	47.99±2.19	6.62±2.56	7.93±1.70	7.80±0.71	20.25±0.67
G2/M	4.67±0.33	4.87±0.79	2.88±0.44	2.31±0.23	2.98±0.38	1.68±0.09	1.57±0.09	1.69±0.36	8.08±1.46	15.35±2.48	2.46±1.30	3.24±0.34

p75-Thy1+

	OB			*WM*			*EPI*			*LP*		
	7DIV	**10DIV**	**14DIV**	**7DIV**	**10DIV**	**14DIV**	**7DIV**	**10DIV**	**14DIV**	**7DIV**	**10DIV**	**14DIV**
G0/1	89.89±1.53	92.81±0.82	92.63±2.82	70.46±0.55	94.03±0.60	93.19±0.67	54.08±0.54	77.83±0.48	94.87±0.31	89.83±0.85	92.29±0.52	89.29±0.48
S	4.99±0.91	3.11±0.05	3.79±3.28	24.26±0.32	2.64±0.23	3.86±0.64	37.30±0.39	13.75±0.93	1.49±0.12	1.31±0.15	2.29±0.20	6.08±0.09
G2/M	4.87±0.63	3.64±0.45	3.26±0.74	5.24±0.26	3.12±0.37	2.79±0.50	6.95±0.81	7.00±0.97	2.46±0.31	5.42±0.25	2.78±0.51	3.24±0.41

p75+Thy1+

	OB			*WM*			*EPI*			*LP*		
	7DIV	**10DIV**	**14DIV**	**7DIV**	**10DIV**	**14DIV**	**7DIV**	**10DIV**	**14DIV**	**7DIV**	**10DIV**	**14DIV**
G0/1				0	40.66±1.55	12.38±6.19						
S				0	53.50±3.32	84.80±8.10						
G2/M				0	5.75±2.18	2.57±1.83						

3 replications of each sample at each time point

Figure 17: Bar charts of flow cytometric simultaneous antigenic and bivariate cell cycle comparison among subpopulations of the four olfactory derivatives at three time points.
A, exemplary gating for G1-phase (blue), S-phase (red), G2-phase (green) on a sample. B, flow cytometric simultaneous antigenic and cell cycle analysis at 7, 10 and 14 days in culture for the p75+Thy1- and p75-Thy1+ subpopulations in all four tissue sources, and the double labelled (p75+Thy1+) population (found only in the WM source). Each point is the mean ± SD of 3 repeats of the proportion of the population in G0/1-phase (dashed line, squares), S-phase (solid line, triangles), G2/M (dotted line, circles).

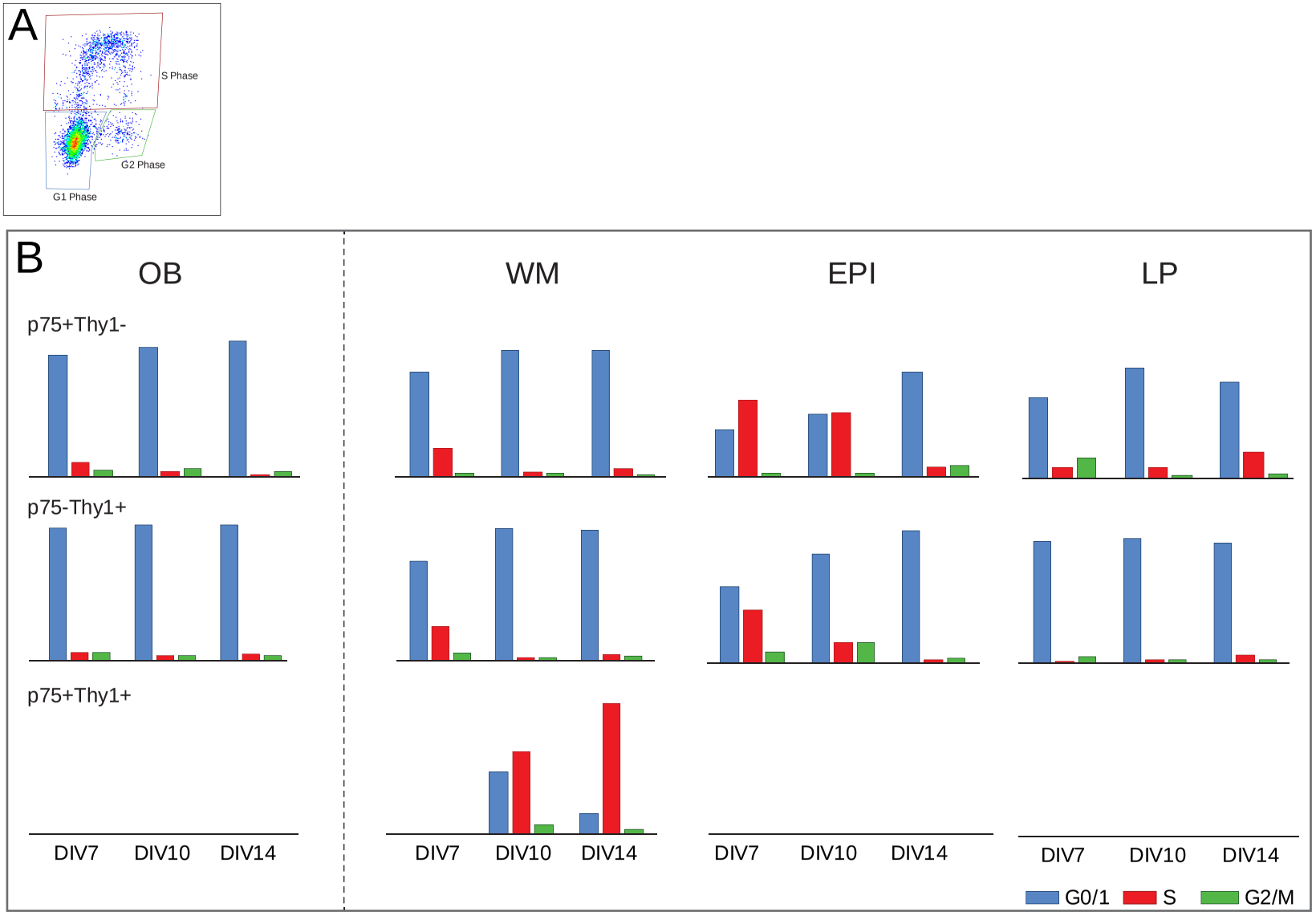
A
S Phase
G2 Phase
G1 Phase
B
OB
WM
EPI
LP
p75+Thy1-
p75-Thy1+
p75+Thy1+
DIV7
DIV10
DIV14
G0/1
S
G2/M

3.2.9 Correlation of relative population size with cell proliferation

To determine the extent to which cell proliferation correlates with changes in population size, a global pair-wise analysis was carried out for all 4 tissue sources over all time points. This is with no assumption of any sources and time differences. Pooling all the individual data points from each of the four tissue sources and each of the three time points, the percentages of the mixed cell population that were OECs (p75+Thy1−) and the percentages that were ONFs (p75−Thy1+) were plotted against the percentages of OECs and ONFs that were EdU labelled (i.e., in S-phase). Plotted in this way, neither the proportion of cells that were OECs nor the proportion of cells that were ONFs were correlated with the numbers of OECs or ONFs that were in S-phase (Pearson's correlation coefficient, $r = 0.511$, $P<0.001$ for the OECs and $r = 0.095$, for the ONFs) (Figure. 18A and B).

To scrutinize this weak global correlation with known factor: source, partial correlation matrix carried out for each of the four tissue sources. However, taking the OB and the mucosal cultures (pooled WM, EPI, and LP) separately (Figure. 19 B1) revealed a highly significant positive correlation for the pooled mucosal cultures at all time points between the percentage of OECs and the proportion of the OECs that were in S-phase ($r = 0.903$, $P < 0.001$). For the OB cultures, there was no significant correlation between the numbers of OECs and the proportion of OECs in S-phase at any of the time points ($r = 0.167$). There were no significant correlations for any of the ONF populations with the proportion of ONFs in S-phase for either the bulbar or the mucosal cultures.

Figure 18: Global correlation of proportions of OECs and ONFs in S-phase from all four sources.
The proportions of all OECs and ONFs in all samples with corresponding percentages of p75 (A) and Thy1 (B) cells in S-phase. n=42.

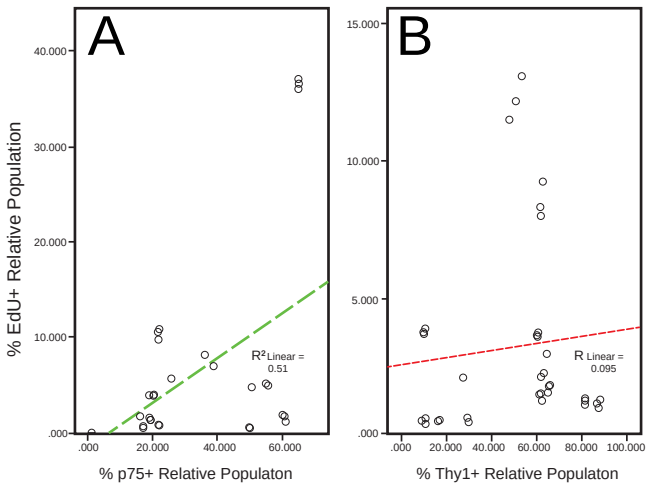
A
B
% EdU+ Relative Population
% p75+ Relative Populaton
% Thy1+ Relative Populaton
R² Linear = 0.51
R Linear = 0.095
40.000
30.000
20.000
10.000
.000
15.000
10.000
5.000
.000
20.000
40.000
60.000
80.000
100.000

Figure 19: Partial correlation of proportions of OECs and ONFs in S-phase from all four sources.
For each of the OB, WM, EPI and LP samples of the proportions of all OECs and ONFs in all samples with corresponding percentages of cells in S-phase. n=31.

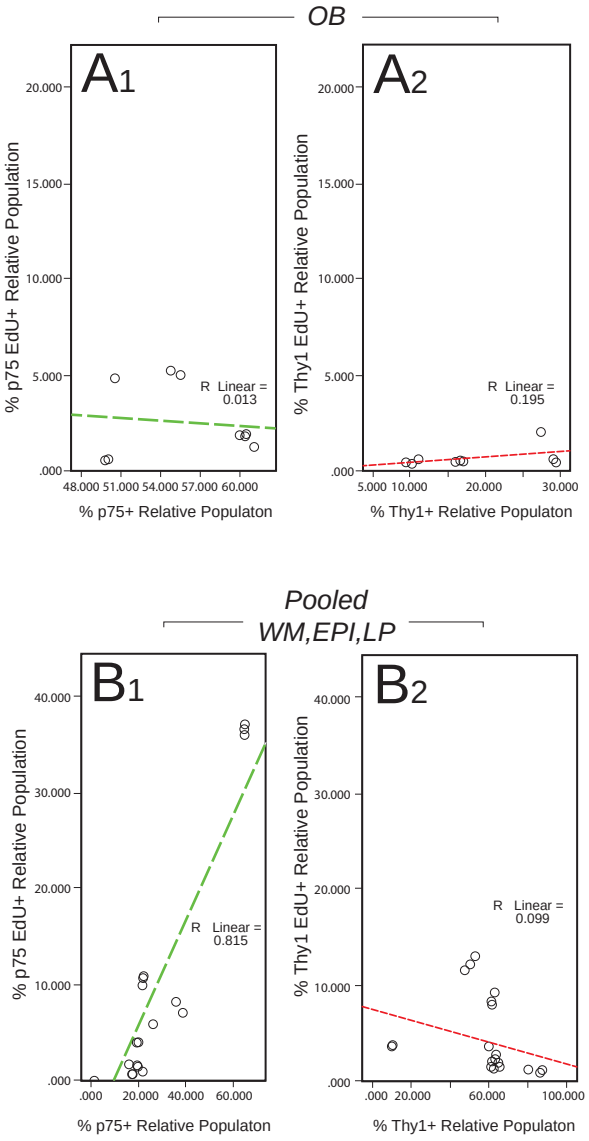
OB
A1
A2
% p75 EdU+ Relative Population
% Thy1 EdU+ Relative Population
R Linear = 0.013
R Linear = 0.195
% p75+ Relative Populaton
% Thy1+ Relative Populaton
Pooled
WM,EPI,LP
B1
B2
R Linear = 0.815
R Linear = 0.099

3.2.10 Further culture of FACS purified cells

To examine the phenotypic stability of the FACS purified populations, cells sorted from the OB and WM tissue samples were maintained for an additional 4DIV and then examined by both morphology and immunocytochemistry (Figure. 11A-F). At this time, the majority of the FACS purified p75+Thy1- cells retained their p75 immunoreactivity and adopted the spindle-shaped morphology comparable to the OECs in the heterogeneous (unsorted) cultures (Figure. 11A and B). It was notable that at lower cell density (<10,000 cells/cm^2), purified OEC lacked cell adherence even on laminin-coated chamber slides.

Unexpectedly, however, the cultures of p75+ cells sorted from the WM sample now consistently generated (a) small clusters of p75-FN+ immunoreactive cells scattered among the majority p75+FN- population (not shown), and (b) cells that were doubly labelled for p75 and FN (Figure. 11B), white arrow heads.

Unlike the purified p75+FN- population, however, the p75-FN+ sorted cells from OB and WM showed no antigenic changes (Figure. 11C and D). They expressed FN and adopted the multipolar morphology observed in the ONFs of the unsorted heterogeneous cultures.

The results provide morphological and immunocytological evidence that OEC and ONFs are present in mucosal sources. The marked difference in the FN expression pattern and the density-dependent survival of purified populations suggest that FN may be important in enhancing population growth.

3.2.11 Deposition of fibronectin

To find clues to which factors might be contributing to persistently weak-to-no correlation of the cell proliferation and its corresponding population percentage in p75-Thy1+, the same partial correlation matrix analysis revealed a significant negative cross-correlation between the p75+Thy1- S-phase and, unexpectedly, the p75-Thy1+ population size (r= -0.883, and -0.913 for the bulbar and mucosal tissue sources respectively).

To validate this statistical analysis, I explored the pattern of fibronectin, a well accepted and commonly secreted factors as an index of the ONFs population, in relation to OEC population growth, an indication of proliferative ability. Cultures of mixed and purified OB and WM tissues were used to compare the level of FN deposition (see Material and Methods) with the percentage of the overall DAPI stained cell population that were p75+. After normalizing the level of FN expression across the different experiments, in mixed cultures, low OEC percentage (20.85%) show high FN secretion, middle OEC percentage (59.87%) show intermediate fibronectin secretion. In purified cultures (98%) showed low fibronectin secretion and the OEC number were maintained over 4d. Figure. 20 showed a clear inverse log relationship between the level of FN deposition and the percentage of p75+ cells. This experimental result validated the predicted effect of cross interaction between OEC and ONFs in the statistical analysis. Hence, one of the external factors that contribute to the ONFs population is OEC proliferation. With the decrease of ONF population, OECs proliferate more.

Figure 20: Correlation of fibronectin deposition with the percentage of p75+ cells.
Correlation graph of the level of FN expression across the different experiment, in mixed and purified cultures with the number of OECs (DAPI).

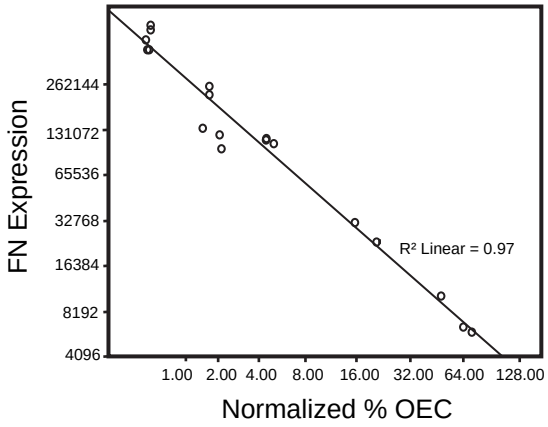
FN Expression
262144
131072
65536
32768
16384
8192
4096
R² Linear = 0.97
1.00
2.00
4.00
8.00
16.00
32.00
64.00
128.00
Normalized % OEC

3.3 Discussion

The interest in culturing OECs is to derive a transplant preparation that will enable the intrinsic reparative capacity of the adult olfactory system to be transferred to CNS lesions that do not regenerate. Central to this is the question of the extent to which spindle shaped cells expressing p75 in culture correspond with OECs *in situ.*

3.3.1 Population heterogeneity and percentage in olfactory source

Comparing the FACS analysis of these sources, dual-parametric antigenic patterns differentiate the 4 tissue sources of OEC/ONFs significantly, in both population heterogeneity and quantity at any particular time point. Using FACS analysis, I was able to carefully quantify the subpopulations in the four sources of OEC: whole mucosa (WM), lamina propria (LP), olfactory epithelium (EPI) and olfactory bulb (OB). Such detailed differential population pattern may not been easily detectable from digital analysis from bright field and confocal micrographs that are commonly used to identify and quantify OEC and ONFs.

In term of heterogeneity, the FACS antigenic time lapse analysis reveals an evolution of one single starting cell population to not only two non-overlapping main populations: $p75^{+}Thy1^{-}$ representing OEC and $p75^{-}$ $Thy1^{+}$ representing ONFs, but also a third populations: $p75^{-}Thy1^{-}$. In addition, specifically to WM after 10 d, $p75^{+}$ $Thy1^{+}$ appears too. The migration patterns over time also shows the tipping point where OEC, ONFs and the other two populations begin to appear, take form and mature. This differential pattern in population shift created a unique signature for each source.

In addition to the increased complexity in heterogeneity, more importantly, each source has a distinct quantitative composition in OEC and ONF populations, which are dependent on the DIV. Both populations fluctuate at different rates for each source. Based on the FACS analysis, although there is no noticeable trend similarity in proportion changes within the peripheral sources (WM, EPI and LP), a distinct difference is observed between the peripheral (WM) and central (OB) sources of OEC/ONFs. The quantitative analysis draws a crucial prerequisite in defining the eventual amount of OEC/ONFs that can be used for purification prior to transplantation and direct transplantation. Thus it subsequently may account for the disparate findings in regard to functional studies between bulbar and mucosal OEC.

It is also noticeable that in DIV0, WM was found to have neither p75+ nor Thy1+ population, while similarly for OB at DIV 7; there was an expanding though still heavily concentrated p75-Thy1-. This observation suggests the effectiveness of Thy1.1 mediated complement lysis in WM purification at DIV 0 or p75 immunopanning purification procedures used in OB at DIV 7. Lack of cells with these antigens presenting surfaces at the point of purification may easily results in a heterogeneous culture, similar to those without purification.

Furthermore, these results showed that cell density defines the morphology of cells in these cultures regardless of the differential pattern in heterogeneity and OEC/ONFs percentage from all the sources. Without proper cell sorting tool, the potential misrepresentation of the morphology of OEC and ONFs can unintentionally lead to miscalculation of the final cell population that would be purified prior to transplantation or expanded for direct transplantation. This may

address the similarity in those *in vivo* lesion models results with those models that used mixed population transplantation.

Morphological and immunocytological *in vitro* observations have generalized olfactory ensheathing cells (OEC) cultures to two populations: OEC and their associated ONFs (ONFs). Previously cell purification protocols were the preferred way to obtain therapeutic OEC without much consideration on the impact of source and length taken to culture OEC for transplantation. (Ramón-Cueto & Nieto-Sampedro, 1992; Chuah & Au, 1993; Barnett *et al.*, 1993; Au & Roskams, 2003). Therefore, comparing the reparative degree of OEC in various central nervous system (CNS) lesion models have been documented with no distinction between sources or DIV in term of cellular composition of cell transplantation. (Toft *et al.*, 2007). This generalized *in vitro* categorization of OEC is used to conclude all type of OEC reparative ability in the CNS lesion models.

3.3.2 p75 and OECs

Histologically, OECs *in situ* are clearly defined by their anatomical relationships (Figure. 7A–F). During development or after lesions, the expression of p75 on the OECs in the olfactory mucosa and bulb is downregulated, as in the case of Schwann cells (Jessen & Mirsky, 1997), by contact with axons (e.g., (Gong *et al.*, 1994; Turner & Perez-Polo, 1994; Wewetzer *et al.*, 2002). In the intact adult OB, p75 immunoreactivity is restricted to the outer nerve fibre layer [Figure. 7D and F; (Au & Roskams, 2002)]. In the LP, p75 appears on the outer surfaces of the OECs, facing fibroblasts (Figure. 7F), but not on the inner surfaces facing axons. This pattern

suggests that p75 may be trafficked selectively to the OEC surfaces facing basal lamina/fibroblasts, but not to the surfaces facing the olfactory nerve fibres.

Transferring the OECs to tissue culture places them in an entirely different situation. Neuronal cell bodies and nerve fibres do not survive, and the OECs lose their asymmetry and their encircling form. The present FACS analysis of the primary dissociated cell cultures shows that in the mucosal tissue samples over 90% of the cells are initially negative for both p75 and Thy1. In contrast, in the bulbar tissue samples over 90% of the cells are initially p75-Thy1+ in culture, but have upregulated p75 at 7DIV. It is unlikely that trypsinization of the bulbar tissue is responsible for the absence of p75 expression since (1) p75 is also lost in mucosal preparations that are not trypsinized, and (2) after the later onset of p75 expression in culture, trypsinization at 7, 10, and 14DIV causes no loss of p75.

The regulated pattern of expression of p75 *in situ*, its early disappearance and later reappearance in culture, and the appearance of FN expression in cultures of sorted purified p75+ cells raise questions about what exactly is the relationship between the OECs in situ and the cells on which p75 appears after 7d in culture.

3.3.3 Bulbar and mucosal OECs

Most experimental transplantation studies have been with OECs of bulbar origin. For clinical purposes, however, obtaining adult OECs for autografting by an intranasal approach to the olfactory mucosa would be preferable to the more invasive procedure of obtaining bulbar OECs by craniotomy. At the genomic level, the transcriptome profiles of purified OEC from OB and the mucosal LP revealed a

pattern of differentially expressed genes, with the suggestion that bulbar OECs generally express genes associated with nervous system development, while mucosal OECs express genes associated with wound healing and extracellular matrix regulation (Franssen *et al.*, 2008; Guérout *et al.*, 2010).

The present results show p75+Thy1- spindles in cultures from both mucosal and bulbar tissue samples, although cultures of tissue samples from the OB consistently give a superior yield of p75+ cells than those from the mucosa. Looking at the overall populations of cells in culture, the FACS analysis reveals considerable differences between the OB, WM, EPI, and LP cultures over 7–14d (Figure. 9, 10 and 15). Most notably, a double positive (p75+Thy1+) population was present in the WM cultures over 10–14d but was absent from the OB cultures. In the cell cycle analysis, the bulbar cells exhibit the general somatic cell cycle pattern (Harper *et al.*, 2010). However, in the mucosal cultures (WM and EPI, but not LP) the highly proliferative cell cycle profile was similar to that in embryonic and neural stem cells (Booth *et al.*, 2008; Werbowetski-Ogilvie *et al.*, 2009).

Cultures from both sources include olfactory nerve associated fibroblasts (ONFs). It is a common observation [e.g., (Nash *et al.*, 2001; Au & Roskams, 2003; Jani & Raisman, 2004; Novikova *et al.*, 2006)] that the evolution of cultures involves a time-dependent decrease in OECs and a corresponding increase in ONFs. At longer times the ONFs completely predominate in the cultures, and p75+ cells disappear. In the present study, there was a strong inverse correlation between the proliferation of p75+ cells and the deposition of FN (an index of cumulative ONF activity).

When the mucosal cells FACS purified to 98% for p75 were cultured for a further 4d, 74–85% of the population of p75+ cells were immunostained for FN (Figure. 11), a level of expression that is beyond what could be the result of contamination. This population is comparable to the doubly labelled p75+Thy1+ population seen at 10 and 14d in the FACS analysis of the WM samples, and was absent from the bulbar samples (Figure. 11). In contrast, in both bulbar and mucosal samples the population of cells FACS purified for Thy1 remains antigenically unchanged after 4 post-purification days in culture, implying that the p75-Thy1+ (ONF) phenotype is a terminally differentiated character under these culture conditions.

There are a number of studies showing functional differences between the behaviour of mucosal and bulbar cells in culture (see Section 3.1.2 above) and after transplantation (see Section 3.1.1 above). Using OEC-axon confrontation assays, (Windus *et al.*, 2010) described a difference in lamellipodial behaviour between LP OEC and OB OEC and different responses to contact with axons. Transplantation of both mucosal and bulbar OECs has beneficial effects on damaged CNS tissue (see Introduction). However, in experiments comparing transplantation of bulbar and mucosal cultures into corticospinal tract lesions, only bulbar cultures induced axon regeneration across the lesion (Li *et al.*, 1998; Yamamoto *et al.*, 2009). The differences between the behaviour of bulbar and mucosal OECs after transplantation may reflect

a. A cell autonomous difference between OECs from these two sources, as indicated in the correlation analysis in the present study.

b. The proportion of OECs in the cultures. As in the present study, the bulbar cultures were far richer in OECs than the mucosal cultures.

c. The nature of accompanying cells. Astroglia and central neurons are present in the primary bulbar tissue samples. In contrast, the mucosal tissue samples include epithelial and glandular cells, and mesenchymal stem cells (Tomé *et al.*, 2009).

3.3.4 Proliferating p75+ cells in the adult olfactory mucosa

Splitting the WM cultures into EPI and LP gave an unexpected result. Despite the fact that the LP is rich in OECs *in situ* (Figure. 7E and F), LP cultures had only low proportions of p75+ cells (1.14%). Conversely, EPI, where p75+ cells are absent either *in situ* (Figure. 7D) or in the initial dissociated cell suspensions, had a high proportion (64.80%) of p75+ cells with the spindle-shaped OEC morphology. In view of the low proportion of p75+ cells in the LP cultures, their presence in the EPI cultures is unlikely to be due to contamination by a small number of LP cells adhering to the EPI as it is separated.

Our results, therefore, suggest the presence of an adult p75-progenitor/stem cell capable of giving rise to p75+ cells with the bipolar morphology resembling OECs in the EPI. At 7 and 10DIV, these cells proliferate at a rate comparable to stem cells (Figure. 17). Multipotent stem cells, have been identified in olfactory mucosa (Murrell *et al.*, 2005; Murdoch & Roskams, 2008; Tomé *et al.*, 2009; Delorme *et al.*, 2010) and assigned to a putative lineage of horizontal to globose basal cells in the epithelial layer (Holbrook *et al.*, 1995; Carter *et al.*, 2004). One or both of these cells

probably corresponds to the cell giving rise to the p75+ population of the present study. Our technique for obtaining this proliferative p75+ population from EPI requires high density culture and is time-limited to 7–10DIV. The failure to maintain division beyond this time probably reflects that the culture conditions I used favour differentiation (Murrell *et al.*, 2005). Various groups have reported conditions and growth factors that enable expansion of neonatal or adult OECs in culture (Pollock *et al.*, 1999; Bianco *et al.*, 2004; Richter *et al.*, 2008; Novikova *et al.*, 2011*a*). These suggest the possibility of taking advantage of the time window for adult EPI cell proliferation to scale up to produce the larger amounts of cells that would be needed in repairs of clinical spinal cord lesions.

Chapter 4 Nanofibre Scaffold

4.1 Introduction

4.1.1 Tissue engineering

In the field of spinal cord injury repair, engineering the spatial and temporal microenvironment of a potential scaffold is critical for recapitulating the endogenous microenvironment that enhances the regeneration of the severed spinal cord. The micro-architecture of the neural scaffold is an important step in inducing favourable cellular response, both exogenous and endogenous. The need for micro-scale control and high fidelity in reproducibility in the neural scaffold has led the development of bioengineering routes that are able to control spatial location of scaffold features.

A wide variety of biodegradable and non-biodegradable biomaterials have been synthesized and engineered with the goal to mediate essential cell functions such as proliferation and migration through cytoskeleton remodelling (Chen *et al.*, 1997). To recapitulate the native environment while modulating behaviour of the cells, these synthetic systems with micro and nano-size geometries have been used to study the behaviour of cells in response to substrates rich in submicron topographical cues (Khademhosseini *et al.*, 2006). Other than random orientated topography such as nanometre roughness from hydrogel (Mapili *et al.*, 2005) and local microporous scaffold from phase separation (Teng *et al.*, 2002; Taboas *et al.*, 2003), cells also have been reported to respond to well-defined submicron features, also known as controlled scaffold (Bhatia *et al.*, 1999; Folch & Toner, 2000).

According to 'pathway hypothesis,' the key to repairing tract injuries in spinal cord is to form a cell-bridging platform to provide a pathway for the innate growth capacity for sprouting axons to be translated into regeneration in the lesion (Li *et al.*, 2005*b*). One of the most promising cell candidates to populate such a bridge are the olfactory ensheathing cells (OECs), which can be obtained from tissue samples from the adult olfactory system, thus allowing for autografts. In order to maximise the potential of OEC to form this cell bridging platform, orientated micro and nano-scale structures would be ideal to promote elongation and arrangement of the limited number of harvestable human OECs and also provide a bridging platform to the regenerating axons. In developing a tunable synthesis system, replica moulding is a technique that allows reasonably close control on macroarchitecture and electrospinning on microarchitecture of scaffold that promotes elongation of cells like OEC and regenerating axons.

4.1.2 Rationale for nanofibre scaffold as microarchitecture platform for OEC

Experimental studies have shown the ability of transplanted adult olfactory ensheathing cells (OECs) to induce regeneration of severed nerve fibres across lesions of the spinal cord and spinal roots (Santos-Benito & Ramón-Cueto, 2003; Li *et al.*, 2005*b*; Raisman & Li, 2007; Richter *et al.*, 2008; Ibrahim *et al.*, 2009; Lindsay *et al.*, 2010; Mackay-Sim & St John, 2011). Current transplantation procedure is to inject a suspension of cultured cells. Introduced in this way into small lesions of the rat spinal cord, the transplanted cells elongate for more than 100μm to form tubular structures which ensheathe the nerve fibres and carry them across the site of the lesion (Li *et al.*, 2005*a*). To produce such a bridge the transplanted cells depend on cues in the host tissue microenvironment which enable them to integrate with the

host astroglial pathways so as to permit the entry of regenerating CNS axons into the bridge and their exit from it.

While these observations provide a proof of principle, the scale of the damage which is caused by human spinal cord injuries is much larger. To be able to translate the small scale repairs achieved in experimental lesions to such a clinical setting, the numbers of cells which can be produced by current protocols is a serious limitation, and even if adequate numbers could be obtained, the large mass of transplanted cells would lack alignment cues. To cross this translational gap, the possibility of deploying the cells on synthetic bridging material may help to maximize the effect of limited number of cells available and at the same time provide physical cues for their alignment (Deumens *et al.*, 2004; Madigan *et al.*, 2009; Straley *et al.*, 2010; Gumera *et al.*, 2011).

To achieve biocompatibility and effectiveness such materials should be able to simulate features of the *in vivo* microenvironments. In the olfactory system *in situ*, OECs lie in a structured microenvironment. Their outer surface, facing the olfactory nerve fibroblasts, is clothed by extracellular matrix (ECM; (Field *et al.*, 2003). After transplantation OECs re-establish the same relationships with fibroblasts. Microarray studies show that OECs secrete a rich array of ECM molecules (Vincent *et al.*, 2005; Au *et al.*, 2007; Franssen *et al.*, 2008; Guérout *et al.*, 2010).

An accumulation of information in a number of different biological systems has shown the rich three-dimensional surface topography of the extracellular matrix (ECM; (Timpl, 1996)) on the submicron scale. The interaction of cells with the

ECM is a two way process. The ECM provides a scaffold for cell guidance, and conversely, cells remodel the ECM (Geiger *et al.*, 2001). The adhesive and mechanical interactions of ECM with the cell surface link to intracellular mechanisms leading to migration, proliferation and differentiation (Watt *et al.*, 1988; Chen *et al.*, 2004). The type of interaction between cells and surfaces has shown to be influenced by the spatial domains, structural composition and mechanical forces at the nano-scale (Sniadecki *et al.*, 2006).

Over the last few years nanotechnology has made it possible to fabricate biodegradable structures at a controlled submicron scale. Their application in biological systems has shown the effect of nanotopography on the behaviour of a variety of cells, including fibroblasts, astrocytes, oligodendrocytes and epithelial cells (Min *et al.*, 2004; Venugopal *et al.*, 2006; Xie *et al.*, 2009; Baiguera *et al.*, 2010).

4.1.3 Rationale for poly(lactic-co-glycolic acid) as biomaterial of choice

The interest of biomaterial in SCI has since been prevalent in applications like hydrogel scaffold, neurotrophin delivery, cell encapsulation, structural scaffolds, or often in combinatorial approach of several of these applications (Babensee *et al.*, 2000; Teng *et al.*, 2002; King *et al.*, 2006; Burdick *et al.*, 2006; Moore *et al.*, 2006; Stokols & Tuszynski, 2006; Mahoney & Anseth, 2006). The suitability of the biomaterial for a neural scaffold relies on the balance of the biocompatible properties of the polymer, such as its biodegradation rate by the cerebral spinal fluid proteases and the feasibility of microfabrication, such as micro and nanostructuring and mechanic stability.

There are a wide variety of natural, synthetic and advanced biomaterials which can be considered for the neural scaffold. Natural biomaterials, such as collagen, support cell attachment and incite a variety of functions in many cells type including OEC, astrocytes and neurons (Folch & Toner, 2000; Mahoney *et al.*, 2005). However, these extracellular matrix (ECM) proteins require difficult bulk material processing. ECM protein extraction and purification directly from tissues often have batch to batch variations in composition and physical properties. Other than that, these ECM proteins have a limited range of physical properties needed for micro and nanostructuring, especially electrospinning (see Section 4.1.5).

The inconsistency of the electrospinning process has a significant impact on the fibre sizes produced, leading to potentially unpredictable cell behaviour. Recently, advanced materials, such as self-assembling synthesis peptide polymers have been developed to overcome these limitations (Tysseling-Mattiace *et al.*, 2008). Although they achieve the desired native-like properties, such as self-assembling into cylindrical nanofibrils to induce neural responses, the limitation lies in the lack of control in directional and continuous assembly (Hartgerink *et al.*, 2002) and the lack of structural features to promote directional cell growth in culture (Song *et al.*, 2009).

A synthetic polymer able to create aligned nano-scale features with parallel fibre architecture is the FDA-approved poly(lactic-*co*-glycolic acid) (PLGA). It is a biodegradable aliphatic polyester which resorbs into human tissue by hydrolysis (Anderson & Shive, 1997). PLGA is also relatively inexpensive and bulk-produced

commercially. Furthermore the by-products of hydrolysis are natural metabolites: lactic acid and glycolic acid found in the cerebrospinal fluid (Posner *et al.*, 1965). Most importantly, the molecular entanglement of high molecular weight PLGA presents a desirable property for micromachining such as the electrospinning process. With suitable polymer formulation and processing equipment precise control of nano-size, orientated fibres can be achieved (Ramakrishna *et al.*, 2005). Figure. 21 is the chemical formula for PLGA (Wise, 2000).

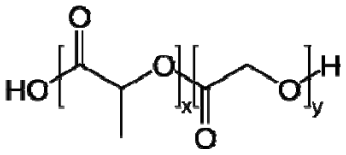

Figure 21: **The molecular structure of poly (lactic-co-glycolic acid).**

The poly(lactic-*co*-glycolic acid) (PLGA) is made up of monomers lactic acid and glycolic acid, in the different proportion of units of lactic acid (x) and units of glycolic acid (y).

Depending on the ratio of the two monomers, PLGA can be formed with different degradation rate. This property enables the fabrication of nanofibre structures which provide mechanical support for cells between the cell seeding stage through to the point of surgical translation to the point of repair and physical and potentially biochemical stimuli to promote cell elongation. The controlled degradation rate allows a specific degradation time to be engineered and regulated metabolite release for nanofibre scaffolds made from a tight distribution of nanofibre diameters.

In this work, I have investigated the degradation rate of several commonly used PLGA blends with different monomer ratios using protease, to create the synthetic protease concentration of the cerebral spinal fluid environment (Grubb, 1988). The rationale to perform the *in vitro* proteolytic degradation, instead of common chemical hydrolysis degradation (e.g sodium acetate), is to understand the degradation from the physiological perspective, as well as the fundamental chemical changes that are incurred on the biomaterial. This is of significant important for the efficacy of scaffold on intended application in SCI.

4.1.4 Micromoulding of PLGA films for scaffold topography

The increased precision of microfabricated devices has systematically enabled the manipulation of biological systems. Meeting the corresponding biomimicry demands a scaffold to repair part of a damaged spinal cord, on a wide variety of length scales. At macroarchitecture level, it ranges from providing a spatial artificial cellular environment for part of a damaged spinal of centimetres in length, to individual neuronal cells on the micron scale to a temporal individual neurotrophic factors on the nano-scale. Such fabrication capabilities have proved invaluable utility in design and development of next generation tissue engineered systems and more importantly, aiding the basic research efforts in understanding the fundamental parameters that governs cellular microenvironment.

One such robust microfabrication is replica moulding. Replica moulding is a straightforward technique used to create microfabricated structures for tissue engineering applications (Borenstein *et al.*, 2002). It encompasses a wide range of moulding processes like solvent casting, injection moulding and hot embossing

(Heckele & Schomburg, 2004). Much of the interests in replica moulding evolve through its desirable benefits for high resolution fabrication process. Moulds with sub-micron resolution can be fabricated using polymeric materials. These microstructures can be produced rapidly and scalable amount across large surface area. Finally, the simplicity in fabrication processes presents itself as an attractive technique for nascent tissue engineering laboratories.

To construct mould for replica moulding process, the key microfabrication techniques remain photolithography and deep silicon etching. In this pilot study, I have chose photolithography to fabricate the replica mould. Photolithographic patterning process is traditionally used to microfabricate integrated circuits and microsystems (Xia *et al.*, 1999). The advent of the manufacturing process in the industry has improved the microfabrication techniques such as increased precision in producing high resolution features in micro- and nano-scale (Schift, 2008).

In fabricating the replica mould, photolithography was used to transfer geometries from a mask pattern into photosensitive etch resistant material (a coat applied on the surface of silicon wafer), using ultra-violet light. The basic photolithographic process flow includes wafer cleaning, adhesion promoter formation, photoresist application; soft baking; mask alignment; exposure and development; and hard baking, as illustrated in Figure. 6 achieve a resolution of ~ 335nm, exposing radiation is typically ultraviolet which wavelength ranged from 365 to 468nm. Deep reactive ion etching using gaseous plasma creates etched microstructures into the surface of the silicon wafer. This becomes the master replication mould.

4.1.5 Electrospinning

Precise control on the cell functions such as adhesion, elongation and proliferation can be done by manipulating cell geometries at the micron and submicron level (Ma *et al.*, 2005). Such control is of increasing importance in the complex environment of tissues such as spinal cord, especially during injury (Nomura *et al.*, 2006). Nanofibres present a topologically rich substrate. The ability to control the nanofibres synthesis process allows micron and submicron diameter fibrous substrate to be produced which in turn allow cells to be manipulated to achieve specific cell geometries and pre-meditated functions.

The numerous methods to produce nanofibres include mechanical drawing, replica-moulding, phase separation and self-assembly. However, electrospinning, an electrostatic drawing process, is a flexible technique to fabricate ultra fine, continuous, uniform, solid fibres at the ordered features of micro and submicron length scale. Its experimental processes inherently allow various level of specific control on the fibre deposition and fabrication with a high level of complexity in two and three dimensions. The collection method of the synthesized electrospun fibres governs the orientation of the fibre alignment (Boland *et al.*, 2001; Sundaray *et al.*, 2004) and fibre patterning (Mauck *et al.*, 2009).

Control over the voltage, and type and concentration of the polymeric solution alter the surface topologies of the fibre, such as porosity (Bognitzki *et al.*, 2001), fibre geometry (ribbon-like vs. round) (Koombhongse *et al.*, 2001), hence increased the complexity of fibre morphology. Electrospinning is also a convenient and

inexpensive method to fabricate biomaterial surfaces with nano-scale features, as compared with costly photomask and wafer processing.

Since the first feasibility study with a wide range of polymeric solutions (Reneker & Chun, 1996), electrospinning has been used to fabricate fibrous scaffold with natural materials such as collagen (Matthews *et al.*, 2002), gelatin (Zhang *et al.*, 2004), silk fibroin (Nazarov *et al.*, 2004) and synthetic material, namely, poly (lactide-*co*-glycolic acid) (PLGA), poly (vinyl alcohol) and poly (ethylene oxide). The diameter of the fibres range from 20nm to 2μm, which can be manipulated by altering the dissolved polymer solution properties such as conductivity, solution concentration and viscosity. Typically the resulting nanofibrous scaffold is a thin three dimensional substrate that consists of randomly oriented, non-woven mesh.

4.1.5.1 Principle of electrospinning

In 1934, Formhals patented a drawing process where polymer filaments were produced using the electrostatic repulsions between surfaces charges (Formhals, 1934). The technique was called electrostatic spinning. Although it was largely forgotten after patenting, Doshi and Reneker revived interest in this 70 year-old technique by describing the production of micro/nano-size fibres using this technique, and shortly after, Reneker and Chun by showing the feasibility of this technique with a range of polymeric solutions (Doshi & Reneker, 1995; Reneker & Chun, 1996). Electrospinning has since gained momentum in both industry and academic as an area of research to study the spinning process and the properties of the fibre material produced.

Figure. 22 is the schematic illustration of the basic setup of the apparatus used for electrospinning. Electrospinning is a process that applies high electric field (10^e4 – 10^e5 V/m) to an anode (metallic needle) filled with polymeric solution that will be spun in the direction of a cathode (grounded collector). The polymer solution is fed through the metallic needle with the aid of a syringe pump at a constant controlled rate (Frenot & Chronakis, 2003; Li & Xia, 2004; Ramakrishna *et al.*, 2005). When the high voltage (ranged from 7kV to 30kV) was applied, the polymer solution droplet at the orifice of the metallic needle begins to form a Taylor cone (Doshi & Reneker, 1995). Once the strength of electric charge surpassed the threshold value, the electrostatic forces overcome the polymer surface tension and a jet shoots off from the tip of the polymeric Taylor cone to form slender and continuous liquid filament. This phenomenon can be related to the suppression of Rayleigh instability. Due to the viscoelastic property of the polymeric jet, the elastic stress response suppresses Rayleigh instability which in turn allows this polymeric jet to travel at a straight line (Yu *et al.*, 2006).

Attracted by a static grounded collector, this electrified polymeric jet then undergoes an elongation and whipping process, and is subsequently deposited as randomly oriented nonwoven mat of polymer nanofibres. The elongation region starts with solvent evaporation from the jet. The evaporation causes the jet to thin. In general as the jet thins, the fibre diameter is significantly reduced from millimetre to ten of nanometres in length. With continuous electrodynamics instabilities, the fibre is further stretched in a zone known as the whipping zone. This stretching in turn increases the surface area of polymeric fibre, leading to further evaporation of

Figure 22: Schematic illustration of the principle of electrospinning.
3D schematic illustration of basic apparatus setup for electrospinning. High positive charge from the high voltage power source (red) is applied to polymeric solution. As the voltage increases, the polymer solution droplet at the orifice of the microfabricated metallic needle (grey) begins to form a Taylor cone (white) formed and maintained at the tip of needle. Once the strength of electric charge surpassed the threshold value, the electrostatic forces overcome the polymer surface tension and a jet shoots off from the tip of the polymeric Taylor cone to form slender and continuous liquid filament. Polymeric jet (white ribbon) elongated (white area) with the differential in electrical charges (red), flow rate (continuous flow syringe pump) and physical distance (white ruler) incurred. Solvent of the polymer evaporate at whipping zone (yellow), so that polymer in nanofibres can be collected. Fibres were collected on the negatively charged collector (dark grey).

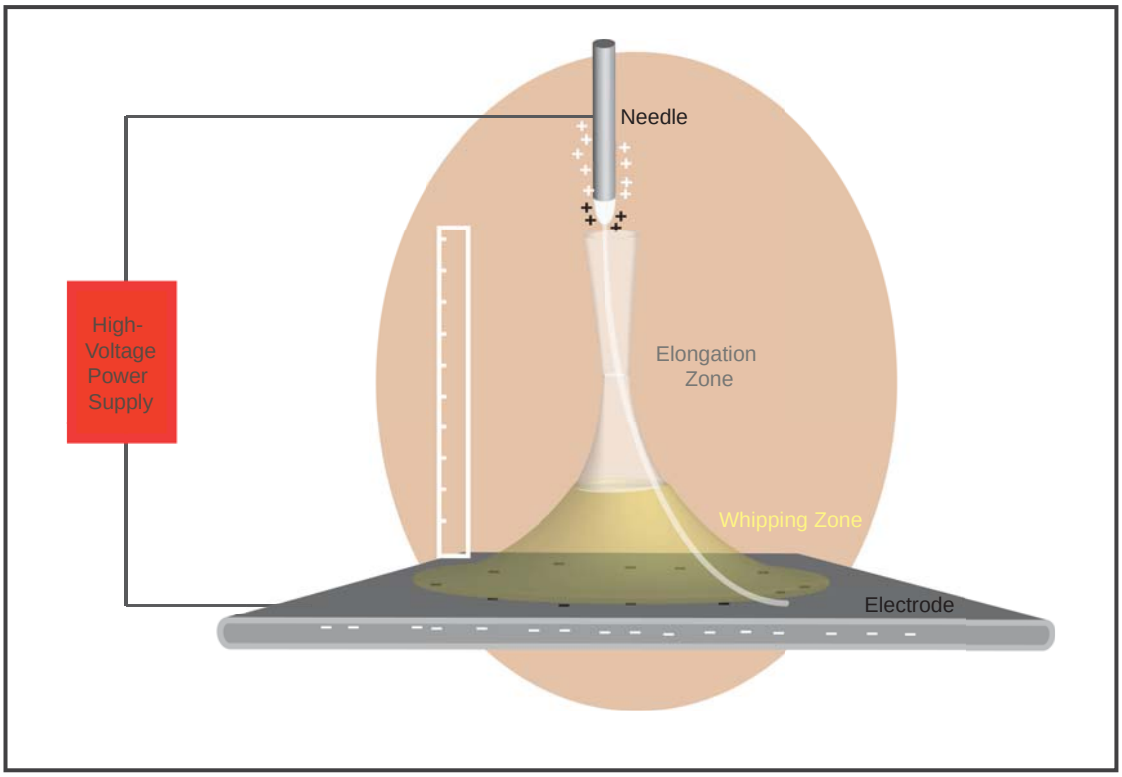
Needle
High-
Voltage
Power
Supply
Elongation
Zone
Whipping Zone
Electrode

solvent. Subsequently the solid fibres are collected at the counter-electrode (Frenot & Chronakis, 2003; Li & Xia, 2004; Ramakrishna *et al.*, 2005).

4.1.5.2 Electrospinning system process

Although the setup of electrospinning is relatively simple in principle, the spinning mechanism presents the high level of complexity in the electro-fluid mechanics (Li & Xia, 2004). Most of the experimental parameters in electrospinning process have been fairly established. The mechanism of producing electrospun fibres which were at the submicron and nanometre length scale were analyzed based on the non experimental and experimental parameters. The fibre morphology and diameter are governed by varying molecular weight and inherent viscosity of polymer, solution concentration, distance between tip to collection plate, the electrostatic field strength applied to the polymer and the flow rate of the injecting syringe and finally the conductivity of the collection plate. Lower concentration or lower molecular weight (MW) polymers give finer fibres but a tendency to form beads, while larger diameter fibres are produced from higher concentration or molecular weight. Longer distance from the tip allows more time to evaporate the solvents, yielding finer fibres.

Prior to spinning, choice of polymer and solvents are determined by inherent viscosity and MW of the polymer; and the solvent volatility. Processing parameters like tip-to-collector distance, effect of collector are also estimated and determined prior to spinning. Ambient parameters such as humidity, temperature and pressure were kept consistency in the laminar hood. Key experimental parameters involved in electrospinning process are 1) Polymer solution parameters: solution

concentration and solvent properties; 2) Processing conditions: voltage and feed rate.

4.1.6 Nanocomposite electrospinning

The fabrication of scaffold with sensor properties is desirable for *in situ* live monitoring in culture and non-invasive post-implantation monitoring for clinical applications. Typical *in vivo* strategies of validating the functional properties of implant often involve *post-mortem* histological evidence and/or post transplantation physiological (such as electrophysiology) and behaviour (such as paw reaching, climbing, or analysis of hind limb function) studies (Li *et al.*, 2003*a*; Ibrahim *et al.*, 2009). While there is significant evidence of repair with scaffold implant (Teng *et al.*, 2002), most unsuccessful SCI repairs *in vivo* studies show lack of sophistication in monitoring the transplant that can potentially elucidate other causation deficiencies such as early degradation, scaffold topographical changes, which otherwise is not reflected in both aforementioned methods. These difficulties in monitoring the dynamic development of the transplant with the endogenous tissue are marginally attributed to the feedback limitation in current imaging devices with intended transplant *in vivo*.

Advanced development of fluorescence sensors using quantum dots have rapidly changed the landscape of non-invasive *in vivo* imaging (Åkerman *et al.*, 2002; Gao *et al.*, 2004). Capitalizing on characteristic mesoscopic properties of semiconductor quantum dots, functionalities such as radioisotopic and magnetic have been extensively studied in cell imaging (Gao *et al.*, 2004) and bio diagnosis clinical trial (Josephson *et al.*, 2002).

4.1.7 Rationale for membrane insert system for cell and tissue culture

Cell expansion is a significant element in advancing scaffold cell transplantation of structurally and metabolically complex organs such as spinal cord. The design and construction of a clinically relevant scaffold system demands a robust and efficient way to handle and manipulate the scaffold at the cell culture level, *en route* to surgical transplantation. The bulk mechanical criteria in the scaffold system design and construction include a) handling during sterilizing process, b) immobilizing electrospun fibre mesh within the cell culture system to aid with cell seeding and adhesion (Zhu *et al.*, 2008), while c) maintaining the tensile and structural form of the micro and nano-scale fibres mesh that support the cell elongation after cell adhesion (Baker *et al.*, 2006), d) compatible with electrospinning formats and *in vitro* functional (organotypic) assay system culture (see Chapter 5), and e) mechanically transferable to the manipulation in surgical procedures after cell expansion. For this reason, I developed a membrane insert system compatible with a multi-well cell culture system, which provides the essential features for topographical culture, microporous interface culture and bulk material manipulation.

4.1.8 Laser patterning

Laser patterning technology presents a number of techniques to craft micro-scale features which are analogous to the tissue micro structure of nerves on biodegradable polymer substrates (Schmalenberg & Uhrich, 2005). One type of micropatterning method utilizes the solid-state nanosecond UV laser to ablate small geometries of approximate size of 10nm with high precision (Kokai *et al.*, 1998; Katayama *et al.*, 2002). Among the typical UV laser types used for ablation are metal vapour,

fluorine, excimer, argon-ion, helium-cadmium, and nitrogen. This ablation is performed by breaking the chemical bonds of target material directly with the minimal thermal damages on the non-machined areas. The emitted photon energy from these UV source is high and pulsed-based, minimizing the dissipation of the thermal energy from the laser extending to the non irradiated portion (Srinivasan & Braren, 1989). Using laser micromachining, high resolution geometries like holes and trenches can be impinged at rapid fashion for scalable production.

As part of the development process of a therapeutic neural scaffold, this process is of importance to define the bulk geometries as the macroarchitecture of a neural scaffold, fashion suitable designs for *in vitro* expansion and clinical manipulation. In this work, I used pulsed-laser micromachining to generate high resolution millimetre-scale patterns from PLGA electrospun fibres scaffold for producing features within the scaffold that address the issue of limited cell number from the patient biopsy and post-culture scaffold transfer prior to surgical transplantation. An ArF excimer UV nanosecond pulse laser was used to produce designed structures. Parametric investigation and material analysis revealed the chemical and physical mechanisms of surface patterning associated with laser processing.

4.1.9 Sterilization methods

The purpose of this study was to determine which methods of sterilization maintain the integrity of the nanocomposite nanofibres with the insert. In migration from the fabrication process to tissue culture, sterilization is an essential procedure on the synthetic scaffold to prevent bacterial and fungal contamination, especially endotoxins during the length of the tissue culture. Compromising the integrity of

cytoscaffold system, bacterial and fungal inoculation in the culture increases the acidity of the media (Leifert & Cassells, 2001), severely interferes with cellular mechanisms (Fogh *et al.*, 1971), while escalate the biodegradation of PLGA than desired. As part of the development of a clinical relevant neural conduit, this step is imperative in the quality assurance required by good manufacturing practice (GMP) (Burger, 2003).

The inherent properties of the nanocomposite PLGA nanofibres and the PMMA membrane insert posed limitation in the common methods of sterilization: irradiation, such as gamma irradiation and high pressure steaming, such as autoclaving. Gamma irradiation interfere with the photoluminescence of quantum dots (Letant & Wang, 2006), while autoclaving distorts and degrades the PMMA membrane insert and the PLGA fibre morphology (data not shown). The available strategy of sterilization is chemical sterilization. Therefore, ethylene oxide and ethanol were selected to be investigated for the appropriateness as choice of sterilization.

4.1.10 Scaffold surface functionalization

Surface modification preserving the fibre morphological dimension of the sterilized substrate is a pivotal step in translating a tissue engineered system to a therapeutic one. Besides the accumulation of negative charges on the fibre mesh after electrospinning, strong reactive conditions posed by the sterilization process may have served as an agent to decrease the biocompatibility of scaffold surface. Susceptibility to cellular attachment and potentially, other enhancing cellular behaviour can be imposed on the substrate using several surface functionalization

processes. Immobilization of adhesive biomolecules such collagen and laminin or neutralization of accumulated charges on the scaffold with positively charged molecules such as poly-L-lysine, poly-D-lysine are among the biomolecules commonly used for the surface functionalization purposes. These biomolecules can be covalently attached, electrostatically adsorbed or self-assembled on the substrate surfaces.

4.1.11 Biocompatibility of OECs to PLGA electrospun scaffold

For the biocompatibility of olfactory ensheathing cells (OEC) to PLGA electrospun scaffold study, I chose to test electrospinning of PLGA (poly (lactic-co-glycolic acid; (Kim *et al.*, 2003), an FDA approved, biodegradable material, to produce fibres on the nano-scale. The optimal concentration of PLGA found was 6%, producing fibres at 707.82±1.646nm. This fibre mesh was defined as Nano-700. The addition of quantum dots to the PLGA has enabled the fabrication of fibres whose dimensions approach those with which cells are associated in their natural environment in tissue at a reduction in diameter to around 237nm (Nano-250). Further population responses, such as the micro- and nano-topographical effect on cell elongation of purified population were investigated take into consideration of the cell density and surface functionalization.

4.1.12 Summary of results

This chapter describes the last stage of the development of clinical relevant neural scaffold. The first part of this chapter described the selection process of the FDA-approved, poly(lactic-*co*-glycolic acid) (PLGA) based on the resorption rate. Results demonstrated on the proteolytic degradation of the PLGA. The middle section of the

chapter demonstrated a novel conglomerate of prevailing microfabrication design and technologies: micromolding, electrospinning, novel membrane insert system and laser patterning. Micromolding provides micro patterns for the cells to self-organize. Basic electrospinning and advanced electrospinning, includes multi-format platform electrospinning serves an augmenting tool to allow precise control on cell growth and motility. To enhance the property of neural scaffold for imaging, nanocomposite electrospinning present an attractive technique to develop the scaffold as an internal monitoring device *in vitro* and *in vivo*. Subsequently the need for *in vitro* cell expansion, namely topographical cultures and microporous interface culture, drove the design and fabrication of membrane insert system for bulk material manipulation. Lastly laser patterning defines the bulk geometries within the neural scaffold, fashion suitable designs for *in vitro* expansion and clinical manipulation. The novel conglomerate of technologies in this development is a novel platform technology. Finally I compared the attachment, morphology and directionality of purified OECs seeded at low density on flat surfaces with those on meshes of sterilized and functionalized nano-scale PLGA fibres.

4.2 Results

4.2.1 Poly(lactic-co-glycolic acid) selection based on proteolytic degradation rate

The relative susceptibility of PLGA to protease was studied from the degradation rate of selected PLGA and measured by mass loss as a result of enzymatic reaction. Electrospinning was used to produce the nanofibre mesh from three PLGA samples (Section 4.1.5 above). Surface erosion was observable with the formation of translucent zone enveloping around the core bundle over time. Upon removal of the core bundle of mesh for drying and weighing a translucent mass waste was left behind.

The effect of the protease XIV *in vitro* degradation on the electrospun fibre mesh is shown in the chart of Figure. 23. All mass loss profiles present an exponential curve, with initial retention of mass until a critical point was met, then a rapid mass loss is experienced. PLGA with the higher stoichiometric ratios of lactic acid to the cyclic dimers (1,4-dioxane-2,5-diones) of glycolic acid reached the critical point more rapidly than those with a lower ratios. The proteolytic degradation rate difference between the two similar stoichiometric ratios lactic and glycolic acid, but with a different molecular weight was only obvious by end of week 5 on the 5 % more mass loss for the higher molecular weight PLGA (from supplier PURAC).

Figure 23: Line graph of the proteolytic degradation rate of the four PLGA polymers.
The kinetic of mass loss by proteases among the four PLGA polymers from three Sigma and one PURAC supplies over 5wk.

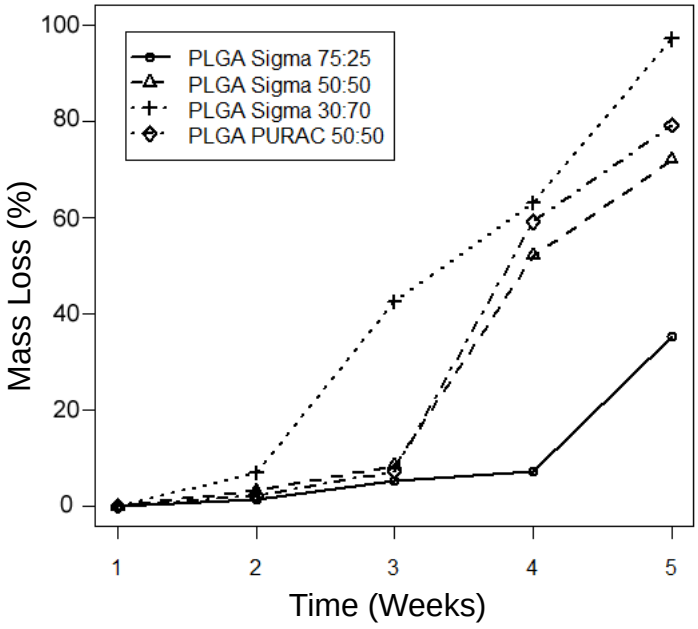
PLGA Sigma 75:25
PLGA Sigma 50:50
PLGA Sigma 30:70
PLGA PURAC 50:50
Mass Loss (%)
100
80
60
40
20
0
1
2
3
4
5
Time (Weeks)

4.2.2 Fabrication of micropatterned replica mould

Figure. 6 and Figure. 24 A1-4 illustrates the process flow for microfabrication to produce micropatterned PLGA replica mould. SEM images of the silicon master verified the patency of the grooves and ridges that form the patterned channels (Figure. 24B). Manual delaminations of the mould from the silicon master were performed with some degree of stretching towards the polymer. The PLGA mould regained most of the defined grooves and ridges after 2h of static incubation. In some cases, the manual delamination process failed to transfer the micro-pattern from the silicon model as the resist remained on the polymeric mould.

In this pilot study, three types of layout for the mould were designed and fabricated. By varying the width of the groove and ridges, each design was used to test the degree of non-selective cell alignment on the grooves, while maximizing the cell attachment. Biocompatibility of the polymer mould was suggested by the cellular attachment within the micro-channels. Due to the initial low densities of cells seeded (27,000 cells/cm^2, a routine cell density for culture vessel); no cells were attached to the polymer mould. Subsequent incremental increase of cell density showed both olfactory ensheathing cells (OEC) and their accompanying ONFs attached abundantly at a density of 81,000 cells/cm^2. This addressed the influence of cell density on the cell viability and attachment.

OEC/ONF mixed cultures respond to the topographical cues of the polymer mould to align according to the direction of the groove and ridges. The design layout in term of width of the grooves had no specific effect on the organization and directional

Figure 24: Fabrication and characterisation of PLGA micropatterned mould.
Schematic illustration showed the manual delamination process to remove the PLGA substrate from the photolithographed silicon mould (A1-4). A spin coating solution of 10wt% PLGA (PURAC, Netherlands) dissolved in hexafluoroisopropanol was dispensed on to the silicon mould master (A1) and then spin-coated at 1800rpm for 1 min to obtain the PLGA replica moulds (A2, PLGA substrate on mould). The PLGA micropatterned mould (A4) was then manually delaminated from the mould master (A3). SEM image of the PLGA substrate (B) showed that the micropattern structures were maintained after delamination process. Scale bar, B, 30μm.

Confocal images showed the compatibility of the PLGA micropatterned mould as a suitable substrate for the culturing of S100β-positive OECs and Thy1-positive ONFs (C and D; white arrows indicating the grooves and ridges of the pattern on the substrate). Scale bar C-D 200μm.

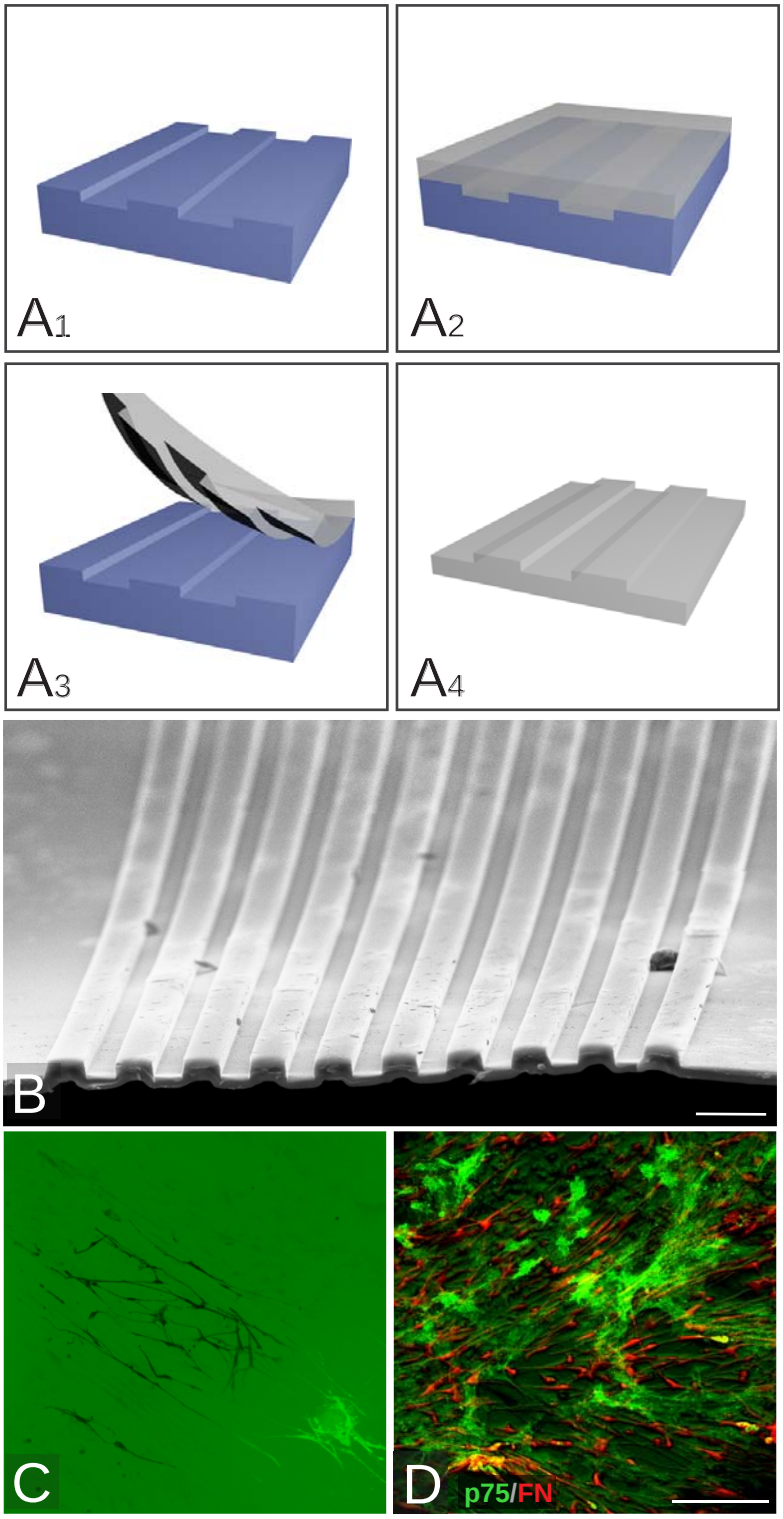
A1
A2
A3
A4
B
C
D
p75/FN

growth of OECs and ONFs. The evidence of Thy1+ ONFs illustrated the secretion of extracellular matrix (i.e. fibronectin) to measure the OEC viability and the presence of ONFs in supporting the elongation of OEC, shown in Figure. 24C and D.

4.2.3 Electrospinning

4.2.3.1 Electrospinning process optimization

The primary pre-experimental parameter after the selection of biomaterial: PLGA PURAC for electrospinning was the solvent for PLGA. Preliminary results in PLGA solution preparation and electrospinning using vertical format with static collector showed that size of fibres produced from PLGA dissolved by tetrahydrofuran (THF) and dichloromethane (DCM) ranged from 1.3 to 2.5μm (data not shown). Estimation on the feasibility of solvent was made based on a few trials with voltage variations and solution concentration. Largely, solution concentration required to produce 1.3μm PLGA fibres ranged from 10% onwards. In contrast, the highly volatile hexafluoroisopropanol (HFIP) was able to dissolve 50% less PLGA than DCM to produce the same fibre size with similar smooth surface morphology. Therefore, HFIP had been selected for further experimental use.

To optimize the process of newly built electrospinning system, I investigated solution concentration (polymer solution parameters), spinning voltage and feed rate (both processing conditions). Other parameters such as the spinning chamber humidity and tip-to-collector height (30cm) were predetermined based on the electrospinning instrumentation. Meshes of randomly woven nanofibres were produced by electrospinning from 50:50 PLGA solutions in hexafluoroisopropanol

(HFIP). A range of polymer concentrations from 3.0 to 7.2% (wt/wt) was studied for fibre morphology (Figure. 25). Lower concentrations resulted in beading, and higher concentrations gave an increased fibre diameter (Figure. 25 and 26). 6% was found to be the optimal concentration to produce beadless, uniform and continuous fibres. A voltage of 9.7kV with a feed rate of 300µl/h was found to produce homogenous uniform fibres with a length weighted average diameter of 707.82±1.646nm (Figure. 30 below). These were defined as Nano-700.

Spinning voltage were then used to further reduce the order magnitude of diameter to submicron (<500nm). The remaining parameters were kept constant. Length weighted mean fibre diameter ($\bar{d}$) was used to calculate the average fibre size for each voltage from 9kV to 25kV. The line graph in Figure. 27A showed the effect of voltage on $\bar{d}$ (with standard deviation, σ as error bars). With the increase of voltage, the initially fluctuating Taylor cone stabilized and then the jet stream narrowed, evidence in decrease of mean fibre diameter from 9kV to 13kV. I found that further increase of the voltage subsequently disrupted the balance between the polymer surface tension and the electrostatic charge, with the emergence of more than one jet stream. Even with the multiple jet streams observed from 13kV, continuous submicron fibres continued to be formed and their diameter remained at the similar range. This continuous increase of electrostatic flow also reduced the size of the Taylor cone and eventually prevented the formation of any Taylor cone. By that moment, the polymeric jet ejaculated in a rapid pulsating rate, caused the fluctuation of the fibre size being produced (as observed in the large error bar in the subsequent voltage increment in Figure. 27A, red outliers). At 23kV the extremely

Figure 25: SEM micrographs of PLGA in the range of concentrations used to electrospun submicron fibres.
The SEM micrographs of the 4.0% (A), 5.0% (B), 5.5% (C), 5.8% (D1, 2), 6.0% (E), 6.2%(F) and 6.4% (G) of PLGA concentration used to produce submicron fibres in electrospinning. Scale bars, 10μm.

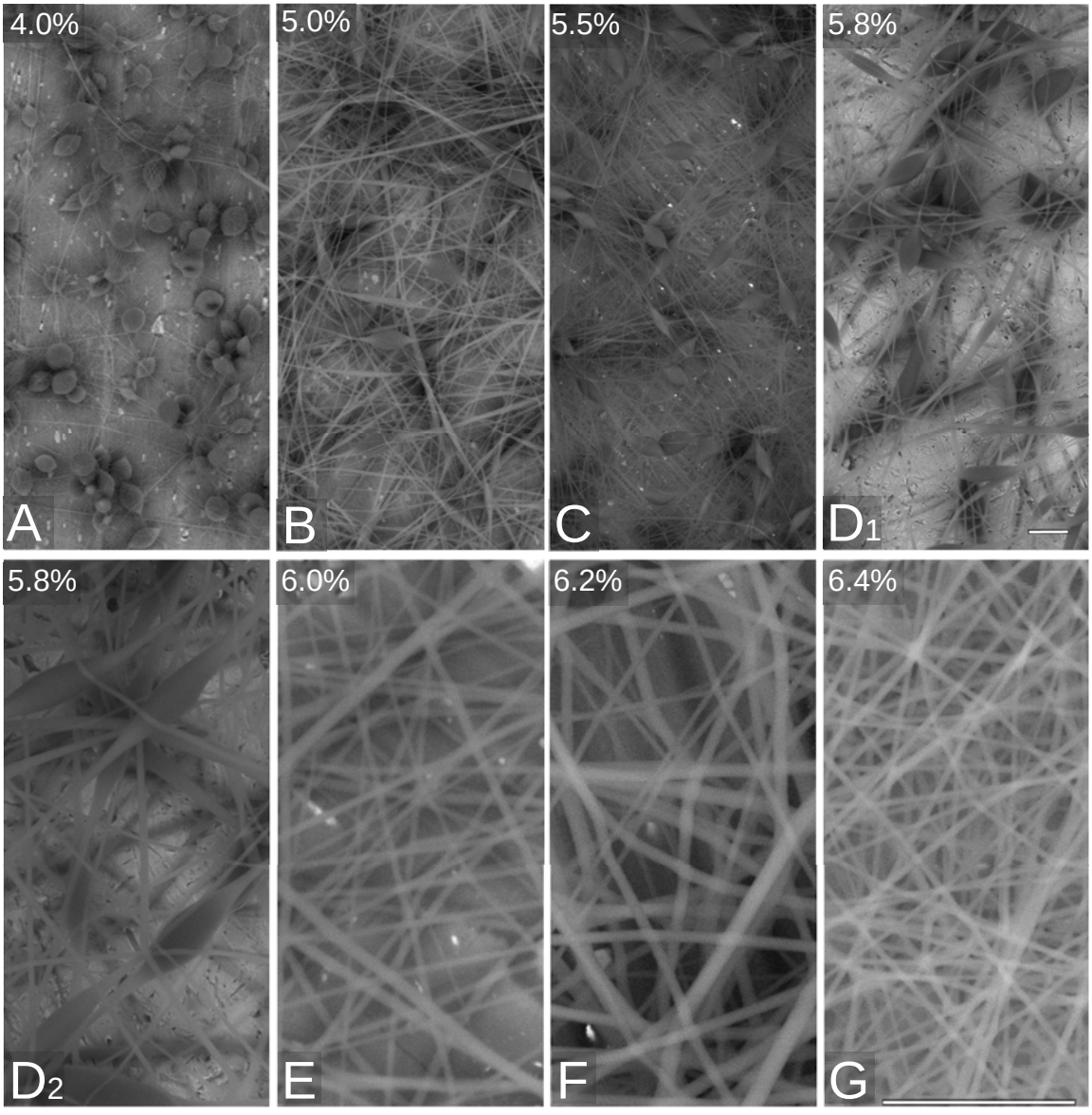
4.0%
5.0%
5.5%
5.8%
A
B
C
D1
5.8%
6.0%
6.2%
6.4%
D2
E
F
G

Figure 26: Analysis of PLGA electrospun fibres in the range of concentrations.

Changes in fibre morphology were evident with the increasing concentration of PLGA from 3.0 - 7.2% (wt/wt). At low concentration, the electrospinning process forms fibres with <100nm diameter but with beads >1000nm diameter. With the increasing concentration the diameter of the beads decreased while that of the fibres increased. The optimal concentration was found to be 6% when the disappearance of the beads was combined with the smallest possible diameter in fibre size. Data on each distribution were collected from a total of 3 SEM pictures in 3 experimental replicates. n=315, error bar, standard deviation.

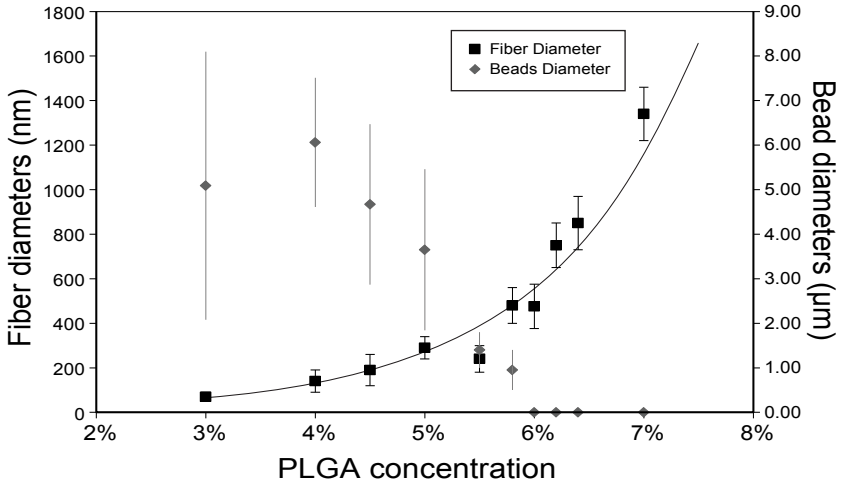
Fiber Diameter
Beads Diameter
Fiber diameters (nm)
Bead diameters (µm)
PLGA concentration
1800
1600
1400
1200
1000
800
600
400
200
0
9.00
8.00
7.00
6.00
5.00
4.00
3.00
2.00
1.00
0.00
2%
3%
4%
5%
6%
7%
8%

Figure 27: Line graphs of fibre diameter at a range of voltages and flow rates.
Changes in the diameter of the fibres at a range of voltages (A) from the high voltage power source using the electrospinning interface software and at a range of maintained flow rates (B) from the syringe pump. n=1300, error bar, standard deviation. Red, discontinuous fibers with beaded phenomenon. error bar, standard deviation.

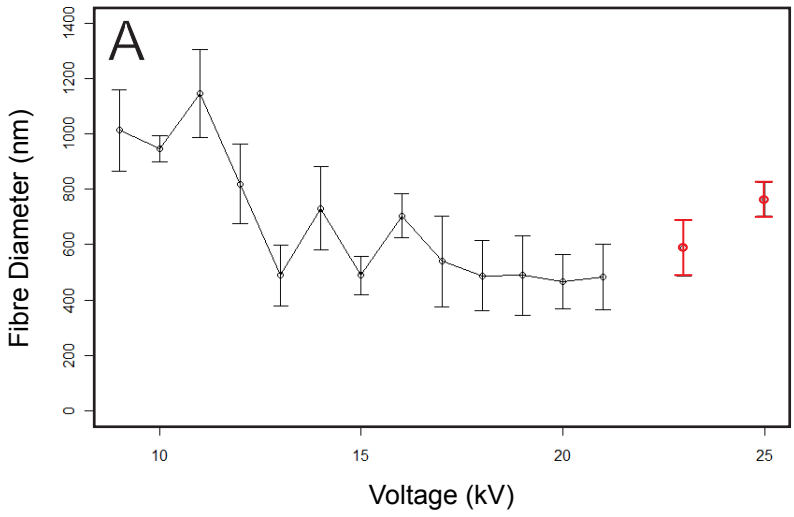
A
Fibre Diameter (nm)
0
200
400
600
800
1000
1200
1400
10
15
20
25
Voltage (kV)

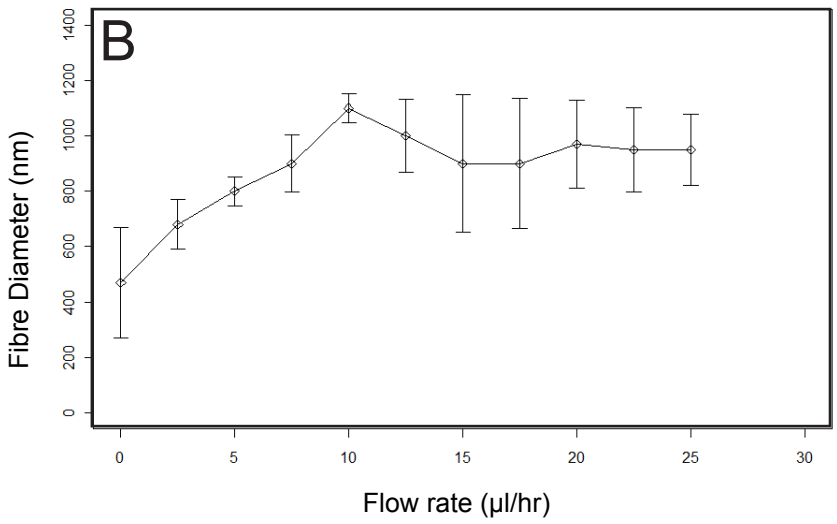
B
Fibre Diameter (nm)
0
200
400
600
800
1000
1200
1400
0
5
10
15
20
25
30
Flow rate (µl/hr)

strong electrostatic charges produced discontinuous fibres and subsequently increased fibre diameter due to the irregularity in the jet stream which were governed by the feed rate.

The effect of feed rate was similar to the effect of spinning voltage, but an opposite threshold trend was also observed in the fibre diameter (line graph in Figure. 27B). At a constant concentration and voltage, the fibre diameter was positive regulated by the feed rate and a threshold was met where the diameter ceased to increase, despite the volume increment in the feed rate.

4.2.3.2 Effect of spinning formats on fibre morphology

Figure. 28 showed the studies of different spinning formats I deployed to produce both random and aligned electrospun PLGA fibres. SEM images (Figure. 28A-D) showed the morphology and diameter of the fibres produced at each of the spinning format photographed (Figure. 5). Randomly arranged fibres were produced using both static and slow rotating collector (≈200rpm), relative to the high speed rotating drum used to produce the aligned fibre mesh. The aligned fibre mesh was produced using the high speed rotating drum (Figure. 5C) at 1200rpm.

In term of fibre size, this result is consistent with other polymers where increase of these 3 key parameters would not necessarily lead to corresponding changes of the fibre diameter as there is the critical point, where any further increase would not influence the diameter.

Figure 28: Fibre morphology and orientation at the different spinning formats.
SEM micrographs of the change in fibre orientation with the different spinning formats: flat vs. improved collector design (see Figure 5) and static vs. rotating motion of the collector. A, random fibres produced by flat static collector. B, static razor blade collector. C, low speed rotating collector. D, high speed rotating collector. Scale bar, A-D, 3μm.

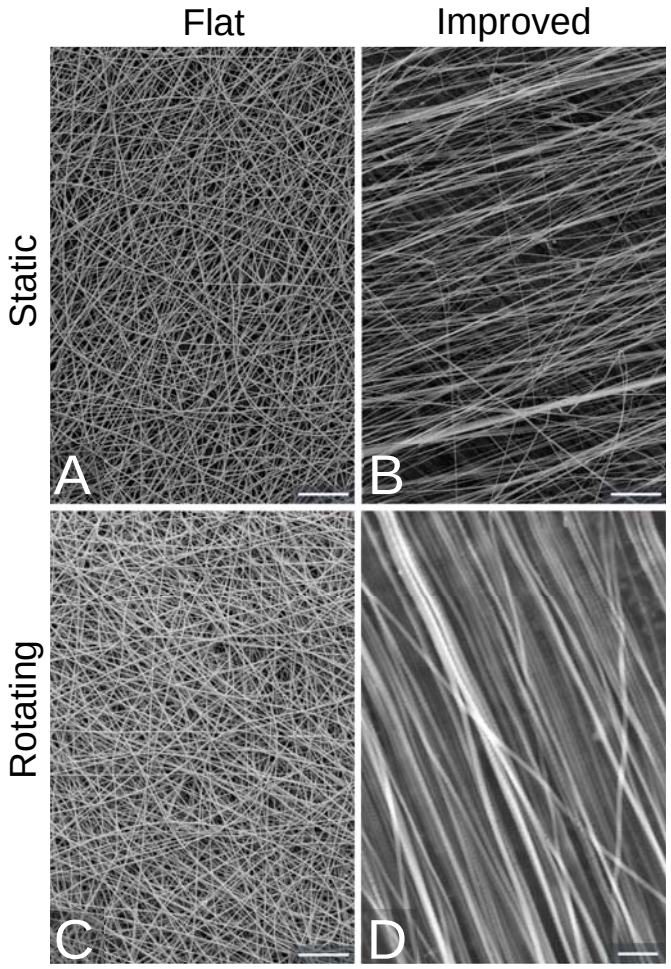
Flat
Improved
Static
Rotating
A
B
C
D

4.2.3.3 Characterization of dual layer electrospinning

High speed is introduced to overcome not only the surface tension of the polymer PLGA but also the rapid discharge of the repulsive charges remained on the scaffold. Figure. 29 showed the alignment of the electrospun fibres on top of a random electrospun fibre mesh.

4.2.4 Fluorescence illumination and dispersion of quantum dots

The relative fluorescence illumination among the two quantum dots-composite nanofibres with control was studied to determine quantum dots dispersion with the PLGA/HFIP during electrospinning. The two quantum dots-composite are PLGA with CdSe/ZnS 480nm and PLGA with CdSe/ZnS 610nm. It is found that compared to control fibres without any nanocrystals, both nanocomposite solution produce fibres which fluoresce at in their respective wavelength when excited with UV light. This result is consistent with the fluorescence spectra provided by the manufacturer. The effect of optoelectronic property of the quantum dots on the electrospinning process was also studied. The gross morphology of the fibres among all these concentrations is shown in SEM images in Figure. 30E-G.

To achieve lower diameter fibres 6% PLGA/HFIP with added CdSe/ZnS 5.2nm diameter quantum dots was electrospun at a voltage of 11.2kV with a feed rate of 400µl/h. These nanocomposite fibres had a similar surface texture, but with an increased uniformity of diameter as reflected in the narrower dispersion of the length weighted lognormal average fibre diameter frequency distribution (Figure. 30B). A 1% concentration of quantum dots yielded fibre diameters of 549.77±1.311. A 2%

Figure 29: The dual layer assembly of the aligned electrospun fibres mesh.
SEM micrographs of the 6% PLGA electrospun fibres mesh showing the unidirectional orientation of top layer of aligned fibre (A) and in high magnification, the underlying random fibre mesh as structural support (B). Scale bars A, 20µm, B, 2µm.

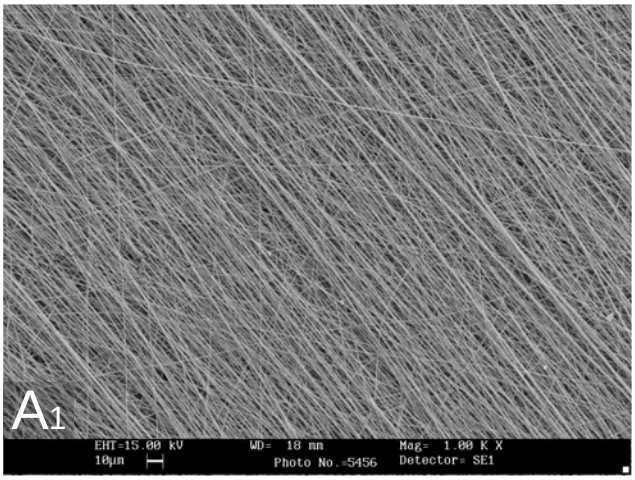
A1
EHT=15.00 kV
WD= 18 mm
Mag= 1.00 K X
10µm
Photo No.=5456
Detector= SE1

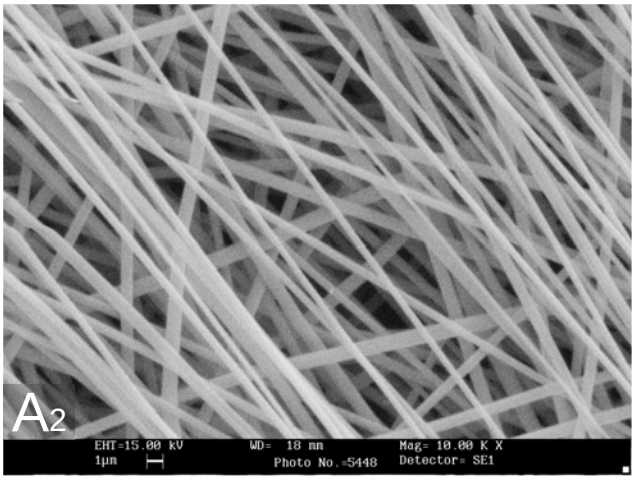
A2
EHT=15.00 kV
WD= 18 mm
Mag= 10.00 K X
1µm
Photo No.=5448
Detector= SE1

Figure 30: Characterisation of nanocomposite electrospun PLGA nanofibres at different concentration of CdSe/Zn 5.2nm quantum dots.
(A,C,D) SEM images showing the characteristic of the electrospun 6% PLGA fibres (A) without and (C,D) with 1 % and 2% CdSe/ZnS quantum dots (Qdt), respectively.

(B) The lognormal distribution curves depict the length weighted lognormal-diameter frequency distribution of fibre diameter of 3 respective nanocomposite electrospun 6% PLGA fiber meshes (Curves, dotted line, No Qdt, dashed line, 1% and solid line, 2%). For each of 3 respective electrospun fiber meshes, fibre length and diameter were measured at average 35 different points along a random straight line drawn across each image. Data on each distribution were collected from a total of 5 SEM pictures in 3 experimental replicate. n=525.

(E,F,G) Confocal images of fluorescent luminescence of the nanocompositie PLGA nanofibres with concentration of quantum dots at 0 (E), 1% (F) and 2% (G). Scale bar, 100μm.

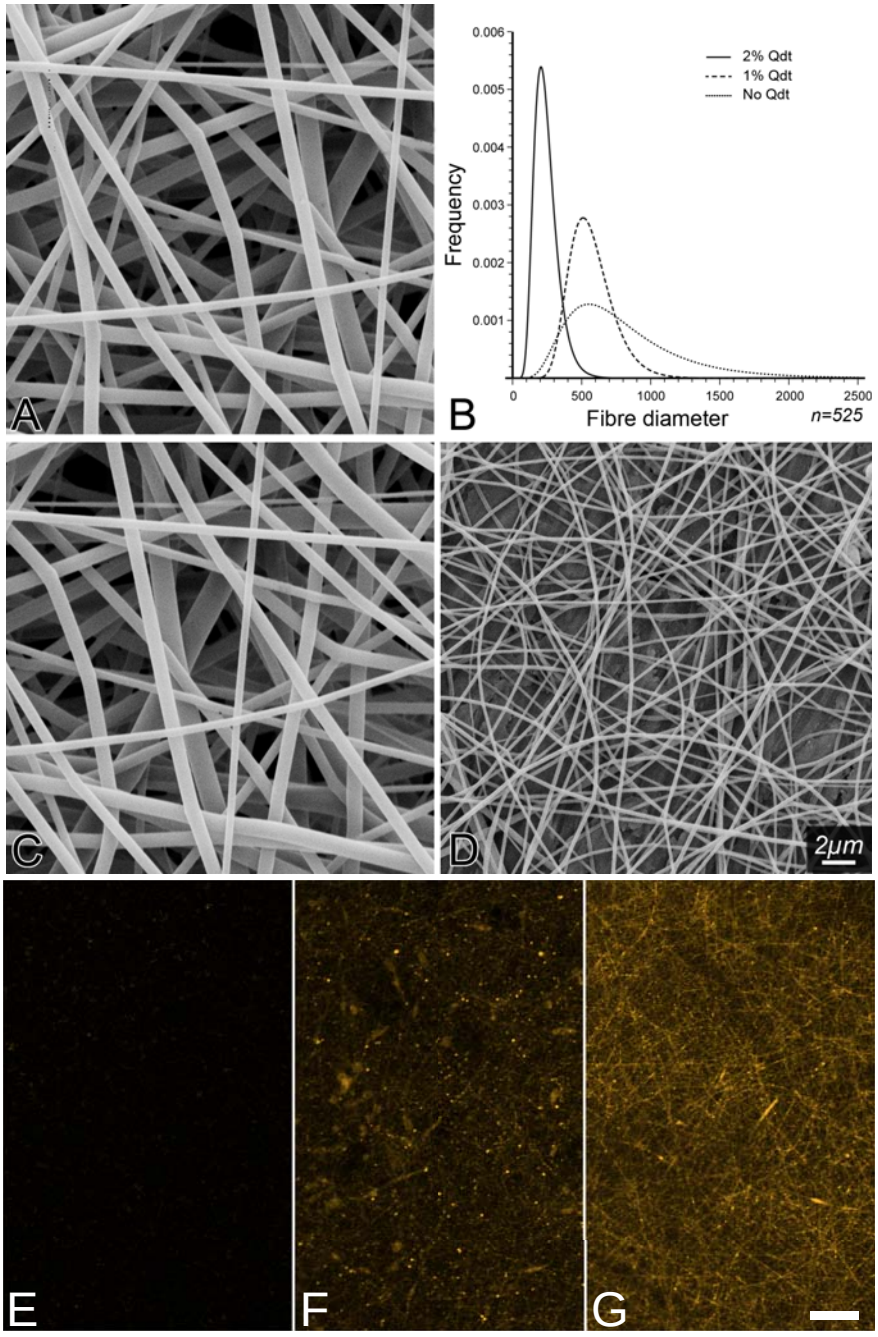
A
B
0.006
0.005
0.004
0.003
0.002
0.001
Frequency
2% Qdt
1% Qdt
No Qdt
0
500
1000
1500
2000
2500
Fibre diameter
n=525
C
D
2µm
E
F
G

concentration produced a further decrease to 237.22±1.390 nm; these fibres were defined as Nano-250. At the nanometre level, individual fibre analysis, based on the inset in Figure. 30G, illustrated the random distribution of the individual nanocrystals within a single fibre.

4.2.5 Membrane insert system

4.2.5.1 Membrane insert design

The designs of the *membrane insert* were based on the existing electrospinning formats, topographical culture system, microporous interface culture system and bulk material manipulation. Considering the topographical and microporous interface culture system, the 6-well and 12-well multi-well plates were selected as the ideal culture vessels and the overall size of the membrane insert were developed based the measurements of each individual well, as shown in representation Figure. 31A. Within the structure of membrane insert, the structural features were further developed in the form of tight complementary fit of groove-ridge. Figure. 31B showed the two components that made up the membrane insert. The *Base-ring* portion of the insert was a thick band (~5mm) ring that was centrally hollow and consisted of a circular groove within the thick band. The *Loop-ring* portion was a thin band (~2mm) ring that was also centrally hollow. *Loop-ring* was the exact fill for the groove within the *Base-ring*. The width of the *Base-ring* band was designed for routine culture media changing and examination of membrane and cells. This design was used for the unwoven electrospun fibres mesh. This *membrane insert* is named *membrane insert type R (MI-R).*

Figure 31: Membrane insert design for tissue culture.
Schematic illustration of a membrane insert (A1) designed to fit in a typical 6-well culture plate with the membrane balanced at the surface of the culture media (A2). This is desirable for the cell culture of OEC and interface culture of the organotypic entorhino-hippocampus culture. The dimensions of the membrane inserts designed to secure random fibre mesh for use in a 6- (B1) and 12-well culture plate (B2). For the dual layer assembly to produce aligned fibres mesh membrane insert for a 6-well culture plate, the dimensions of membrane insert design consisted of an additional feature (B3, red aerial line) to allow fastening of the membrane insert within the high speed rotating drum (C).

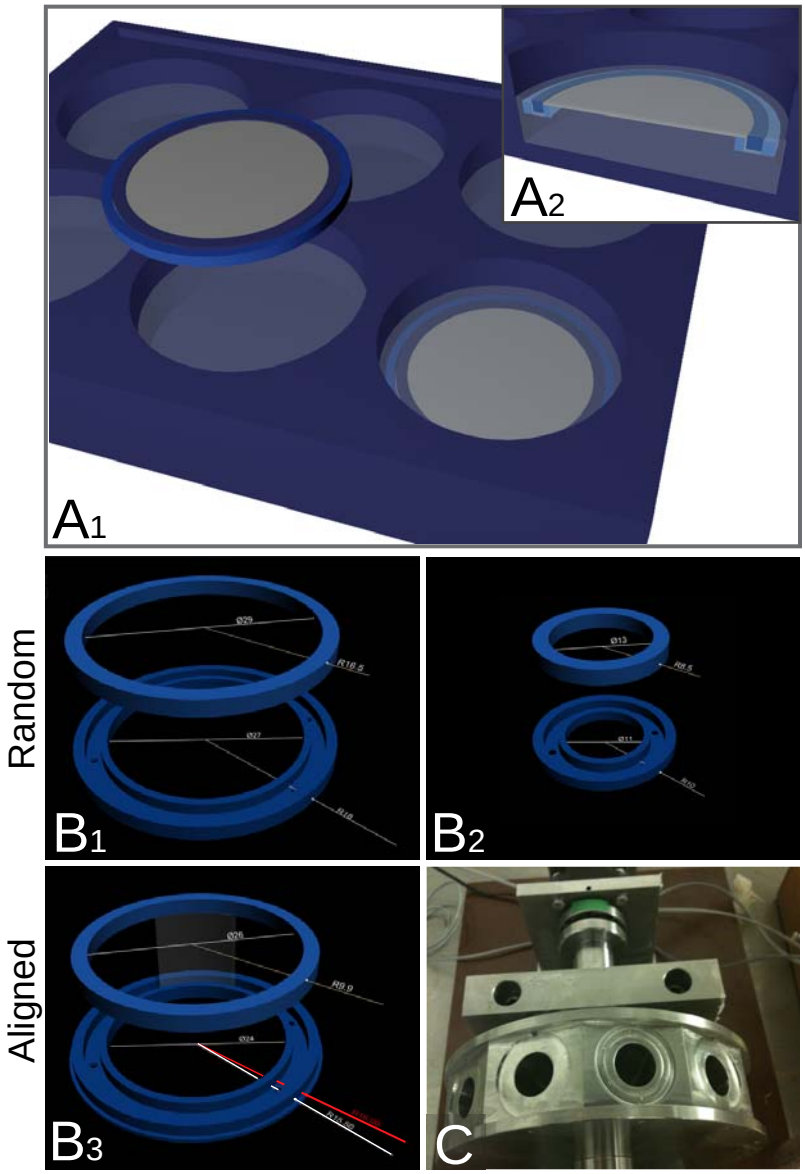
A1
A2
Random
B1
B2
Aligned
B3
C

Maintaining the core design of the *membrane insert*, feature variation around the edges was introduced in the *Base-ring* to accommodate the rotating electrospinning drum format for aligned fibres collection. This in turn reduced the inner dimension of the hole in *Base-ring* by a factor of 1mm. As shown in Figure. 31 B3 (red aerial line), an additional half millimetre thickness of the band was trenched off from the outer side of the *Base-ring* to be used as a fastening rim around the ring with the two tuneable screws in the *insert* mould on the rotator during high speed rotation. This *membrane insert* is named *membrane insert type A (MI-A)*.

4.2.5.2 Scaffold casting

Figure. 32 illustrates the casting process of the electrospun fibre mesh on the *membrane insert* that was custom fabricated commercially. Random fibre mesh was electrospun for 2h and then carefully detached from the aluminium-foil collector. The *Base-ring* was then placed beneath the fibre mesh for a full coverage of the entire *Base-ring*. Above the *Base-ring* and fibre mesh set up, *Loop-ring* was then positioned preciously on top of the groove of the *Base-ring*. After adjusting the tensile of fibre mesh, the *Loop-ring* was then depressed into the allocated groove to fasten the fibre mesh onto the insert. The excess flank fibre mesh around the *Loop-ring* was then subsequently easily removable from the *insert* system. The depression of the *Loop-ring* produced similar fibre morphology and scaffold tensile without any distortion, seen in Figure. 32 C1 and C2.

Similarly, shown in Figure. 5C, using the rotating drum electrospinning format to obtain aligned fibres, while the *Base-ring* from *MI type A* was from the allocated slot, depression of the *Loop-ring* from *MI type A* was into the groove of the *Base-*

Figure 32: Techniques of casting fibre mesh on to the membrane insert.
A series of step-by-step photographs (A1-D1) and diagrams (A2-D2) of the techniques used to fasten fibre mesh on to the membrane insert. Note, the tensile strength of the fiber mesh was maintained (See SEM images of fibre mesh in Figure 33, 36 A-B and 37 A1-E1) using the design of the membrane insert with the loop ring inserted within the groove of the base ring. Scale bar, as indicated in SEM micrographs.

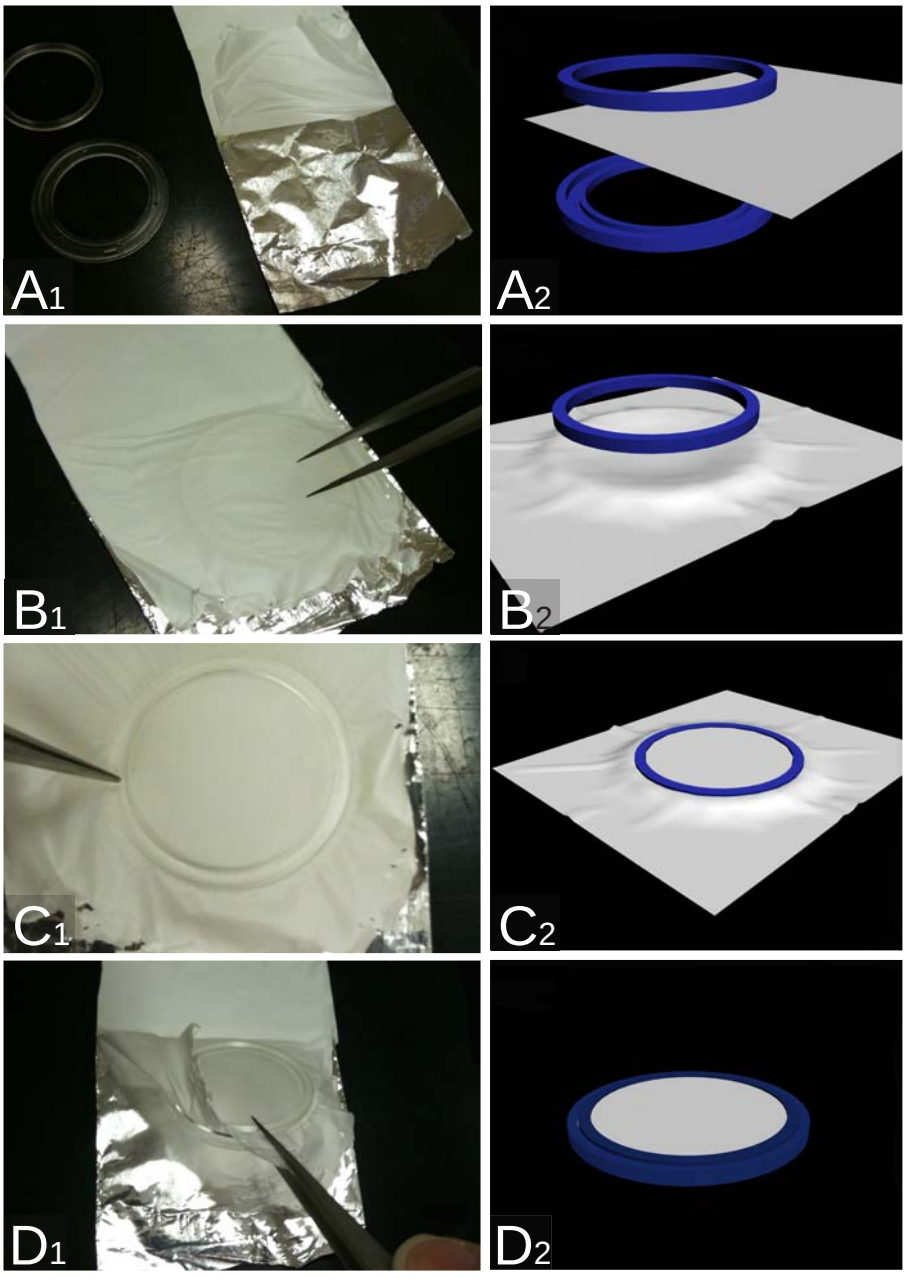
A1
A2
B1
B2
C1
C2
D1
D2

ring was able to fasten the aligned fibre mesh on to the insert without morphology distortion to the individual fibres. Upon *insert type A* removal from the insert mould on the rotator, the fibre mesh within the insert was readily detached from flanking fibre coil undisturbed, allowing easy and rapid transfer of the fibre mesh onto the *membrane insert*.

The additional holes dispersed around the base of the groove in the *Base-ring* were useful to detach the *Loop-ring* from its mould in the *Base-ring*. The detachment of the *Loop-ring* with *Base-ring* released the bulk sheet of fibre mesh with minimal disturbance to both scaffold sheet and the adhered cells on the scaffold.

In term of material suitable for tissue culture, the selected poly(methyl methacrylate) material was able to provide a suspended culture fashion that allow permeation of media from the bottom and air exchanges from the top, suitable culture condition for both OEC (Section 3.2.2 above) and organotypic slice culture (see Chapter 5).

4.2.6 Laser ablation

4.2.6.1 Bulk geometries design rationale: fashioning a clinical neural scaffold

An ideal neural scaffold for clinical transplantation from the clinical standpoint is one that 1) exhibits structural and topographical properties that address the issue of a limited number of olfactory ensheathing cells from a clinical biopsy and 2) maximize the ensheathment of nerve fibres (Ibrahim *et al.*, 2006). From the neurosurgical standpoint, it is one that is mechanically robust yet flexible to allow smooth transfer post-culture, prior to surgical transplantation. A critical aspect of the design is to

maintain the micro-features of the fibre mesh fabricated from electrospun PLGA of low tensile strength.

In all the designs (e.g. shown in Figure. 33A and B), two *coupons* were formulated with one to support the OEC growth and the other to allow manual manipulation with surgical tools to aid transfer to transplantation. Situated centrally in the electrospun fibre mesh, the two *coupons* were separated and supported by easily cut legs (spokes), which would be easily excised by a trepanned thermal knife, hot stamp or die. Various designs of spokes proximity were used to evaluate the supportiveness for the cell *coupons* in term of scaffold tensile and fibre morphology, after laser ablation. The rationale for these thin spokes is the ease and rapid cut by the surgeon immediately before implantation. One of the remaining squares used as a tab to pick up the tissue without damaging the cells on the other square. Aligned fibres would run from left to right.

The resultant of these requirements is a clinically compliant tissue scaffold which embraces cell and culture technology platforms to enable the controlled differentiation of olfactory ensheathing cells. The cell laden scaffold is presented in a form for easy surgical manipulation.

4.2.6.2 Coupon design for the PLGA scaffold

Coupons designed as shown in Figure. 33A were used as a template for laser ablating the PLGA electrospun fibre mesh that was mounted on the PMMA membrane insert. Several bulk geometries designs were attempted and failure. PLGA electrospun nanofibre mesh ablated with previous design was deemed as

Figure 33: Characterisation of the design of the coupons under laser ablation.
Fabrication of two designs of contact brass plates for the use as a laser patterning mask for PLGA electrospun fibre meshes (A1-2). The electrospun fibre mesh was assembled in dual layers and then fastened on to the membrane insert. SEM micrographs of laser ablated fibre mesh using the respective brass mask coupon design. At both macro- (B1-2) and nano-scale (C1-2), A1 design resulted in deformation of the bulk geometries structure and the fibre features (B1, C1), while in A2 design, bulk and nano-structures were maintained (B2, C2).

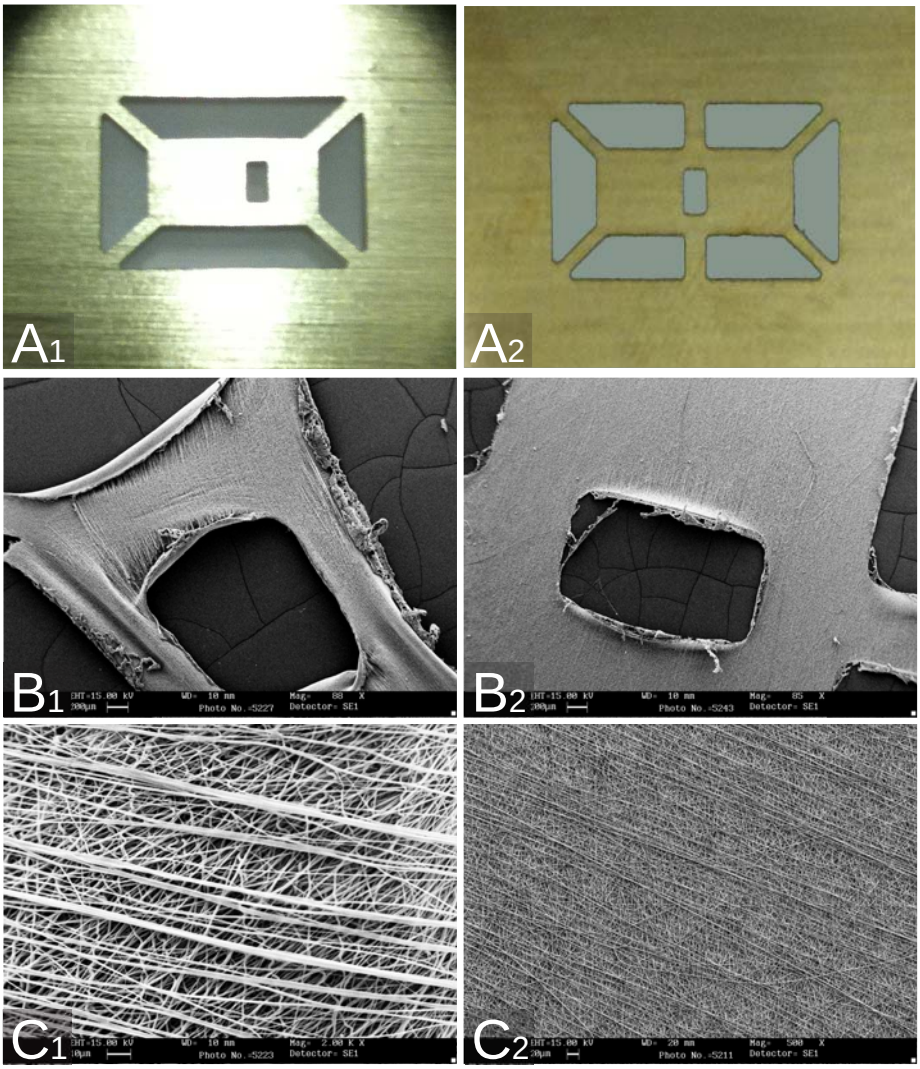
A1
A2
B1
B2
C1
C2

inappropriate scaffold as the corners of the coupon geometries soon collapsed after laser ablation (data not shown). Lack of spokes support at the corners of PLGA coupons contributed to the overall structure collapse. The improvised configuration, portrayed in design A1 shifted the spokes support from the diagonal and medial of the coupons geometries to their edges. Although the edges of the coupons were supported, SEM images in Figure. 33 B1 and C1 showed PLGA fibre mesh with design A1 still exhibited deformation at the global structures level, due to lack of medial spokes support between the two coupons. Figure. 33 B1 showed the collapse of the fibre tensile within the PLGA fibrous mesh, where the fibres were loosely bonded nanofibres, with many showing curling impression (Figure. 33 C1). It is noted that the individual fibre morphology remain intact, in term of diameter and surface of fibres, as the control. However, PLGA electrospun fibre mesh with design A2 exhibited the most reliable dual-coupons structure supported by the sufficient spokes, where the global tensile of the structure was maintained (Figure. 33 B2) and the morphology of the fibres (Figure. 33 C1) was intact after ablation.

4.2.6.3 Contact mask placement

Figure. 34A showed the two different placements of the brass mask, relative to the dual layer electrospun fibre mesh during ablation. When the stencil was placed above the scaffold bound *membrane insert*, the 1mm height of the *Loop-ring* prevented the collapse of the structure on to the stencil during ablation (Figure. 34 B1–before and C1–after). However, when brass stencil was placed directly on the membrane insert scaffold, it was evident that PLGA ablated structure was drawn upward and subsequently adhered to the mask, evident in Figure. 34 B2 (before) and C2 (after).

Figure 34: Characterisation of the contact placement of the brass plate under laser ablation.
Photomicrographs of two opposite placement position of contact brass plate relative to membrane insert cast, dual layered PLGA electrospun fibres. Brass plate positioned above (A1-C1) or beneath (A2-C2) membrane insert with fibre mesh.

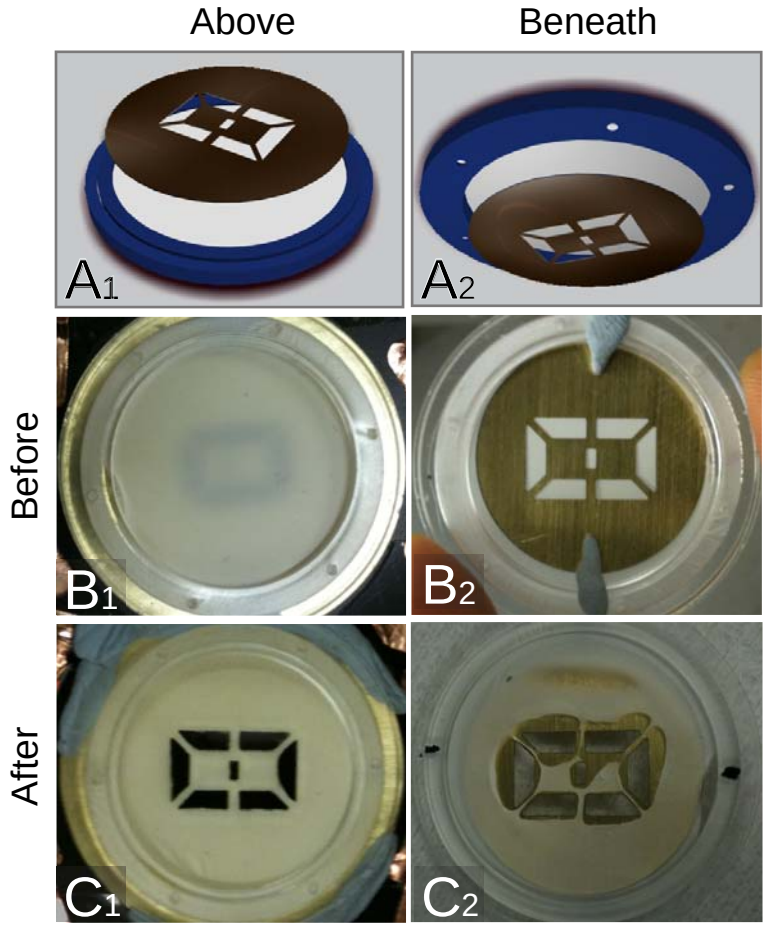
Above
Beneath
Before
After
A1
A2
B1
B2
C1
C2

4.2.6.4 Laser intensity

The profile of the energy illustrated the concentration of the laser energy resided mainly on the centre of the laser, with rapid reducing intensity at the outermost rim of the energy area (data not shown). With this disuniformity on the energy profile, I tested several laser configurations ranging from frequency of 1-3Hz and laser intensity of 120-300mJ. The laser frequency was determined by the percentage of fibres being ablated and among the frequency 1 to 3Hz, 3 Hz has shown to be the optimal repeats of the same laser intensity. 3Hz was considered optimal as the pulse repetition frequency was adequate to remove the remnant of the exposed PLGA fibres, without compromising the machined features. The setting of laser intensity minimized the extension of the dissipated of the thermal energy from the laser to the non-irradiated portion, producing consistent machined features on this biodegradable polymer.

For the laser beam beam energy, at the high laser intensity, e.g. 245mJ, Figure. 35 A1 and A2 showed SEM images of the PLGA electrospun fibre mesh ablated using design A2. The aligned fibre layer was disrupted from its assembly and minor deformations in the bulk geometries of the structure were also observed. At the laser beam energy of 129mJ, Figure. 35E showed the ablation of design A2 consistently produced uniform ablated edges of the global structure, the preservation of the dual layer assembly and the nano-scale feature of the individual fibres in all three experimental replicates.

Figure 35: Characterisation of the laser power on the macrostructure under laser ablation.
SEM images of macrostructure showing the disruption of the top layer of the aligned fibres (A1) in dual-layer assembled PLGA electrospun fibre mesh as high as 245mJ and the infolding of the sizable area that were excessively ablated (A2). At the same frequency, i.e. 3Hz, the optimal laser power of 129mJ consistently produced uniform ablated edges of the global structure (B1), the preservation of the dual layer assembly and the nano-scale feature of the individual fibres (B2). n=3 experimental replicates. Scale bar, A1, B1 and B2, 200μm, A2, 20μm.

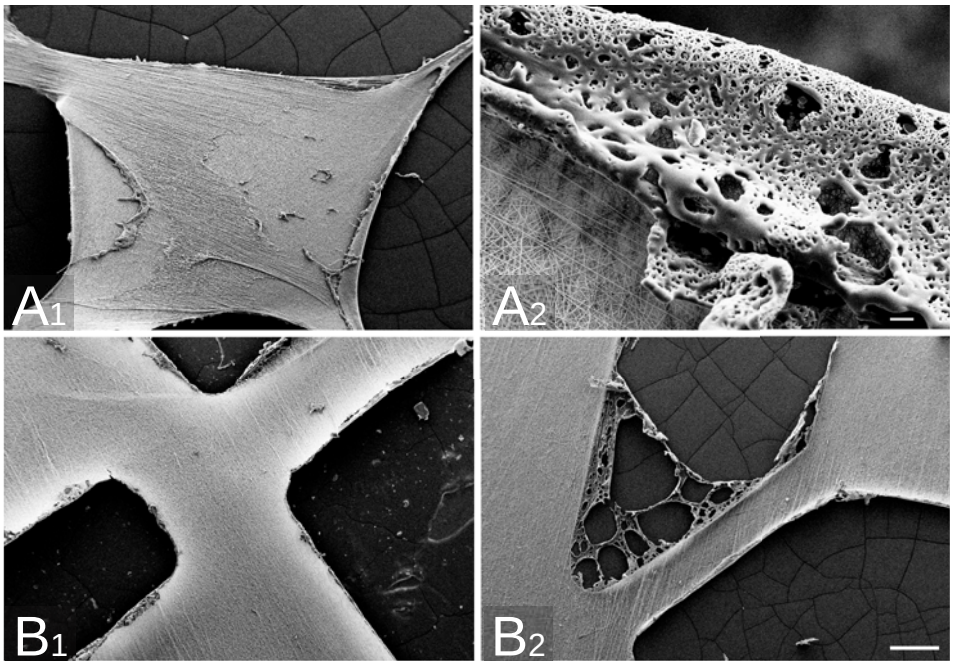
A1
A2
B1
B2

4.2.7 Sterilization

I assessed the relative susceptibility to the PLGA and PMMA to the chemical and irradiation steps involved in the sterilization process. The sterilization of fibre mesh mounted membrane insert under three conditions was investigated to determine the effect of each mechanism individually. The effects on fibre morphology were shown in the SEM images (Figure. 36) captured after the sterilization process, compared with the same batch of fibre mesh prior to sterilization as a control. The UV sterilization process resulted in the melting of the polymeric fibres, deforming the nanometre features of the electrospun nanofibre morphology. For the ethanol sterilization, the global structure of the fibrous mesh shrank in size, detaching part of the fastened portion of the mesh from the membrane insert. Digital image analysis from SEM images, showed in Figure. 36 showed that average fibre diameter expanded by 21.1% ($\bar{d}_{\mathrm{EOa}}$= 1.08μm; $\bar{d}_{\mathrm{EOb}}$=0.89 μm). Meanwhile, the average fibre diameter after ethylene oxide sterilization remains relatively similar to those prior to sterilization. ($\bar{d}_{\mathrm{EtOa}}$= 0.85μm; $\bar{d}_{\mathrm{EtOb}}$=0.82μm). Therefore, EtO sterilization proved to be a superior process than the two processes previously described for sterilizing electrospun nanofibre scaffold. The PMMA membrane inserts were inert to all sterilization processes.

4.2.8 Surface functionalization

The high fidelity of the submicron scale features in the PLGA electrospun fibres mesh after functionalization (and then air-drying) was verified through SEM (Figure. 37 B1-E1). The effect of functionalization on the nanofibres was then studied by analysing the responses of cells seeded on a mesh of randomly orientated nanofibres.

Figure 36: SEM micrographs of the 6% nanocomposite fibre mesh before and after 3 different sterilization processes.
SEM images showing the PLGA fibre mesh (A,C,E) before, and (B,D, F) after undergoing 3 different sterilization processes, namely (A,B) ethylene oxide (EtO), (C,D) 70% ethanol (EtOH) and (E,F) UV for 15mins. Scale bars, 50μm (A,B), 200μm (C,D), 20μm (E,F).

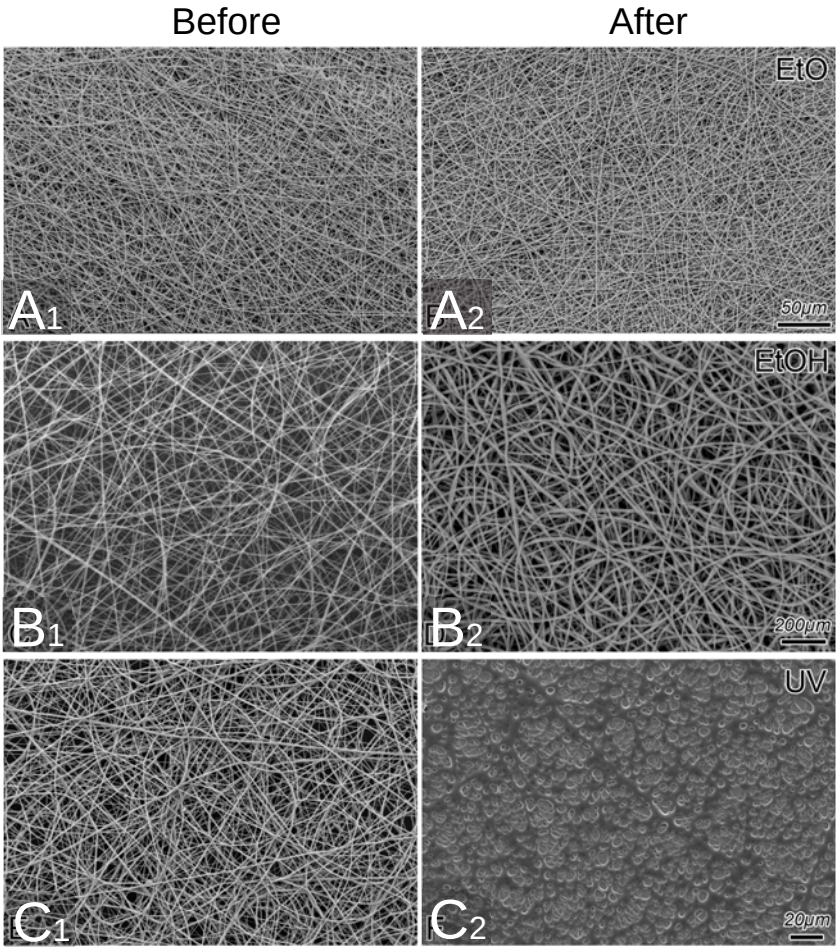
Before
After
EtO
A1
A2
50μm
EtOH
B1
B2
200μm
UV
C1
C2
20μm

After 4d of culturing, the responses of seeded purified OEC on the four type of functionalization were investigated using immunofluorescence microscopy. All four coatings promoted cell attachment, when compared to the non-functionalized PLGA electrospun nanofibres mesh (Figure. 37 B2-E2 vs. Figure. 37 A2). All four nanotopographical functionalization maintain native morphology of OEC seen in chamber slide (Figure. 11A and B). The fingerprint of contact guidance response was evident in the newly adopted bipolar shape by OEC in all the scaffolds, compared to the extended cell area projection in the chamber slides.

The degree and extent of cell attachment differed significantly between the nanofibre meshes, regardless of the molecules used for functionalization, as compared with the poly-lysine coated chamber slides. The extent of cell attachment was highly dependent on cell density. FACS purified OEC cultured on the collagen and laminin coated nanotopographic scaffold exhibited an extended bipolar projection, shown in Figure. 37 D2 and E2, at cell density as low as 10,000 cells/cm^2, whereas pLL and pDL coated scaffold (Figure. 37B2 and C2) required a higher cells density at 81,000 cells/cm^2 to have the similar cell projection profile as seem in collagen and laminin.

4.2.9 Cell adhesion and growth of OECs on poly-lysine functionalized surfaces

To demonstrate the basic response of OECs to nanotopography without the use of adhesion enhancing molecules such as laminin or collagen, poly-lysine was selected.

(a) Cultured on flat surfaces: Dissociated cells from olfactory bulbar or mucosal tissue samples cultured for 10d were FACS purified to 98% p75+Thy1- (verified on a second sort) and cultured for a further 4d on flat surface poly-lysine coated

Figure 37: Characterisation of PLGA electrospun fibre meshes after functionalization and culture of purified OEC.
SEM of PLGA electrospun fibre meshes without functionalization (A1) and after functionalization with poly-L-lysine (B1), poly-D-lysine (C1), collagen (D1) and laminin (E1). The corresponding confocal images of these fibre meshes used for culturing of purified OECs (green) from OM (A2, B2, D2,E2) and OB (C2) n=9. A2 illustrates the luminescence of the quantum dots in the nanocomposite nanofibres with purified OECs in a confocal microscope setting, excited using Helium-Neon 633nm laser line and laser filters of 550-633nm in the LSM 510 meta (Zeiss, UK). Scale bars, A1-E1, 2µm and A2-E2, 200µm.

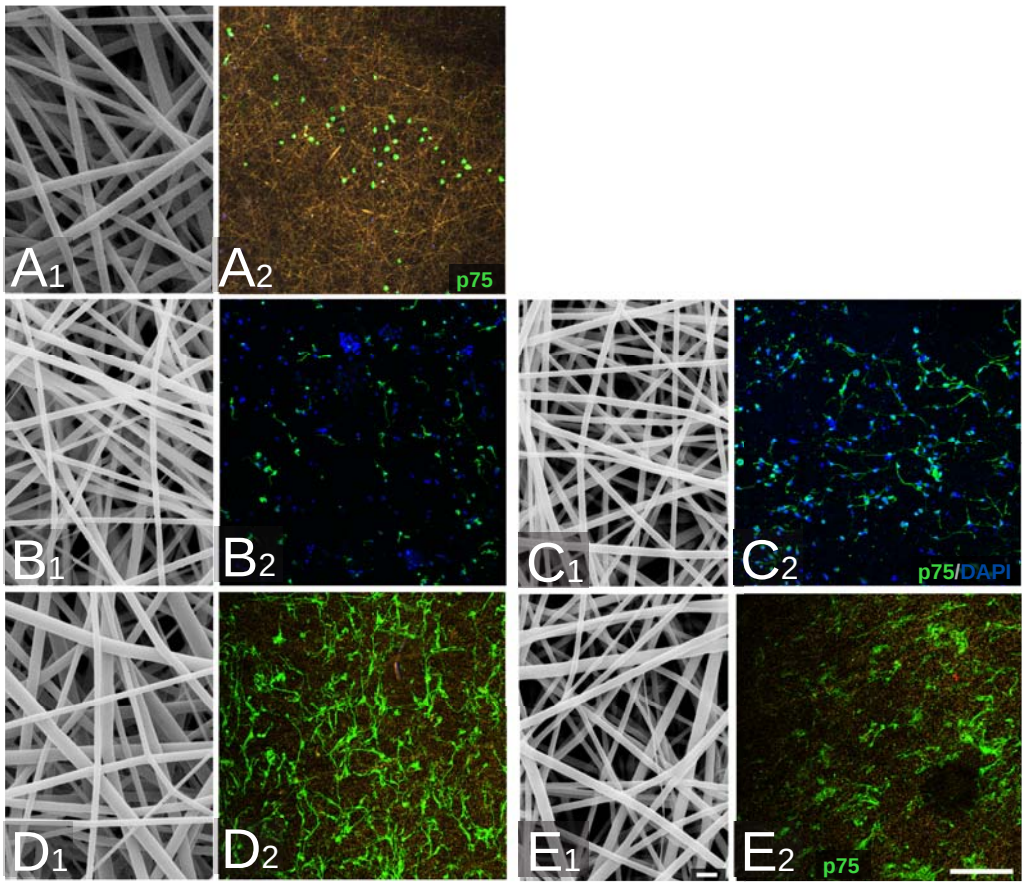
A1
A2
p75
B1
B2
C1
C2
p75/DAPI
D1
D2
E1
E2
p75

chamber slides. The purified cells attached and continued to grow. As described in previous study (Kueh *et al.*, 2011), cells plated at high density (≈ 81,000 cells/cm^2) adopt a radial morphology of elongated branches with narrow cell bodies. However under low density culture conditions (≈10,000 cells/cm^2) the cells adopted a flattened, wide bodied morphology with no distinction between branches and cell body (Figure. 38 A,D). Immuno-staining confirmed the consistent expression of p75 and S100. Bulbar and mucosal OECs were indistinguishable in their individual morphology and antigenic expression.

(b) Cultured on Nano-700 and Nano-250 fibres: FACS purified bulbar and mucosal OECs were seeded at low density (≈10,000 cells/cm^2) on sterilised meshes of randomly orientated Nano-700 and Nano-250 fibres. After culture for 4d the cells were examined by immunofluorescence microscopy. On uncoated fibres the OECs adhered poorly and remained as small rounded cells. There were no detectable differences in the numbers of adherent OECs between the Nano-700 and Nano-250 fibres (Figure. 38 B-F).

4.2.10 Cytomorphometric comparison of OECs cultured on flat surfaces with Nano-700 and Nano-250 fibres

Compared with low density OEC cultures on the flat surfaces, immunofluorescence and SEM images suggest that OECs cultured at the same density on the Nano-700 and Nano-250 fibre meshes responded by increased elongation (Figure. 38K-L). Cytomorphometric analysis based on the p75 immunofluorescence images demonstrated a major reduction in surface area and minimum Feret diameter (an indication of narrowing of the cell body; Figure. 39A,B).

Figure 38: Characterisation of cell adhesion and growth of purified OEC on different surfaces.
Immunofluorescent confocal images of purified OECs sorted from (A, B, and C) primary bulbar and (D, E and F) mucosal tissue cultured at low density (≈10,000 cells/cm^2) for a total of 14 days on different surfaces: (A and D) Flat surface, (B and E) Nano-700 and (C and F) Nano-250. Scale bar, 200μm. Tracing diagrams of representative single cells on each surface, using the cell tracing method indicated in the Materials and Methods, depicting the morphology and orientation (not numbers) of cells cultured each corresponding surface (G, flat, H, Nano-700, J, Nano-250). Representative cells on each surface (K, Flattened on flat surface; L, stellar on Nano-700 and M, bipolar on Nano-250), showing the parameters used for all quantitative analysis. Circularity was expressed as $C=4(\pi)\ A/P^2$, where A is the surface area (filling, light grey) and P is the perimeter (outline, dark grey) of the cell. Roundness was expressed as $R=4A/(\pi)r_1^2$, where r_1 is the major axis (dotted line across the ellipse, black), obtained from best fit ellipse (dotted elliptical shape, black). As the complexity of the cells decreased when cultured on surfaces of smaller fiber diameter (from Nano-700 to Nano-250), the perimeter decreased while the major axis increased, polarizing the values of both circularity and roundness (Bettinger et al. 2006). Quantitative analysis in Figure 39.

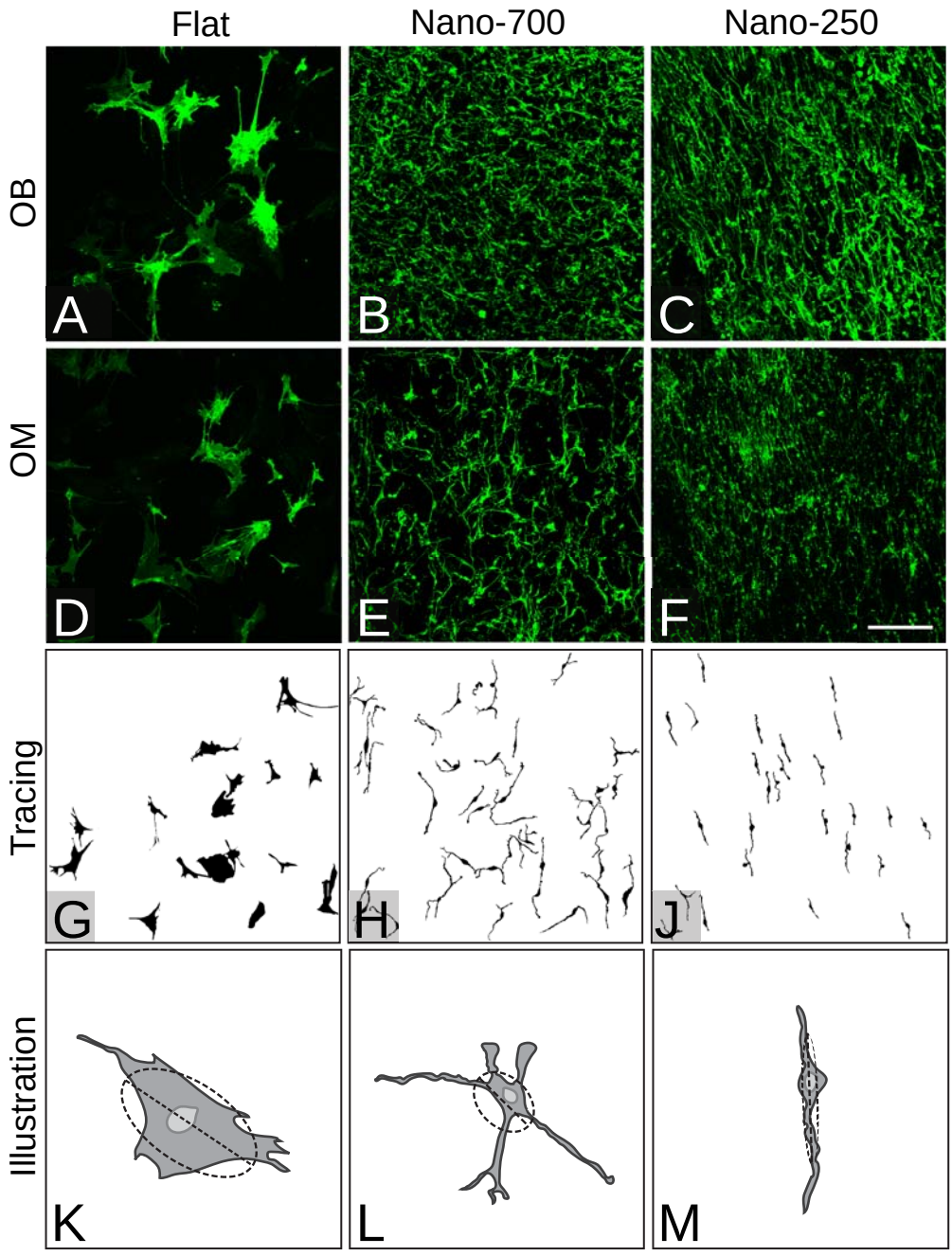
Flat
Nano-700
Nano-250
OB
OM
Tracing
Illustration
A
B
C
D
E
F
G
H
J
K
L
M

On the Nano-700 meshes the majority of the elongated OECs exhibit multiple, radiating cell protrusions. On the Nano-250 meshes the majority of the cells were shorter, and virtually all had adopted a bipolar geometry (e.g. Figure. 38M). Cytomorphometric evaluation of the cell shapes based on the particle analysis concepts of 'circularity' (this estimates the extent to which the cell extends its perimeter into processes) and 'roundness' (this estimates the overall compactness of the cell) confirmed the statistical significance of these differences between the OECs grown on these two substrates (Figure. 39C and D).

Strikingly, the population of elongated bipolar OEC grown on Nano-250 fibres showed more unidirectional growth when compared with the anisotropic growth on Nano-700 fibres (Figure. 38B and E vs. 38C and F). This is despite the randomness of the orientation of the fibres in the mesh. The histogram of cell angle alignment indicates a clear peak of a particular angle (in this instance, 120°) for Nano-250 fibre meshes, compared to the random range of angles for OECs grown on both flat surfaces and Nano-700 fibre meshes (Figure. 40).

4.2.11 Scanning electron microscopy

The Nano-700 and Nano-250 fibres were recognised as unbranched, smooth-surfaced, and of uniform diameter. The OECs remain on top of the fibre mesh so that their processes are seen running in continuity over the underlying fibre mesh. On the Nano-700 fibres the OEC cell bodies are elongated oval shapes, occasionally tripolar or stellate (Figure. 41A) with long smoothly tapering processes, and which do not weave into the underlying fibre mesh. The overall population of OECs shows a tendency to lie in the same orientation. On the Nano-250 mesh only tapering,

Figure 39: Bar charts of cytomorphometric analysis of purified OECs cultured on flat and nanofibre meshes.
Cytomorphometric analysis of the purified OEC on the flat, Nano-700 and Nano-250 surfaces. A, surface area; B, minimum Feret's diameter; C, circularity; D, roundness. Bar charts, mean and SEM, $p<0.001$ (**) ; $p<0.05$ (*), n=240 (cells).

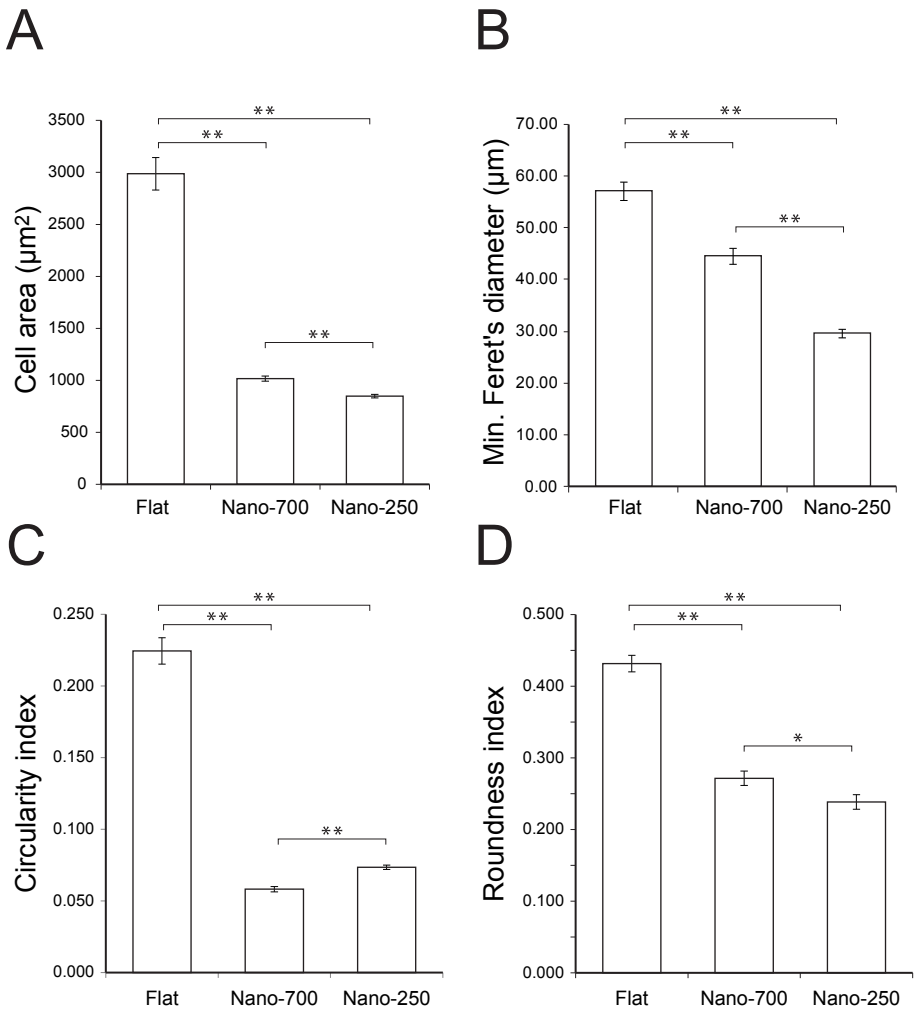
A
B
C
D
Cell area (µm²)
Min. Feret's diameter (µm)
Circularity index
Roundness index
Flat
Nano-700
Nano-250
**
*

Figure 40: Graphs of directionality analysis of purified OECs cultured on flat and nanofibre meshes.
Histogram of pixels directionality based the Fourier transform analysis, of traced cells cultured on each surface (A) (Delgado-Rivera et al. 2011). n=12. For flat surface, pixel distribution independent of direction was depicted in graph with multiple peaks, with high dispersion degree (B; $p<0.05$ (*)) and poor Gaussian fit (C; all $p<0.01$). As the feature complexity of the surface increased from flat to Nano-250, the pixel intensities concentrated in a specific angle, producing a graph with single peak that fit a Gaussian distribution (0.98/1.00; in C), with low dispersion degree (25° in B).

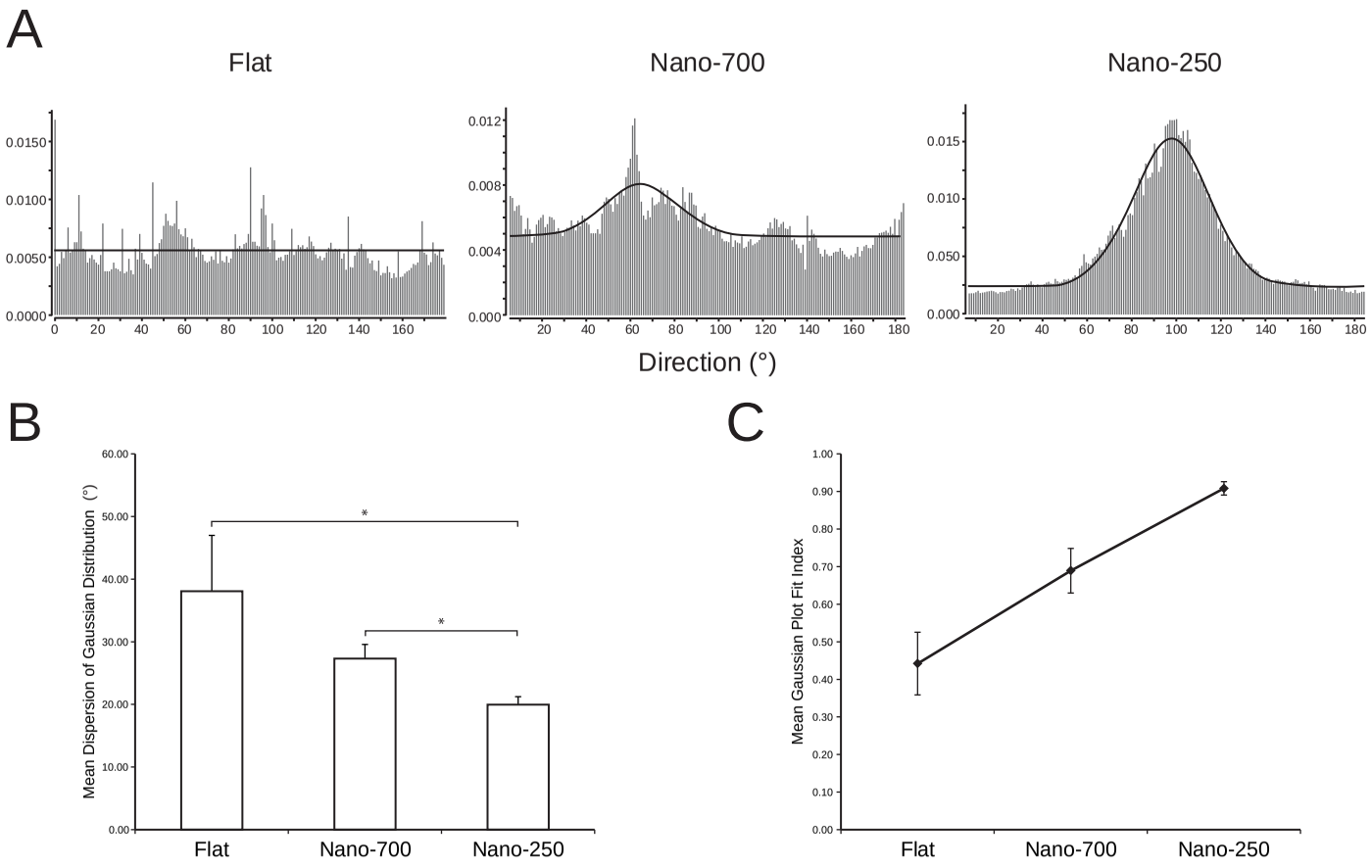
A
Flat
Nano-700
Nano-250
0.0150
0.0100
0.0050
0.0000
0.012
0.008
0.004
0.000
0.015
0.010
0.050
0.000
0 20 40 60 80 100 120 140 160
20 40 60 80 100 120 140 160 180
Direction (°)
B
Mean Dispersion of Gaussian Distribution (°)
60.00
50.00
40.00
30.00
20.00
10.00
0.00
*
*
Flat
Nano-700
Nano-250
C
Mean Gaussian Plot Fit Index
1.00
0.90
0.80
0.70
0.60
0.50
0.40
0.30
0.20
0.10
0.00
Flat
Nano-700
Nano-250

Figure 41: SEM micrographs of purified OECs on Nano-700 and Nano-250 fibre meshes.
SEM imaging of purified OEC (green) on electrospun fibre mesh. A, tripolar (*) and bipolar cells on Nano-700. B, expanded lamellipodial termination and C, fine elongated filopodial termination on Nano-250. Scale bars, 10μm (A), 1μm (B,C).

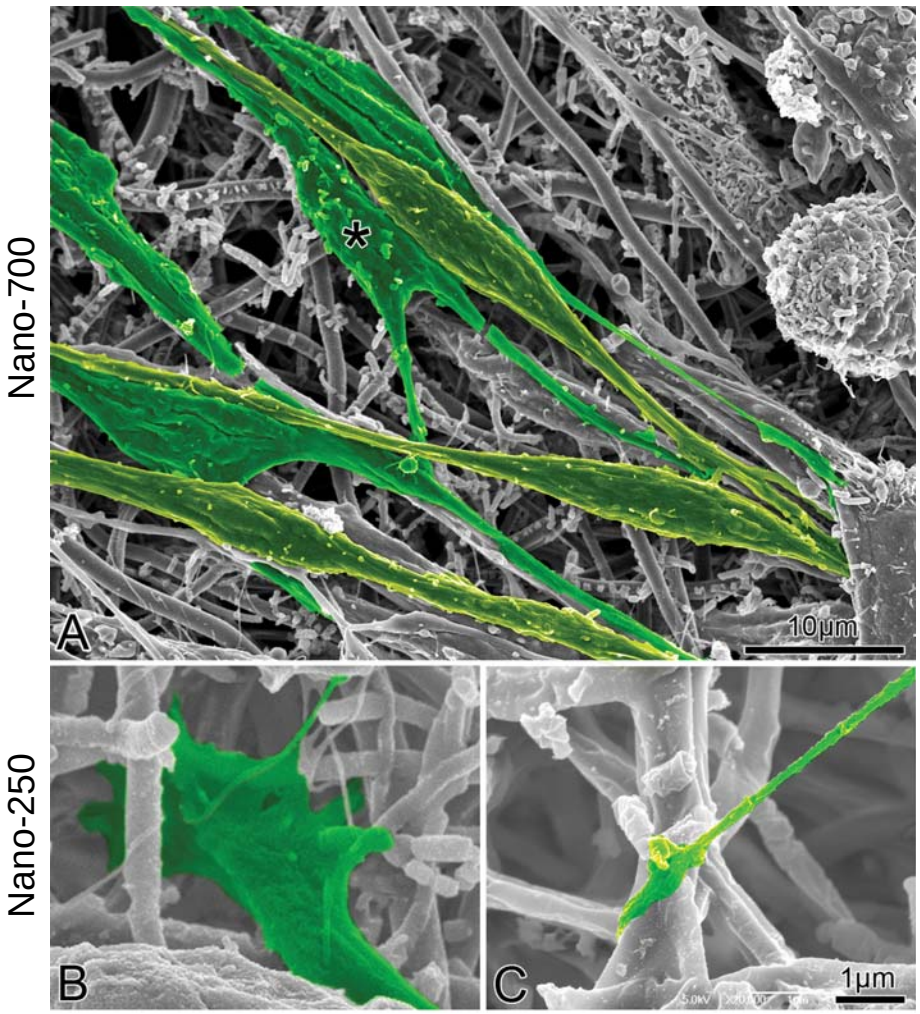
Nano-700
Nano-250
A
10μm
B
C
1μm

bipolar cells were seen, and, as in the confocal micrographs, the uniform directionality becomes dominant.

Two examples of the mode of termination of the OEC process on Nano-250 mesh are shown in Figure. 41B,C. In B the process terminates in a small lamellipodial expansion generating a mass of irregular fine filopodia. In C a long, fine filopodial process terminates as an expanded claw-like structure wrapped over a point of intersection of the underlying nanofibres.

I have only some preliminary observations on ONFs. What is clear is that, compared with the OECs, ONFs form much closer contacts with the Nano-250 fibres, following more closely the contours of the underlying mesh (Figure. 42B, C). In future studies of cell mixtures I hope to investigate whether this would result in an overall separation of the two cell types.

4.3 Discussion

Injections of suspensions of cultured adult olfactory ensheathing cells are able to provide pathways for regenerating axons to cross small lesions in rat spinal cord and allow restoration of function. The fabrication of a scaffold for the transplanted cells provides a possibility to bridge larger lesions.

Figure 42: SEM micrographs of purified ONFs on Nano-700 and Nano-250 fibre meshes.
Purified ONFs from whole mucosa on Nano-700 (A) and the unique web-like fibrous covering superficially at the space existed among the top layer of random Nano-250 fibres (B). Purified ONFs (red) from OB on Nano-250. Note, no web-like fibrous structure was observed in ONFs from OB. Scale bar, A, 10μm, B-C, 1μm.

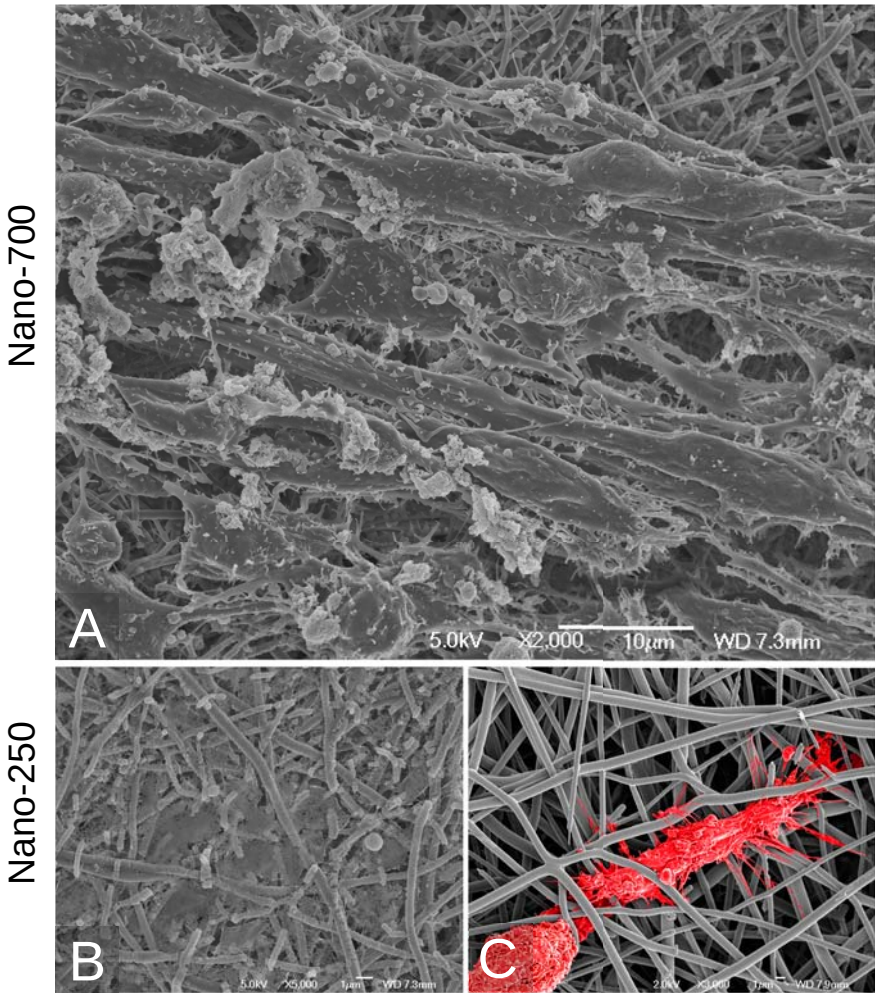
Nano-700
Nano-250
A
5.0kV X2,000 10μm WD 7.3mm
B
C

4.3.1 Suitability of PLGA material for clinical use

Poly (lactic-*co*-glycolic) acid is often known as the entrepreneurial polymeric biomaterial due to its compatibility with cell phenotype and behaviour (Hutmacher, 2000). In versatility in controllable degradation and resorbable rate it constitutes a robust biomaterial for tissue engineering. The trend of the kinetic fibrous mass degradation plots are consistent with previous reports on bulk, which have elucidated the nature of PLGA biodegradation rate is dependent to the stoichiometric ratio of lactic acid and glycolic acid (Jain, 2000; Chung *et al.*, 2006) and the molecular weight of PLGA (Park, 1994; Waeckerle-Men & Groettrup, 2005; Huang *et al.*, 2006*b*). In this proteolytic degradation, the mechanism of hydrolysis has been identified as random ester cleavage (in basic media) or chain-end cleavage "unzipping" (in acidic media) (Schliecker *et al.*, 2003).

Under the anticipated phagocytic and protease activity as estimated in damaged (Crowe *et al.*, 1997) or undamaged CNS tissue (Brylev, 2009) PLGA 50:50 would have a degradation time of about 3 weeks. PLGA 50:50 also have the advantage of an inherent viscosity of < 1 dl/g and high molecular weight in PLGA 50:50 PURAC, which improves the spinnability of the polymer at a relative lower concentration, making PLGA 50:50 PURAC as used in peripheral nerve repair (Huang *et al.*, 2003) an attractive relatively low cost candidate. Therefore, PLGA 50:50 from PURAC of Holland was chosen to conduct further studies.

4.3.2 Nanocomposite electrospinning

Embedded in the PLGA fibres, the photoluminescence of various size quantum dots was evident once excited with UV light. In addition, it also enhanced the spinnability of polymer PLGA/HFIP by significantly reducing the fibre diameter. The high photoluminescence observed from the fibre is a good indication that concentration of neither PLGA nor HFIP (high volatility solvent) affects the optoelectronic property of the quantum dots, which previous report have been addressed of the significant of blending polymer concentration when incorporating quantum dots (Li *et al.*, 2007). In addition to its high signal-to-noise ratio and stability against photobleaching (Chan *et al.*, 2002), taking into account the enhanced characteristic to the PLGA fibres, these "free-standing" nanocrystals made itself an attractive candidate as an internal monitoring device *in vitro* and *in vivo*. However such application would still need to overcome the cytotoxicity issue as recent toxicity assessments of quantum dots (Fischer and Chan 2007; Hauck et al. 2010; Wu et al. 2010) that revealed diverse results on the response from both *in vitro* and *in vivo* system.

4.3.3 Development of a clinical relevant neural scaffold

An effective way to reinforce the micro and nanostructure provided by the electrospun fibre mesh, while maintaining the tensile strength of the scaffold in a cell culture system is the complementary groove-ridge fit *membrane insert* system I developed for this study. The ease operating the scaffold reinforcement in the membrane insert system design allowed any form of mesh to attach to the insert in short time, without significant distortion to inherent mechanical properties such as

tensile strength and fibre morphology. This arrangement was important for seeding limited numbers of cells and subsequently entorhino-hippocampal slice culture.

The design and structure development strategy using laser ablation in this study allows rapid production of high resolution PLGA nerve repair structure without compromise on the scaffold intrinsic nanotopography. The laser configuration and mask-polymer arrangement employed in this strategy are compatible with the need for scaffold production and chemical and physical properties of the polymer used to fabricate the scaffold.

4.3.4 Directionality and bipolarity of olfactory ensheathing cells on electrospun nanofibres

While macroengineering of an artificial bridge provides a overall biomimetic structure (Wong *et al.*, 2008) at the microengineering level, the precision in nanotopography serves as a tool to modulate contact guidance, such as cell elongation, directional growth and changes in cellular function (Dalby *et al.*, 2003), often specific to cell types (Lim & Donahue, 2007). Anisotropic stress generated from nanotopography is generally considered as one of the mechanism of morphological response (Bettinger *et al.*, 2006; Hoffman-Kim *et al.*, 2010).

Our results confirm that the attachment and growth of the OECs on the nanofibres required functionalization of the scaffold (Schnell *et al.*, 2007). Functionalization with a range of ECM molecules and short peptides (biological macromolecules, together with changes in the nanotopography, have been reported (Casper *et al.*, 2005; King *et al.*, 2006; Mukhatyar *et al.*, 2011). In the present study I used the

positively charged macromolecule, poly-lysine (Rainaldi *et al.*, 1998) to demonstrate the basic response of OECs to nanotopography without the use of adhesion enhancing molecules such as laminin or collagen (Wang *et al.*, 2006; Möllers *et al.*, 2009).

Compared with growth of the artificial flat surfaces of standard tissue culture, growth on the nano-scale fibres engendered a morphological change from rounded to elongated stellate cells and an increase in the numbers of cells attached. This increase maybe due either to increased adhesion (i.e. retention of a larger proportion of the seeded suspension) or to increased cell survival or proliferation (Qian *et al.*, 2009; Shen *et al.*, 2010).

Further improvements were obtained by nanocomposite electrospinning PLGA with quantum dots. This enabled us to increase the uniformity of the size distribution of the nanocomposite nanofibres and achieve diameters down to the 237.22±1.390nm. At this dimension the fibres are approaching the scale of surface structures (such as type IV collagen fibres at 40-60nm) which the OECs encounter in their microenvironment. The reduction in the fibre diameter from 707.82±1.646nm (Nano-700) to 237.22±1.390nm (Nano-250) elicited a step change in the response of the OECs from the elongated, randomly arranged stellate population to the unidirectional arrangement of small bipolar cells.

I suggest that the morphological response of the OECs to the decreasing diameter of the nanofibres reflects increased density of the surface features presented by the

nanofibres to the cells - either the fine grain discontinuity of the molecular interaction and/or the charge presentation.

Shen et al, culturing OECs on silk fibre scaffolds, similarly reported unidirectionality was produced when the fibre diameter was 300nm as compared with random orientation on 1,800nm fibres (Shen *et al.*, 2010). OECs cultured on naturally occurring ECM fibres (Qian *et al.*, 2009) or self-assembled IKVAV peptides (Xu *et al.*, 2009), both of which were <100nm diameter, also achieved unidirectionality, although an additional factor in these studies could be the high density culture.

Taken together these results suggest that unidirectionality is influenced both by the density of attachment and the diameter of the substrate fibres. In the present study, cell unidirectionality occurred on flat surface culture where the attached cell density results in close cell to cell contact. Culture on the Nano-700 (707.82±1.646nm) fibres increased cell attachment as compared with flat surface culture, but unidirectionality at the same attachment density was only achieved on Nano-250 (237.22±1.390nm) fibres.

In this study, as in those of (Qian *et al.*, 2009), (Shen *et al.*, 2010) and (Xu *et al.*, 2009), unidirectionality of OECs was achieved on randomly oriented (isotropic) fibre substrates. The most likely source of this unidirectionality is cell-cell interactions. The use of aligned (anisotropic) fibre or patterned substrates would enable the orientation of alignment to be controlled (Lim & Donahue, 2007; Madigan *et al.*, 2009).

The ability of nanofibres to determine the attachment, growth, morphology and directionality of OECs *in vitro* provides an indication of the requirements for the biomaterials to be developed for bridging the larger lesions currently under investigation in clinical trials of OEC transplantation (Mackay-Sim *et al.*, 2008). Our development of a viable of ethylene oxide vapour sterilisation process and subsequent functionalization which preserve the nanotopography of the biodegradable PLGA scaffold and enhance cell adhesion and viability provide indications of a possible route for future GMP. The increased attachment of cells from the seeded suspension improves the efficiency of retention of the limited numbers of cells available. The nanofibres mediate the transformation to a bipolar morphology such as has been observed when transplants bridge small rat lesions, and provide a situation in which the cells can assemble in a uniform direction.

Chapter 5 Preliminary Studies of Nanofibres as a Neural Scaffold

5.1 Introduction

5.1.1 Development of *in vitro* assay

With the engineering of an artificial scaffold that can integrate with olfactory ensheathing cells underway, the next practical step towards formulating a technology for repair of spinal cord injury is to develop a reliable model for studying the effect of the OEC bearing scaffold on regeneration of axons *in vitro*.

Among *in vitro* neural models established to study the axonal biology, the range span from *a)* neurite outgrowth assays, such as CNS brain and spinal cord explants (Weiss, 1934), CNS retinal ganglion cell (RGC) cultures (Bray *et al.*, 1980), PNS dorsal root ganglia (DRG) explant (Bunge *et al.*, 1967) and PNS sciatic nerve explants (Morrissey *et al.*, 1991), and compartmentalised 'Campenot' chambers (Campenot, 1977); *b)* growth cone dynamic studies, such as chick RGC (Kapfhammer & Raper, 1987), isolated rat hippocampal pyramidal neurons (Mattson *et al.*, 1988); *c)* gliosis assays, such as interface culture of astrocytes from cerebral cortex explants with dissociated hippocampal neurons (Rudge & Silver, 1990), or with retinal neurons (Fawcett *et al.*, 1989; McKeon *et al.*, 1991); and microglial-neuron interface culture (Thanos *et al.*, 1993; Gimsa *et al.*, 2000); *d)* myelination assays, such as confrontation study of various neurons with oligodendrocytes from

optic nerve glial (Schwab & Caroni, 1988), with Schwann cells (Wood *et al.*, 1990), with OECs (Devon & Doucette, 1995; Sorensen *et al.*, 2008).

In these assays, a) the readily accessible explants or primary culture of neurons and glial components and b) the relative ease to culture on different substrates while maintain for an extended period (up to 4 weeks) made them an attractive approach to study the nerves tissue behaviour and interactions. Moreover, the reductionist nature of these assays allows studies of neuronal parameters at the cellular and molecular levels, and enables both qualitative and quantitative *in vitro* analysis. Parameters analyzed include neurite growth and arborisation; axonal trajectories, growth cone morphology, neuronal phenotype and excitatory/inhibitory molecular cues. Understanding gained from these analyses has since permitted experimental manipulations with different stimuli (such as myelin inhibitory products, reactive astrocytes) that are often present in the post-injury environment.

More recently, micropatterning and microfluidic *in vitro* neuronal systems, an improved system from Campenot chamber, not only compartmentalised axonal growth from growth factor influence but also allowed modulation reactions from other chemical insults to the cell microenvironment to obtain a desirable outcome (Taylor *et al.*, 2005; Park *et al.*, 2006).

Ideally the most appropriate *in vitro* system to mimic the failure of regeneration in adult spinal cord injuries is one in which it is possible to study the factors determining the ability of identified cut axons of CNS origin make their correct specific pattern of connections in central neuropil. Organotypic slice models present

as such *in vitro* system. Among the established *in vitro* organotypic slice models are three-dimensional spinal cord slice culture (Varga *et al.*, 1995; Bonnici & Kapfhammer, 2008), fimbria-fornix septal cholinergic cultures (Schinstine & Cornbrooks, 1989; Law *et al.*, 2010), and entorhinal hippocampal slice cultures (Li *et al.*, 1996; Prang *et al.*, 2001; Radojevic & Kapfhammer, 2004).

Based on the local expertise with organotypic slice co-cultures of early postnatal material in which fibre connections develop in culture (Li *et al.*, 1993, 1994, 1995, 1996), I chose the entorhino-dentate gyrus and entorhino-hippocampal confrontations in which axons regenerate across a direct contact interface to form correctly laminar terminal arborisations. By separating the co-cultures at increasing distances I was able to determine the extent of the gap across which the axons could not regenerate. In this model of regeneration failure I then tested the ability of an interposed PLGA nanocomposite nanofibre scaffold to bridge the gap.

5.1.2 Brief overview of neuroanatomy of hippocampal formation

In rat, from a three dimensional view of the hippocampal formation, it is an elongated structure, double horseshoe-shaped cortical structure in the medial of the cerebrum. Its long axis is extending in a C-shaped manner from the midline of the brain near the septal nuclei (rostrodorsally) over and behind the thalamus into the incipient temporal lobe (caudoventrally). This long axis is known as septotemporal axis, while the orthogonal axis as transverse axis (Figure. 43). From the perspective of transverse view, the hippocampal formation is made up for four cytoarchitectonical regions: dentate gyrus (DG), hippocampus (HP), subicular field

Figure 43: Schematic representation of the hippocampus in sections along the septo-temporal axis of the rat brain.
Schematic representation of hippocampus (HP) structure in 3D positioning views in rat brain (A1). A2 representative sections along the septo-temporal axis. Dentate gyrus (orange), entorhinal cortex region (yellow). BS, brain stem, ctx, cerebral cortex, OB, olfactory bulb. Adapted from the magnetic resonance imaging of the hippocampus structure in Andersen 2007.

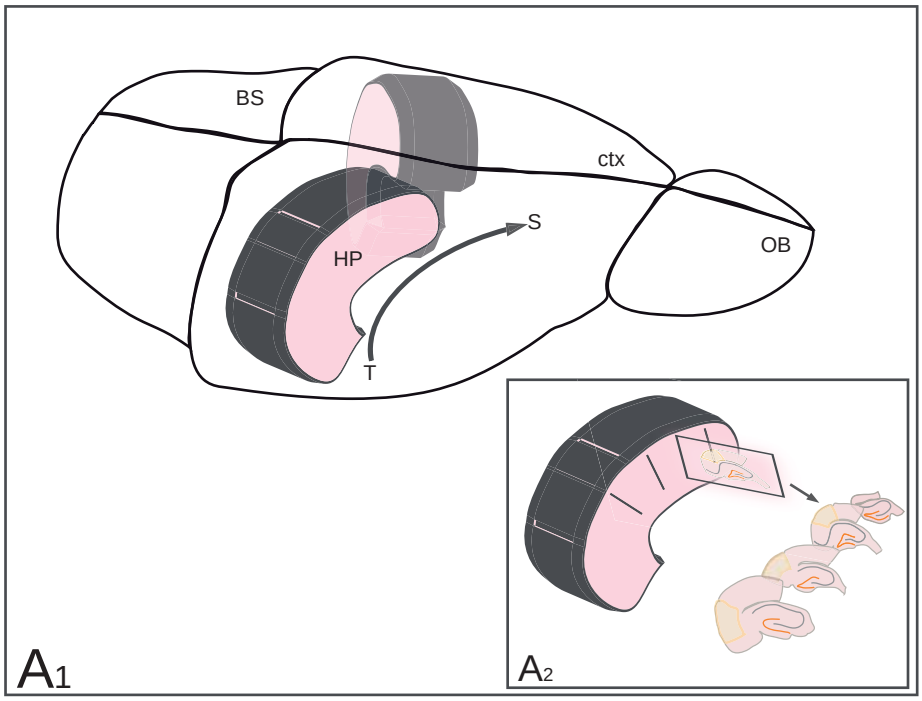
BS
ctx
S
OB
HP
T
A1
A2

(SC) and entorhinal cortex (EC) (Figure. 44). These four regions are seen in different composition along the septotemporal axis. The complexity of hippocampal formation is extended to its cytoarchitecture and network of fibres (Anderson *et al.*, 1971).

The dentate gyrus is a trilaminate cortical region that has the U or V shape characteristic. At the most superficial layer to hippocampal fissure is the relatively cell-free *stratum moleculare* (*sm*), followed by the cellular *stratum granulosum* (*sg*) and the deepest layer, the *stratum polymorphe* (*sp*). As the principle cell layers of DG, the *stratum granulosum* comprised of four to eight cell layers, depending on its location along the septotemporal axis. These granule cells have elliptical cell bodies with cone-shaped tree of spiny dendrites. The DG receives projections from the EC through the alvear and perforant path route to the *sg* from the EC. In turn the DG projects to the hippocampus proper, through efferent mossy fibres (*sp* to the *stratum lucidum* of field CA3 *(sl)*) (Anderson *et al.*, 1971).

The entorhinal cortex receives convergent sensory input from the cortex (Naber *et al.*, 2001) and which, after processing via the hippocampus is relayed back to neocortex (Insausti *et al.*, 1997). As a multilaminar cortex EC lamination is organized in six layers with four cellular layers (layer II, III, V and VI) and two acellular (layer I and IV). **Layer I**, the most superficially plexiform or molecular layer is cell poor but rich in transversely oriented fibres. **Layer II** contains large stellate cells, with occasional dense cluster (in islands) of small pyramidal cells population, particularly in lateral entorhinal area. Both stellate and pyramidal cells project to the dentate gyrus. Most of the cells have dendrites confined to superficial

Figure 44: Schematic illustration of hippocampal formation in horizontal section.
Hippocampal formation include the cytoarchitectonically distinct adjoining regions that include dentate gyrus (DG), hippocampus (HP), subiculum (Sub), pre- and para-subiculum (PS), and entorhinal cortex (EC). Fb, fimbria. The rhinal fissure (arrow) at junction of neo- and entorhinal cortex region. The hippocampal fissure (arrow head) separates the dentate gyrus from the subiculum (Fanselow and Dong 2010; van Strien et al. 2009; Sugar et al. 2011)

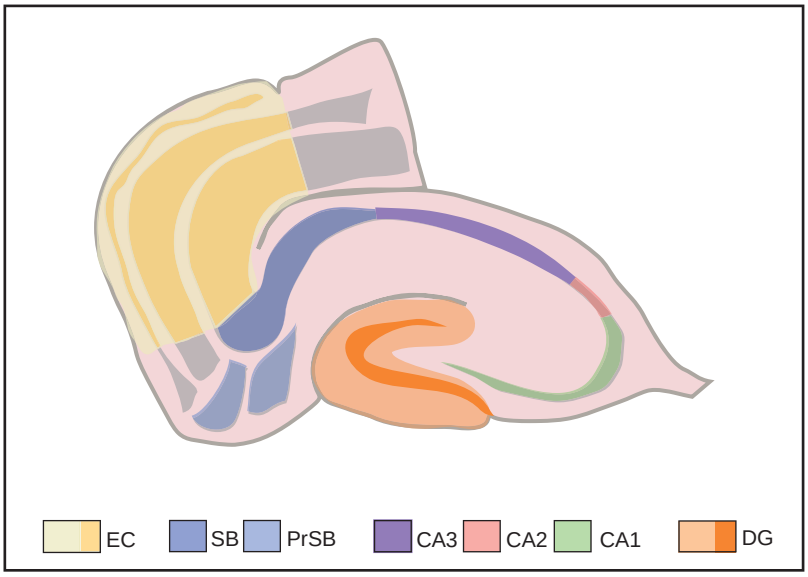
EC
SB
PrSB
CA3
CA2
CA1
DG

layer I and II. **Layer III**, with the predominant triangular-shaped pyramidal cells. They gave rise to the perforant path and alvear path to CA1 and subiculum. **Layer IV** is cell-free, most conspicuous in portions near rhinal fissure. **Layer V** has band of large, darkly stained pyramidal neurons, with large apical dendrites that ascend to layer II, and continues on to layer I. This layer also has horizontal cells and polymorphic cells. Horizontal cells have apical dendrites that project to layer I and the dendrites confined largely to layer V. The polymorphic cells are multipolar with long wavy dendrites that travel to angular bundle, and then to subiculum. In term of intrinsic fibre projections, entorhinal cortex gives origin to the perforant (layer I to *sm*) and alvear pathways (EC to CA1) to the hippocampus (Anderson *et al.*, 1971).

5.2 Results

5.2.1 Cytoarchitectonics of cultured entorhinal-hippocampal slices.

After 10DIV, using thionin staining, the macro- and microscopical appearance of the majority of the intact entorhino-hippocampal slice cultures retained the cytoarchitectonic organisation present when the slices were taken. During the period in culture, the slices flattened from the initial thickness of 300-350μm to approximately 100μm (noted, the 100μm measurement is estimated from a pre-measured slice and measurement was observed under stereo microscope). An average 4 out of 5 slices per experiment were suitable and a total of 10 experimental repeats were done (n=40).

For the sub-slice co-culture, at macroscopical observation, individual slices for Series A (i.e. no gap) resembled fresh intact hippocampal slices on average 4 out of

5 slices per experiment with 10 repeats (n=40). In series B (i.e. 0.5mm and 1.0mm gap), individual slices, resembled fresh intact hippocampal slices on an average 3 out of 5 slices (60%) per experiment with 5 repeats (n=15). While the hippocampal slices tend to flattened to 100μm, the entorhinal slices flattened to approximately less than 100μm, occasionally to 50μm. Thionin staining showed despite the flattening effect, microscopically, the cell body of EC slice remain morphologically intact.

For series C slices (performed in 5 repeats; total slices: 25), similar observation was obtained for HP slices, with 60% retained the cytoarchitectonic organisation present when the slices were taken (n=15). Of the 15 EC slices, average 1 out 3 slices survived the flattening, evidence on intact cell body from thionin staining (n=5). The other EC slices flattened but subsequently detached from the membrane surface after 5-6DIV.

5.2.2 Immunofluorochemistry and orthograde labelling of entorhino-hippocampal slices.

Immunochemistry of the entorhino-hippocampal intact slice after 10DIV showed that the laminar structure with the neuronal and astrocytic component was intact. The colocalisation of NeuN, a mature neuronal market with nucleus marker, 4',6-diamidino-2-phenylindole (DAPI) at the dentate gyrus (DG) region gave evidence of the integrity of the slice after 10DIV (Figure. 45). It also showed layers of approximate 6 to 8-cell thick with cells of elliptical to round cell body, densely packed alongside one another, resembling the granule cells at the *stratum granulosum* (Figure. 45 B1 ; (Li *et al.*, 1993). These layers of cells were also

Figure 45: Neuronal populations in an intact entorhino-hippocampus slice.
A, Montage of confocal images of an intact slice showing the cytoarchitectonic structure and integrity of the neuron populations, evidence in the immunoreactivity to NeuN (green), which and DAPI (blue). B1, high magnification of the dentate gyrus (DG) structure in A, showing layers of approximate 6 to 8-cell thick with cells at the *stratum granulosum*, which is also calbindin positive (B2, from a different slice). C1, high magnification of the entorhinal cortex (EC) structure in A, showing two major multilaminar layer of cells, visibly separated by an acellular layer. C2, only cells at the most superficial layer of the outer multilaminar was positive for calbindin. Scale bar, A, 200μm, B-C 100μm.

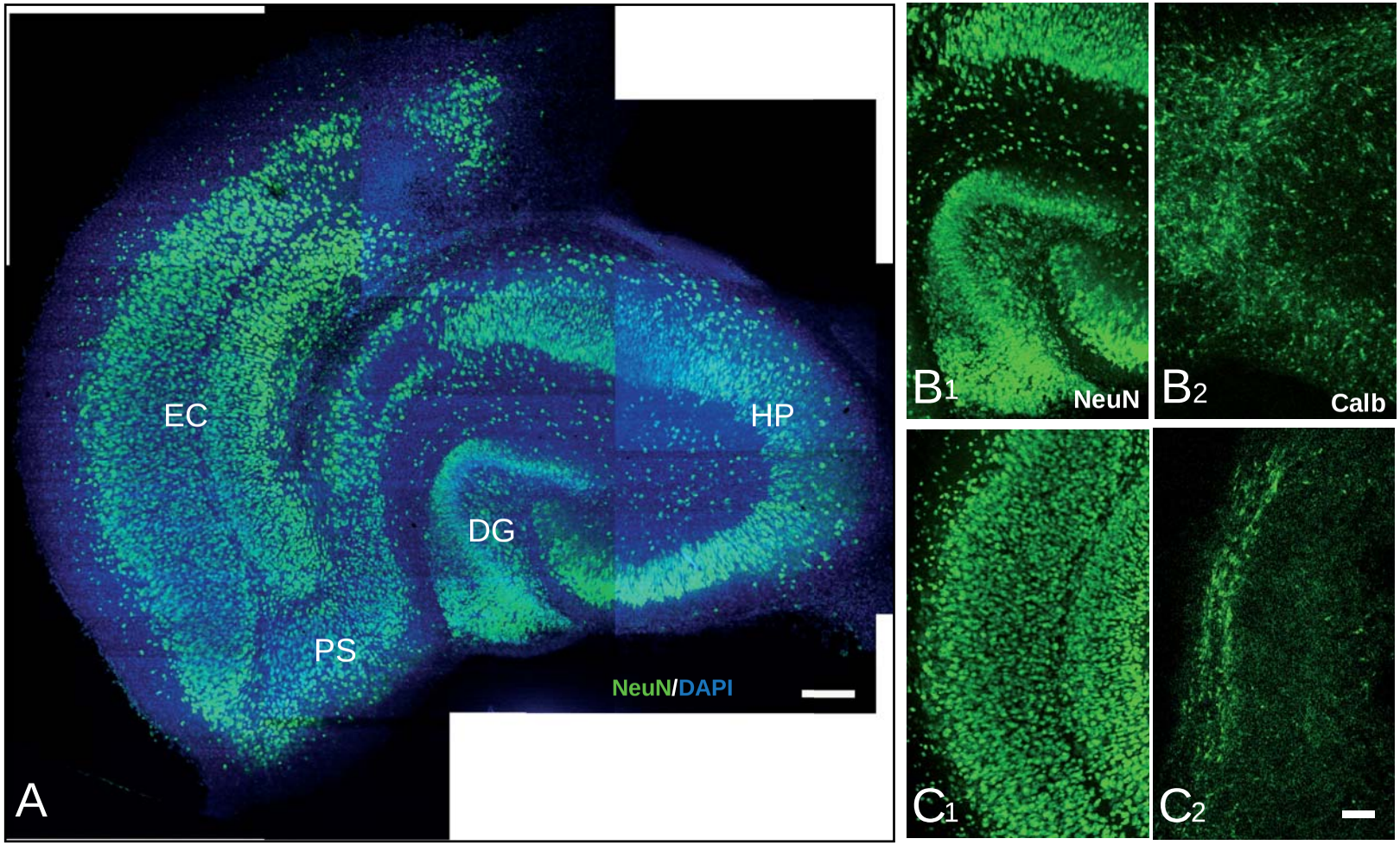
EC
HP
DG
PS
NeuN/DAPI
A
B1
NeuN
B2
Calb
C1
C2

calbindin+ (colocalized with the banded DAPI+ cells) (Figure. 45 B1 and B2). At the entorhinal cortex (EC) region of the intact hippocampus, immunochemistry with NeuN and DAPI showed two major multilaminar layer of loosely packed cells (relative to DG), visibly separated by an acellular layer (Figure. 45 A and C1). Only cells at the most superficial layer of the outer multilaminar was positive for calbindin (Figure. 45 B2).

Orthograde biocytin tracing and neurofilament (NF) immunostaining was used to identify axonal projections (Figure. 46). NF showed the intrinsic connection in laminar pathway throughout the intact slice, specifically, in the current context, the connection from the EC layer II to the outer DG *stratum moleculare* (Figure. 46B). A further group of EC-DG projection fibres was labelled by the orthograde biocytin staining (Figure. 46A). Most likely explanation is different fibre diameter spectrum.

At the macroscopical level, GFAP immunochemistry showed the extensive web-like astrocytic laminar structure, complementary with the cytoarchitecture of the NeuN+ neurons, as in the hippocampal formation *in situ*. In DG, the GFAP+ cells have stellar projection of processes, while in the CA1 to CA3 region, they were bipolar, and organized radially along the entire region (Figure. 47, label b and s). Separating the CA1 from the DG region, GFAP+ cells were predominantly bipolar, organised perpendicularly in a crescent laminar. Deep in the EC layer, the GFAP+ cells adopted the stellar shaped with multi processes projection radially. In the superficial layer of EC region, organisation of predominantly bipolar GFAP+ cells resembled those in the CA1-3 regions of the hippocampus (Figure. 47).

Figure 46: Axonal projections in an intact entorhino-hippocampus slice.
A, Montage of confocal images of an intact slice showing the axonal projections, evidence in the immunoreactivity (red) to a crystal of biocytin placed on the EC (asterisk). B Montage of confocal images of an intact slice showing the dual staining of the axonal projections with biocytin (green) and neurofilament (NF; red) in the molecular layer (sm) of the DG. Note, although NF immunoreactivity and orthograde biocytin tracing were used to identify various fibre projections, there was no evidence of co-localization of the two markers on the axonal processes at EC projection *en route* to DG. Scale bar, 200μm.

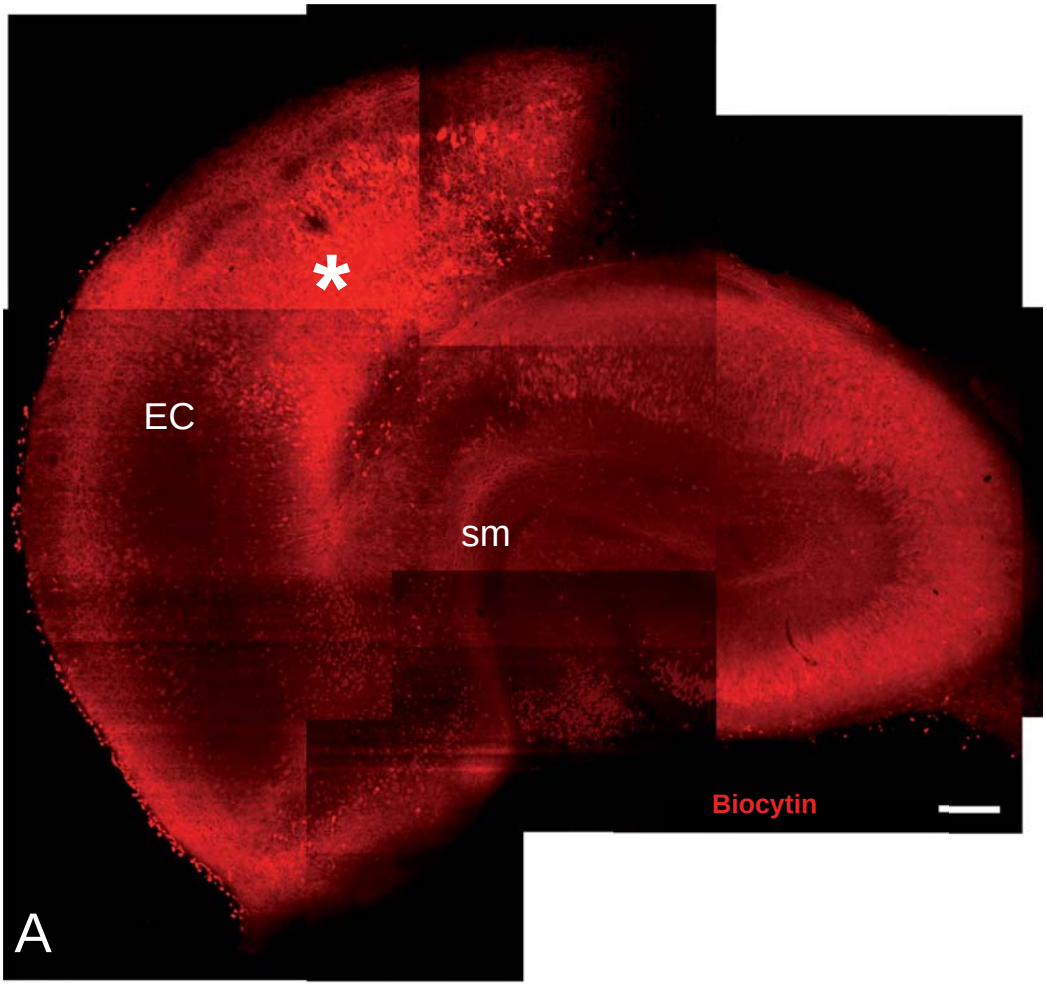
*
EC
sm
Biocytin
A

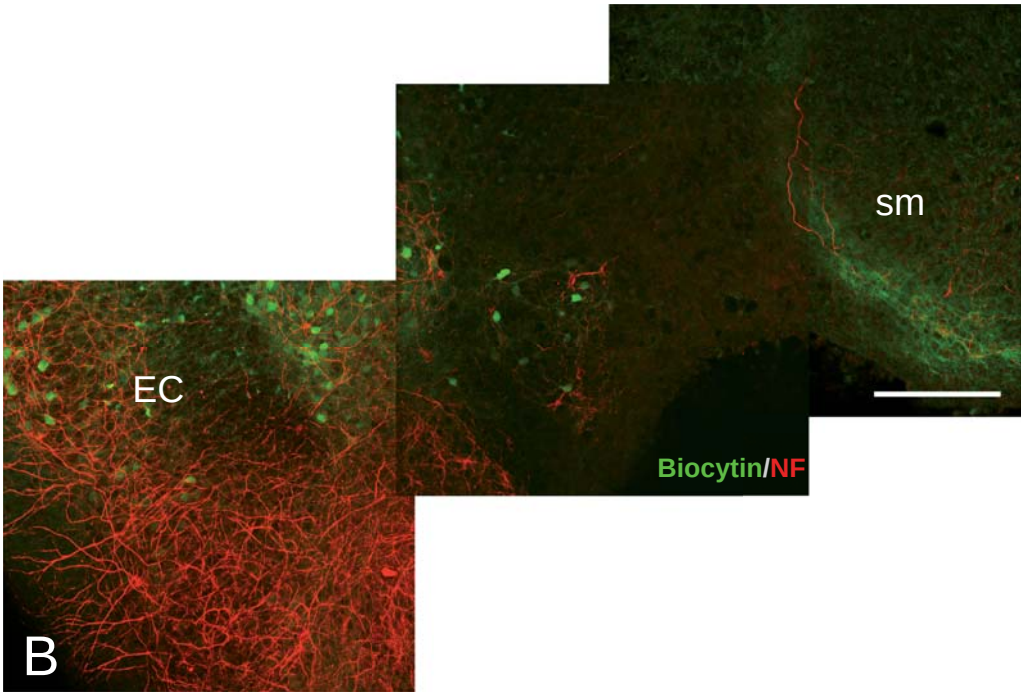
sm
EC
Biocytin/NF
B

Figure 47: Montage of astrocytic populations in control slices.
A, Confocal images of the GFAP immunoreactivity in an intact entorhino-hippocampus slice, showing an organization of the uniform morphologies ranges from bipolar (b) to stellate (s) according to the regions. B, montage of confocal images of GFAP immunoreactivity in a control Series A slice, *p* position (B), where sub-slices were co-cultured without any separation between the EC and the HP. White arrow, showing elevated GFAP expression at the interface region. Scale bar, 200μm.

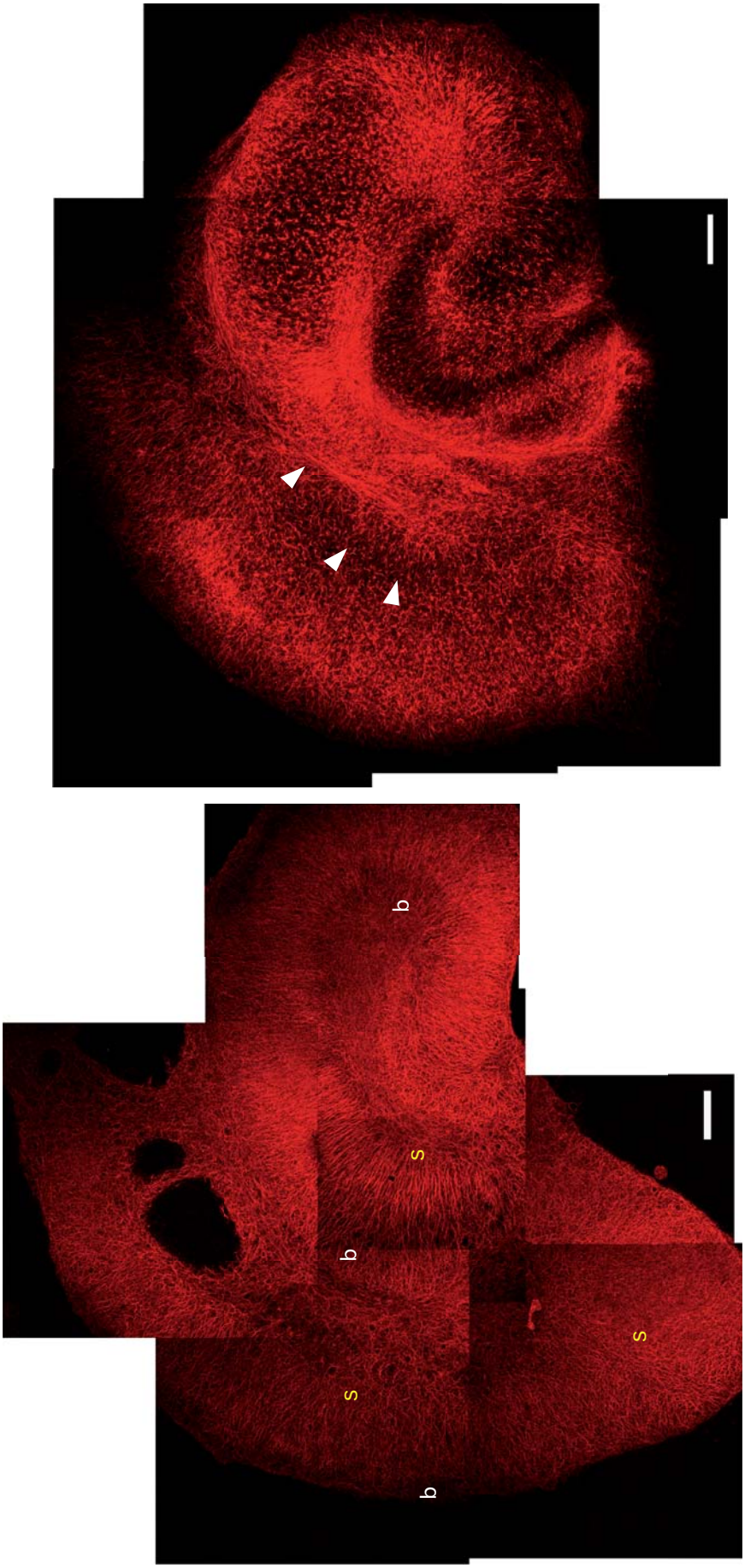
b
s
b
s
s
b

In control series A where sub-slices were co-cultured without any separation between the EC and the hippocampus (HP), immunofluorochemistry using similar markers showed that the NeuN+ neurons survived and the cytoarchitecture was maintained in both orientations (*p*, EC caudal to DG; *q*, EC ventral to DG). NF immunoreactivity at junction between the separated EC and HP showed fibres projecting across both sub-slices on the *p* spatial orientation but not in *q* orientation (Figure. 48). In *p* orientation, orthograde biocytin, injected in the EC sub-slice (calbindin+ at superficial cellular layer) on 8DIV labelled fibres crossing into the calbindin+ DG region (*sg*) after 10DIV (Figure. 48). GFAP immunoreactivity showed elevated expression co-localised with densely packed DAPI+cells (data not shown) at the axotomized interfaces of the sub-slices. (Figure. 47B)

With the introduction of 0.5mm (both *p* and *q* orientation) and 1.0mm separations (only *q*) at series B, NeuN and GFAP immunoreactivity showed the maintenance of the cytoarchitecture of the neurons and astrocytes within the sub-slices (Figure. 49 B1 and C1). Between the DG and HP sub-slices, GFAP immunoreactivity showed the outgrowth of astrocytes from both sides, completely bridging the physical gap (Figure. 49 C1). While there is no evidence of NeuN+ neuronal cell bodies on the newly formed astrocytic bridge, orthograde biocytin tracing and NF labelling confirmed that reconnection of nerve fibres has occurred across the gap (Figure. 49 B and C2).

With further distance increase of the gap between the HP and the EC to 2.0mm (Series C), NeuN immunostaining showed a loss of neurons in 20/25 EC slices, in the 5/25 cases with surviving EC, astrocytes continued to migrate from both the EC

Figure 48: Characterisation of fibre projections of the control Series A cut slice.

A, schematic illustration of the sub-slices of EC and HP confronted at two orientations (see text): p (A1) and q (A2). B, confocal images of the biocytin and NF immunoreactivity showing fibres crossing the junctional interface between EC and HP at *p* orientation. C, confocal images of the NeuN and NF immunoreactivity at junctional interface between EC and HP at *q* orientation. Scans through the depth of the slice show there are no NF-positive fibres projecting across both sub-slices in *q* orientation. Scale bar, 200μm.

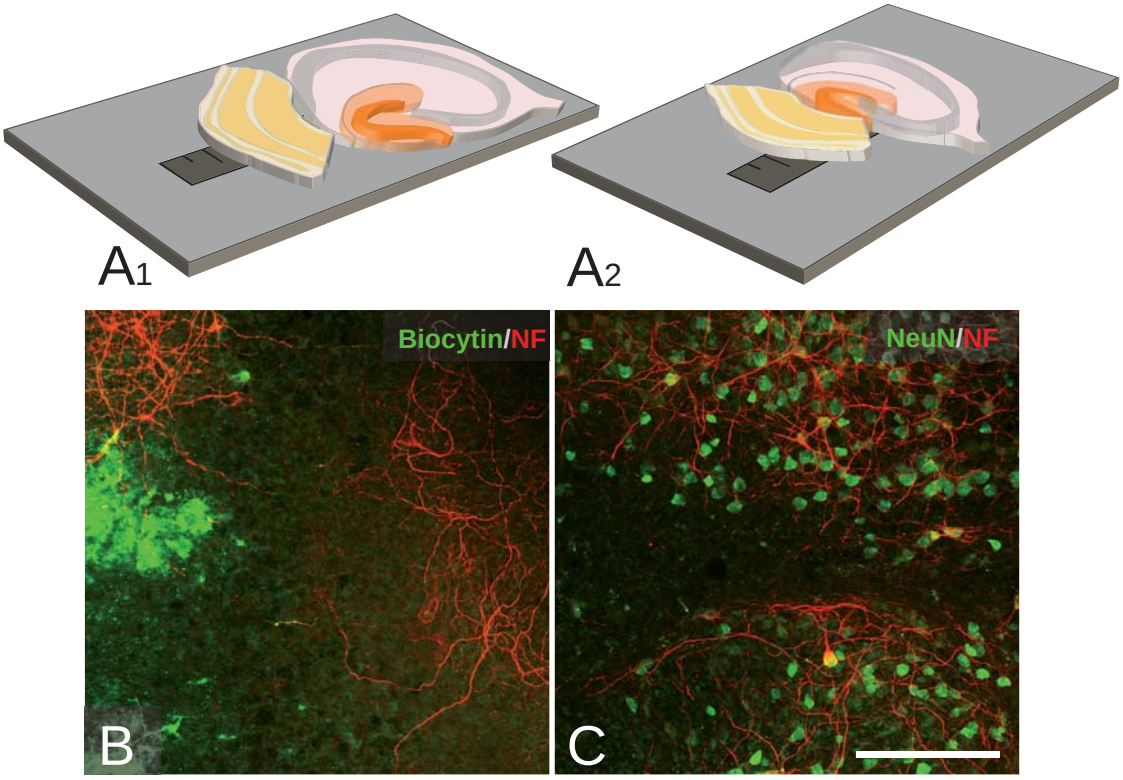
A1
A2
Biocytin/NF
NeuN/NF
B
C

Figure 49: Sub-slices with 0.5 and 1.0mm separation.
A, schematic illustration of the sub-slices of EC and HP separated at a distance (i.e. 0.5mm or 1.0mm) at two orientation: p (A1) and q(A2). B, montage of the NF-positive projections across the 0.5mm gap (*p* orientation) with the integrity of the sub-slices (NeuN-positive). C, montages of confocal images of sub-slices separated at the *q* orientation, bridged by the GFAP-positive astrocytic (red) populations (C1) with fibre projections traced by biocytin crystals placed on the EC sub-slice at 1.0mm gap (C2). Scale bar, 200μm.

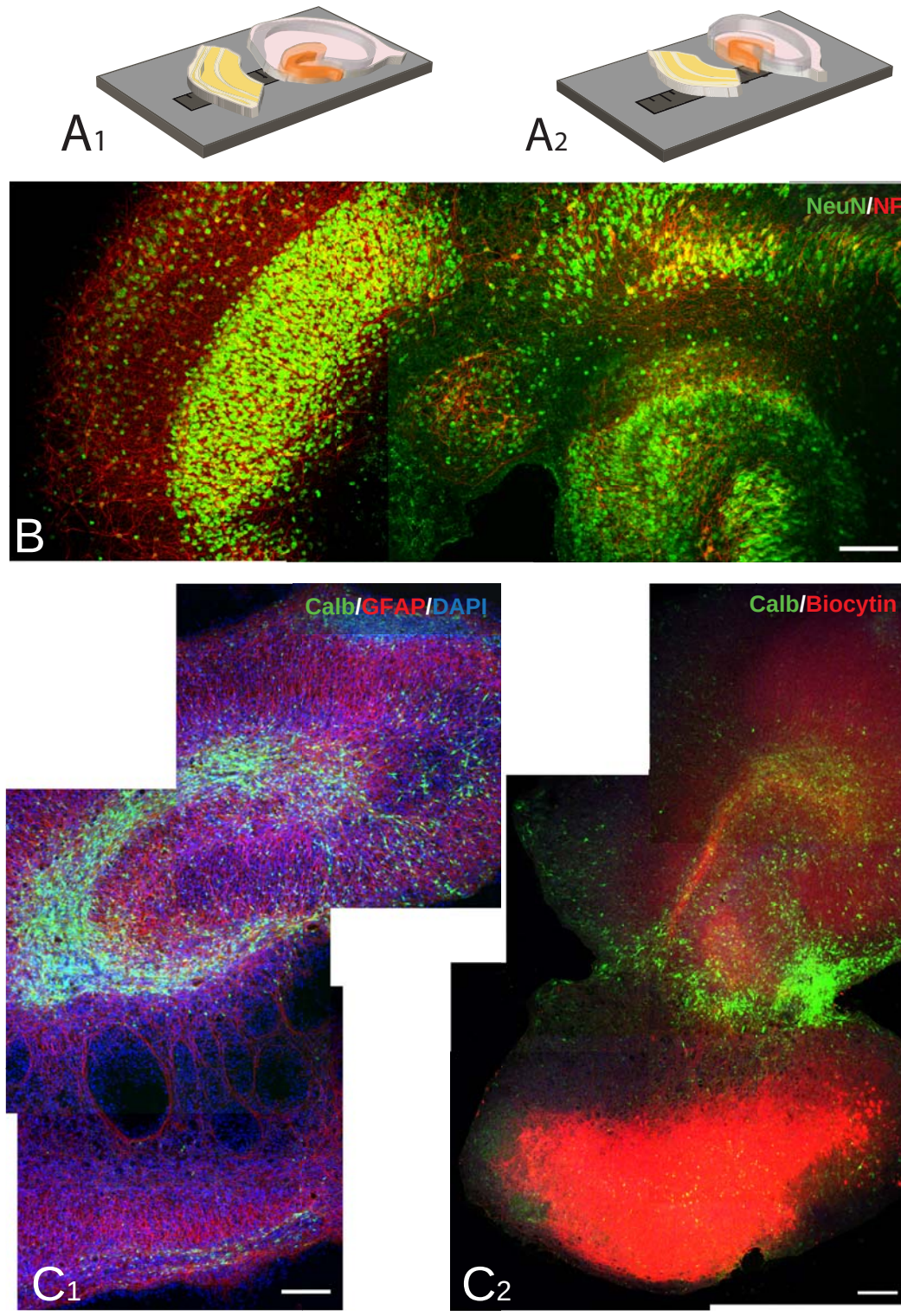
A1
A2
NeuN/NF
B
Calb/GFAP/DAPI
Calb/Biocytin
C1
C2

and HP slices but failed to form a complete bridge (Figure. 50A). Orthograde biocytin tracing showed regenerating EC fibres co-extensive with the astrocytic outgrowth but they did not reach the DG (Figure. 50A).

5.2.3 Introduction of nanocomposite nanofibre mesh into the gap between co-cultures

Co-cultures with 2mm separation (Series C) were plated with pieces of electrospun nanocomposite nanofibre mesh cut to 2x4-5mm introduced across the gap. The introduction of the mesh maintained the integrity of the EC tissue on average 2 out of 3 slices (66%, n=6/9 (3 repeats) for each orientation) based on the NeuN and DAPI staining. Calbindin+ cells from DG and GFAP+ astrocytes from both sides infiltrated for up to 1.0mm in the mesh although not completely crossing the gap (Figure. 50 B1). Along the full width of the DG ventral blade an infiltration of calbindin staining extends for up to about 0.5mm into the mesh. Astrocytic staining (GFAP) extends from both the DG and EC surfaces, a few cells seem to form a continuous bridge across the mesh filling the gap between the co-cultures (Figure. 50 B1). On through depth focusing these astrocytes are seen to be travelling over the surface of the mesh. Evidence of only a few biocytin labelled axons that colocalize with calbindin positive cell bodies could be traced across the mesh in either *p* or *q* orientations (Figure. 51).

Figure 50: Sub-slices with 2.0mm separation with response to the introduction of a nanofibre mesh.
A, confocal image of biocytin positive fibre projections from sub-slice EC, separated at a distance of 2.0mm, failed to reach the sub-slice HP. B, montage of confocal images of a series C sub-slices with 2.0 x 5.0mm nanofibre mesh as a scaffold (sca) in place of the 2.0mm gap, with the infiltration of the GFAP-positive astrocytic population (B1, red) along with both calbindin-positive neurons (B2, green). Scale bar, 200μm.

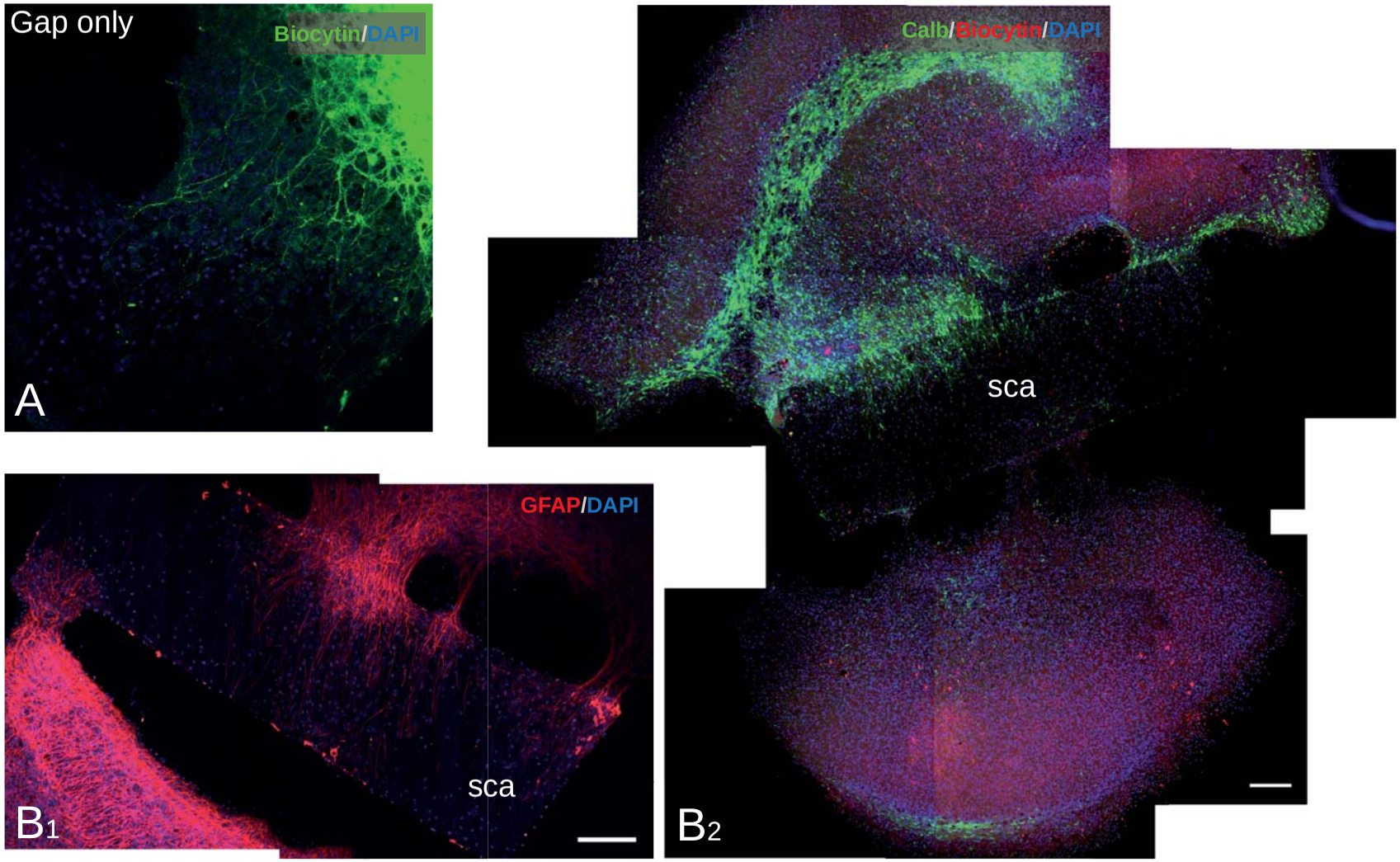
Gap only
Biocytin/DAPI
A
Calb/Biocytin/DAPI
sca
GFAP/DAPI
sca
B1
B2

Figure 51: Characterisation of neuronal population and traced fibres projections at the junction of sub-slices and scaffold.

A, high magnification of the montage in Figure 50 of the calbindin-positive neurons projecting biocytin-positive fibres into the scaffold. White arrowheads, cell body of the neurons and pink arrowheads, the corresponding fibre projections. Dotted line, interface of sub-slices and scaffold. sca, Scaffold. Scale bar, 200μm.

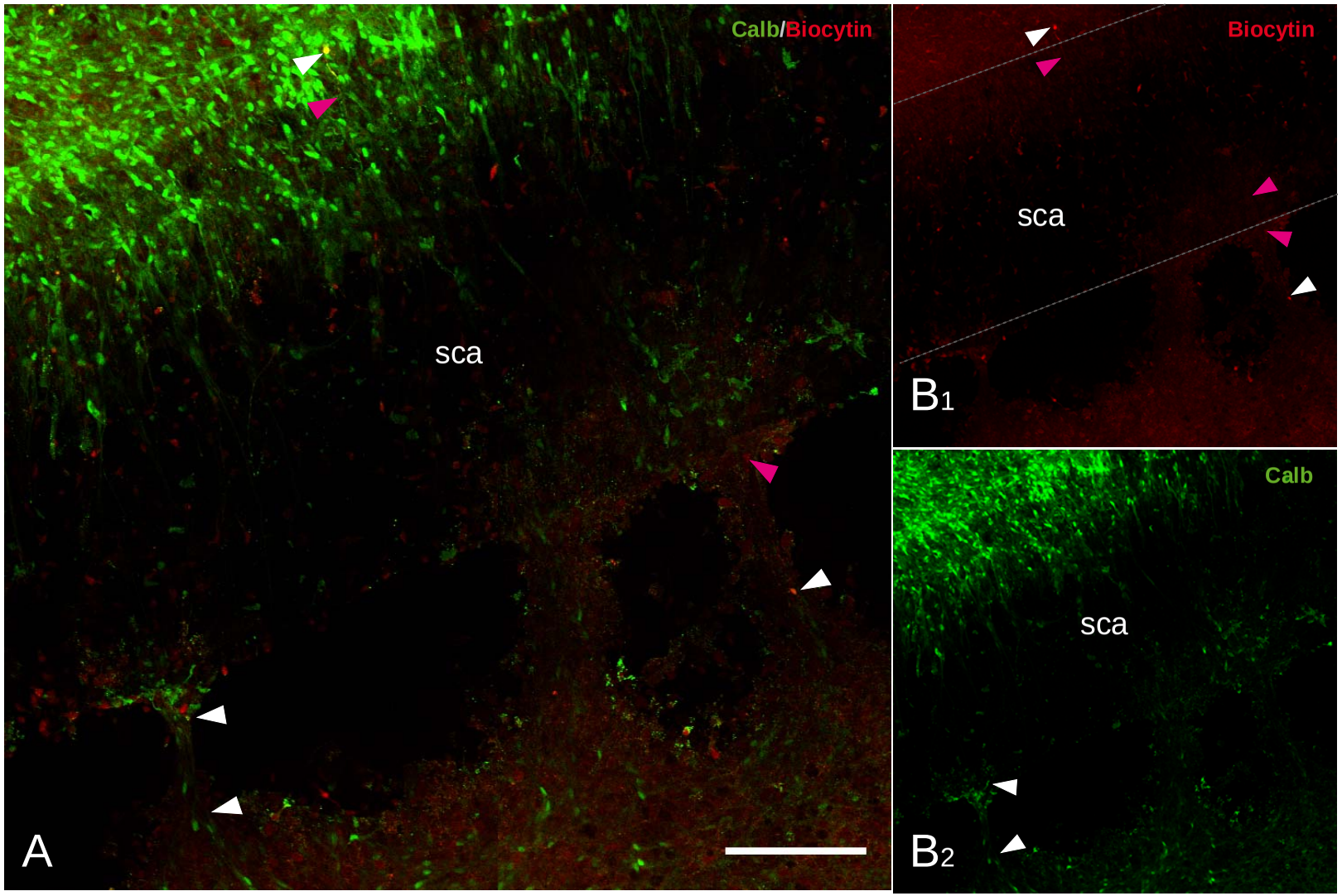
Calb/Biocytin
sca
A
Biocytin
sca
B1
Calb
sca
B2

5.3 Discussion

The objective of these preliminary functional studies on entorhino-hippocampal organotypic slice culture was 1) to establish the spatial arrangement and the appropriate distance of separation between the sub-slices that were known to have an origin-to-target connection, and 2) to test the biocompatibility of nanocomposite nanofibre, electrospun from the PLGA in the established assay. The organotypic slice co-culture paradigm provides a model of the failure of axon growth invoked by distance, and is a surrogate for the concept of pathway hypothesis where loss of pathway is centred in developing repair for spinal cord injury. The physical distance imposed resembled the lesion gap, often seen in spinal injury in rat experimental *in vivo* model such as corticospinal tract, hemisection model. The neuron-to-target of the EC and DG tissue mimicked the directionality of surviving axons for any functional reconnection. The assay also consisted of the glia components that are also present in the *in vivo* model. The purpose of this system was not to investigate the induction of fibre growth in an adult system such as the corticospinal tract, but by selecting this experimental developmental system in which fibres regenerate I was able to look at the interaction of growing fibres with the nanocomposite nanofibre PLGA scaffolds.

The preliminary observations of the different gap widths introduced between neuron source and its target were able to determine the distance needed for failure of regeneration. Figure. 49 C1 showed that an astrocytic bridge (GFAP immunocytochemistry) was present in the co-cultures in which nerve fibres grew between the slices (Li *et al.*, 1996; Sobkowicz *et al.*, 2006; Law *et al.*, 2010).

Using GFAP, it was evident that the astrocytes in the present entorhino-hippocampal slice co-cultures adopted a variety of morphological patterns. Despite the classical evidence for clear localised differences in astrocytic morphology (Cajal, 1911) the functional significance of these variations is only now coming under serious scrutiny (Zhang & Barres, 2010). While in my present preliminary co-culture observations I am not able to ascribe functional differences to the varying astrocytic morphological species, a study of cultured astrocytes has shown the differential role of these astrocytic morphological species in promoting neurite growth and migration (Denis-Donini *et al.*, 1984; Cavalcante *et al.*, 1996; Hirsch & Bähr, 1999).

The nanofibre bridge (fabricated based on technology described in Chapter 4), even without OECs (Figure. 50 and 51), enabled the separated slices to establish biological interactions between hippocampal and entorhinal organotypic slices across a 2.0mm gap. This shows that the nanocomposite electrospun nanofibre mesh is compatible with CNS tissue and it provides medium enabling tissues to interact with each other across gaps which would otherwise prevent interaction.

The observations did not amount to a reconstruction of the neural pathways which occur in slices interacting across direct contact. However, the migration of GFAP+ astrocytes from the juxtapositional sides of both EC and HP (i.e. the side closest to each other) raises the encouraging possibility that the nanofibres might have a similar effect perhaps 'opening' astrocytic scars in tissue lesions *in vivo*. The outgrowth of calbindin positive axons from the hippocampal side (Figure. 50) gives us our first indication that nerve fibres can also respond by growth on to the nanofibre mesh.

The bridging effects of the nanofibre mesh showed the biocompatibility of this material. Its effects on fibre projectors are limited, and this provides a highly encouraging platform to enhance them further by future experiments incorporating OEC/ONFs into the mesh. This *in vitro* system gives the first indication of how transplantation prosthesis of OEC bearing nanofibres may eventually be employed *in vivo.*

Previous attempts in this laboratory to introduce OECs (without nanofibres) as cellular bridges between slice co-cultures, led to massive overgrowth of the OECs and disorganization of the structure (personal communication from Dr Daqing Li: "*When OECs were placed in between the severed white matter structure in organotypic culture they glued the two cut ends together. However, they aggregated at the joining point and formed an OEC-rich cluster which pulled the joined tissue towards it and caused disorganization of the structure. A small number of OECs elongated into the host tissue from the cluster but never left it*.") Future investigations adding OECs to the bridge mesh may prevent this problem, and will indicate whether the inclusion of OECs in the mesh will lead to further improvements in forming a bridge for regenerating axons.

Chapter 6 Concluding Remarks

Olfactory ensheathing cells have become established as one of the promising cell types for transplantation in spinal cord injury. The potential for clinical translation has focused attention on research into reliable cell sources and the cell biology of these OEC, specifically the interplay of the cell behaviour governed by their microenvironment.

In the field of tissue engineering, the desire to create a biomimicry system, a current mandate, is met with the development of new and/or modification of existing materials and microengineering systems at the nano-scale. Electrospinning has so far known as the superior technique in producing fibres at nano-scale and laser microfabrication in producing macroarchitecture structure for bulk design. The interplay between the understanding of OEC cellular behaviour and designing an artificial microenvironment using systems such as electrospinning is essential in developing scaffolds that facilitate tissue regeneration.

The current project has attempted to implement both area of research in unison to study the translational ability of the appropriate adult olfactory ensheathing cells on electrospun nanofibres, in the long term goal of designing a functional neural prosthesis.

The presence of an unexpected highly proliferative p75+ population in the stripped mucosal epithelium presents this accessible tissue as an attractive new candidate to

increase the limited numbers of OECs. These purified OECs that elongated on a nano-scale fibre mesh are comparable to that which occurs in *in vivo* transplants when the transplanted OEC convey regenerating fibres across small lesions. Together with the biocompatibility of these nanocomposite nanofibres in the organotypic slice co-culture assay, these combinatory preliminary studies lay groundwork for future possibilities.

6.1 Summary of novel academic findings

The present thesis presents first description of novel academic findings, listed as following:

1) A systematical study that quantitatively characterise the relative proportions of the OEC, ONF and previously yet to be described (p75-Thy1-) populations in culture of all the olfactory tissue derivatives.

2) The discovery of the double positive p75+Thy1+ population after 10DIV in only whole mucosal tissue. This population was highly proliferative and showed significant in the increasing of the OEC cell numbers. Previous immunocytochemistry technique and digital imaging analysis was not able to discern this unique population in the olfactory mucosa.

3) The uncharacteristised highly proliferative p75+ cell population in the stripped epithelial tissue from the olfactory mucosa. Simultaneous bivariate cell cycle analysis showed the resemblance of its cycling activity to that of neural and embryonic stem cells. Previous olfactory stem cell studies were

able to illustrate the presence of p75+ differentiated cells or highly proliferative stem cells from mucosal tissue.

4) A novel multiplex flow cytometric technique, named simultaneous antigenic bivariate cell proliferation assay (See Section 2.4) to identify and quantify the individual cell cycle phase (G1/0, S or G2) of specific populations within a heterogeneous population of cells (consisting of p75+Thy1- , p75+Thy1+ , p75-Thy1- or p75- Thy1+) all at once. It was developed by combining the two classical flow cytometric assays, which is antigenic assay and bivariate cell cycle assay which commonly used BrdU. This multiplex technique in this study showed 4-color analysis (2 on cell cycle analysis and 2 on antigenic analysis), although this technique is robust to include more antigenic analysis, provided that wavelength spectrum of all colours are taken in account for spectrum overlap.

5) A unique combinatorial technique of microfabrications, used to design and construct a clinical relevant neural scaffold, which took into consideration the feasibility of the fabricated fiber mesh used for cell culture (e.g the complementary groove-ridge fit *membrane insert* system) and subsequent potential for use in neurosurgery.

6) The unidirectionality and bipolarity of purified OECs when cultured on mesh of PLGA electrospun nanofibres of estimated 250nm.

7) A novel *in vitro* 3D organotypic tissue culture model of axonal failure. Using entorhino-hippocampus sub-slices, co-culture of the source and target slices were cultured with a calculated distance of separation to induce both astrocytic and neuronal failure.

6.2 Possibilities for future work

This thesis provided the background information needed to produce a prosthesis consisting of nanofibres coated with OECs. In further development for chronic spinal cord injuries, this prosthesis could be use to bridge the gap where there is physical discontinuity and separation between the proximal and distal ends of the spinal cord. This approach has the potential for advancing from the current clinical technique of multiple sites of suspension injection, which cannot obtain or deliver sufficient numbers of cells to bridge the gap or ensure their alignment to form a pathway for regenerating axons.

The next stages, in practical terms, predicted by this work are:

1. To compare the behaviour of ONFs and the mixed cultures of OEC and ONFs. The preliminary evidence of ONF weaving superficially among the uppermost nanofibres in Figure. 42, has showed the striking contrast of cellular interaction with nanofibres between OEC and ONF. Based on the histological arrangements seen in transplant situations described in this laboratory (Li *et al.*, 1998, 2003*b*), it is hypothesized that spontaneous lamination of OECs and ONFs would be the ideal situation for regenerating fibres to cross the lesion.

2. To evaluate the proposed prostheses in *in vivo* CNS models. The organotypic culture assay has established the biocompatibility of the nanocomposite fibre mesh with entorhino-hippocampus slice, a surrogate of CNS tissue *in vivo*. The initial *in vivo* model proposed is the column assay, initially described in this laboratory (Brook *et al.*, 2001). This model enables the screening of tissue responses such as inflammation, vascularisation, and ingrowths of endogenous glia and axons. A later testing of an OEC/nanofibre prosthesis should involve an established *in vivo* spinal cord lesion model (such as Li et al. 1998) which examines both anatomical re-connection and functional restoration.

Ideally a prosthesis would 1) allow reparative OEC cells to be spread thinly and orientate their alignment in the best configuration that would provide a pathway for the regeneration of endogenous nerve fibres across the prosthesis, 2) be porous enough to provide physical attachment for the invading endothelium cells to vascularise the transplant in the lesion site, 3) allow transplanted OECs to come into close proximity with the reactive astrocytes at the glial scar in order to form a continuous cellular substrate for surviving fibres to grow across.

The anticipated use of on olfactory ensheathing cell / nanofibre prosthesis would be in the application of autologous human olfactory ensheathing cells for bridging the gap in spinal cord lesions.

Appendix Letter from Publisher

From: Jones, Jennifer (ELS-OXF)
To: Kueh, Jacqueline
Subject: RE: Obtain Permission
Date: 22 August 2011 16:53:16
Attachments: ole0.bmp
ole1.bmp

Dear J Kueh

We hereby grant you permission to reprint the material detailed below at no charge **in your thesis** subject to the following conditions:

1. If any part of the material to be used (for example, figures) has appeared in our publication with credit or acknowledgement to another source, permission must also be sought from that source. If such permission is not obtained then that material may not be included in your publication/copies.

2. Suitable acknowledgment to the source must be made, either as a footnote or in a reference list at the end of your publication, as follows:

> "This article was published in Publication title, Vol number, Author(s), Title of article, Page Nos, Copyright Elsevier (or appropriate Society name) (Year)."

3. Your thesis may be submitted to your institution in either print or electronic form.

4. Reproduction of this material is confined to the purpose for which permission is hereby given.

5. This permission is granted for non-exclusive world **English** rights only. For other languages please reapply separately for each one required. Permission excludes use in an electronic form other than submission. Should you have a specific electronic project in mind please reapply for permission

6. Should your thesis be published commercially, please reapply for permission.

Yours sincerely

Jennifer Jones
Rights Associate

Bibliography

Aguayo AJ, Rasminsky M, Bray GM, Carbonetto S, McKerracher L, Villegas-Pérez MP, Vidal-Sanz M & Carter DA (1991). Degenerative and regenerative responses of injured neurons in the central nervous system of adult mammals. *Philos Trans R Soc Lond, B, Biol Sci* **331,** 337–343.

Åkerman ME, Chan WCW, Laakkonen P, Bhatia SN & Ruoslahti E (2002). Nanocrystal targeting in vivo. *Proceedings of the National Academy of Sciences of the United States of America* **99,** 12617–12621.

Andersen P (2007). *The hippocampus book*. Oxford University Press.

Anderson JM & Shive MS (1997). Biodegradation and biocompatibility of PLA and PLGA microspheres. *Advanced Drug Delivery Reviews* **28,** 5–24.

Anderson KD (2004). Targeting Recovery: Priorities of the Spinal Cord-Injured Population. *Journal of Neurotrauma* **21,** 1371–1383.

Anderson P, Bliss TV & Skrede KK (1971). Lamellar organization of hippocampal pathways. *Exp Brain Res* **13,** 222–238.

Aoki M, Kishima H, Yoshimura K, Ishihara M, Ueno M, Hata K, Yamashita T, Iwatsuki K & Yoshimine T (2010). Limited functional recovery in rats with complete spinal cord injury after transplantation of whole-layer olfactory mucosa. *J Neurosurg Spine* **12,** 122–130.

Au E, Richter MW, Vincent AJ, Tetzlaff W, Aebersold R, Sage EH & Roskams AJ (2007). SPARC from olfactory ensheathing cells stimulates Schwann cells to promote neurite outgrowth and enhances spinal cord repair. *Journal of Neuroscience* **27,** 7208.

Au E & Roskams AJ (2002). Culturing olfactory ensheathing glia from the mouse olfactory epithelium. *Methods in molecular biology (Clifton, NJ)* **198,** 49–54.

Au E & Roskams AJ (2003). Olfactory ensheathing cells of the lamina propria in vivo and in vitro. *Glia* **41,** 224–236.

Audisio C, Raimondo S, Nicolino S, Gambarotta G, Di Scipio F, Macrì L, Montarolo F, Giacobini-Robecchi MG, Porporato P, Filigheddu N, Graziani A, Geuna S & Perroteau I (2009). Morphological and biomolecular characterization of the neonatal olfactory bulb ensheathing cell line. *J Neurosci Methods* **185,** 89–98.

Babensee JE, McIntire LV & Mikos AG (2000). Growth Factor Delivery for Tissue Engineering. *Pharmaceutical Research* **17,** 497–504.

Baiguera S, Del Gaudio C, Fioravanzo L, Bianco A, Grigioni M & Folin M (2010). In vitro astrocyte and cerebral endothelial cell response to electrospun poly (ε-caprolactone) mats of different architecture. *Journal of Materials Science: Materials in Medicine* **21,** 1353–1362.

Baker SC, Atkin N, Gunning PA, Granville N, Wilson K, Wilson D & Southgate J (2006). Characterisation of electrospun polystyrene scaffolds for three-dimensional in vitro biological studies. *Biomaterials* **27,** 3136–3146.

Bareyre FM, Kerschensteiner M, Raineteau O, Mettenleiter TC, Weinmann O & Schwab ME (2004). The injured spinal cord spontaneously forms a new intraspinal circuit in adult rats. *Nat Neurosci* **7,** 269–277.

Barnett SC, Alexander CL, Iwashita Y, Gilson JM, Crowther J, Clark L, Dunn LT, Papanastassiou V, Kennedy PG & Franklin RJ (2000). Identification of a human olfactory ensheathing cell that can effect transplant-mediated remyelination of demyelinated CNS axons. *Brain* **123 (Pt 8),** 1581–1588.

Barnett SC & Chang L (2004). Olfactory ensheathing cells and CNS repair: going solo or in need of a friend? *Trends Neurosci* **27,** 54–60.

Barnett SC, Hutchins AM & Noble M (1993). Purification of olfactory nerve ensheathing cells from the olfactory bulb. *Dev Biol* **155,** 337–350.

Barnett SC & Roskams AJ (2008). Olfactory ensheathing cells: isolation and culture from the neonatal olfactory bulb. *Methods Mol Biol* **438,** 85–94.

Benfey M, Bünger UR, Vidal-Sanz M, Bray GM & Aguayo AJ (1985). Axonal regeneration from GABAergic neurons in the adult rat thalamus. *J Neurocytol* **14,** 279–296.

Bettinger CJ, Orrick B, Misra A, Langer R & Borenstein JT (2006). Microfabrication of poly (glycerol-sebacate) for contact guidance applications. *Biomaterials* **27,** 2558–2565.

Bhardwaj N & Kundu SC (2011). Electrospinning: A fascinating fiber fabrication technique. *Biotechnology Advances* **28,** 325–347.

Bhatia SN, Balis UJ, Yarmush ML & Toner M (1999). Effect of cell-cell interactions in preservation of cellular phenotype: cocultivation of hepatocytes and nonparenchymal cells. *FASEB J* **13,** 1883–1900.

Bianco JI, Perry C, Harkin DG, Mackay-Sim A & Féron F (2004). Neurotrophin 3 promotes purification and proliferation of olfactory ensheathing cells from human nose. *Glia* **45,** 111–123.

Bognitzki M, Czado W, Frese T, Schaper A, Hellwig M, Steinhart M, Greiner A & Wendorff JH (2001). Nanostructured Fibers via Electrospinning. *Advanced Materials* **13,** 70–72.

Boland ED, Wnek GE, Simpson DG, Pawlowski KJ & Bowlin GL (2001). Tailoring tissue engineering scaffolds using electrostatic processing techniques: a study of poly (glycolic acid) electrospinning. *Journal of Macromolecular Science, Part A* **38,** 1231–1243.

Bonnici B & Kapfhammer JP (2008). Spontaneous regeneration of intrinsic spinal cord axons in a novel spinal cord slice culture model. *European Journal of Neuroscience* **27,** 2483–2492.

Booth BW, Mack DL, Androutsellis-Theotokis A, McKay RDG, Boulanger CA & Smith GH (2008). The mammary microenvironment alters the differentiation repertoire of neural stem cells. *Proceedings of the National Academy of Sciences* **105,** 14891 –14896.

Borenstein JT, King KR, Terai H & Vacanti JP (2002). Capillary formation in microfabricated polymer scaffolds. In *Materials Research Society Symposium - Proceedings*, pp. 163–168. Available at: http://www.scopus.com/inward/record.url?eid=2-s2.0-0036346087&partnerID=40&md5=0d134839faadb1f49c1af2a725ceb0da [Accessed September 1, 2010].

Boyd JG, Lee J, Skihar V, Doucette R & Kawaja MD (2004). LacZ-expressing olfactory ensheathing cells do not associate with myelinated axons after implantation into the compressed spinal cord. *Proc Natl Acad Sci USA* **101,** 2162–2166.

Boyd JG, Skihar V, Kawaja M & Doucette R (2003). Olfactory ensheathing cells: historical perspective and therapeutic potential. *Anat Rec B New Anat* **271,** 49–60.

Bray D, Wood P & Bunge RP (1980). Selective fasciculation of nerve fibres in culture. *Experimental Cell Research* **130,** 241–250.

Bretzner F, Liu J, Currie E, Roskams AJ & Tetzlaff W (2008). Undesired effects of a combinatorial treatment for spinal cord injury - transplantation of olfactory ensheathing cells and BDNF infusion to the red nucleus. *European Journal of Neuroscience* **28,** 1795–1807.

Brook GA, Lawrence JM & Raisman G (2001). Columns of Schwann cells extruded into the CNS induce in-growth of astrocytes to form organized new glial pathways. *Glia* **33,** 118–130.

Brylev LV (2009). Proteinase inhibitors in the cerebrospinal fluid in neurological diseases. *Neurochem J* **3,** 214–220.

Bunge MB, Bunge RP, Peterson ER & Murray MR (1967). A light and electron microscope study of long-term organized cultures of rat dorsal root ganglia. *J Cell Biol* **32,** 439–466.

Burdick JA, Ward M, Liang E, Young MJ & Langer R (2006). Stimulation of neurite outgrowth by neurotrophins delivered from degradable hydrogels. *Biomaterials* **27,** 452–459.

Burger SR (2003). Current regulatory issues in cell and tissue therapy. *Cytotherapy* **5,** 289–298.

Cajal R y (1911). Histologie du Système Nerveux de l'Homme et des Vertébrés. *Paris: Maloine*.

Campenot RB (1977). Local control of neurite development by nerve growth factor. *Proc Natl Acad Sci USA* **74,** 4516–4519.

Carter LA, MacDonald JL & Roskams AJ (2004). Olfactory Horizontal Basal Cells Demonstrate a Conserved Multipotent Progenitor Phenotype. *J Neurosci* **24,** 5670–5683.

Casper CL, Yamaguchi N, Kiick KL & Rabolt JF (2005). Functionalizing Electrospun Fibers with Biologically Relevant Macromolecules. *Biomacromolecules* **6,** 1998–2007.

Cavalcante LA, Garcia-Abreu J, Moura Neto V, Silva LC & Barradas PC (1996). Heterogeneity of median and lateral midbrain radial glia and astrocytes. *Rev Bras Biol* **56 Su 1 Pt 1,** 33–52.

Chan WCW, Maxwell DJ, Gao X, Bailey RE, Han M & Nie S (2002). Luminescent quantum dots for multiplexed biological detection and imaging. *Current Opinion in Biotechnology* **13,** 40–46.

Chen A, Xu XM, Kleitman N & Bunge MB (1996). Methylprednisolone administration improves axonal regeneration into Schwann cell grafts in transected adult rat thoracic spinal cord. *Experimental Neurology* **138,** 261–276.

Chen CS, Mrksich M, Huang S, Whitesides GM & Ingber DE (1997). Geometric Control of Cell Life and Death. *Science* **276,** 1425–1428.

Chen CS, Tan J & Tien J (2004). Mechanotransduction At Cell-Matrix And Cell-Cell Contacts. *Annu Rev Biomed Eng* **6,** 275–302.

Choi D, Law S, Raisman G & Li D (2008). Olfactory ensheathing cells in the nasal mucosa of the rat and human. *Br J Neurosurg* **22,** 301–302.

Chuah MI & Au C (1993). Cultures of ensheathing cells from neonatal rat olfactory bulbs. *Brain Research* **601,** 213–220.

Chuah MI, Choi-Lundberg D, Weston S, Vincent AJ, Chung RS, Vickers JC & West AK (2004). Olfactory ensheathing cells promote collateral axonal branching in the injured adult rat spinal cord. *Exp Neurol* **185,** 15–25.

Chuah MI, Hale DM & West AK (2011). Interaction of olfactory ensheathing cells with other cell types in vitro and after transplantation: glial scars and inflammation. *Exp Neurol* **229,** 46–53.

Chung T-W, Tsai Y-L, Hsieh J-H & Tsai W-J (2006). Different ratios of lactide and glycolide in PLGA - affect the surface property and protein delivery characteristics of the PLGA - microspheres with hydrophobic additives. *Journal of Microencapsulation: Micro and Nano Carriers* **23,** 15.

Crespo D, Asher RA, Lin R, Rhodes KE & Fawcett JW (2007). How does chondroitinase promote functional recovery in the damaged CNS? *Exp Neurol* **206,** 159–171.

Crowe MJ, Bresnahan JC, Shuman SL, Masters JN & Crowe MS (1997). Apoptosis and delayed degeneration after spinal cord injury in rats and monkeys. *Nat Med* **3,** 73–76.

Dalby MJ, Riehle MO, Johnstone HJH, Affrossman S & Curtis ASG (2003). Nonadhesive nanotopography: fibroblast response to poly(n-butyl methacrylate)-poly(styrene) demixed surface features. *J Biomed Mater Res A* **67,** 1025–1032.

David S & Aguayo AJ (1981). Axonal elongation into peripheral nervous system 'bridges' after central nervous system injury in adult rats. *Science* **214,** 931–933.

Delgado-Rivera R, Griffin J, Ricupero CL, Grumet M, Meiners S & Uhrich KE (2011). Microscale plasma-initiated patterning of electrospun polymer scaffolds. *Colloids and Surfaces B: Biointerfaces* **84,** 591–596.

Delorme B, Nivet E, Gaillard J, Häupl T, Ringe J, Devèze A, Magnan J, Sohier J, Khrestchatisky M, Roman FS, Charbord P, Sensebé L, Layrolle P & Féron F (2010). The human nose harbors a niche of olfactory ectomesenchymal stem cells displaying neurogenic and osteogenic properties. *Stem Cells Dev* **19,** 853–866.

Deng YB, Liu Y, Zhu WB, Bi XB, Wang YZ, Ye MH & Zhou G-Q (2008). The co-transplantation of human bone marrow stromal cells and embryo olfactory ensheathing cells as a new approach to treat spinal cord injury in a rat model. *Cytotherapy* **10,** 551–564.

Denis-Donini S, Glowinski J & Prochiantz A (1984). Glial heterogeneity may define the three-dimensional shape of mouse mesencephalic dopaminergic neurones. *Nature* **307,** 641–643.

Deumens R, Koopmans GC, Den Bakker CGJ, Maquet V, Blacher S, Honig WMM, Jérôme R, Pirard JP, Steinbusch HWM & Joosten EAJ (2004). Alignment of glial cells stimulates directional neurite growth of CNS neurons in vitro. *Neuroscience* **125,** 591–604.

Deumens R, Koopmans GC, Honig WMM, Hamers FPT, Maquet V, Jérôme R, Steinbusch HWM & Joosten EAJ (2006). Olfactory ensheathing cells, olfactory nerve fibroblasts and biomatrices to promote long-distance axon regrowth and functional recovery in the dorsally hemisected adult rat spinal cord. *Exp Neurol* **200,** 89–103.

Devon R & Doucette R (1995). Olfactory ensheathing cells do not requirel-ascorbic acid in vitro to assemble a basal lamina or to myelinate dorsal root ganglion neurites. *Brain Research* **688,** 223–229.

Doshi J & Reneker DH (1995). Electrospinning process and applications of electrospun fibers. *Journal of Electrostatics* **35,** 151–160.

Dosunmu OO, Chase GG, Kataphinan W & Reneker DH (2006). Electrospinning of polymer nanofibres from multiple jets on a porous tubular surface. *Nanotechnology* **17,** 1123–1127.

Doucette JR (1984). The glial cells in the nerve fiber layer of the rat olfactory bulb. *Anat Rec* **210,** 385–391.

Doucette JR, Kiernan JA & Flumerfelt BA (1983). The re-innervation of olfactory glomeruli following transection of primary olfactory axons in the central or peripheral nervous system. *J Anat* **137 (Pt 1),** 1–19.

Doucette R & Devon R (1994). Media that support the growth and differentiation of oligodendrocytes do not induce olfactory ensheathing cells to express a myelinating phenotype. *Glia* **10,** 296–310.

Fanselow MS & Dong H-W (2010). Are the dorsal and ventral hippocampus functionally distinct structures? *Neuron* **65,** 7–19.

Fawcett JW, Housden E, Smith-Thomas L & Meyer RL (1989). The growth of axons in three-dimensional astrocyte cultures. *Developmental Biology* **135,** 449–458.

Féron F, Mackay-Sim A, Andrieu JL, Matthaei KI, Holley A & Sicard G (1999). Stress induces neurogenesis in non-neuronal cell cultures of adult olfactory epithelium. *Neuroscience* **88,** 571–583.

Féron F, Perry C, Cochrane J, Licina P, Nowitzke A, Urquhart S, Geraghty T & Mackay-Sim A (2005). Autologous olfactory ensheathing cell transplantation in human spinal cord injury. *Brain* **128,** 2951–2960.

Féron F, Perry C, McGrath JJ & Mackay-Sim A (1998). New techniques for biopsy and culture of human olfactory epithelial neurons. *Arch Otolaryngol Head Neck Surg* **124,** 861–866.

Field P, Li Y & Raisman G (2003). Ensheathment of the olfactory nerves in the adult rat. *Journal of neurocytology* **32,** 317.

Fischer HC & Chan WC (2007). Nanotoxicity: the growing need for in vivo study. *Current Opinion in Biotechnology* **18,** 565–571.

Fogh J, Holmgren N & Ludovici P (1971). A review of cell culture contaminations. *In Vitro Cellular & Developmental Biology - Plant* **7,** 26–41.

Folch A & Toner M (2000). Microengineering Of Cellular Interactions. *Annu Rev Biomed Eng* **2,** 227–256.

Formhals A (1934). Process and Apparatus for Preparing Artificial Threads.

Fortun J, Hill CE & Bunge MB (2009). Combinatorial strategies with Schwann cell transplantation to improve repair of the injured spinal cord. *Neuroscience Letters* **456,** 124–132.

Franceschini IA & Barnett SC (1996). Low-Affinity NGF-Receptor and E-N-CAM Expression Define Two Types of Olfactory Nerve Ensheathing Cells That Share a Common Lineage. *Developmental Biology* **173,** 327–343.

Franklin RJ & Barnett SC (2000). Olfactory ensheathing cells and CNS regeneration: the sweet smell of success? *Neuron* **28,** 15–18.

Franklin RJ, Gilson JM, Franceschini IA & Barnett SC (1996). Schwann cell-like myelination following transplantation of an olfactory bulb-ensheathing cell line into areas of demyelination in the adult CNS. *Glia* **17,** 217–224.

Franssen EHP, De Bree FM, Essing AHW, Ramon-Cueto A & Verhaagen J (2008). Comparative gene expression profiling of olfactory ensheathing glia and Schwann cells indicates distinct tissue repair characteristics of olfactory ensheathing glia. *Glia* **56,** 1285–1298.

Frenot A & Chronakis IS (2003). Polymer nanofibers assembled by electrospinning. *Current Opinion in Colloid & Interface Science* **8,** 64–75.

Gale K, Kerasidis H & Wrathall JR (1985). Spinal cord contusion in the rat: behavioral analysis of functional neurologic impairment. *Exp Neurol* **88,** 123–134.

Gao X, Cui Y, Levenson RM, Chung LWK & Nie S (2004). In vivo cancer targeting and imaging with semiconductor quantum dots. *Nat Biotech* **22,** 969–976.

García-Escudero V, García-Gómez A, Gargini R, Martín-Bermejo MJ, Langa E, de Yébenes JG, Delicado A, Avila J, Moreno-Flores MT & Lim F (2010). Prevention of senescence progression in reversibly immortalized human ensheathing glia permits their survival after deimmortalization. *Mol Ther* **18,** 394–403.

García-Escudero V, Gargini R, Gallego-Hernández MT, García-Gómez A, Martín-Bermejo MJ, Simón D, Delicado A, Moreno-Flores MT, Avila J & Lim F

(2011). A neuroregenerative human ensheathing glia cell line with conditional rapid growth. *Cell Transplant* **20,** 153–166.

Geiger B, Bershadsky A, Pankov R & Yamada KM (2001). Transmembrane crosstalk between the extracellular matrix and the cytoskeleton. *Nat Rev Mol Cell Biol* **2,** 793–805.

Ghosh A, Haiss F, Sydekum E, Schneider R, Gullo M, Wyss MT, Mueggler T, Baltes C, Rudin M, Weber B & Schwab ME (2010). Rewiring of hindlimb corticospinal neurons after spinal cord injury. *Nat Neurosci* **13,** 97–104.

Gimsa U, Peter SV, Lehmann K, Bechmann I & Nitsch R (2000). Axonal damage induced by invading T cells in organotypic central nervous system tissue in vitro: involvement of microglial cells. *Brain Pathol* **10,** 365–377.

Gong Q, Bailey MS, Pixley SK, Ennis M, Liu W & Shipley MT (1994). Localization and regulation of low affinity nerve growth factor receptor expression in the rat olfactory system during development and regeneration. *The Journal of Comparative Neurology* **344,** 336–348.

Gorrie CA, Hayward I, Cameron N, Kailainathan G, Nandapalan N, Sutharsan R, Wang J, Mackay-Sim A & Waite PME (2010). Effects of human OEC-derived cell transplants in rodent spinal cord contusion injury. *Brain Res* **1337,** 8–20.

Graziadei PP & Monti Graziadei GA (1980). Neurogenesis and neuron regeneration in the olfactory system of mammals. III. Deafferentation and reinnervation of the olfactory bulb following section of the fila olfactoria in rat. *J Neurocytol* **9,** 145–162.

Graziadei PPC & Monti-Graziadei GA (1978). The olfactory system: a model for the study of neurogenesis and axon regeneration in mammals. *Neuronal plasticity*131–153.

Grubb A (1988). Safer proteinase treatment of sciatica A biochemical preview of chymopapain inhibitors. *Acta Orthop* **59,** 63–65.

Gudiño-Cabrera G & Nieto-Sampedro M (1996). Ensheathing cells: Large scale purification from adult olfactory bulb, freeze-preservation and migration of transplanted cells in adult brain. *Restor Neurol Neurosci* **10,** 25–34.

Guérout N, Derambure C, Drouot L, Bon-Mardion N, Duclos C, Boyer O & Marie J-P (2010). Comparative gene expression profiling of olfactory ensheathing cells from olfactory bulb and olfactory mucosa. *Glia* **58,** 1570–1580.

Guest JD, Herrera L, Margitich I, Oliveria M, Marcillo A & Casas CE (2008). Xenografts of expanded primate olfactory ensheathing glia support transient behavioral recovery that is independent of serotonergic or corticospinal axonal regeneration in nude rats following spinal cord transection. *Exp Neurol* **212,** 261–274.

Guest JD, Rao A, Olson L, Bunge MB & Bunge RP (1997). The ability of human schwann cell grafts to promote regeneration in the transected nude rat spinal cord. *Experimental Neurology* **148,** 502–522.

Gumera C, Rauck B & Wang Y (2011). Materials for central nervous system regeneration: bioactive cues. *J Mater Chem* **21,** 7033.

Hagg T & Oudega M (2006). Degenerative and Spontaneous Regenerative Processes after Spinal Cord Injury. *Journal of Neurotrauma* **23,** 263–280.

Harper L, Costea D, Gammon L, Fazil B, Biddle A & Mackenzie I (2010). Normal and malignant epithelial cells with stem-like properties have an extended G2 cell cycle phase that is associated with apoptotic resistance. *BMC Cancer* **10,** 166.

Hartgerink JD, Beniash E & Stupp SI (2002). Peptide-amphiphile nanofibers: A versatile scaffold for the preparation of self-assembling materials. *Proceedings of the National Academy of Sciences of the United States of America* **99,** 5133–5138.

Hauck TS, Anderson RE, Fischer HC, Newbigging S & Chan WCW (2010). In vivo Quantum-Dot Toxicity Assessment. *Small* **6,** 138–144.

Heckele M & Schomburg WK (2004). Review on micro molding of thermoplastic polymers. *Journal of Micromechanics and Microengineering* **14,** R1–R14.

Hirsch S & Bähr M (1999). Growth promoting and inhibitory effects of glial cells in the mammalian nervous system. *Adv Exp Med Biol* **468,** 199–205.

Hoffman-Kim D, Mitchel JA & Bellamkonda RV (2010). Topography, Cell Response, and Nerve Regeneration. *Annu Rev Biomed Eng* **12,** 203–231.

Holbrook EH, Szumowski KEM & Schwob JE (1995). An immunochemical, ultrastructural, and developmental characterization of the horizontal basal cells of rat olfactory epithelium. *J Comp Neurol* **363,** 129–146.

Houle JD & Johnson JE (1989). Nerve growth factor (NGF)-treated nitrocellulose enhances and directs the regeneration of adult rat dorsal root axons through intraspinal neural tissue transplants. *Neuroscience Letters* **103,** 17–23.

Huang H, Chen L, Wang H, Xi H, Gou C, Zhang J, Zhang F & Liu Y (2006*a*). Safety of fetal olfactory ensheathing cell transplantation in patients with chronic spinal cord injury. A 38-month follow-up with MRI. *Zhongguo xiu fu chong jian wai ke za zhi= Zhongguo xiufu chongjian waike zazhi= Chinese journal of reparative and reconstructive surgery* **20,** 439.

Huang M-C, Chen K-C, Chuang T-Y, Chang W-C, Lee L-S, Huang W-C & Cheng H (2003). Cervical root repair in adult rats after transection: Recovery of forelimb motor function. *Experimental Neurology* **180,** 101–109.

Huang Y, Qi M, Zhang M, Liu H & Yang D (2006*b*). Degradation mechanisms of poly (lactic-co-glycolic acid) films in vitro under static and dynamic environment. *Transactions of Nonferrous Metals Society of China* **16,** s293–s297.

Huang Z, Wang Y, Cao L, Su Z, Zhu Y, Chen Y, Yuan X & He C (2008). Migratory properties of cultured olfactory ensheathing cells by single-cell migration assay. *Cell Res* **18,** 479–490.

Hutmacher DW (2000). Scaffolds in tissue engineering bone and cartilage. *Biomaterials* **21,** 2529–2543.

Ibrahim A, Li Y, Li D, Raisman G & El Masry WS (2006). Olfactory ensheathing cells: ripples of an incoming tide? *The Lancet Neurology* **5,** 453–457.

Ibrahim AG, Kirkwood PA, Raisman G & Li Y (2009). Restoration of hand function in a rat model of repair of brachial plexus injury. *Brain* **132,** 1268–1276.

Imaizumi T, Lankford KL, Burton WV, Fodor WL & Kocsis JD (2000). Xenotransplantation of transgenic pig olfactory ensheathing cells promotes axonal regeneration in rat spinal cord. *Nat Biotechnol* **18,** 949–953.

Imaizumi T, Lankford KL, Waxman SG, Greer CA & Kocsis JD (1998). Transplanted olfactory ensheathing cells remyelinate and enhance axonal conduction in the demyelinated dorsal columns of the rat spinal cord. *J Neurosci* **18,** 6176–6185.

Insausti R, Herrero MT & Witter MP (1997). Entorhinal cortex of the rat: cytoarchitectonic subdivisions and the origin and distribution of cortical efferents. *Hippocampus* **7,** 146–183.

Ito D, Ibanez C, Ogawa H, Franklin RJM & Jeffery ND (2006). Comparison of cell populations derived from canine olfactory bulb and olfactory mucosal cultures. *Am J Vet Res* **67,** 1050–1056.

Ivanco TL & Greenough WT (2000). Physiological consequences of morphologically detectable synaptic plasticity: potential uses for examining recovery following damage. *Neuropharmacology* **39,** 765–776.

Iwatsuki K, Yoshimine T, Kishima H, Aoki M, Yoshimura K, Ishihara M, Ohnishi Y & Lima C (2008). Transplantation of olfactory mucosa following spinal cord injury promotes recovery in rats. *Neuroreport* **19,** 1249–1252.

Jain RA (2000). The manufacturing techniques of various drug loaded biodegradable poly(lactide-co-glycolide) (PLGA) devices. *Biomaterials* **21,** 2475–2490.

Jani HR & Raisman G (2004). Ensheathing cell cultures from the olfactory bulb and mucosa. *Glia* **47,** 130–137.

Jessen KR & Mirsky R (1997). Embryonic Schwann cell development: the biology of Schwann cell precursors and early Schwann cells. *J Anat* **191 (Pt 4),** 501–505.

Josephson L, Kircher MF, Mahmood U, Tang Y & Weissleder R (2002). Near-Infrared Fluorescent Nanoparticles as Combined MR/Optical Imaging Probes. *Bioconjugate Chemistry* **13,** 554–560.

Kapfhammer JP & Raper JA (1987). Collapse of growth cone structure on contact with specific neurites in culture. *J Neurosci* **7,** 201–212.

Katayama S, Horiike M, Hirao K & Tsutsumi N (2002). Structures induced by irradiation of femto-second laser pulse in polymeric materials. *Journal of Polymer Science Part B: Polymer Physics* **40,** 537–544.

Keyvan-Fouladi N, Raisman G & Li Y (2003). Functional repair of the corticospinal tract by delayed transplantation of olfactory ensheathing cells in adult rats. *J Neurosci* **23,** 9428–9434.

Khademhosseini A, Langer R, Borenstein J & Vacanti JP (2006). Microscale technologies for tissue engineering and biology. *Proceedings of the National Academy of Sciences of the United States of America* **103,** 2480–2487.

Kim K, Yu M, Zong X, Chiu J, Fang D, Seo Y-S, Hsiao BS, Chu B & Hadjiargyrou M (2003). Control of degradation rate and hydrophilicity in electrospun non-woven poly(D,L-lactide) nanofiber scaffolds for biomedical applications. *Biomaterials* **24,** 4977–4985.

King VR, Phillips JB, Hunt-Grubbe H, Brown R & Priestley JV (2006). Characterization of non-neuronal elements within fibronectin mats implanted into the damaged adult rat spinal cord. *Biomaterials* **27,** 485.

Kokai F, Niino H & Yabe A (1998). Laser ablation of polysulfone films: a laser ionization TOF mass spectrometric study. *Applied Physics A: Materials Science & Processing* **67,** 607–612.

Koombhongse S, Liu W & Reneker DH (2001). Flat polymer ribbons and other shapes by electrospinning. *Journal of Polymer Science Part B: Polymer Physics* **39,** 2598–2606.

Kosaka K, Toida K, Aika Y & Kosaka T (1998). How simple is the organization of the olfactory glomerulus?: the heterogeneity of so-called periglomerular cells. *Neuroscience research* **30,** 101–110.

Krudewig C, Deschl U & Wewetzer K (2006). Purification and in vitro characterization of adult canine olfactory ensheathing cells. *Cell and Tissue Research* **326,** 687–696.

Kueh JL-L, Raisman G, Li Y, Stevens R & Li D (2011). Comparison of bulbar and mucosal olfactory ensheathing cells using FACS and simultaneous antigenic bivariate cell cycle analysis. *Glia* **59,** 1658–1671.

Lakatos A, Smith PM, Barnett SC & Franklin RJM (2003). Meningeal cells enhance limited CNS remyelination by transplanted olfactory ensheathing cells. *Brain* **126,** 598 –609.

Lamothe G, Muller F, Vital J-M, Goossens D & Barat M (2011). Evolution of spinal cord injuries due to cervical canal stenosis without radiographic evidence of trauma (SCIWORET): A prospective study. *Ann Phys Rehabil Med* **54,** 213–224.

Law S, Raisman G & Li D (2010). Organotypic slice co-cultures reveal that early postnatal hippocampal axons lose the ability to grow along the fimbria, while retaining the ability to invade and arborise in septal neuropil. *Eur J Neurosci* **31,** 1352–1358.

Leifert C & Cassells A (2001). Microbial hazards in plant tissue and cell cultures. *In Vitro Cellular & Developmental Biology - Plant* **37,** 133–138.

Letant SE & Wang TF (2006). Semiconductor Quantum Dot Scintillation under [gamma]-Ray Irradiation. *Nano Lett* **6,** 2877–2880.

Levi A, Guenard V, Aebischer P & Bunge R (1994). The functional characteristics of Schwann cells cultured from human peripheral nerve after transplantation into a gap within the rat sciatic nerve. *J Neurosci* **14,** 1309–1319.

Li D, Field PM & Raisman G (1995). Failure of axon regeneration in postnatal rat entorhinohippocampal slice coculture is due to maturation of the axon, not that of the pathway or target. *Eur J Neurosci* **7,** 1164–1171.

Li D, Field PM & Raisman G (1996). Connectional specification of regenerating entorhinal projection neuron classes cannot be overridden by altered target availability in postnatal organotypic slice co-culture. *Exp Neurol* **142,** 151–160.

Li D, Field PM, Starega U, Li Y & Raisman G (1993). Entorhinal axons project to dentate gyrus in organotypic slice co-culture. *Neuroscience* **52,** 799–813.

Li D, Field PM, Yoshioka N & Raisman G (1994). Axons regenerate with correct specificity in horizontal slice culture of the postnatal rat entorhino-hippocampal system. *Eur J Neurosci* **6,** 1026–1037.

Li D & Xia Y (2004). Electrospinning of Nanofibers: Reinventing the Wheel? *Advanced Materials* **16,** 1151–1170.

Li M, Zhang J, Zhang H, Liu Y, Wang C, Xu X, Tang Y & Yang B (2007). Electrospinning: A Facile Method to Disperse Fluorescent Quantum Dots in

Nanofibers without Förster Resonance Energy Transfer. *Advanced Functional Materials* **17,** 3650–3656.

Li Y, Decherchi P & Raisman G (2003*a*). Transplantation of Olfactory Ensheathing Cells into Spinal Cord Lesions Restores Breathing and Climbing. *J Neurosci* **23,** 727–731.

Li Y, Field PM & Raisman G (1997). Repair of adult rat corticospinal tract by transplants of olfactory ensheathing cells. *Science* **277,** 2000–2002.

Li Y, Field PM & Raisman G (1998). Regeneration of Adult Rat Corticospinal Axons Induced by Transplanted Olfactory Ensheathing Cells. *J Neurosci* **18,** 10514–10524.

Li Y, Field PM & Raisman G (2005*a*). Olfactory ensheathing cells and olfactory nerve fibroblasts maintain continuous open channels for regrowth of olfactory nerve fibres. *Glia* **52,** 245–251.

Li Y, Li D, Khaw PT & Raisman G (2008). Transplanted olfactory ensheathing cells incorporated into the optic nerve head ensheathe retinal ganglion cell axons: possible relevance to glaucoma. *Neurosci Lett* **440,** 251–254.

Li Y, Li D & Raisman G (2005*b*). Interaction of olfactory ensheathing cells with astrocytes may be the key to repair of tract injuries in the spinal cord: The 'pathway hypothesis'. *Journal of Neurocytology* **34,** 343–351.

Li Y, Sauvé Y, Li D, Lund RD & Raisman G (2003*b*). Transplanted olfactory ensheathing cells promote regeneration of cut adult rat optic nerve axons. *J Neurosci* **23,** 7783–7788.

Lim F, Martín-Bermejo MJ, García-Escudero V, Gallego-Hernández MT, García-Gómez A, Rábano A, Díaz-Nido J, Avila J & Moreno-Flores MT (2010). Reversibly immortalized human olfactory ensheathing glia from an elderly donor maintain neuroregenerative capacity. *Glia* **58,** 546–558.

Lim JY & Donahue HJ (2007). Cell Sensing and Response to Micro- and Nanostructured Surfaces Produced by Chemical and Topographic Patterning. *Tissue Engineering* **13,** 1879–1891.

Lima C, Pratas-Vital J, Escada P, Hasse-Ferreira A, Capucho C & Peduzzi JD (2006). Olfactory Mucosa Autografts in Human Spinal Cord Injury: A Pilot Clinical Study. *J Spinal Cord Med* **29,** 191–203.

Lindsay SL, Riddell JS & Barnett SC (2010). Olfactory mucosa for transplant-mediated repair: a complex tissue for a complex injury? *Glia* **58,** 125–134.

Liu H, Edel JB, Bellan LM & Craighead HG (2006). Electrospun polymer nanofibers as subwavelength optical waveguides incorporating quantum dots. *Small* **2,** 495–499.

Lu J, Féron F, Ho SM, Mackay-Sim A & Waite PM (2001). Transplantation of nasal olfactory tissue promotes partial recovery in paraplegic adult rats. *Brain Res* **889,** 344–357.

Lu P, Jones LL & Tuszynski MH (2005). BDNF-expressing marrow stromal cells support extensive axonal growth at sites of spinal cord injury. *Exp Neurol* **191,** 344–360.

Lu P, Yang H, Culbertson M, Graham L, Roskams AJ & Tuszynski MH (2006). Olfactory Ensheathing Cells Do Not Exhibit Unique Migratory or Axonal Growth-Promoting Properties after Spinal Cord Injury. *J Neurosci* **26,** 11120–11130.

Lu P, Yang H, Jones LL, Filbin MT & Tuszynski MH (2004). Combinatorial therapy with neurotrophins and cAMP promotes axonal regeneration beyond sites of spinal cord injury. *J Neurosci* **24,** 6402–6409.

Ma Z, Kotaki M, Inai R & Ramakrishna S (2005). Potential of Nanofiber Matrix as Tissue-Engineering Scaffolds. *Tissue Engineering* **11,** 101–109.

Mackay-Sim A, Féron F, Cochrane J, Bassingthwaighte L, Bayliss C, Davies W, Fronek P, Gray C, Kerr G, Licina P, Nowitzke A, Perry C, Silburn PAS, Urquhart S & Geraghty T (2008). Autologous olfactory ensheathing cell transplantation in human paraplegia: a 3-year clinical trial. *Brain* **131,** 2376–2386.

Mackay-Sim A & St John JA (2011). Olfactory ensheathing cells from the nose: Clinical application in human spinal cord injuries. *Experimental Neurology* **229,** 174–180.

Madigan NN, McMahon S, O'Brien T, Yaszemski MJ & Windebank AJ (2009). Current tissue engineering and novel therapeutic approaches to axonal regeneration following spinal cord injury using polymer scaffolds. *Respiratory Physiology & Neurobiology* **169,** 183–199.

Mahoney MJ & Anseth KS (2006). Three-dimensional growth and function of neural tissue in degradable polyethylene glycol hydrogels. *Biomaterials* **27,** 2265–2274.

Mahoney MJ, Chen RR, Tan J & Mark Saltzman W (2005). The influence of microchannels on neurite growth and architecture. *Biomaterials* **26,** 771–778.

Mapili G, Lu Y, Chen S & Roy K (2005). Laser-layered microfabrication of spatially patterned functionalized tissue-engineering scaffolds. *Journal of biomedical materials research Part B, Applied biomaterials* **75,** 414.

Marino RJ, Ditunno JF Jr, Donovan WH & Maynard F Jr (1999). Neurologic recovery after traumatic spinal cord injury: data from the Model Spinal Cord Injury Systems. *Arch Phys Med Rehabil* **80,** 1391–1396.

Matthews JA, Wnek GE, Simpson DG & Bowlin GL (2002). Electrospinning of collagen nanofibers. *Biomacromolecules* **3,** 232–238.

Mattson MP, Dou P & Kater SB (1988). Outgrowth-regulating actions of glutamate in isolated hippocampal pyramidal neurons. *J Neurosci* **8,** 2087–2100.

Mauck RL, Baker BM, Nerurkar NL, Burdick JA, Li W-J, Tuan RS & Elliott DM (2009). Engineering on the straight and narrow: the mechanics of nanofibrous assemblies for fiber-reinforced tissue regeneration. *Tissue Eng Part B Rev* **15,** 171–193.

McKeon RJ, Schreiber RC, Rudge JS & Silver J (1991). Reduction of neurite outgrowth in a model of glial scarring following CNS injury is correlated with the expression of inhibitory molecules on reactive astrocytes. *J Neurosci* **11,** 3398–3411.

Min BM, Lee G, Kim SH, Nam YS, Lee TS & Park WH (2004). Electrospinning of silk fibroin nanofibers and its effect on the adhesion and spreading of normal human keratinocytes and fibroblasts in vitro. *Biomaterials* **25,** 1289–1297.

Möllers S, Heschel I, Damink LHHO, Schügner F, Deumens R, Müller B, Bozkurt A, Nava JG, Noth J & Brook GA (2009). Cytocompatibility of a Novel, Longitudinally Microstructured Collagen Scaffold Intended for Nerve Tissue Repair. *Tissue Engineering Part A* **15,** 461–472.

Moore MJ, Friedman JA, Lewellyn EB, Mantila SM, Krych AJ, Ameenuddin S, Knight AM, Lu L, Currier BL, Spinner RJ, Marsh RW, Windebank AJ & Yaszemski MJ (2006). Multiple-channel scaffolds to promote spinal cord axon regeneration. *Biomaterials* **27,** 419–429.

Morrissey TK, Kleitman N & Bunge RP (1991). Isolation and functional characterization of Schwann cells derived from adult peripheral nerve. *J Neurosci* **11,** 2433–2442.

Mukhatyar VJ, Salmerón-Sánchez M, Rudra S, Mukhopadaya S, Barker TH, García AJ & Bellamkonda RV (2011). Role of fibronectin in topographical guidance of neurite extension on electrospun fibers. *Biomaterials* **32,** 3958–3968.

Murdoch B & Roskams AJ (2008). A Novel Embryonic Nestin-Expressing Radial Glia-Like Progenitor Gives Rise to Zonally Restricted Olfactory and Vomeronasal Neurons. *J Neurosci* **28,** 4271–4282.

Murrell W, Féron F, Wetzig A, Cameron N, Splatt K, Bellette B, Bianco J, Perry C, Lee G & Mackay-Sim A (2005). Multipotent stem cells from adult olfactory mucosa. *Dev Dyn* **233,** 496–515.

Naber PA, Lopes da Silva FH & Witter MP (2001). Reciprocal connections between the entorhinal cortex and hippocampal fields CA1 and the subiculum are in register with the projections from CA1 to the subiculum. *Hippocampus* **11,** 99–104.

Nash HH, Borke RC & Anders JJ (2001). New method of purification for establishing primary cultures of ensheathing cells from the adult olfactory bulb. *Glia* **34,** 81–87.

Nash HH, Borke RC & Anders JJ (2002). Ensheathing Cells and Methylprednisolone Promote Axonal Regeneration and Functional Recovery in the Lesioned Adult Rat Spinal Cord. *J Neurosci* **22,** 7111–7120.

Nazarov R, Jin HJ & Kaplan DL (2004). Porous 3-D scaffolds from regenerated silk fibroin. *Biomacromolecules* **5,** 718–726.

Nomura H, Tator CH & Shoichet MS (2006). Bioengineered strategies for spinal cord repair. *Journal of Neurotrauma* **23,** 496–507.

Novikova LN, Brohlin M, Kingham PJ, Novikov LN & Wiberg M (2011*a*). Neuroprotective and growth-promoting effects of bone marrow stromal cells after cervical spinal cord injury in adult rats. *Cytotherapy* **13,** 873–887.

Novikova LN, Lobov S, Wiberg M & Novikov LN (2011*b*). Efficacy of olfactory ensheathing cells to support regeneration after spinal cord injury is influenced by method of culture preparation. *Exp Neurol* **229,** 132–142.

Novikova LN, Mosahebi A, Wiberg M, Terenghi G, Kellerth J & Novikov LN (2006). Alginate hydrogel and matrigel as potential cell carriers for neurotransplantation. *Journal of Biomedical Materials Research Part A* **77A,** 242–252.

Paino CL & Bunge MB (1991). Induction of axon growth into schwann cell implants grafted into lesioned adult rat spinal cord. *Experimental Neurology* **114,** 254–257.

Park JW, Vahidi B, Taylor AM, Rhee SW & Jeon NL (2006). Microfluidic culture platform for neuroscience research. *Nat Protoc* **1,** 2128–2136.

Park TG (1994). Degradation of poly(d,l-lactic acid) microspheres: effect of molecular weight. *Journal of Controlled Release* **30,** 161–173.

Pearse DD, Marcillo AE, Oudega M, Lynch MP, Wood PM & Bunge MB (2004). Transplantation of Schwann cells and olfactory ensheathing glia after spinal cord injury: does pretreatment with methylprednisolone and interleukin-10 enhance recovery? *J Neurotrauma* **21,** 1223–1239.

Pearse DD, Sanchez AR, Pereira FC, Andrade CM, Puzis R, Pressman Y, Golden K, Kitay BM, Blits B, Wood PM & Bunge MB (2007). Transplantation of Schwann cells and/or olfactory ensheathing glia into the contused spinal cord: Survival, migration, axon association, and functional recovery. *Glia* **55,** 976–1000.

Plant GW, Christensen CL, Oudega M & Bunge MB (2003). Delayed transplantation of olfactory ensheathing glia promotes sparing/regeneration of supraspinal axons in the contused adult rat spinal cord. *J Neurotrauma* **20,** 1–16.

Pollock GS, Franceschini IA, Graham G, Marchionni MA & Barnett SC (1999). Neuregulin is a mitogen and survival factor for olfactory bulb ensheathing cells and an isoform is produced by astrocytes. *European Journal of Neuroscience* **11,** 769–780.

Pool M, Thiemann J, Bar-Or A & Fournier AE (2008). NeuriteTracer: A novel ImageJ plugin for automated quantification of neurite outgrowth. *Journal of Neuroscience Methods* **168,** 134–139.

Posner JB, Swanson AG & Plum F (1965). Acid-Base Balance In Cerebrospinal Fluid. *Arch Neurol* **12,** 479–496.

Pouw MH, van Middendorp JJ, van Kampen A, Curt A, van de Meent H & Hosman AJF (2011). Diagnostic criteria of traumatic central cord syndrome. Part 3: descriptive analyses of neurological and functional outcomes in a prospective cohort of traumatic motor incomplete tetraplegics. *Spinal Cord* **49,** 614–622.

Prang P, Del Turco D & Kapfhammer JP (2001). Regeneration of entorhinal fibers in mouse slice cultures is age dependent and can be stimulated by NT-4, GDNF, and modulators of G-proteins and protein kinase C. *Exp Neurol* **169,** 135–147.

Qian LM, Zhang ZJ, Gong AH, Qin RJ, Sun XL, Cao XD, Liu JB, Jiang P & Chen YC (2009). A novel biosynthetic hybrid scaffold seeded with olfactory ensheathing cells for treatment of spinal cord injuries. *Chinese medical journal* **122,** 2032.

Radojevic V & Kapfhammer JP (2004). Repair of the entorhino-hippocampal projection in vitro. *Exp Neurol* **188,** 11–19.

Radtke C, Akiyama Y, Brokaw J, Lankford KL, Wewetzer K, Fodor WL & Kocsis JD (2004). Remyelination of the nonhuman primate spinal cord by transplantation of H-transferase transgenic adult pig olfactory ensheathing cells. *FASEB J* **18,** 335–337.

Radtke C, Lankford KL, Wewetzer K, Imaizumi T, Fodor WL & Kocsis JD (2010). Impaired spinal cord remyelination by long-term cultured adult porcine olfactory ensheathing cells correlates with altered in vitro phenotypic properties. *Xenotransplantation* **17,** 71–80.

Radtke C, Sasaki M, Lankford KL, Vogt PM & Kocsis JD (2008). Potential of olfactory ensheathing cells for cell-based therapy in spinal cord injury. *J Rehabil Res Dev* **45,** 141–151.

Rainaldi G, Calcabrini A & Santini MT (1998). Positively charged polymer polylysine-induced cell adhesion molecule redistribution in K562 cells. *Journal of Materials Science: Materials in Medicine* **9,** 755–760.

Raineteau O & Schwab ME (2001). Plasticity of motor systems after incomplete spinal cord injury. *Nat Rev Neurosci* **2,** 263–273.

Raisman G (1969). Neuronal plasticity in the septal nuclei of the adult rat. *Brain Research* **14,** 25–48.

Raisman G (1985). Specialized neuroglial arrangement may explain the capacity of vomeronasal axons to reinnervate central neurons. *Neuroscience* **14,** 237–254.

Raisman G (2001). Olfactory ensheathing cells - another miracle cure for spinal cord injury? *Nat Rev Neurosci* **2,** 369–375.

Raisman G & Li Y (2007). Repair of neural pathways by olfactory ensheathing cells. *Nat Rev Neurosci* **8,** 312–319.

Ramakrishna S, Fujihara K, Teo WE, Lim TC & Ma Z (2005). *An introduction to electrospinning and nanofibers*. World Scientific Pub Co Inc, Singapore.

Ramer LM, Au E, Richter MW, Liu J, Tetzlaff W & Roskams AJ (2004). Peripheral olfactory ensheathing cells reduce scar and cavity formation and promote regeneration after spinal cord injury. *J Comp Neurol* **473,** 1–15.

Ramón-Cueto A (2011). Olfactory ensheathing glia for nervous system repair. *Exp Neurol* **229,** 1.

Ramón-Cueto A, Cordero MI, Santos-Benito FF & Avila J (2000). Functional recovery of paraplegic rats and motor axon regeneration in their spinal cords by olfactory ensheathing glia. *Neuron* **25,** 425–435.

Ramón-Cueto A & Nieto-Sampedro M (1992). Glial cells from adult rat olfactory bulb: immunocytochemical properties of pure cultures of ensheathing cells. *Neuroscience* **47,** 213–220.

Ramón-Cueto A & Nieto-Sampedro M (1994). Regeneration into the spinal cord of transected dorsal root axons is promoted by ensheathing glia transplants. *Exp Neurol* **127,** 232–244.

Ramón-Cueto A, Plant GW, Avila J & Bunge MB (1998). Long-distance axonal regeneration in the transected adult rat spinal cord is promoted by olfactory ensheathing glia transplants. *J Neurosci* **18,** 3803–3815.

Ramón-Cueto A & Valverde F (1995). Olfactory bulb ensheathing glia: a unique cell type with axonal growth-promoting properties. *Glia* **14,** 163–173.

Rege TA & Hagood JS (2006). Thy-1, a versatile modulator of signaling affecting cellular adhesion, proliferation, survival, and cytokine/growth factor responses. *Biochim Biophys Acta* **1763,** 991–999.

Reneker DH & Chun I (1996). Nanometre diameter fibres of polymer, produced by electrospinning. *Nanotechnology* **7,** 216–223.

Richardson PM, Issa VMK & Aguayo AJ (1984). Regeneration of long spinal axons in the rat. *Journal of Neurocytology* **13,** 165–182.

Richter M, Westendorf K & Roskams AJ (2008). Culturing olfactory ensheathing cells from the mouse olfactory epithelium. *Methods Mol Biol* **438,** 95–102.

Richter MW, Fletcher PA, Liu J, Tetzlaff W & Roskams AJ (2005). Lamina propria and olfactory bulb ensheathing cells exhibit differential integration and migration and promote differential axon sprouting in the lesioned spinal cord. *J Neurosci* **25,** 10700–10711.

Richter MW & Roskams AJ (2008). Olfactory ensheathing cell transplantation following spinal cord injury: hype or hope? *Exp Neurol* **209,** 353–367.

Riddell JS, Enriquez-Denton M, Toft A, Fairless R & Barnett SC (2004). Olfactory ensheathing cell grafts have minimal influence on regeneration at the dorsal root entry zone following rhizotomy. *Glia* **47,** 150–167.

Rubio M-P, Muñoz-Quiles C & Ramón-Cueto A (2008). Adult olfactory bulbs from primates provide reliable ensheathing glia for cell therapy. *Glia* **56,** 539–551.

Rudge JS & Silver J (1990). Inhibition of neurite outgrowth on astroglial scars in vitro. *J Neurosci* **10,** 3594–3603.

Santos-Benito FF & Ramón-Cueto A (2003). Olfactory ensheathing glia transplantation: a therapy to promote repair in the mammalian central nervous system. *Anat Rec B New Anat* **271,** 77–85.

Schift H (2008). Nanoimprint lithography: An old story in modern times? A review. *Journal of Vacuum Science & Technology B: Microelectronics and Nanometer Structures* **26,** 458.

Schinstine M & Cornbrooks CJ (1989). Effect of nerve growth factor on the elongation of neurites from axotomized rat embryonic septal-basal forebrain neurons: an in vitro analysis. *J Neurosci Res* **23,** 371–383.

Schliecker G, Schmidt C, Fuchs S & Kissel T (2003). Characterization of a homologous series of D,L-lactic acid oligomers; a mechanistic study on the degradation kinetics in vitro. *Biomaterials* **24,** 3835–3844.

Schmalenberg KE & Uhrich KE (2005). Micropatterned polymer substrates control alignment of proliferating Schwann cells to direct neuronal regeneration. *Biomaterials* **26,** 1423–1430.

Schnell E, Klinkhammer K, Balzer S, Brook G, Klee D, Dalton P & Mey J (2007). Guidance of glial cell migration and axonal growth on electrospun nanofibers of poly-ε-caprolactone and a collagen/poly-ε-caprolactone blend. *Biomaterials* **28,** 3012–3025.

Schwab M & Caroni P (1988). Oligodendrocytes and CNS myelin are nonpermissive substrates for neurite growth and fibroblast spreading in vitro. *J Neurosci* **8,** 2381–2393.

Schwab ME (2010). How hard is the CNS hardware? *Nat Neurosci* **13,** 1444–1446.

Seiler MJ, Aramant RB, Thomas BB, Peng Q, Sadda SR & Keirstead HS (2010). Visual restoration and transplant connectivity in degenerate rats implanted with retinal progenitor sheets. *Eur J Neurosci* **31,** 508–520.

Shen Y, Qian Y, Zhang H, Zuo B, Lu Z, Fan Z, Zhang P, Zhang F & Zhou C (2010). Guidance of Olfactory Ensheathing Cell Growth and Migration on Electrospun Silk Fibroin Scaffolds. *Cell Transplantation* **19,** 147–157.

Shenoy SL, Bates WD, Frisch HL & Wnek GE (2005). Role of chain entanglements on fiber formation during electrospinning of polymer solutions: good solvent, non-specific polymer-polymer interaction limit. *Polymer* **46,** 3372–3384.

Smith PM, Lakatos A, Barnett SC, Jeffery ND & Franklin RJM (2002). Cryopreserved cells isolated from the adult canine olfactory bulb are capable of extensive remyelination following transplantation into the adult rat CNS. *Experimental neurology* **176,** 402–406.

Sniadecki NJ, Desai RA, Ruiz SA & Chen CS (2006). Nanotechnology for cell-substrate interactions. *Ann Biomed Eng* **34,** 59–74.

Sobkowicz HM, Waclawik AJ & August BK (2006). The astroglial cell that guides nerve fibers from growth cone to synapse in organotypic cultures of the fetal mouse spinal cord. *Synapse* **59,** 183–200.

Soleimani M, Nadri S, Salehi M, Sobhani A & Hajarizadeh A (2008). Characterization of fibroblast-like cells from the rat olfactory bulb. *Int J Dev Biol* **52,** 979–984.

Song Y, Zheng Q, Wu Y & Guo X (2009). Two-dimensional effects of hydrogel self-organized from IKVAV-containing peptides on growth and differentiation of NSCs. *Journal of Wuhan University of Technology--Materials Science Edition* **24,** 186–192.

Sorensen A, Moffat K, Thomson C & Barnett SC (2008). Astrocytes, but not olfactory ensheathing cells or Schwann cells, promote myelination of CNS axons in vitro. *Glia* **56,** 750–763.

Srinivasan R & Braren B (1989). Ultraviolet laser ablation of organic polymers. *Chemical Reviews* **89,** 1303–1316.

Steward O, Sharp K, Selvan G, Hadden A, Hofstadter M, Au E & Roskams J (2006). A re-assessment of the consequences of delayed transplantation of olfactory lamina propria following complete spinal cord transection in rats. *Exp Neurol* **198,** 483–499.

Stokols S & Tuszynski MH (2006). Freeze-dried agarose scaffolds with uniaxial channels stimulate and guide linear axonal growth following spinal cord injury. *Biomaterials* **27,** 443–451.

Stoppini L, Buchs P-A & Muller D (1991). A simple method for organotypic cultures of nervous tissue. *Journal of Neuroscience Methods* **37,** 173–182.

Straley KS, Foo CWP & Heilshorn SC (2010). Biomaterial design strategies for the treatment of spinal cord injuries. *J Neurotrauma* **27,** 1–19.

van Strien NM, Cappaert NLM & Witter MP (2009). The anatomy of memory: an interactive overview of the parahippocampal-hippocampal network. *Nat Rev Neurosci* **10,** 272–282.

Sugar J, Witter MP, Strien NM van & Cappaert NLM (2011). The retrosplenial cortex: intrinsic connectivity and connections with the (para)hippocampal region in the rat. An interactive connectome. *Front Neuroinform* **5,** 7.

Sundaray B, Subramanian V, Natarajan TS, Xiang RZ, Chang CC & Fann WS (2004). Electrospinning of continuous aligned polymer fibers. *Applied physics letters* **84,** 1222.

Taboas JM, Maddox RD, Krebsbach PH & Hollister SJ (2003). Indirect solid free form fabrication of local and global porous, biomimetic and composite 3D polymer-ceramic scaffolds. *Biomaterials* **24,** 181–194.

Takami T, Oudega M, Bates ML, Wood PM, Kleitman N & Bunge MB (2002). Schwann Cell But Not Olfactory Ensheathing Glia Transplants Improve Hindlimb Locomotor Performance in the Moderately Contused Adult Rat Thoracic Spinal Cord. *J Neurosci* **22,** 6670–6681.

Taylor AM, Blurton-Jones M, Rhee SW, Cribbs DH, Cotman CW & Jeon NL (2005). A microfluidic culture platform for CNS axonal injury, regeneration and transport. *Nat Methods* **2,** 599–605.

Teng YD, Lavik EB, Qu X, Park KI, Ourednik J, Zurakowski D, Langer R & Snyder EY (2002). Functional recovery following traumatic spinal cord injury mediated by a unique polymer scaffold seeded with neural stem cells. *Proceedings of the National Academy of Sciences of the United States of America* **99,** 3024–3029.

Thanos S, Mey J & Wild M (1993). Treatment of the adult retina with microglia-suppressing factors retards axotomy-induced neuronal degradation and enhances axonal regeneration in vivo and in vitro. *J Neurosci* **13,** 455–466.

Thuret S, Moon LDF & Gage FH (2006). Therapeutic interventions after spinal cord injury. *Nature Reviews Neuroscience* **7,** 628–643.

Timpl R (1996). Macromolecular organization of basement membranes. *Current Opinion in Cell Biology* **8,** 618–624.

Toft A, Scott DT, Barnett SC & Riddell JS (2007). Electrophysiological evidence that olfactory cell transplants improve function after spinal cord injury. *Brain* **130,** 970–984.

Tomé M, Lindsay SL, Riddell JS & Barnett SC (2009). Identification of Nonepithelial Multipotent Cells in the Embryonic Olfactory Mucosa. *Stem Cells* **27,** 2196–2208.

Turner CP & Perez-Polo JR (1992). Regulation of the low affinity receptor for nerve growth factor, p75NGFR, in the olfactory system of neonatal and adult rat. *International Journal of Developmental Neuroscience* **10,** 343–359.

Turner CP & Perez-Polo JR (1994). Changes in expression of the low affinity receptor for neurotrophins, p75NGFR, in the regenerating olfactory system. *International Journal of Developmental Neuroscience* **12,** 767–773.

Tysseling-Mattiace VM, Sahni V, Niece KL, Birch D, Czeisler C, Fehlings MG, Stupp SI & Kessler JA (2008). Self-assembling nanofibers inhibit glial scar formation and promote axon elongation after spinal cord injury. *J Neurosci* **28,** 3814–3823.

Varabhas JS, Chase GG & Reneker DH (2008). Electrospun nanofibers from a porous hollow tube. *Polymer* **49,** 4226–4229.

Varga ZM, Bandtlow CE, Eurlkar SD, Schwab ME & Nicholls JG (1995). The Critical Period for Repair of CNS of Neonatal Opossum (Monodelphis domestica) in Culture: Correlation with Development of Glial Cells, Myelin and Growth-inhibitory Molecules. *European Journal of Neuroscience* **7,** 2119–2129.

Venugopal JR, Zhang Y & Ramakrishna S (2006). In vitro culture of human dermal fibroblasts on electrospun polycaprolactone collagen nanofibrous membrane. *Artificial organs* **30,** 440–446.

Vidal-Sanz M, Bray GM, Villegas-Pérez MP, Thanos S & Aguayo AJ (1987). Axonal regeneration and synapse formation in the superior colliculus by retinal ganglion cells in the adult rat. *J Neurosci* **7,** 2894–2909.

Vincent AJ, Taylor JM, Choi-Lundberg DL, West AK & Chuah MI (2005). Genetic expression profile of olfactory ensheathing cells is distinct from that of Schwann cells and astrocytes. *Glia* **51,** 132–147.

Waeckerle-Men Y & Groettrup M (2005). PLGA microspheres for improved antigen delivery to dendritic cells as cellular vaccines. *Advanced Drug Delivery Reviews* **57,** 475–482.

Wang B, Zhao Y, Lin H, Chen B, Zhang J, Zhang J, Wang X, Zhao W & Dai J (2006). Phenotypical analysis of adult rat olfactory ensheathing cells on 3-D collagen scaffolds. *Neuroscience letters* **401,** 65–70.

Watt FM, Jordan PW & O'Neill CH (1988). Cell shape controls terminal differentiation of human epidermal keratinocytes. *Proceedings of the National Academy of Sciences of the United States of America* **85,** 5576–5580.

Weiss P (1934). In vitro experiments on the factors determining the course of the outgrowing nerve fiber. *Journal of experimental Zoology* **68,** 393–448.

Werbowetski-Ogilvie TE, Bosse M, Stewart M, Schnerch A, Ramos-Mejia V, Rouleau A, Wynder T, Smith M-J, Dingwall S, Carter T, Williams C, Harris C, Dolling J, Wynder C, Boreham D & Bhatia M (2009). Characterization of human embryonic stem cells with features of neoplastic progression. *Nat Biotech* **27,** 91–97.

Wewetzer K, Radtke C, Kocsis J & Baumgärtner W (2011). Species-specific control of cellular proliferation and the impact of large animal models for the use of olfactory ensheathing cells and Schwann cells in spinal cord repair. *Exp Neurol* **229,** 80–87.

Wewetzer K, Verdú E, Angelov D & Navarro X (2002). Olfactory ensheathing glia and Schwann cells: two of a kind? *Cell and Tissue Research* **309,** 337–345.

Windus LCE, Lineburg KE, Scott SE, Claxton C, Mackay-Sim A, Key B & St John JA (2010). Lamellipodia mediate the heterogeneity of central olfactory ensheathing cell interactions. *Cell Mol Life Sci* **67,** 1735–1750.

Wise DL (2000). *Biomaterials and bioengineering handbook*. Marcel Dekker.

Wong DY, Leveque J-C, Brumblay H, Krebsbach PH, Hollister SJ & LaMarca F (2008). Macro-Architectures in Spinal Cord Scaffold Implants Influence Regeneration. *Journal of Neurotrauma* **25,** 1027–1037.

Wood P, Schachner M & Bunge R (1990). Inhibition of Schwann cell myelination in vitro by antibody to the L1 adhesion molecule. *J Neurosci* **10,** 3635–3645.

Wu C, Shi L, Li Q, Jiang H, Selke M, Ba L & Wang X (2010). Probing the Dynamic Effect of Cys-CdTe Quantum Dots toward Cancer Cells in Vitro. *Chemical Research in Toxicology* **23,** 82–88.

Xia Y, Rogers JA, Paul KE & Whitesides GM (1999). Unconventional Methods for Fabricating and Patterning Nanostructures. *Chemical Reviews* **99,** 1823–1848.

Xie J, Willerth SM, Li X, Macewan MR, Rader A, Sakiyama-Elbert SE & Xia Y (2009). The differentiation of embryonic stem cells seeded on electrospun nanofibers into neural lineages. *Biomaterials* **30,** 354–362.

Xu H, Shao Z, Wu Y, Deng C, Yu X, Ding F, Zhang B & Xu W (2009). [Effects of self-assembled IKVAV peptide nanofibers on olfactory ensheathing cells]. *Sheng Wu Gong Cheng Xue Bao* **25,** 292–298.

Xu XM, Chen A, Guénard V, Kleitman N & Bunge MB (1997). Bridging Schwann cell transplants promote axonal regeneration from both the rostral and caudal stumps of transected adult rat spinal cord. *Journal of Neurocytology* **26,** 1–16.

Xu XM, Guenard V, Kleitman N, Aebischer P & Bunge MB (1995). A combination of BDNF and NT-3 promotes supraspinal axonal regeneration into Schwann cell grafts in adult rat thoracic spinal cord. *Experimental Neurology* **134,** 261–272.

Yamamoto M, Raisman G, Li D & Li Y (2009). Transplanted olfactory mucosal cells restore paw reaching function without regeneration of severed corticospinal tract fibres across the lesion. *Brain Res* **1303,** 26–31.

Yu JH, Fridrikh SV & Rutledge GC (2006). The role of elasticity in the formation of electrospun fibers. *Polymer* **47,** 4789–4797.

Zhang Y & Barres BA (2010). Astrocyte heterogeneity: an underappreciated topic in neurobiology. *Curr Opin Neurobiol* **20,** 588–594.

Zhang Y, Ouyang H, Lim CT, Ramakrishna S & Huang ZM (2004). Electrospinning of gelatin fibers and gelatin/PCL composite fibrous scaffolds. *Journal of Biomedical Materials Research Part B: Applied Biomaterials* **72,** 156–165.

Zhu X, Cui W, Li X & Jin Y (2008). Electrospun Fibrous Mats with High Porosity as Potential Scaffolds for Skin Tissue Engineering. *Biomacromolecules* **9,** 1795–1801.